CONTRIBUTION TO THE DEVELOPMENT OF NEW PHOTONIC SYSTEMS FOR FIBER OPTIC SENSING APPLICATIONS

PhD. dissertation by Mikel Bravo Acha
Supervisor: Prof. Dr. Manuel López-Amo Sainz
Pamplona, 2015

upna
Universidad
Pública de Navarra
Nafarroako
Unibertsitate Publikoa

upna
Universidad
Pública de Navarra
Nafarroako
Unibertsitate Publikoa

reconocimientos

Este trabajo se ha llevado a cabo gracias a las aportaciones económicas recibidas de los siguientes organismos y empresas:

- Secretaría de Estado de Investigación, Desarrollo e Innovación, Ministerio de Economía y Competitividad de España a través del programa de Formación del Personal Investigador y asociado al proyecto de investigación TEC2010-20224-C02-01.

- Grupo de investigación de Comunicaciones Ópticas y Aplicaciones Electrónicas de la Universidad Pública de Navarra mediante la financiación de material y participación en congresos.

- Universidad Pública de Navarra mediante las ayudas a tesis doctorares.

- Acción Europea COST- TD1001: Novel and Reliable Optical Fibre Sensor Systems for Future Security and Safety Applications (OFSeSa)

- También se ha recibido financiación del Proyecto de Investigación de la Secretaría de Estado de Investigación, Desarrollo e Innovación, Ministerio de Economía y Competitividad de España TEC2013-47264-C2-2-R, de Innocampus, del Proyecto Europeo SUDOE-ECOAL-Intereg Project ECOAL-MGT y de los Fondos FEDER.

- Eurocontratas S. A.

- Asfaltos y Construcciones del Baztán S. L.

agradecimientos

Es complicado agradecer en unas simples líneas todo el apoyo que he recibido de todos los que me rodean. Han sido varios años de dedicación a esta tesis en los que mucha gente ha colaborado activa, pasiva y moralmente.

En primer lugar, nada hubiese sido posible sin el continuo apoyo, motivación y empuje de mi director de tesis, el profesor Manuel López-Amo Sainz. O como nosotros lo conocemos, Manolo. Él ha sido mi padre en la ciencia, el cual se ha esforzado por darnos, a mí y al resto del grupo, los mejores equipos, financiación y viajes. También nos ha defendido ante todos los problemas que se nos han presentado. Por otro lado, es una parte fundamental de esta tesis, tanto científica como literariamente. Ha sido un lujo disfrutar de las numerosas reuniones en las que desarrollábamos los trabajos aquí descritos.

Tampoco podría haberse concluido este trabajo sin el apoyo del resto del grupo de investigación. Rosa Ana Pérez, Cesar Elosua, Santi Tainta, Daniel Leandro, Ander Zornoza, Alayn Loayssa, Mikel Sagues, Javier Urricelqui, Jon Mariñelarena... Seguro que me olvido de alguien... Como no, debo un agradecimiento especial a mis estrechos colaboradores. Montse Fernández, con la que he pasado innumerables horas en el laboratorio y ha dado un toque elegante a mis trabajos. Xabier Angulo que, aunque pertenece a otro grupo y universidad, ha sido como de la familia. Hemos disfrutado mucho dentro y fuera del trabajo. No puedo dejar a Ana Pinto, la portuguesa. ¡Como son los físicos! Disfrutamos mucho en las discusiones y birras científicas en compañía de Sergio Rota, mi gran amigo y apoyo durante todos estos años.

This thesis has not only taken place in Pamplona. I have been lucky enough to visit two fantastic abroad laboratories where I met great people with which I share huge moments. First of all, people form INESC laboratories in the wonderful city of Porto, Portugal. I want to thank prof. José Luis Santos, prof. José Manuel Baptista and Dr. Orlando Frazao their warm welcome in their group. I want also to acknowledge the great moments enjoyed with the "FPAE": Susana, Carlos, Marta, Ricardo, Pedro Jorge, Hugo and, in special, to the fantastic "pitonisa", my friend Luisa. Muito obrigado amigos.

I have been also visiting City University laboratories in the awesome city of London. I am very grateful to prof. Tong Sun her hospitality during my stay as a member of the Sensors and Photonics group. I also met the very nice people who formed the group, in special Shanika, Matthias, Colum, Martin, Stephen, Miodrag, Bochao, Xao and Shuo.

También quiero agradecer al resto de personas de diferentes instituciones con las que he trabajado que, finalmente, son parte activa de esta tesis. Investigadores visitantes como Angel Ullan y Alessandro Candiani. Colaboradores como Miguel Gonzalez y Sonia Martín y miembros de la propia universidad como Miguel Angel Erro y Jose Mari Algueta. De diferentes empresas a Javier Saenz de Eurocontratas y Julen Rodríguez de Urkolaser por toda la ayuda y consejos recibidos. También agradecer a Santi De Miguel su ayuda técnica en muchos de los trabajos y su buen humor.

Fuera del ámbito de la universidad, hablando en varias ocasiones con Sergio sobre la tesis, hemos comentado que esto es una carrera de fondo y hay que saber guardar fuerzas. En mi caso una parte importante de desconexión y recarga de pilas durante este tiempo ha sido la Agrupación Navarra de Astronomía. La astronomía es una gran afición que me ha permitido abstraerme de este mundo poniéndome los pies en la Tierra. Todos estos momentos los he pasado en compañía de mis compañeros Natxo, Iñigo, Aurelio, Bea, Gonzalo, Satur, Iñaki, Carlos y otros muchos con los que he aprendido a aprender sobre nuestro universo.

Del mismo modo, muchos amigos han sufrido las grandes "chapas" sobre la fibra, la tesis y mis penas. Por un lado está la cuadrilla de Deba: Mariño, Varela, Feijoo, Aitor, Esnaola, Gorka, Osa... ¡hasta 30 "Txerritxuletas" que somos! También la gente de Pamplona que ha vivido más de cerca todo el proceso: Mónica, Blanca, Paola, Leo y en especial a Javi.

Finalmente, mi familia. Sin duda alguna, el pilar más importante. Siempre me han dicho que a la familia no se elije, te toca. Pues a mí me ha tocado la lotería. Agradecer a mis padres Mª Nieves y Manuel todo el apoyo incondicional que nos regalan día a día al resto de la familia. He de reconocer que sin su esfuerzo y tesón a lo largo de mi vida, nunca podría haber llegado a este punto. Aun esforzándome al máximo, sería imposible explicar lo mucho que me han dado. Principalmente, en cuestión de valores y educación. Mis hermanos, que decir... También son parte esencial de la tesis. Cada uno con su granito de arena han aportado su toque a esta tesis. Ana con la edición, Imanol con el inglés y Miriam con que entre en el traje el día de la presentación. El trabajo más duro, sin duda, lo tiene Miriam. Finalmente esta familia, como nos vamos haciendo viejos, la cierran la cuadrilla de sobrinos que tengo. Lorena, Eneko, Miren y Lucas que han tenido durante unos meses un tío un poco ausente.

Nuestra familia no solo se queda en los Bravo Acha. Somos una gran familia repartida por el país. Los Bravo en la parte sur y los Acha en el Norte. Como ya he comentado antes, es una gran suerte pertenecer a esta familia. Geográficamente, la relación con los

Acha ha sido más estrecha y han sido parte importante durante todos estos años. Por ejemplo, el germen de esta tesis se formó en una comida cuando mi tío Juan Antonio me retó a ver si era capaz de pesar camiones con fibra óptica. Es un placer disfrutar de sobremesas con una familia tan heterogénea en la cual siempre se aprende y surgen grandes cosas.

Finalmente, agradecer y dedicar esta tesis a mi abuela Joaquina, la Amoma. Es un punto de referencia personal y familiar. Es nuestra Estrella Polar.

resumen

En este trabajo de doctorado se presentan nuevos sistemas y subsistemas de sensores de fibra óptica. Así, se proponen y desarrollan nuevas técnicas, componentes y tecnologías basadas en láseres de fibra con espejos distribuidos (random), fibras de cristal fotónico, estructuras de luz lenta, multiplexores de inserción y extracción (add and drop), conmutadores tele-alimentados por luz, reflectometría óptica tanto en el dominio del tiempo como de la frecuencia o filtros ópticos reconfigurables. También se han demostrado nuevas aplicaciones para estructuras de sensores tradicionales y técnicas de medida ya conocidas. Todas ellas dirigidas a la mejora del funcionamiento de los actuales transductores, redes de sensores y aplicaciones de monitorización de salud estructural.

De este modo, y en primer lugar, se han desarrollado nuevos transductores puntuales. En concreto, dos sensores interferométricos basados en fibras de cristal fotónico y otro basado en una estructura resonante en anillo.

También se han realizado diferentes redes de sensores utilizando OTDRs comerciales. Por un lado, se han multiplexado diferentes sensores utilizando una red en forma de bus y, por el otro, se ha interrogado de manera remota un sensor FLM/LPG a una distancia de 253 km sin necesidad de amplificación.

Se han estudiado láseres basados en efecto de realimentación distribuida random (RDFB) para su uso en interrogación de sensores. Para ello, se han demostrado dos nuevos láseres multilongitud de onda y también, por primera vez, se ha modulado un laser random.

Después, se han demostrado experimentalmente varias redes de sensores de fibra óptica teniendo en cuenta los principales desafíos que estas presentan: multiplexar varios sensores en una misma red y permitir su monitorización de manera remota. En primer lugar, se han multiplexado sensores basados en la modulación de la intensidad óptica utilizando técnicas de multiplexación en dominio del tiempo. En segundo lugar, se han multiplexado sensores basados en fibras de cristal fotónico. En tercer lugar, se presentan tres nuevos métodos para la medida remota de sensores. Por último, se incluye la demostración de un conmutador de fibra óptica tele-alimentado a través de luz. Éste se utiliza en tres redes diferentes para añadir robustez e incrementar la versatilidad en la multiplexación.

Finalmente, se han realizado tres pruebas de campo para aplicaciones de monitorización de salud estructural.

abstract

In this PhD work, different new photonic systems and subsystems for fiber optic sensing are presented. The aim of this thesis has been to contribute to the fiber optic sensors field using modern techniques, components and technologies such as random fiber lasers, photonic crystal fibers, slow light structures, add and drop multiplexers, powered by light switches, optical frequency and time domain reflectometry or reconfigurable optical filters, among others. New applications of traditional sensing structures or techniques have been also demonstrated. All of them focused on improving the performance of current sensors transducers, multiplexing networks and structural health monitoring applications.

Thus, new point transducers have been developed: two of them are interferometric sensors based on photonic crystal fibers; and another one is based on a fiber ring resonator structure.

Fiber optic sensor networks using commercial OTDRs have been also explored. On the one hand, different sensors have been successfully multiplexed in the same bus network. And, on the other hand, a FLM/LPG sensor was remotely interrogated at a distance of 253 km without using amplification.

Random distributed feedback (RDFB) lasers have been explored for sensors interrogation. Two multi-wavelength Raman fiber lasers suitable for sensors interrogation have been demonstrated. Also, a random fiber laser has been internally modulated for the first time.

Then, some experimental demonstrations of fiber optic sensors networks have been carried out taking into account the principal challenges they pose: multiplexing a number of optical sensors in a single networks, and enabling the possibility of remote sensing. Firstly, intensity sensors using TDM technology have been multiplexed. Secondly, PCF sensors have been successfully multiplexed. Thirdly, three new approaches to enable remote sensing are presented. Finally, a remote powered by light fiber optic switch have been included in three networks in order to add robustness and multiplexing versatility.

Finally, three different in field applications for SHM have been experimentally demonstrated.

list of figures

CHAPTER I. OVERVIEW OF THE BASIC TECHNOLOGIES EMPLOYED

CHAPTER II. DEVELOPMENT OF NEW FIBER OPTIC SENSING HEADS

CHAPTER III. FIBER OPTIC DOMAIN REFLECTOMETRY FOR SENSORS INTERROGATION

CHAPTER IV. RANDOM DISTRIBUTE FEEDBACK FIBER OPTIC LASERS

CHAPTER V. FIBER OPTIC SENSOR NETWORKS

CHAPTER VI. THREE APPLICATIONS OF FIBER OPTIC SENSORS IN SHM

list of tables

CHAPTER I. OVERVIEW OF THE BASIC TECHNOLOGIES EMPLOYED

CHAPTER VI. THREE APPLICATIONS OF FIBER OPTIC SENSORS IN SHM

index of contents

chapter I
OVERVIEW OF THE BASIC TECHNOLOGIES EMPLOYED

INTRODUCTION

This chapter is mainly devoted to introduce briefly the most important concepts of fiber optic sensor (FOS) technology and related optical techniques which have been used in the following chapters. Because this overview is far from complete, an extensive bibliography about the actual state of the art is provided.

Fiber optic sensors and the systems surrounding this technology are basically based on the light propagation along the cylindrical dielectric waveguide called optical fiber. Therefore, this chapter is open by briefly introducing the light propagation through the fibers and their characteristics. Next, a general classification of the fiber optic sensors is presented in combination with some of the sensing technologies used along the manuscript. It is also shown the special propagation characteristics and properties of the photonic crystal fibers before introducing one important element used in this PhD work, the fiber optic laser. Finally, fiber optic sensor networks are introduced.

1.1. FIBER OPTIC LIGHT PROPAGATION AND ITS USE IN FIBER OPTIC SENSING

Optical communication fibers' development in the last of 20th century revolutionized fields as telecommunications and sensing, leading to the creation of high sensitivity and controlled systems based on light guidance.

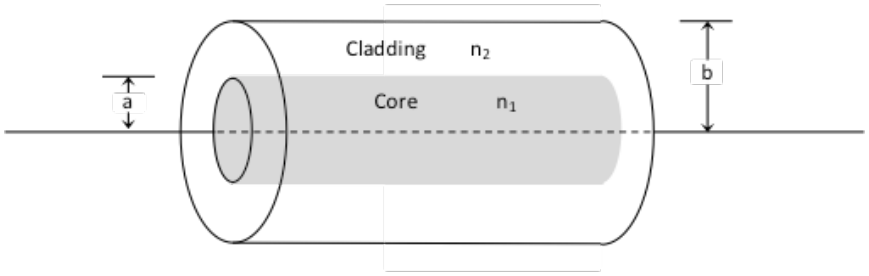

Figure 1.1 Schematic diagram of an optical fiber.

An optical fiber is a cylindrical dielectric waveguide made of low-loss materials such as silica glass. It has a central core in which the light is guided, embedded into an outer cladding of slightly lower refractive index $n_2<n_1$ (figure 1.1). The light travels along the axis of the waveguide carried by modes; having each mode a distinct propagation constant (β) and group velocity (v_g), maintaining its transverse spatial distribution and its polarization. When the core diameter is small enough, and for a certain wavelength only a single propagation mode (HE_{11}) is permitted, the fiber is said to be a single-mode fiber. Fibers with larger core diameters are called multi-mode fibers because several propagation modes travel through the waveguide. Taking into account the refractive index variation between the cladding and the core, there are two classical types of fiber: step-index, when the refractive index at the core-cladding interface changes abruptly and, graded-index, when the refractive index decreases gradually inside the core [1].

The propagation of light in optical fibers is governed by Maxwell's equations. The solutions to these equations for step-index fibers (see ref [2]), taking into account fibers´ birefringence, loss and non-linear effects; define the propagation characteristics that can be usually seen as an issue for communications. However, birefringence, loss and non-lineal effects have been used to develop sensors from long ago. In this Ph.D. work these effects will be also used in new sensing structures.

1.1.1 Birefringence

Optical fibers exhibit a variation in the shape of their core along the fiber length. They may also experience non-uniform stress which varies the cylindrical symmetry of the fiber. Therefore, degeneracy between the orthogonally polarized fiber modes is removed and consequently, the fiber acquires birefringence. The degree of modal birefringence is defined by

$$B_m = |\bar{n}_x - \bar{n}_y| \qquad (1.1)$$

Where $\bar{n}_x$ and $\bar{n}_y$ are the mode effective indices for the orthogonally polarized fiber modes. Birefringence leads to a periodic power exchange between the two polarization components. This period is defined as the beat length and is given by

$$L_B = \lambda / B_m \qquad (1.2)$$

There are fibers in which a large amount of birefringence is introduced intentionally, called polarization-maintaining fibers or high-birefringence (HiBi) fibers. Thus, small random birefringence fluctuations do not significantly affect the light polarization. On the other hand, the velocities´ difference between the two polarization components results in a phase shift between the fast and the slow modes [2].

1.1.2 Fiber Loss

Fiber loss represents a limiting factor in optical waveguides because they reduce the optical power reaching the fiber end. The fiber loss is represented by the attenuation coefficient (α) usually expressed in dB/km and relates the input power with the output power.

Fiber loss is also dependent on the wavelength of the transmitted light. Figure 1.2 illustrates the loss spectrum $\alpha(\lambda)$ of a single-mode fiber. The lowest value, ranging around 0.2 dB/km, is exhibited in the wavelength region near 1.55 μm. This value is close to the fundamental limit of about 0.16 dB/km for silica fibers [2]. Several factors contribute to overall losses. The two most important among them are material absorption and Rayleigh scattering.

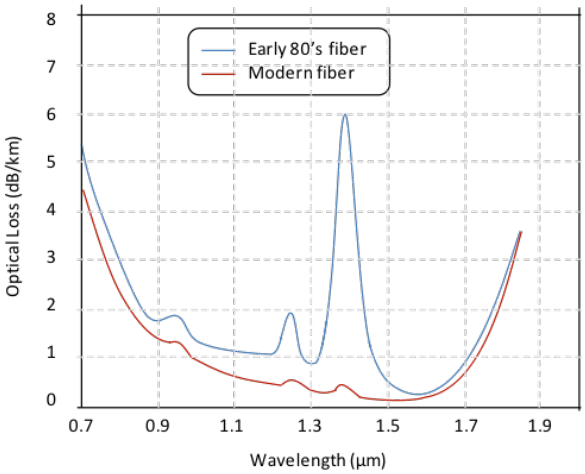

Figure 1.2. Loss spectrum of single-mode fibers.

Material absorption can be divided in two categories. Intrinsic absorption losses correspond to absorption by fused silica, for instance, UV absorption, IR absorption and Rayleigh scattering. Extrinsic absorption is related to losses caused by impurities within silica. For example, the impurities of residual water vapor in silica (OH^-). The three spectral peaks seen in figure 1.2 are due to the presence of this OH^- ions in silica. In current fibers the OH^- ion concentration is reduced to such low levels that the 1.39 μm peak almost disappears as the red trace of figure 1.2 depicts [3].

Rayleigh scattering is a fundamental loss mechanism arising from local microscopic material inhomogeneities taking place during fiber fabrication. Density fluctuations lead to random fluctuations of the refractive index on a scale smaller than the optical wavelength λ. Light scattering in such a medium is known as Rayleigh scattering [4]. The intrinsic loss of silica fibers from Rayleigh scattering can be written as

$$\alpha_R = C/\lambda^4 \qquad (1.3)$$

where the constant C ranges from 0.7 to 0.9 (dB/km)/μm^{-4}, depending on the constituents of the fiber core. The Rayleigh scattering is characterized as elastic scattering. This means that the scattered photons maintain their energy, therefore having the same frequency as the incident light. A part of the scattered light is not radiated; it is back-

scattered along the fiber. The Rayleigh backscattered light is the basis for some fiber optic reflectometric devices, random distributed feedback lasers and distributed sensor systems.

Imperfections or external perturbations also contribute to reduce the optical power in the fiber. Imperfections at the core-cladding interface can lead to additional losses (e.g., random core-radius border variations). An important loss mechanism used for fiber optic sensor systems are the fiber bends. Two kinds of bending in fibers are usually studied: micro and macro-bends. A bend is considered as a micro-bend when the bending radius is comparable or lower than the fiber diameter. On the contrary, when the bending radius is bigger than the fiber diameter, it is usual to consider that the fiber is suffering macro-bend losses. The bending loss is proportional to $exp(-R/R_c)$, where R is the radius of curvature of the fiber bend and $R_c = a/(n_1^2 - n_2^2)$. For single-mode fibers, R_c = 0.2 - 0.4 μm typically, thus, the bending loss is negligible for bending radius R > 5 mm.

Finally, many other sources of optical loss may exist in a fiber cable. These are used to be related to splices and connectors used to deploy a fiber link or network. [2]

1.1.3 Nonlinear effects in fiber optics

Due to the waveguide geometry that confines light to a small cross section over long fiber lengths, it results in important nonlinear effects in silica fibers. The nonlinear effects briefly explained below have high influence in the applications presented in following chapters.

Since light does not travel in free space or vacuum, it interacts with the material and different effects appear due to these interactions. As mentioned above, Rayleigh scattering is characterized as an elastic scattering. Other scattering effects, commonly observed in high power conditions, are called inelastic scattering effects. In those cases, the scattered photons have different frequency since energy transference arises from or to the medium. From a quantum mechanical point of view, it is the interaction between photons, that is, discrete quantities of light and medium excitation respectively. When the scattered photons are down-shifted in frequency, they are usually known as Stokes components. On the contrary, when they are up-shifted, so the incident photons gain energy from the medium, they are called anti-Stokes components.

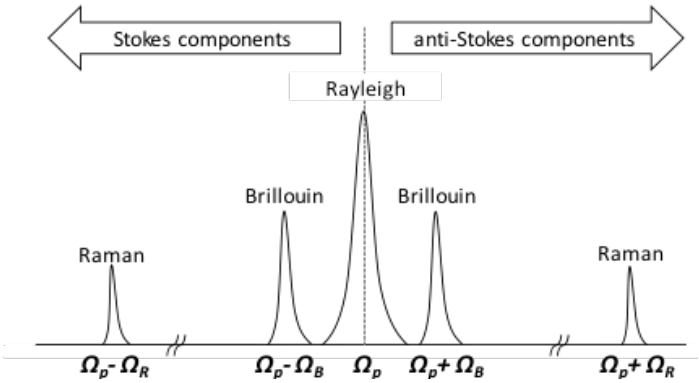

Figure 1.3. Spectral components of the scattered light in an inhomogeneous medium.

There are two inelastic scattering processes, Brillouin and Raman scattering. Brillouin scattering is originated by propagating pressure waves, originated by acoustic phonons, which frequency shift is determined by the acoustic velocity in the medium. The physical process behind this effect is the tendency of materials to become compressed in the presence of an electric field, a phenomenon termed electrostriction [5]. For an oscillating electric field at the pump frequency Ω_p, this process generates an acoustic wave at some frequency Ω. Spontaneous Brillouin scattering can be viewed as scattering of the pump wave from this acoustic wave, resulting in creation of a new wave at frequency Ω_s. Below, two expressions which define two important parameters of the SBS are presented. The mathematical development of both equations can be found in references [2, 6]. The first parameter refers to the Brillouin frequency shift (BFS) and it is given by:

$$\nu_B = \Omega_B / 2\pi = (2\bar{n}\nu_A) / \lambda_p \qquad (1.4)$$

where $\bar{n}$ is the fundamental mode's effective refractive index, ν_A is the acoustic velocity of the pressure wave in the medium and λ_p is the pump wavelength. Another important parameter is the SBS gain (g_B). It depends on frequency because of finite damping time T_B of acoustic waves (the photons' lifetime). If the acoustic waves decay as $\exp(-t/T_B)$, the Brillouin gain shows a Lorentzian spectral profile given by [7]

$$g_B(\Omega) = \frac{g_B(\Omega_B)}{1 + (\Omega - \Omega_B)^2 T_B^2} \qquad (1.5)$$

SBS analysis in time domain is a successful technique for distributed sensing using standard optical fibers as will be presented. Although its gain spectrum is limited ($\Delta\nu_B \approx 50$ MHz), these nonlinear processes can be also used as an amplification source for different applications [8].

Stimulated Raman scattering occurs in optical fibers when an intense pump wave is scattered by the silica molecules. This effect is the result of the interaction between the light wave and the optical vibration modes of the molecules constituting the material. Some pump photons give up their energy to create other photons of reduced energy at a lower frequency; the remaining energy is absorbed by silica molecules, which end up in an excited vibrational state.

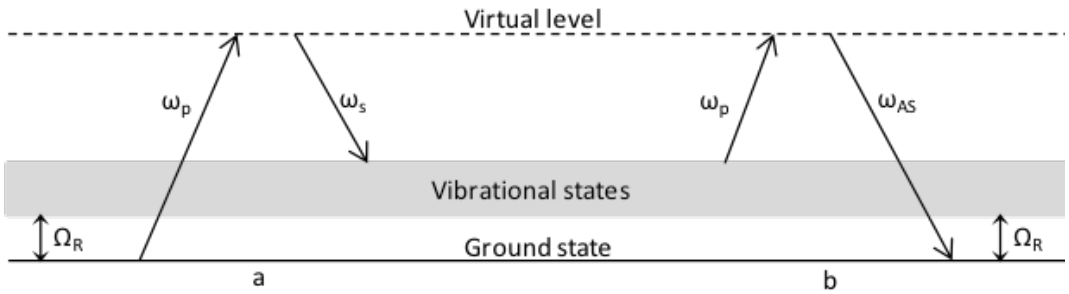

Figure 1.4. Energy diagram of the spontaneous Raman scattering process. a) Stokes and b) anti-Stokes scattering.

For the continuous wave case, the evolution of the pump power (P_p) and signal power (P_s) along the longitudinal axis of the fiber z can be expressed by the following equations

$$\frac{dP_s}{dz} = g_R P_p P_s - \alpha_s P_s \qquad (1.6)$$

$$\frac{dP_p}{dz} = -\frac{\omega_p}{\omega_s} g_R P_p P_s - \alpha_p P_p \qquad (1.7)$$

where g_R is the Raman gain coefficient (the material gain coefficient, $g_R \approx 6.6 \times 10^{-14}$ m/W at 1550 nm for silica fibers), α_p and α_s are the attenuation coefficients at the pump and signal wavelengths, and ω_p and ω_s are the angular frequencies of the pump and signal. The first term of both equations represents the signal gain due to Raman scattering and the second term the intrinsic loss.

The threshold power P_{th} is defined as the incident power at which half of the pump power is transferred to the Stokes field at the output end of a fiber of length L.

$$P_{th} \approx \frac{16A_{eff}}{g_r L_{eff}} \qquad (1.8)$$

where A_{eff} is the effective area of the pump power inside the fiber in square meters and L_{eff} is the fiber effective interaction length in meters [9, 10]

1.2. TYPES OF FIBER OPTIC SENSORS

Since the early 1970s, when some of the first experiments on low-loss optical fibers were performed for sensing purposes, many fiber optic sensors (FOS) for different applications have been developed. In table 1.1 it is presented an optical fiber sensors' classification. The classification is divided into four groups: the magnitude to be measured, the spatial distribution of the measurements, the nature of the transduction, and the modulation induced by the measurement.

Table 1.1: Classification of fiber optic sensors

FIBER OPTIC SENSORS				
Magnitude to be measured		Spatial distribution	Transduction mechanism	Measurand induced modulation
Physical	Bio Chemical			
Curvature / bend	Gas	Point	Intrinsic	Intensity (amplitude)
Displacement/strain	Molecular	Distributed	Extrinsic	Interferometric (phase)
Electromagnetic	DNA	Quasi distributed		Polarimetric (polarization)
Pressure	Protein			Spectroscopy (wavelength)
Temperature	Humidity and pH			
Torsion/twist				
Transversal load				
Refractive index				
Vibration				

The principal advantages of fiber optic sensors are the following:

- Electromagnetically passive.
- Chemically and biologically inert.
- Small-sized and light-weighted.
- Distributed sensing capability.
- Remote sensing capability.
- Sensor multiplexing using fiber optic networks.

Due to the previous characteristics, over the past three decades, fiber optic sensors have undergone a transition from basic lab. prototypes to commercial products. A broad variety of commercial sensors and instruments are nowadays available, which enjoy increased acceptance and widespread use in different fields and industries. FOS solutions are commonly used in real-life applications including the structural sensing and health monitoring of materials and constructions, pressure and temperature sensors for oil and gas reservoir monitoring, high voltage and high current sensing systems for the power industry and biomedical patient devices, among others [11]. Subsequently, some of the sensing technologies developed during the past are briefly presented to introduce the main concepts that will be used in the following chapters.

The first sensor to be mentioned had an enormous impact since the early 90s and also nowadays. It is one of the most popular technologies for fiber optic sensing applications: the fiber Bragg grating [12].

Next, sensors based on interferences will be presented and, finally, the mature technology of the intensity sensors and, in particular, bending based sensors will be detailed.

1.2.1. Fiber Bragg Gratings

A FBG consists of a periodic perturbation of the refractive index along a fiber length which is created by exposing the core to an intense optical interference pattern. FBGs can be used as narrowband filters/reflectors and have been reported for measurements of strain, temperature, pressure, dynamic electric or magnetic fields, vibrations, certain chemical effects and others. Figure 1.5 shows the working principle of the FBG. The following equation represents the resonant wavelength value of the Bragg structure

$$\lambda_{Bragg} = 2n_{eff}\,\Lambda \qquad (1.9)$$

where n_{eff} is the effective refractive index of the fiber core and Λ (pitch) is the repetition period of the refractive index modulation. Thus, when the incident light is equal to the λ_{Bragg}, an amount of light proportional to the reflectivity of the structure is reflected and the rest is transmitted.

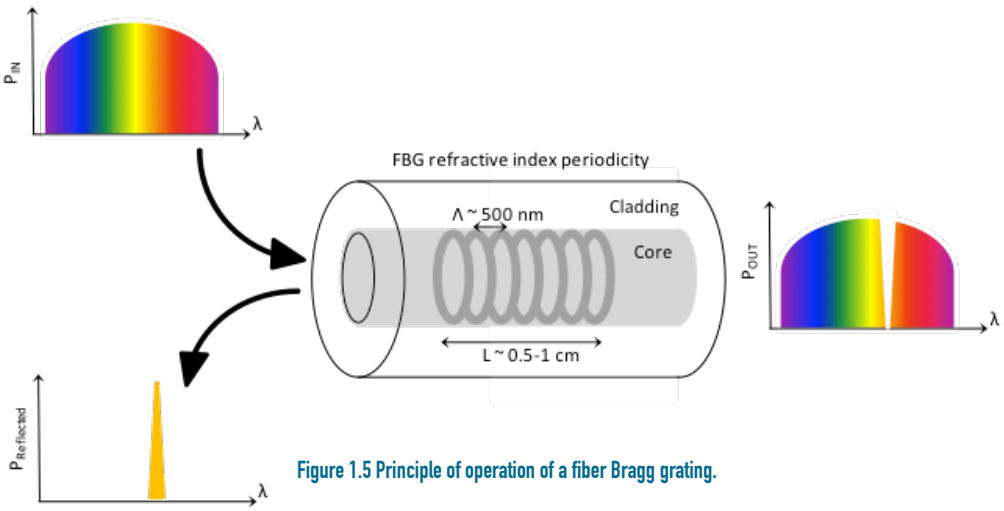

Figure 1.5 Principle of operation of a fiber Bragg grating.

The FBG central wavelength varies with the change of the aforesaid parameters. As strain and temperature have been so far the dominating measurands of interest, we will analyze the corresponding wavelength variations [13, 14].

Strain directly affects the response of FBGs, through the expansion and compression of the grating pitch size and also through the strain-optic effect. That is, the strain induced modifications of the refractive index due to photo-elastics effects. The relative wavelength shift, $\Delta\lambda_B$, for an applied longitudinal strain $\Delta\varepsilon$ is given by

$$\Delta\lambda_B = \lambda_B (1 - \rho_\alpha)\Delta\varepsilon \qquad (1.10)$$

where ρ_α is the photo-elastic coefficient of the fiber defined by

$$\rho_\alpha = \frac{n^2}{2}[\rho_{12} - \nu(\rho_{11}+\rho_{12})] \qquad (1.11)$$

Where ρ_{11} and ρ_{12} are the components of the fiber optic strain tensor, *n* is the RI (refractive index) of the core and ν is the Poisson's ratio. For a typical optical fiber, $\rho_{11} = 0.113$, $\rho_{12} = 0.252$, $\nu = 0.16$ and $n = 1.482$. Substituting these values in equations 1.10 and 1.11 the measured strain response at constant temperature is found to be:

$$\frac{1}{\lambda_B}\frac{\Delta\lambda_B}{\Delta\varepsilon} = 0.7873x10^{-6}\ \mu\varepsilon^{-1} \qquad (1.12)$$

Thus, for a 1 $\mu\varepsilon$ of deformation applied to the fiber at ~1550 nm, a wavelength shift of 1.22 pm/$\mu\varepsilon$ is achieved [15].

On the other hand, the temperature sensitivity of an FBG occurs principally due to the thermal expansion of the grating spacing and the RI. The wavelength shift for a temperature change ΔT may be written as

$$\Delta\lambda_B = \lambda_B\,(\alpha + \xi)\,\Delta T \qquad (1.13)$$

where α is the thermal expansion coefficient for the fiber and ξ represents the thermo-optic coefficient. Because the temperature sensitivity of a bare fiber is primarily due by the thermo-optic effect, the normalized thermal sensitivity at constant strain is

$$\frac{1}{\lambda_B}\frac{\Delta\lambda_B}{\Delta T} = 6.7x10^{-6}\ ^{\circ}C^{-1} \qquad (1.14)$$

For a 1550 nm FBG, the temperature sensitivity obtained by previous equation is 10.3 pm/°C [16].

Finally, in order to interrogate the FBG sensors, there are different techniques depending on: the type of application and range to be measured, accuracy and sensitivity required, number of sensors being interrogated and cost of the instrumentation.
Fiber Bragg gratings sensors have been utilized for a wide variety of mechanical sensing applications including monitoring of civil structures, smart manufacturing, non-destructive testing, remote sensing, smart structures, as well as traditional strain, pressure and temperature applications [17-24]

There are 3 main types of FBG sensor interrogation techniques. Passive detection schemes, active detection schemes and other schemes such as wavelength-tunable sources, mode locked fiber lasers with wavelength-time conversion, frequency modulation... Interrogation techniques are required to extract the measurand information from the optical signal. Depending on the complexity of the interrogation technique, the resolution, dynamic range or multiplexing capability varies. Table 1.2 shows an interrogation types summary.

Table 1.2: FBG interrogation alternatives

FIBER GRATING SENSORS INTERROGATION TYPES [26]		
Year / ref.	Types	Technologies
1997/[25]	Passive detection schemes	Linearly wavelength-dependent device
1997/[26]	"	Identical chirped-grating pair
2000/[27]	"	Power detection
2002/[28]	"	CCD spectrometer
1996/[29]	Active detection schemes	Michelson interferometer
1998/[30]	"	Matched FBG pair
1999/[31]	"	Fiber Fourier transform spectrometer
1999/[32]	"	Fabry–Perot filter
2000/[33]	"	Acousto-optic tunable filter
2000/[34]	"	Unbalanced Mach–Zehnder interferometer
2000/[35]	"	LPG pair interferometer
1996/[36]	Other schemes	Intra-grating sensing
1997/[37]	"	Mode-locked fiber laser with wavelength-time conversion
1998/[38]	"	Wavelength-tunable source
1999/[39]	"	Optical CDMA correlator
1999/[40]	"	Frequency modulation

1.2.2 Fiber optic interferometers and their use as sensors

The use of interferometers in optical measurement has been well established for many decades. These structures have a long history and the creation of the fiber optic equivalent of bulk-optic interferometric systems for displacement monitoring was a natural development following the introduction of low-loss optical fiber, to enable a range of remote measurements to be taken [41].

A fiber optic interferometer uses the interference between two or multiple beams that have propagated through different optical paths of a single fiber or different fibers. So, they require beam splitting and beam combining components in each configuration [42]. For fiber optic sensing, one of the optical paths should be arranged to be easily affected by external perturbations. Since the interferometers give a lot of temporal and spectral information inside their signal, the measurand can be quantitatively determined by different ways of detecting the changes. Thus, interferometers can be used by analyzing their wavelength response, or their phase or intensity. They can show a remarkable performance obtaining large dynamic ranges, high accuracy, and high sensitivity [43, 44].

The main representative types of fiber optic interferometers are called Mach-Zehnder, Michelson, fiber-Fizeau, ring resonator and Sagnac interferometers, as well as the multiple beam fiber Fabry-Perot. Interferometric sensors have been developed for measuring a number of parameters such as strain, acoustic pressure, magnetic and electric fields, acceleration, hydrostatic pressure, temperature, flow and various other measurands [45].

1.2.2.1 Sagnac interferometer

Fiber Sagnac interferometers have been extensively investigated, because of their wide applications in many fields such as fiber optic gyros and other fiber optic interferometric sensors [46]. The basic idea, firstly demonstrated by Georges Sagnac in 1913 [47], consists of the light from an optical source that is divided through a beam splitter such that it propagates in opposite directions around a loop. If that loop is rotated, a phase shift between the propagating and counter propagating fields occurs and, thus, an interference at the splitter. In consequence, Sagnac basic structure detects rotation. The original Sagnac structure, created in bulk optics, can be translated to fiber optics technology by using a common directional optical coupler (Figure 1.6) as beam splitter and a high birefringence fiber into the loop. In this case, the phase shift between the polarization states is now the origin of the interference. This special Sagnac structure is commonly known as high-birefringence fiber loop mirror (HiBi-FLM)

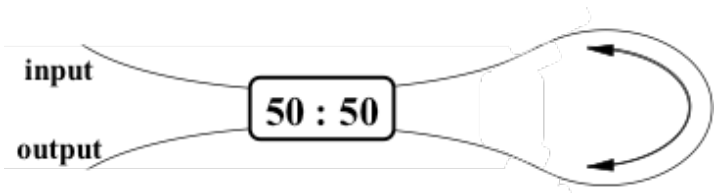

Figure. 1.6. Schematic depiction of the basic structure of a fiber loop mirror.

Fiber loop mirror basic structure is shown in figure 1.6. It consists of a loop of optical fiber formed between the output ports of a directional coupler. D. B. Mortimore thoroughly studied this structure in [48] and, when birefringence is considered in the mathematical development of the Jones matrix for this birefringence situation, the transmission coefficient between the input and output port at wavelength λ is as follows:

$$T = [\sin \theta \cos (\pi l \lambda_0 / (L_B \lambda)]^2 \qquad (1.15)$$

where L_B refers to the fiber beat length at wavelength λ_0, l is the HiBi fiber length and $\theta = \theta_1 + \theta_2$ that denotes the difference between the rotation angle of the polarization states before and after the HiBi fiber section [49]. Thus, the polarization angle dependence limits the transmission coefficient. It should not be forgotten that there is a reflection coefficient in the input port involved that is the inverse of the transmission coefficient (R = 1 - T). By simulating a HiBi FLM structure of 2 meters length of a high birefringence fiber with a beat length of 3.45 mm, the result of the simulation for a center wavelength of 1550 nm is depicted in figure 1.7.

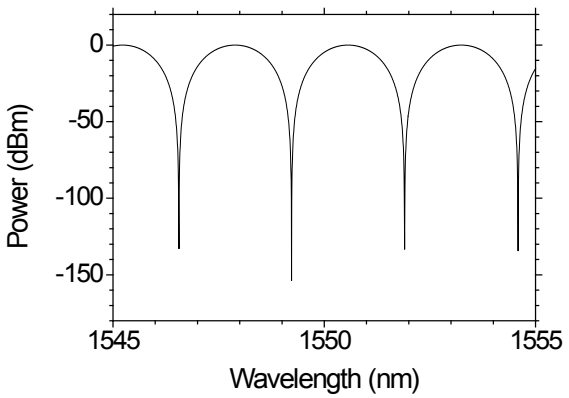

Figure 1.7. Simulated interference pattern for the transmission coefficient.

Therefore, extrapolating these concepts to the fiber optic sensing field, the Sagnac interferometer can be used as sensor by changing the phase between the propagating and counter propagating fields or the birefringence of the fiber and, thus, the phase between both propagation directions resulting in a phase shift in the interfe-

rence. The main and most used magnitude measured with a Sagnac interferometer is the gyroscope but other magnitudes as strain, temperature and pressure, among others can be measured with this structure.

1.2.2.2 Fiber ring resonators

Ring resonators use transverse coupling to bring about multiple circulations of power inside a mirrorless cavity. There is power storage on resonance. The frequency response is similar to that of a Fabry-Perot etalon.

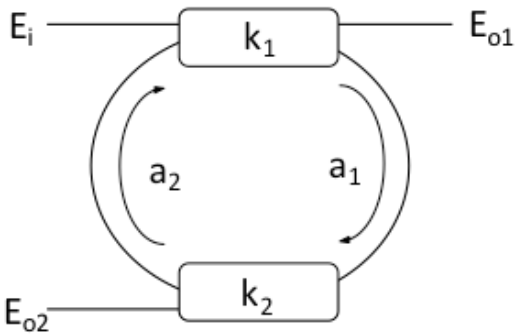

Figure 1.8. Schematic diagram of a basic ring resonator structure.

Both channel blocking and channel-passing filtering responses are possible if the rings are designed appropriately. In channel blocking there is a high output off resonance and a low output on resonance; it is characteristic of a Fabry-Perot resonator used in reflection. In channel passing the opposite applies; it is characteristic of a Fabry-Perot resonator used in transmission. A kind of ring that can demonstrate both types of filtering is shown in figure 1.8. In all cases the input used is the top left-hand port. Channel-blocking filtering is obtained from the top right-hand port, and channel-passing filtering is obtained from the bottom left-hand port [50]. Both filtering spectra are defined by the following expressions [51]:

$$\frac{E_{o1}}{E_{\iota}} = \frac{k_1 \exp\left(\frac{iwnL}{c}\right) - k_2 a_1 a_2}{\exp\left(\frac{iwnL}{c}\right) - k_1 k_2 a_1 a_2} \qquad (1.16)$$

$$\frac{E_{o2}}{E_{\iota}} = 1 - \frac{k_1 \exp\left(\frac{iwnL}{c}\right) - k_2 a_1 a_2}{\exp\left(\frac{iwnL}{c}\right) - k_1 k_2 a_1 a_2} (1-k_2)\, a_1 \qquad (1.17)$$

In the case of a ring of $k_1 = k_2 = 0.9$, and the ring length meters, the simulated results are as figure 1.9 depicts.

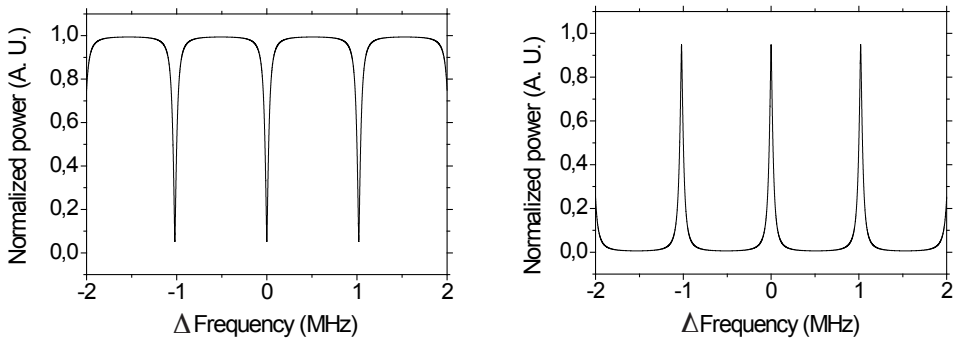

Figure 1.9. Simulated transfer functions of the transmitted and reflected resonances of the ring structure.

1.2.2.3 All fiber multimode interferometers

In the past, multimode interference theory has been utilized in the design and fabrication of devices such as modulators [52] and Mach–Zehnder switches [53]. For an input field centered symmetrically around the optical axis incident on the input facet of a multimode fiber (MMF), multimode interference effects result in periodic longitudinal locations within the fiber where the source field is duplicated. Through characterization of this reimaging effect in a MMF, it is possible to design and fabricate a device that provides a mechanism to overcome the natural tendency for the light to diverge when exiting the fiber [54].

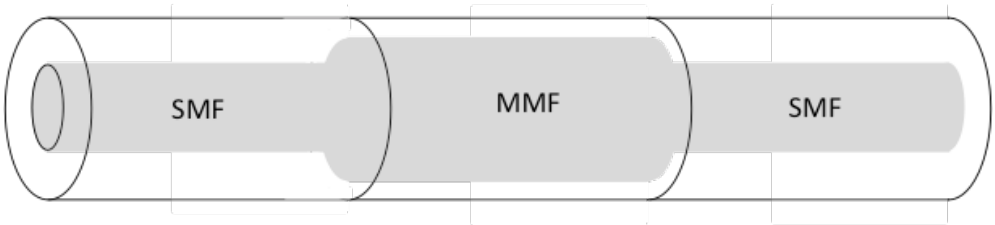

Figure 1.10. Basic structure of an all fiber SMF-MMF-SMF interferometer.

The multimode interference can be achieved by creating structures such as the single-mode, multimode, single-mode (SMF-MMF-SMF) structure (figure 1.10). The single mode guided into a SMF is coupled to the different propagation modes of a multimode fiber. These modes travel independently through the MMF and they will recombine in the second MMF-SMF interface interfering proportionally to the phase shift of the different propagation modes of the MMF [55].

This structure has been extensively used as sensor transducer for many parameters such as refractive index [56], bending [57], temperature [58], strain [59] and others.

1.2.3 Intensity modulation sensors

Fiber optic transducers that use the intensity of the transmitted signal for sensing was one of the first proposed families of sensors due to its simple working principle. All of them relate light's intensity variations with the perturbations to be measured.

Intensity modulated fiber sensors can be classified in different types. A first one may be the measured parameter, for instance, fiber displacement sensors. In a first configuration, two optical fibers are occupied for this measurement and are placed in series with each other. Alternatively, a reflective configuration may be used for displacement measurements. The source and detecting fibers are placed in parallel with each other while the reflective target object (which moves) is placed in a close distance to the fiber ends. Another type of intensity sensors that measure displacement is the shutter-modulated sensor. This includes the methods of shutter, grating, optical wedge, fringe tracking (counting), moving lens and optical micro-switch.

Other intensity sensors can be used for measuring different parameters. For example, the evanescent field sensor. It involves the phenomenon of frustrated total reflection method. Some of the above mentioned sensors will be explained in deep next, as well as the bending sensors. This last kind of sensors use the modulation of the transmitted light by bending the fiber [60].

The bending sensor is one of the earliest utilized fiber optic sensors. Bending losses have always been a problem to the cable designer. However, this issue in optical fibers is exploited by the sensor designer who has adapted the bending effect to the measurement of many physical magnitudes. These magnitudes include displacement, pressure, strain, vibration, temperature, humidity and others [61].

Sensors based on bending loss in optical fibers were firstly proposed and demonstrated in 1980 [62], [63], although careful experiments done earlier had demonstrated vibration-induced intensity modulation of light in bent fibers [64]. Since this early work, much has been done to understand microbend sensors and to investigate how to increase dynamic range and to improve the sensitivity to the parameter to be measured while reducing sensitivity to unwanted variables [65].

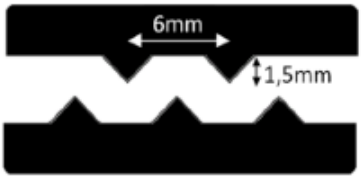

Figure 1.11. Diagram of a couple of microbending plates for the development of displacement or force sensors.

In 1987 [66], an analysis about the operation of microbend sensors was presented by Lagakos *et al.* They derived some very useful equations for bending sensors modeling and design (figure 1.11 shows an example of a microbender). The change in light transmission, T, through a microbend sensor can be written as

$$\Delta T = \left(\frac{\Delta T}{\Delta X}\right) \Delta F \left(k_f + \frac{A_s Y_s}{l_s} \right)^{-1} \qquad (1.18)$$

where ΔX is the displacement of the deforming plates, $\Delta T/\Delta X$ is the sensitivity (slope of the transmission versus displacement response curve for a microbender), ΔF is the applied force, A_s, Y_s and l_s, are the area, Young's modulus, and thickness of the spacer material between the deformer plates, and k_f is the effective spring constant of the optical fiber clamped between the deforming plates

$$k_f^{-1} = \frac{\Lambda^3}{3\pi Y d^4 \eta} \qquad (1.19)$$

where Λ is the deforming tooth spacing, Y is the Young's modulus for the glass, d is the fiber diameter and η refers to the number of bends [65].The technique of bending losses has been successfully applied to the measurement of many magnitudes, including displacement [67], pressure [68], strain [69, 70], vibration [71], temperature [72] and humidity [73].

1.2.4 Photonic crystal fibers sensors

Since 1996 [74] a new kind of special silica fibers characterized by a periodic arrangement of air-holes running along the entire length of the fiber has been developed. Those fibers are called Photonic Crystal Fibers (PCF).

Their geometry is characterized by a micro-structured air-hole cladding running along the entire length of the fiber surrounding the core. Although all fibers that fulfill this condition are called micro-structured, only those which exhibit a photonic band gap light guidance must be called PCF [75]. However, it is easy to find ambiguous definitions in the literature. Even, the scientist who discovered these fibers, consider the modified total internal reflection as guidance mechanism in PCF [76]. Hence, in this PhD work we assume that all fibers that confine light by a periodic arrangement of air holes are PCF.

As so, PCFs can be divided in two families based on their geometry: solid-core and hollow-core PCFs. Solid-core PCFs, as can be deducted from the name, present a solid-core surrounded by a periodic array of microscopic air holes, running along its entire length (Figure 1.12 a). Hollow-core photonic crystal fibers present an air hole as the core being surrounded by a micro-structured air hole cladding (Figure 1.12 b).

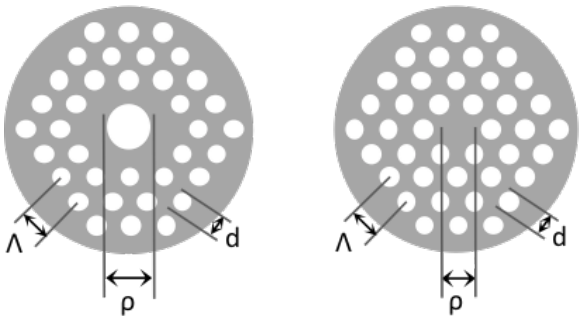

Figure 1.12. Schematic diagram of the solid (a) and hollow core (b) photonic crystal fibers.

The major difference between both kinds of fibers relies on the fact that the waveguide properties of photonic crystal fibers are not due to spatially varying glass composition, as in conventional fibers, but from an arrangement of very tiny and closely spaced air-holes which go through the whole fiber length.

In contrast with standard optical fibers, photonic crystal fibers can be made of a single material and have several geometric parameters that can be manipulated offering great flexibility of design. Even more, photonic crystal fibers offer also the possibility of light guiding in a hollow-core, and opened new perspectives in fields such as nonlinear fiber optics, fiber lasers, supercontinuum generation, particle guidance, and fiber sensors [77-79].

The modes guiding mechanism is characterized by the normalized frequency or simply the V-parameter. The generalized V-parameter for PCFs is defined by [75, 80]

$$V_{gen} = \frac{2\pi}{\lambda} \Lambda \sqrt{n_{co}^2 - n_{cl(PCF)}^2} \qquad (1.20)$$

where Λ is the pitch (interhole spacing), n_{co} is the core refractive index and $n_{cl(PCF)}$ is the cladding effective refractive index. $n_{cl(PCF)}$ is defined as the root-mean-square area average of the materials refractive indices used to construct a particular geometrical shape of photonic crystal. This parameter plays an important role in determining the modes cutoff condition. Therefore, the guiding properties of a PCF can be tuned by changing the basic design's parameters: the pitch (Λ) the core's diameter (ρ) and the holes' diameter (d).

Despite of its youth in the sensing field, PCFs have stimulated the interest of many scientific groups due to their promising characteristics. The main attraction in PCFs is that by varying the size and location of the cladding holes and/or the core, the fiber transmission spectrum, mode shape, nonlinearities, dispersion, air filling fraction and birefringence, among others, can be tuned to reach values that are not achievable with conventional fibers. Additionally, the existence of air holes gives the possibility of light propagation in air, or alternatively provides the ability to insert liquids/gases into the air holes [77].

Due to the PCFs diversity of features, they introduce a large number of new applications in the fiber optic sensing field [81]. PCF fibers has been used in different structures and interrogation schemes to measure a large amount of parameters such as curvature/bending [82], displacement/strain [83, 84], electric and magnetic field [85], pressure [86], temperature [87], torsion/twisting [88], transversal loading [89], refractive index [90], vibration [91], multi-parameter [92], gasses [93], molecular [94], humidity [95] and pH [96].

In the framework of this PhD work, the birefringence characteristic of PCFs was exploited for displacement and strain measurements as well as multi-wavelength lasing generation. Birefringence in PCFs, like SMF, is achieved when the refractive indices seen by the polarization components of a LP mode are quite different. It is generally obtained due to an asymmetric distribution of the effective refractive index, dependent on the size and spatial distribution of the air holes. The first high birefringence PCF was presented in 2000 [97].

Therefore, when a HiBi-PCF is inserted into an inter-polarization based interferometer, birefringence variations due to external perturbations are measured. In that way, displacement and strain measurements can be developed. Furthermore, this interference pattern can be used as comb filter, for example, in multi-wavelength lasing applications [98-100], as will be shown in chapter 4.

1.3. FIBER OPTIC LASERS

Albert Einstein described the theory of stimulated emission already in 1917 [101]. By stimulated emission is understood that a photon can force an atomic transition from an excited energy state by emitting a second photon with the same properties (phase, energy, polarization, and direction) as the first one. Using this process, an ensemble of many of the same photons can be generated when passing them through an excited medium, i.e., having a population inversion, forming a state of coherent light [102]. This technology was not applied in the fiber laser field until Elias Snitzer's proposal in 1961 [103]. The initial emphasis was focused in neodymium (Nd) based fiber lasers due to the high efficiency. Soon thereafter, erbium-doped fiber lasers appeared as the best option. The first Er-doped fiber laser was developed in 1985 by Mears *et al.* [104]. Since that time, Er-doped fiber laser has attracted the attention of the research community due to the radiative transmission around 1550 nm corresponding to the lowest loss for silica fibers [105]. Regardless, other rare-earth ions have been also used as dopants in silica or fluoride fibers, allowing new lasing or pumping wavelengths [106]. Finally, other amplification processes based on stimulated scattering non-linear effects can be also used as gain medium for fiber lasers development. The Raman amplification is an appealing effect for this purpose [13].

A basic fiber laser scheme requires of two key elements. A gain material that provides amplification and an optical cavity that traps the light creating a positive feedback. Thus, the total gain of the amplification must overcome the total cavity loss to achieve the lasing condition. Depending on the gain medium, different fiber lasers can be obtained.

Rare earths as neodymium, praseodymium, ytterbium, samarium or thulium are used as gain medium for fiber optic lasing but the most extended doped fiber for amplification purposes is the erbium doped one. Erbium doped fiber laser (EDFL) will be discussed in this section more in depth. Brillouin and Raman nonlinear effects can be also used as amplification medium for laser applications. In this PhD work, Raman´s effect has been also used in fiber optic lasers structures.

In order to control the emission wavelength of a fiber laser, different filters are usually placed into the laser cavities. FBG, already presented in point 1.2.1 for sensing purposes, are the most extended filters due to the wavelength selective reflective characteristic. They play the role of high reflective mirror and narrow band filter. Other kind of filters can be used in fiber optic laser development such as the ones based on Fabry-Perot, Sagnac loop mirror, Fox-Smith interferometer, ring resonator, SM-MM-SM interferometric structures and others. In this context, by combining different FBG reflectors, the fringe pattern of the interferometers or other kind of filters into the laser cavity, it can be created multi-wavelength fiber lasers (MWFL). This kind of lasers are characterized by simultaneously generate more than one coherent wavelength in a single cavity. Such optical sources offer a high number of channels over large wavelength span, moderate output powers with good OSNR and spectral flatness. They can also achieve single longitudinal mode operation of each laser line, tunability and accurate positioning on the ITU specification frequency grid [107, 108].

In this way, fiber lasers, in comparison with solid-state and gas laser systems, are simpler, more compact, reliable and can be pumped with diodes. If they are compared with laser diodes, they are spectrally cleaner and can be modulated with less chirp and signal distortion; having a 100% coupling compatibility with optical fiber devices and networks. Thus some of the merits of fiber lasers are [13]:

- High pump intensity.
- Signal and pump light waveguiding.
- Independence of pump spot size and gain medium length.
- Compact gain medium.
- Good heat dissipation.
- Beam quality.
- Robustness.
- Easy design.

On the other hand, fiber lasers also face a number of challenges:

- Limitations due to nonlinear effects.
- Risk of fiber damage with high pump powers.

- Difficult short resonators developing.
- Complex maintenance.

Diverse design parameters have to be taken into consideration in order to obtain appropriate fiber lasers for each application. Amplification type, number of emission lines, output power requirements and cavity architecture are some of the key parameters for a proper fiber laser development.

1.3.1 Types of fiber optic laser cavities

The most used configurations to design the fiber cavity lasers are the Fabry-Perot-cavity (or linear-cavity) and ring-cavities. The main difference between them is the path of light. Light in Fabry-Perot-cavities bounces back and forth between two mirrors. On the other hand, in ring cavities, light does round trips (in opposite directions if no optical isolator is introduced into the cavity, as shown in Fig. 1.13.b).

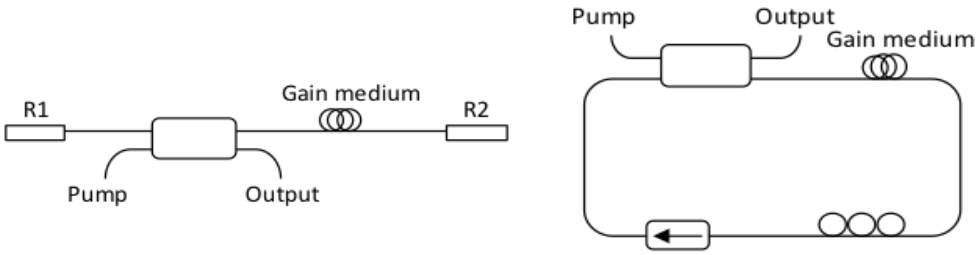

Figure 1.13 Two basic designs of fiber lasers, a) linear and b) ring

Figure 1.13 illustrates two basic schemes for the Fabry-Perot and ring cavities in fiber lasers. Fabry-Perot cavities are made by placing the gain medium between two high-reflecting mirrors. The main advantages are its simplicity and the possibility to make very short cavities. Linear cavities are ideal for compact single-longitudinal mode lasers and for high power applications [13, 105].

Ring cavities are mirror-less structures. Usually ring cavities use the gain provided by the gain medium more efficiently and have a cavity free spectral range twice as large for the same cavity length, compared to linear cavity lasers [105]. As was explained before, by using a narrowband filter inside the ring, a wavelength selection can be performed.

Finally, it is possible hybrid configurations by combining ring and linear cavities [109] or other kind of resonators as the Fox-Smith used in [105]

1.3.2. Erbium-doped fiber laser

Erbium-doped fiber lasers radiating at about 1550 nm are especially important for applications in telecommunications or sensing that take advantage of the low losses in silica fibers [110]. Owing to their versatility, useful gain bandwidths, high pumping efficiency, low intrinsic noise and low gain dependence on light polarization, EDFAs are the most extended amplifiers for many network applications. They are optical amplifiers that consist of a single mode optical fiber whose core has been doped with erbium.

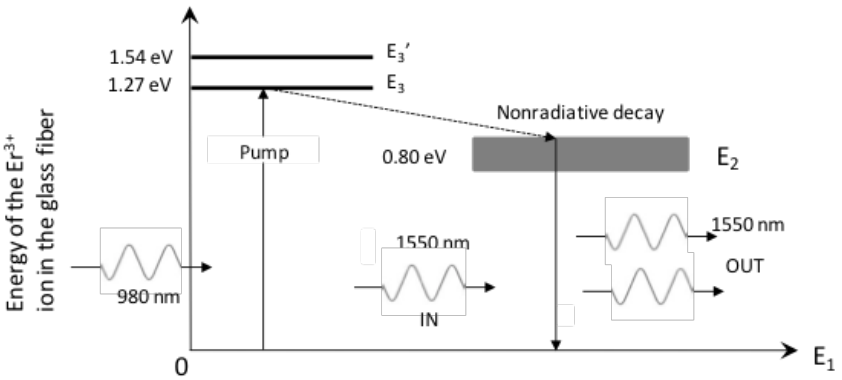

Figure 1.14 Schematic energy diagram for the Er_3^+ ion in the glass fiber medium and light amplification process.

There are three different situations in the interaction of the materials with light. Firstly, when an input photon induces a transition from the upper energy level into the lower one (stimulated emission) an additional photon will be produced with the same properties as the stimulating photon and thus, amplifying the signal intensity. On the other hand, when an input photon induces a transition from the lower level to the upper one the photon is absorbed by the material. Finally, the random transition between a higher level and a lower one is called spontaneous emission. This spontaneous emission in amplifying fibers is called amplified spontaneous emission (ASE). Therefore, for amplification and laser applications the desired situation is when the electrons are placed in the higher level to achieve the stimulated emission. This condition is known as population inversion and it is obtained by illuminating or pumping the material.

In the case of the erbium-doped fiber the population inversion occurs when the fiber is pumped by, in the most efficient case, a wavelength at 980 nm. Thus, these photons are absorbed by the material and excite the electrons to higher levels achieving the population inversion that allows the amplification process. This process is illustrated in figure 1.14. When the Er_3^+ is pumped, its electrons are excited to the highest levels labeled E_3' and E_3. The electrons decay rapidly from this levels in a radiationless transition to a long-lived energy level at E_2 which has a lifetime of about ~10 ms. So, the electrons are accumulated at E_2 which is 0.80 eV above the ground level. Signal photons at 1550 nm have energy of 0.80 eV, or E_2-E_1, and give rise to stimulated transitions of electrons from E_2 to E_1.

The principal applications of EDFLs cover from sensing to telecommunications fields. Some examples are wavelength-division multiplexed sources, fiber-optic sensors, optical signal processing, sensor network schemes, optical spectroscopy, soliton sources, etc. [111-115]. Up to date, a number of investigations have been performed in order to improve the EDFLs performance, for example, in terms of narrower band single-mode operation [116, 117] or multi-wavelength operation [118, 119].

1.3.3. Raman fiber lasers

Raman fiber lasers (RFL) exploit stimulated Raman scattering (SRS) to overcome the fiber losses and create the positive feedback at the shifted Stokes wavelengths using the transmission fiber itself [13].

In the early 1970s, Stolen and Ippen [120] demonstrated Raman amplification in optical fibers. However, throughout the 1970s and the first half of the 1980s, Raman amplifiers were restricted to laboratory research works. The potential of both fiber amplifiers and lasers based on Raman scattering was first demonstrated in the mid-1980's by Stolen, Lin, and co-workers, where Raman lasers operating between 0.3–2.0 μm were constructed [121]. In the mid-1980s, many researches were carried out in the Raman amplifier field showing a great commercial niche [122]. These amplifiers possessed many attractive features such as low noise, polarization insensitive gain, and the ability to achieve amplification in ordinary germanosilicate transmission fiber. However, the main trouble was that all the work was overtaken by EDFAs by the late 1980s due to the unavailability of high-power diode laser pump sources [123, 124].

RFLs offer important characteristics such as not requiring special fibers to gain's achievement being the gain medium the conventional transmission low-loss silica fibers. RFL

present high spectral flexibility due to the reconfigurability of the amplification spectrum by using multiple pump wavelengths. As in EDFA based lasers, it is pump direction independent. Consequently, pumping can be co/forward, counter/back or bidirectional with respect to the signal. On the other hand, the lasing efficiency with respect of EDFLs is relatively poor at low signal powers. Raman amplifiers also require longer gain fibers to achieve a good efficiency when compared with EDFA based lasers. Other disadvantage of RFL regards to the fast response time which gives rise to new sources of noise. It refers to two main noises, the amplified spontaneous scattering (ASS) and Rayleigh backscattering (RBS). The ASS is due to the amplification of spontaneously scattered photons, which is an unavoidable by-product of gain in all optical amplifiers. It is broadband, randomly polarized and grows bi-directionally in the fiber. On the other hand, RBS makes a marked contribution to the lasers total noise [13]. Finally, in multi-wavelength fiber lasers configurations there are concerns of nonlinear penalty in the emission lines. For example, power depletion should occur due to BFS or four wave mixing (FWM) [122].

Raman fiber lasers have commercial potential in a variety of practical cases. Their suitability for multi-wavelength operation makes them attractive CW sources in applications such as long-distance remote sensing [13, 125-127], optical tomography, supercontinuum generation or as high power pump sources for telecommunication systems [128]. Apart from that, they offer an opportunity to increase the cavity length by orders of magnitude compared to other lasers' types [129] that can be used for remote sensing as was mentioned before. In the last years, several researches have been developed ultra long RFL, reaching 300 km [130]. Some of the above mentioned lasers used distributed mirrors, being the so called Random distributed feedback fiber lasers. The distributed gain contributions along the fiber open a broad field of research as is it explained below.

1.3.3.1 Random distributed feedback fiber lasers

Random distributed feedback (RDFB) based on Rayleigh scattering through Raman amplification have been nowadays the subject of intense theoretical and experimental studies [131]. Random lasers are characterized by open-cavities or mirror-less-cavities. This means that, unlike conventional fiber lasers, their principle of operation relies on distributed scattering events along the fiber cavity. Since the experimental demonstration in 2010 of the RDFB based on Rayleigh scattering [132], some research groups are devoted to use its interesting characteristics to propose different lasing structures. S. A. Babin *et al*. have presented a complete overview of the art up to date in [133]. That review describes the fundamentals of the RDFB fiber lasers, various lasing schemes, the basic output characteristic, a theoretical model, its experimental demonstration, and potential applications of various RDFB fiber lasers.

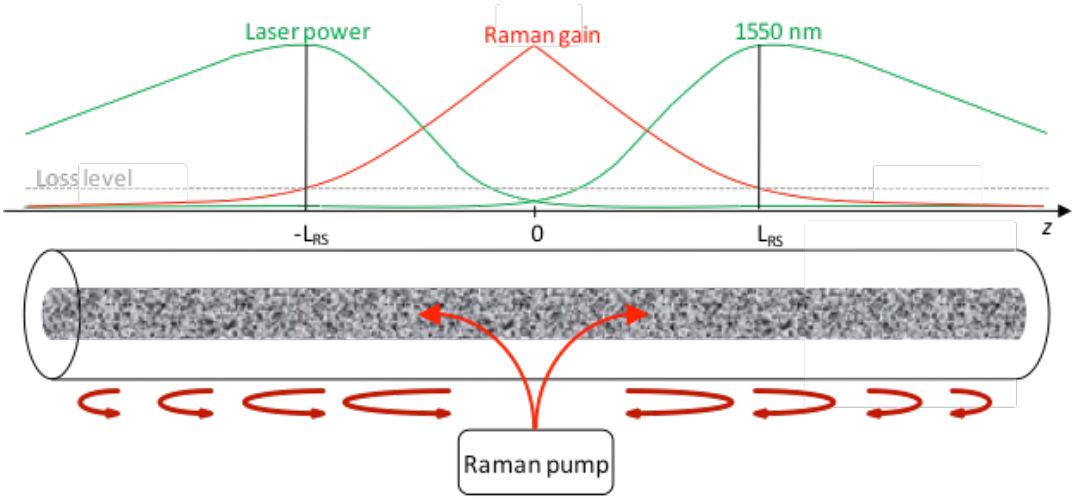

Figure 1.15. Schematic diagram of a random distributed feedback fiber laser operation.

Figure 1.15 shows a basic RDFB fiber laser setup where standard single mode fiber is pumped from the center of the fiber to both ends [134]. Trying to explain the RDFB effect in simple words, as it was aforementioned, standard fibers presents material inhomogeneities due to the fiber's fabrication process. Owing to these inhomogeneities, Rayleigh scattering occurs and the backscattered light is amplified by the SRS effect in each point along the fiber. These amplified Rayleigh backscattering contributions also generate double backscattering events along the cavity. All these random events produced inside the cavity generate, when the gain overcomes the losses, the random distributed feedback lasing process.

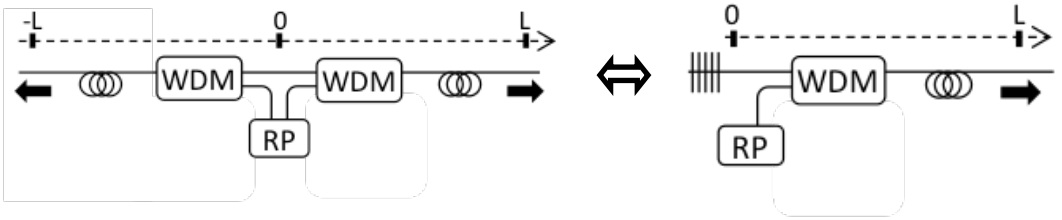

Figure 1.16. Schematic diagrams of the forward-pumped RDFB configurations.

There exist three different basic configurations of the RDFB fiber laser (figure 16, 17 and 18) [133]. Figure 16 scheme is called the forward-pumped configuration. It is due the laser output is co-propagating with the pump wave. It can be formed of a symmetrical

scheme based on 2 fiber spans of lengths L. It has an equivalent configuration in which only one fiber span of length L and only one pump laser is used with a mirror of 100% reflectivity placed at z=0.

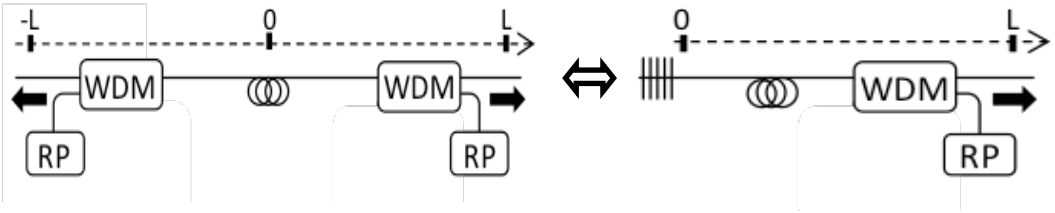

Figure 1.17. Schematic diagrams of the backward-pumped RDFB configurations.

Configuration shown in figure 17 is called backward-pumped because the output generated wave is counter-propagating with the pump wave. Its equivalent scheme has the only difference that the reflection mirror is placed at the opposite fiber's extreme than the pump source.

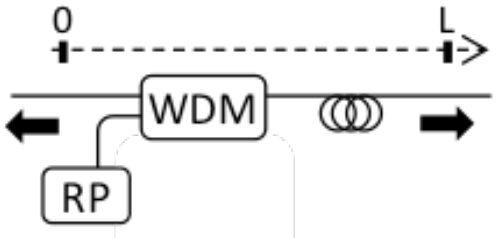

Figure 1.18. Schematic diagram of the single-arm RDFB configuration.

Finally, figure 18 scheme comprises a fiber span of length L with one pump laser placed at z = 0. In this case, there is no any reflector, thus the laser is operated via the RDFB only. It is called single-arm configuration.

The fiber length required for lasing based on the RDFB can be estimated as follows [132]. Neglecting pump depletion due to Stokes wave generation, the longitudinal distribution of the Raman gain $g_R P_P(z)$ is defined by the pump power attenuation:

$$P_P(z) = P_0 \exp[-\alpha_P |z|] \qquad (1.21)$$

where $\alpha_P \approx 0.057\ km^{-1}$. Thus, the length of the amplification region estimated through the gain/loss balance condition, $g_R P_P(L_{RS}) = \alpha$, gives:

$$L_{RS} = \frac{\ln(g_R P_0/\alpha)}{\alpha_P} \qquad (1.22)$$

As will be presented in chapter 4 and in part of chapter 5, the forward-pumped configuration was selected for this PhD work. This choice was due to the output port of this configuration is placed at L or – L allowing remote configurations.

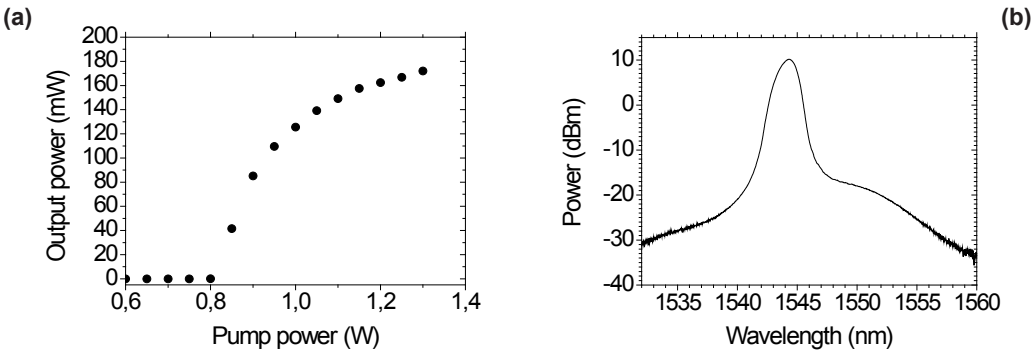

Figure 1.19. (a) Typical output power performance of a single arm forward-pumped RDFL and (b) its generated spectrum.

RDFB lasers have a clear generation threshold as depicted in figure 1.19 (a). They generate a well-confined optical spectrum with a typical width of 1 nm (124). They have attracted a lot of attention because of their advantages such as simple technology (no need to form a precise micro-cavity), low production costs, stability and special spectral properties. While conventional lasers have longitudinal modes associated to the cavity length; random lasers, which have infinite distributed cavities along the fiber, excite the whole of the lasing spectrum, achieving an emission line as wide as the optical gain spectrum permits. This characteristic allows modulating random lasers without the locking frequency problems of the conventional fiber laser configurations [135] and besides, it is an appealing structure for multi-wavelength laser generation. They are also able to reach long distances [134, 136]. However, for many applications, their current performance has to be modified to be able to challenge conventional lasers. Various schemes can be applied to improve the performance of random lasers with the challenging goal of achieving stationary operation with beam quality comparable to those of the conventional lasers [132].

The generation of radiation due to the Raman gain and the propagation of the generated waves in the fiber cavity in terms of the time averaged optical power is given by a system of differential equations, often called the power balance model [9]. This model takes into account all important physical effects, including fiber losses, Raman gain, pump depletion, amplified spontaneous emission, Rayleigh backscattering and propagation trough the fiber. By using these equations and assuming the forward-pumped configuration, one can derive an analytic expression for the threshold in the long-length limit $L >> 2L_{RS}$:

$$P_0 = \frac{\alpha}{g_r}\left(1+\ln\left(\frac{g_r P_{th}}{\alpha}\right)\right) + \frac{\alpha_P}{2g_r}\ln\left(\frac{1}{\varepsilon}\sqrt{\frac{\alpha\alpha_P}{\pi}}\right) \approx 0.8\ \mathrm{W} \qquad (1.23)$$

In short, RDFB technology represents a new field of research that brings together such diverse areas of science as laser physics, the theory of disordered systems, fiber optics and nonlinear science. Hence, RDFB fiber lasers are important for practical engineering applications such as laser radars, biomedical imaging, remote sensing, communications, ranging and distance measuring and optical astronomy. However, problems in wave transport and the interactions of light with random media also present challenges to modern science [132].

1.4. FIBER OPTIC SENSOR NETWORKS

An important advantage of fiber optic sensors is the ability of being multiplexed. By multiplexing it is understood that multiple sensing points can be measured in a single sensor network using the same signal header and transmission channel thus reducing the overall cost of the systems. Multiplexing of optical fiber sensors is a concept that includes three basic tasks [137].

- Launching of optical signals with the correct power level, spectral distribution, polarization and modulation into the network.
- Detection of the optical power portion codified or modulated by the sensor element, sent by means of transmission or reflection.
- Unique identification of the information corresponding to each sensor in the network, by means of proper addressing, polling and decoding.

Different kinds of fiber optic sensors networks are resumed in table 1.3. Sensor networks are classified following the type of sensor to be multiplexed, the sensor distribution and the network topology. Regarding to the sensors, the classification differen-

tiates between networks depending on the combination of sensors, one kind of sensor (simple) or different kinds (hybrid), the type of sensor and the modulation used to codify each sensor.

Table 1.3: Classification of the multiplexing fiber optic sensor networks

SENSOR NETWORKS CLASSIFICATION

Sensors			Distribution	Topology
Combination	Type	Modulation		
Simple Hybrid	Transmissive Reflective	TDM WDM CDM PDM	Point multiplexed Distributed	Serial bus Dual bus o ladden Star Tree Mesh

As presented in table 1.3 there are different multiplexing topologies that are all depicted in figure 1.20. They are bus, dual bus or ladder, star, tree and mesh from “a)” to “e)” respectively.

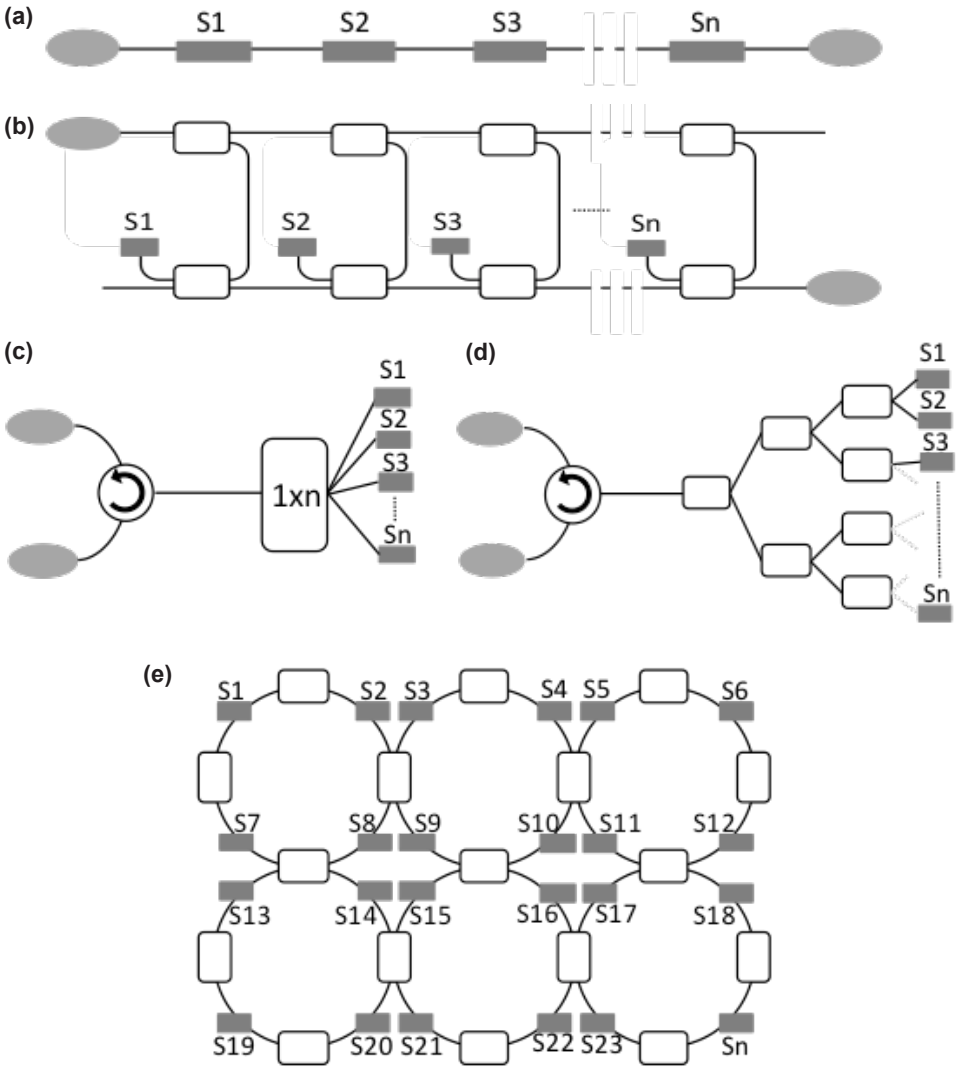

Figure 1.20. Different point multiplexing topologies schematic diagrams. a) bus, b) double bus or ladder, c) star, d) tree and e) mesh.

Using previous topologies, large amount of sensors can be interrogated. High performance architectures can theoretically be extended to interrogate at least 192 [138] to 256 [139] sensors through two fibers. Recently this technique has been extended to a novel architecture considered to be the best approach to support high resolution. Liao *et*

al. show the viability to interrogate up to 4096 sensors using only commercial components through one pair of telemetry fibers [140].

Other kinds of sensor networks are the distributed optical fiber sensors. They are attracting an increasing interest due to their wide range of potential industrial applications in strategic sectors such as energy [141], defense, security [142], or transportation. The term distributed refers to the ability to simultaneously detect scale and location of a measurand anywhere along a continuous length of sensing fiber. This differs from the concept of multi-point sensing, where the measurement is done at specific locations with point sensors. The use of distributed sensing was stimulated by the optical time domain interferometry (OTDR) technique. This technique, as further discuses below, uses the Rayleigh backscattered light from an optical pulse propagating through the fiber [143]. Different distributed sensing techniques will be presented in section 1.4.2.

Additionally, due to the noise and loss induced by Rayleigh scattering and attenuation along the fiber respectively, the maximum transmission distance without amplification is usually limited up to few tens of km [144, 145]. Because of that, the maximum measurement distance of fiber sensor networks comes out to be a practical issue. A lot of work has been done to increase the measuring distance of the sensors, however most of the proposals make them setups quite complicated as presented next [137].

1.4.1. Fiber optic networks for remote sensing

Remote sensing using optical fiber systems has received an increasing attention in recent years because it has proved to be a useful tool for monitoring a wide range of parameters in many fields. In general, the main idea behind remote sensing concept is the continuous monitoring of structures from a central station located tens or hundreds of kilometers away from the field through the critical location of sensors. These sensors send information to the central station, without the necessity of electrical power feeds in the remote locations [146-148]. Due to the noise and loss induced by the Rayleigh scattering and attenuation along the fiber respectively, the maximum transmission distance with a broadband light source without using optical amplification is usually limited up to few tens of km [149, 150]. Being it so, the maximum measurement distance of fiber sensor systems comes out to be a practical issue. In this PhD work, because the low loss transmission characteristic of the technology, only distances above 50 km (approximately the typical high speed data transmission limit without amplification) will be considered remote sensing. A lot of work has been done to increase the measuring distance of the fiber sensor, however most of the developed networks use quite com-

plicated set-ups. In table 4 the state of the art of remote fiber-optic sensor systems is presented [137].

Table 1.4: Remote fiber optic sensors systems state of the art summary

Year / ref.	Network length (km)	Laser resource / amplification type	Remarks
2005/[151]	50	MWFL	PS-FBG temperature and strain sensors
2007/[152]	120	No amplification	Strain sensors
2007/[153]	100	Rayleigh backscatter	Remote fiber dynamic strain sensing system
2008/[154]	230	EDFA	Strain sensors
2010/[155]	100	Raman + EDFA	Temperature sensors 30 dB signal noise ratio
2011/[156]	100	Raman + EDF	Vibration (from 1 Hz to 1000 Hz) sensor system
2011/[157]	120	BOTDA + bi-directional Raman amplification	2 m spatial resolution and a strain/temperature accuracy of 45 με/2.1 °C
2011/[158]	100	Hybrid Brillouin + Raman	Temperature sensors; 30 dB OSNR; immunity from the light source power fluctuations
2011/[159]	155	Raman + EDFA + Brillouin	Sensing temperature changes with a sensitivity of 10 pm/°C
2011/[160]	200/250	Raman	Temperature sensors two simple systems
2011/[161]	253	No amplification	Displacement sensor system based on a fiber loop mirror
2011/[162]	100	Brillouina	Temperature and strain sensor system; 50 m spatial resolution
2011/[163]	50	Dual-wavelength Raman fiber laser	Simultaneous measurement of bending and temperature
2011/[164]	150	Raman + EDFA	Temperature and vibration sensor system
2012/[165]	50	EDFA and an Optical Time Domain Reflectometry (OTDR)	Hybrid FBG and displacement sensors based on microbenders
2012/[166]	171	No amplification based on self-heterodyne detection	Remote FBG sensors system based on the self-heterodyne detection. Two temperature sensors (11 pm/°C)
2013/[167]	75	Raman + EDFA	Ladder structure

Year / ref.	Network length (km)	Laser resource / amplification type	Remarks
2013/[168]	200	Raman + EDFA	200 km remote lasers for FBGs multiplexing
2013/[169]	50	Switchable EDFL	Strain measurements
2013/[170]	50	Raman + FBG commercial interrogator	Resilient remote power-by-light switching for FBG array interrogation
2013/[171]	71	BOTDA + Raman	Temperature sensing with 5 m spatial resolution with 1.5 °C measurement uncertainly
2013/[172]	62.5	ØOTDR + Raman	Vibration sensing with 10m spatial reso lution at 380 Hz
2014/[173]	100	OTDR	Refractive index measurements
2014/[174]	50	Raman + EDFA	MWFL for interrogating two sensor networks

In table 4, four works overcome 200 km, and are explained next. Firstly, Saitoh *et al.* proposed in [154] a 230 km remote system for one FBG interrogation. A tunable laser was amplified by an EDFA before 230 km of SMF fiber. After the 230 km fiber, a single FBG sensor was placed. This FBG reflected the corresponding wavelength and, after the 230 km coming back, the highly attenuated FBG signal was detected by an avalanche photodiode (APD). The system included unwanted Rayleigh backscattered noise suppression to improve the OSR.

Secondly, M. Fernandez-Vallejo *et al.* present in [160] a dual path ultra-long FBG sensors network. In a first approach, an array of four FBG was placed 200 km away. The FBG network was scanned by a tunable laser that was amplified by Raman amplification. In order to avoid the Rayleigh backscattering, the second fiber collected the FBG information and guided it to be detected by an OSA. In the same publication, they reach 250 km with an equivalent setup. Notwithstanding, in order to make a more efficient procedure, a monitoring station improvement was performed. An in deep study of the emission line propagation's issues was done. A high dependence of the line width with the line power was observed. Hence, they developed a home-made tunable fiber optic laser with an optimized line width. Thus, they improve the system's OSNR up to 18 dB at 250 km.

Finally, as will be presented in chapter 3 of this PhD work, a single displacement sensor was interrogated 253 km away [161]. This distance was reached by using a commercial OTDR without any amplification mechanism.

1.4.2 Distributed sensor networks

An important advantage of fiber optic sensors is that, by combining fiber sensing with fiber telemetry, unique forms of sensors can be created. In the distributed sensing technology the measurand field acts on a length of fiber that can be monitored in both, the temporal and spatial domains [175]. The most important parameters and conditions to be optimized for best distributed fiber sensing are three. The primary key parameter is the signal-to-noise ratio (SNR) on the raw response (temporal trace or equivalent). The next important parameter is the sensitivity of the response to the measured quantity. This parameter also impacts on all the sensor's properties, since for a given target accuracy on the measured quantity a higher sensitivity requires a smaller SNR. The last important parameter is the linear depletion due to the interaction. This must remain small enough to prevent from an excessive cumulated depletion of the activating signal. Now the distributed sensors can be classified into 2 broad categories. Those based on backscattering events and those based on a coherent coupling through a resonant longitudinal structure, such as a distributed Bragg reflector. Within this broad framework, following are classified the different existing distributed fiber sensors [176]:

- Raman-based sensors
- Spontaneous Brillouin-based sensors (BOTDR)
- Stimulated Brillouin-based sensors (BOTDA)
- Coherent Rayleigh-based sensors (C-OTDR)
- Dynamic Brillouin gratings sensing (DBG)
- Faint long gratings (FLOG)

In this PhD work, an important part is based on the Rayleigh scattering effect for distributed or quasi distributed sensing. Rayleigh scattering, as it was aforementioned, is the major source of attenuation in modern telecommunications networks in the entire wavelength range from 800 to 1700 nm. As mentioned before, this linear scattering effect is a consequence of the microscopic inhomogeneities of the optical fiber material. When a light wave interacts with such material fluctuations, it is partly scattered [177]. Part of this scattered power is recaptured by the fiber and counter-propagates. This effect is the basis of the reflectometric techniques used in following systems allowing distributed measurements.

1.4.2.1 Optical Time Domain Reflectometry (OTDR)

The widespread use of single-mode optical fiber in communication and sensor systems generated the development of a new family of instruments for fiber networks analysis. One of such instruments that were commercialized is the optical time domain reflec-

tometer [178] (OTDR) used for the analysis of attenuation and scatter in optical fibers. Conventional OTDRs use pulsed optical sources in their operation. In this respect, they are an application of the laser radar principle to fiber optics [179] measuring the range and scattering or reflections from fiber discontinuities. The resolution is determined by the pulse rise time [180].

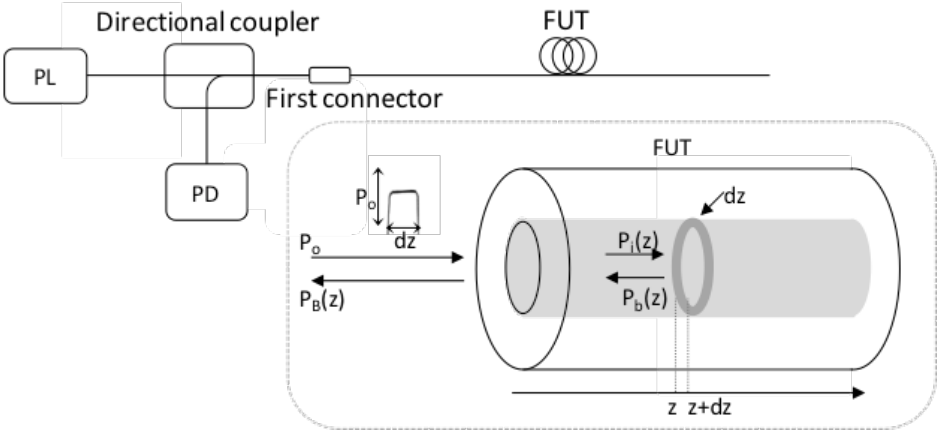

Figure 1.21. Basic setup for an optical backscatter reflectometer.

A basic scheme of an OTDR is illustrated in figure 1.21. The working principle of the OTDR becomes with the emission of an optical pulse (P_o and dz) through a coupler which enters the fiber under test. As the optical pulse travels along the fiber generating simultaneously, due to the Raleigh effect aforementioned, a backscattered signal ($P_b(z)$) proportional to the optical pulse power ($P_i(z)$) at this point (z). Thus, a continuous backscattering light is generated along the fiber. Afterwards, this backscattered light ($P_B(z)$) is collected by the directional coupler to be detected by the photodiode. In time, the detected signal is proportional to the backscattered light generated by the optical pulse along the fiber and transmitted back to the detector. Therefore, each time contribution refers to the backscattered light of a specific zone of the fiber. Numerically, the backscattered power measured at the fiber input/output is given by:

$$dP_B(z) = dP_b(z)e^{-\alpha_{tot}z}dz = P_0 B_c(\lambda,z)\alpha_s(\lambda,z)e^{-2\alpha_{tot}z}dz \qquad (1.24)$$

Where α_{tot} is the total attenuation coefficient, is the scattering coefficient (both in km^{-1}) and B_c is the backscatter captured fraction that quantifies the amount of light propagating backwards to the source. As light travels at a finite group velocity, it takes a time *t* for this pulse to reach the position , which is equal to:

$$z = v_g t \qquad (1.25)$$

Thus, in a simplest form, the signal called OTDR trace can be rewritten as:

$$S(z) = K - \alpha'(z) \qquad (1.26)$$

where *K* is a constant and is the attenuation coefficient expressed in dB/km. Figure 1.22 illustrates an example of an OTDR trace in which the different events that can be observed in a typical network are detailed.

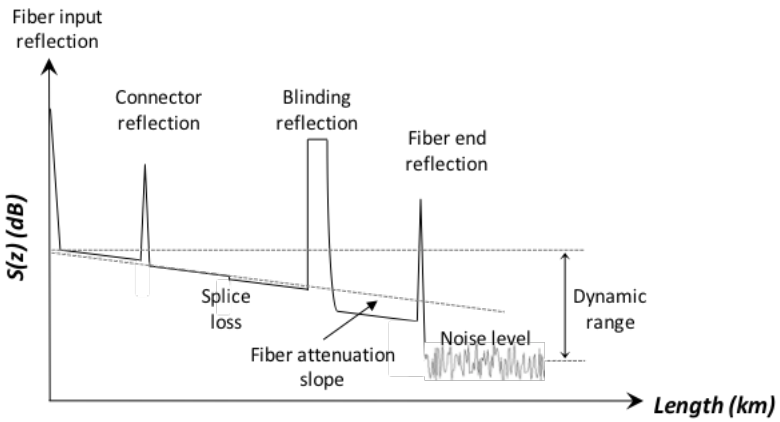

Figure 1.22. OTDR trace sample showing different events in a fiber optic network

The first reflection peak makes reference to the optical pulse at the input connector. The second peak is the Fresnel reflection created in the fiber connectors. After it, a small slope is created by a lossy splice or it can be also caused by, i.e., a micro bend. Other event presented in the OTDR trace is the blinding reflection. It is obtained when a very

high reflection saturates the photo-detector and it presents a maximum value while it is saturated. Finally, when the fiber end is not adapted, a Fresnel reflection appears just before the detection noise level. The value between the noise level and the power after the input reflection determines the available measurement dynamic range for the selected OTDR configuration. It is also highlighted the fiber attenuation slope. This slope has to fit with the nominal fiber attenuation provided by the manufacturer. The attenuation slope of the SMF28 fibers used during the experiments of this PhD work was ~0.19 dB/km.

There are three key parameters which define the OTDR performance: the dynamic range, the spatial resolution and the pulse width. The dynamic range quantifies the maximum loss that can be measured by the OTDR. The spatial resolution is the ability of an OTDR to distinguish between two close events. The correspondence between the spatial resolution is given by . The pulse width (*W*) value has a direct impact on the spatial resolution and the dynamic range. The wider the pulse, the lesser the spatial resolution and higher dynamic range and vice versa [177].

Optical time domain reflectometry is a suitable technique to interrogate different kinds of sensors and thus, to measure the induced change in the optical intensity at different locations along the fiber. Parameters like strain and displacement can be measured by detecting the Rayleigh backscattered light loss. OTDR is one of the most important sensor measurement techniques and its importance in structural health monitoring (SHM) has increased due to its suitability for real time monitoring of the large civil engineering structures' deformation [181-184].

1.4.2.2 Optical Frecuency Domain Reflectometry (OFDR)

As was explained before, OTDR range resolution is set by pulse duration. For high resolution performance, coherent systems have been developed improving overall sensitivity by the use of a heterodyne receiver.

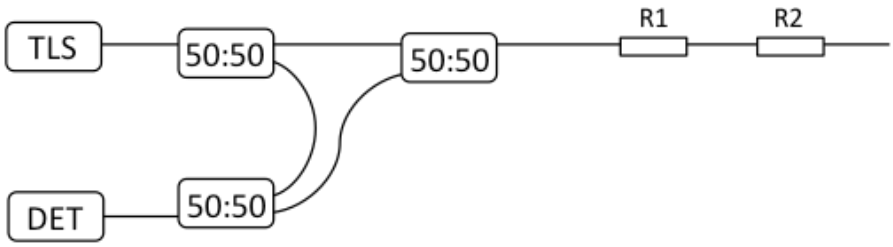

Figure 1.23. Schematic diagram of a basic OFDR system.

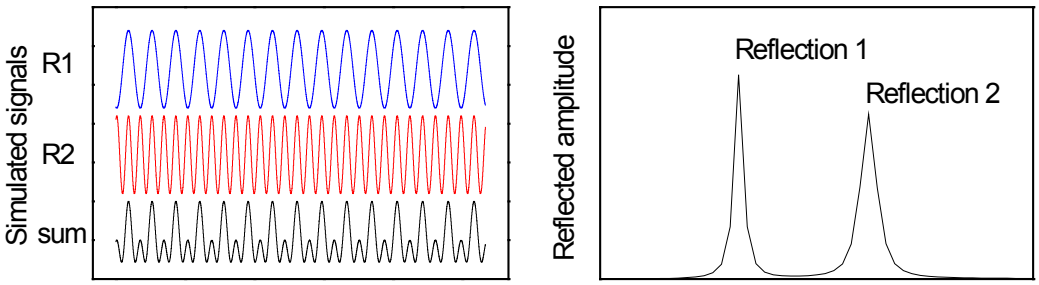

Figure 1.24. Simulation of the response of an OFDR system to two reflectors placed in between a fiber.

In the simplest version of coherent OFDR in a Mach-Zehnder based interferometer (figure 1.23), highly monochromatic low power light is coupled into the fiber. The optical frequency ω is slowly varied by a time-linear sweep. For coherent detection, the backscattered wave is mixed with a coherent reference wave at the detector [185]. To better understand the working principle, if two ideal reflectors are placed in the middle of the fiber under test (figure 1.23) and no more backscattered contributions are considered, two different interferences would be obtained due to different reflector position. Due to the phase shift variation between both reflections, a different frequency of the interference patterns is expected. The two isolated patterns and the combination of both are presented in figure 1.24. To obtain the spatial position of both reflections, a Fourier analysis is performed and the contributions obtained are in agreement of the real position of both reflectors.

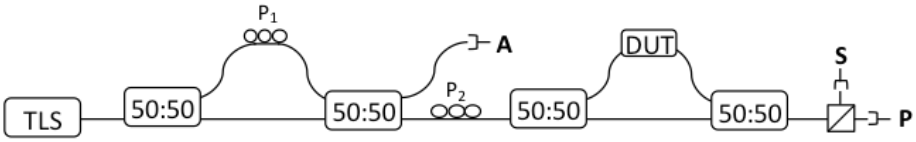

Figure 1.25. Basic structure of an optical backscatter reflectometer.

In this PhD work an optical backscatter reflectometer (OBR 4600) from Luna INC will be used to characterize and study the optical behavior and propagation characteristics of different special fiber and structures. The working principles of the OBR are published by the manufacturer in [186]. From an optical point of view, this equipment is formed of two Mach-Zender interferometers, two polarization controllers, a polarization beam

splitter and three photodiodes. The schematic is depicted in figure 1.25. Explained in a few words, the Mach-Zehnder interferometer of the left has the objective of creating two time-shifted, orthogonal polarization states which simultaneously interrogate the device under test (DUT). Hence, the photodiode "A" is used to control the correct alignment of the polarization by minimizing the fringe amplitude at the detector. The second polarization controller, P2, is used to ensure that the field components associated with the two branches of the first interferometer are divided equally between the orthogonal polarization states defined by the polarization splitter. Finally, the field that propagates through the upper branch of the second interferometer experiences a polarization dependent loss and phase shift due to the DUT. Thus, the detected fields in S and P are the interference of the two orthogonally aligned polarization states; and applying a Fourier analysis, a reconstruction of the backscattered events along the DUT can be performed.

1.5. CONCLUSIONS

This chapter has summarized the basis and the state of the art of the main technological concepts to be used in the following chapters of this PhD work. Thus, chapters 2,3,4,5 and 6 are intended to contribute to de development of new: single fiber optic sensing heads, reflectometric based interrogation schemes, RDFB fiber lasers, fiber optic sensor networks and, finally, three different applications of fiber optic sensors in structural health monitoring.

1.6. REFERENCES

[1] *B. E. A. Saleh, M. C. Teich, "Fiber optics, Chapter 8 in Fundamentals of Photonics", Ed. John Wiley & Sons, Inc, 1991.*

[2] *G. P. Agrawal, "Optical Fibers, Chapter 2 in Fiber-Optic Communication Systems", Ed. John Wiley & Sons, Inc, 2002.*

[3] *G. A. Thomas, B. L. Sharaiman, P. F. Glodis, and M. K. Stephan, "Towards the clarity limit in optical fibre" Nature 404, 262, 2000*

[4] *M. Born and E. Wolf, "Principles of Optics", Cambridge University Press, 1999*

[5] *R. W. Boyd, "Nonlinear Optics" Academic Press, 1992*

[6] *X. Angulo Vinuesa, "Ultra-Long Range Brillouin Optical Time Domain Analysis", PhD Thesis, Universidad de Alcalá (2014)*

[7] *D. Cotter, "Observation of stimulated Brillouin scattering in low loss silica fiber at 1.3μm", Electronic Letters, 18, 495-496, 1982*

[8] *J. L. Santos, O. Frazao, J. M. Baptista, P. A. S. Jorge, I. Dias, F. M. Araujo and L. A. Ferreira, "Optical fiber sensing networks" in SBMO/IEEE MTT-S International Microwave and Optoelectronics Conference Proceedings, pp. 290-298, 2009*

[9] *G. P. Agrawal, Nonlinear fiber optics, 3rd ed. Academic Press, 2001.*

[10] *C. C. O.Frazao, M.T.M. Rocco Giraldi, M.B. Marques, H.M. Salgado, M.A.G. Martinez, J.C.W.A. Costa, A.P. Barbero and J.M. Baptista, "Stimulated Raman Scattering and its Applications in Optical Communications and Optical Sensors," The Open Optics Journal 2009.*

[11] *A. Mendez, "Three decades of optical fiber sensors commercialization: dawn, present and future", Invited paper 23rd OFS (2014)*

[12] *J. M. Lopez-Higuera, Handbook of Optical Fiber Sensing Technology, Chapter 1, Introduction to Fibre Optic Sensing Technology, 1-23, Ed by J. M. Lopez-Higuera*

[13] *M. Fernandez-Vallejo, "Contribution to the Development of Optical Networks for Fiber Optic Sensors Using Fiber Lasers", PhD Thesis, Universidad Pública de Navarra (2012)*

[14] *A. Othonos, "Fiber Bragg gratings", Review of Scientific Instruments, 68, 12, 4309-4341 (1997)*

[15] *A. D. Kersey, M. A. Davis, H. J. Patrick, M. LeBlanc, K. P. Koo, C. G. Askins, M. A. Putnam and E. J. Friebele, "Fiber grating sensors", Journal of Lightwave Technology, 15, 1442-1462 (1997)*

[16] *K. O. Hill and G. Meltz, "Fiber Bragg Grating Technology Fundamentals and Overview", Journal of Lightwave Technology, 15, 8, 1263-1276 (1997)*

[17] *J. R. Casas and P. J. S. Cruz, "Fiber optic sensors for bridge monitoring", Journal of Bridge Eng., 8, 362-373 (2003)*

[18] *W. Ecke, I. Latka, R. Willsch, A. Reutlinger and R. Graue, "Fiber optic sensor network for spacecraft health monitoring", Measurement Science and Technology, 12, 974-980* **(2001)**

[19] T, K. Gangopadhyay, M. Majumder, A. Kumar Chakraborty, A. Kumar Dikshit and D. Kumar Bhattacharya, "Fiber Bragg grating strain sensor and study of its packaging material for use in critical analysis on steel structure", Sens. Actuators A Phys, 150, 78-86 (2009)

[20] A. Hongo, S. Kojima and S. Komatsuzaki, "Applications of fiber Bragg grating sensors and high-speed interrogation techniques" Structural Control and Health Monitoring, 12, 269-282 (2005)

[21] H. Li, D. Li and G. Song, "Recent applications of fiber optic sensors to health monitoring in civil engineering" Eng. Struct. 26, 1647-1657 (2004)

[22] K. Schröder, W. Ecke, M. Kautz, S. Willett, A. Tchertoriski, M. Jenzer and G. Kaluza, "Fiber optical sensor network embedded in a current collector for defect monitoring on railway catenary", in Proceedings of SPIE, 6585, art, no. 65850R (2007)

[23] L. Yan, Z. Zhang, K. Wen, W. Pan and B. Luo, "Optical sensor networks for high-speed railway applications", in IET Conference Publications, (574CP), 128-129 (2010)

[24] B. Lee, "Review of the present status of optical fiber sensors", Optical Fiber Technology, 9, 57-79 (2003).

[25] M. Song, S.B. Lee, S.S. Choi, B. Lee, "Fiber laser strain sensor using an LPG (long period grating) Bragg wavelength demodulation filter", in: The 2nd Optoelectronics and Communications Conference (OECC '97) Technical Digest, Seoul, Korea, 1997, pp. 676–677.

[26] R. W. Fallon, L. Zhang, A. Gloag, I. Bennion, "Identical broadband chirped grating interrogation technique for temperature and strain sensing", Electron. Lett. 33 (1997) 705–706.

[27] V. Grubsky, J. Feinberg, "Long-period fiber gratings with variable coupling for real-time sensing applications", Opt. Lett. 25 (4) (2000) 203–205.

[28] R. Willsch, W. Ecke, H. Bartelt, "Optical fiber grating sensor networks and their application in electric power facilities", Aerospace and Geotechnical Engineering, in: The 15th Optical Fiber Sensors Conference Technical Digest, Portland, OR, 2002, pp. 49–54.

[29] Y. J. Rao, D. A. Jackson, L. Zhang, I. Bennion, "Dual-cavity interferometric wavelength-shift detection for in-fiber Bragg grating sensors", Opt. Lett. 21 (19) (1996) 1556–1558.

[30] S. C. Kang, S. Y. Kim, S. B. Lee, S. W. Kwon, S. S. Choi, B. Lee, "Temperature-independent strain sensor system using a tilted fiber Bragg grating demodulator", IEEE Photon. Technol. Lett. 10 (10) (1998) 1461–1463.

[31] K. B. Rochford, S. D. Dyer, "Demultiplexing of interferometrically interrogated fiber Bragg grating sensors using Hilbert transform processing", J. Lightwave Technol. 17 (5) (1999) 831–836.

[32] P. J. Henderson, D. J. Webb, D. A. Jackson, L. Zhang, I. Bennion, "Highly-multiplexed grating-sensors for temperature-referenced quasi-static measurements of strain in concrete bridges", in: Proceedings of the 13th International Conference on Optical Fiber Sensors (OFS-13), Kyongju, Korea, in: Proc. SPIE, Vol. 3746, 1999, pp. 320–323.

[33] J. P. Dakin, M. Volanthen, "Distributed and multiplexed fibre grating sensors, including discussion of problem areas", IEICE Trans. Electron. E83-C (3) (2000) 391–399.

[34] M. Song, S. Yin, P. B. Ruffin, "Fiber Bragg grating strain sensor demodulation with quadrature sampling of a Mach–Zehnder interferometer", Appl. Opt. 39 (7) (2000) 1106–1111.

[35] J. Jung, Y. W. Lee, B. Lee, "High-resolution interrogation technique for fiber Bragg grating strain sensor using long period grating pair and EDF", in: The 14th International Conference on Optical Fiber Sensors (OFS-14), Venice, Italy, 2000.

[36] M. LeBlanc, S. Y. Huang, M. Ohn, R. M. Measures, A. Guemes, A. Othonos, "Distributed strain measurement based on a fiber Bragg grating and its reflection spectrum analysis", Opt. Lett. 21 (1996) 1405–1407.

[37] M. A. Putnam, M. L. Dennis, J. U. Kang, T. E. Tsai, I. N. Duling, I. E. J. Friebele, "Sensor grating array demodulation using a passively mode-locked fiber laser", in: Technical Digest of the Optical Fiber Communication Conference, Dallas, TX, 1997, Paper WJ4, pp. 156–157.

[38] S. H. Yun, D. J. Richardson, B. Y. Kim, "Interrogation of fiber grating sensor arrays with a wavelength-swept fiber laser", Opt. Lett. 23 (11) (1998) 843–845.

[39] K. P. Koo, A. B. Tveten, S. T. Vohra, "Dense wavelength division multiplexing of fibre Bragg grating sensors using CDMA", Electron. Lett. 35 (1999) 165–167.

[40] P. K. C. Chan, W. Jin, J. M. Gong, M. S. Demokan, "Multiplexing of fiber Bragg grating sensors using an FMCW technique", IEEE Photon. Technol. Lett. 11 (11) (1999) 1470–1472.

[41] K. T. V. Grattan and T. Sun, "Fiber optic sensor technology: an overview", Sensors and actuators A Phys, 82, 40-61 (2000)

[42] B. H. Lee, J. B. Eom, K. S. Park, S. J. Park, M. J. Ju, "Specialty fiber coupler; Fabrications and applications.", J. Opt. Soc. Korea, 14, 326-332, (2010)

[43] K. T. V. Grattan, B. T. Meggitt, "Optical Fiber Sensor Technology"; Chapman & Hall: Orange, CA, USA, 1995.

[44] B. H. Lee, Y. H. Kim, K. S. Park, J. B. Eom, M. J. Kim, B. S. Rho and H. Y. Choi, "Interferometric Fiber Optic Sensors" Sensors, 12, 2467-2486 (2012)

[45] A. D. Kersey, "Recent Progress in Interferometric Fiber Sensor Technology", Proc, SPIE in Fiber Optic and Laser Sensors VIII, 1367, 1-12 (1990)

[46] B. Culshaw, "The optical fiber Sagnac interferometer: an overview of its principles and applications", Measurement Science and Technology, 17, R1-R16, (2005).

[47] G. Sagnac, "L'éther lumineux d´emontré par l'effet du vent relatif d'éther dans un interféromètre en rotation uniforme". C. R. Acad. Sci. 95, 708-710, (1913).

[48] D. B. Mortimore, "Fiber Loop Reflectors. Journal of Lightwave Technology" 6, 1217-1224, (1988).

[49] L. Liu, Q. Zhao, G. Zhou, H. Zhang, S. Chen, L. Zhao, Y. Yao, P. Guo and X. Dong, "Study on an optical filter

constituted by concatenated Hi-Bi fiber loop mirrors", Microwave and Optical Technology Letters, 43, 23–26, (2004).

[50] *P. Urquhart, "Compound optical-fiber-based resonators" Journal of the Optical Society of America, 5, 803-812 (1988)*

[51] *S. Rota-Rodrigo, M. Gonzalez-Herraez and M. Lopez-Amo, "Compound lasing fiber optic ring resonators for sensing" Proc. SPIE, 23rd OFS conference, Postdeadline papers (2014)*

[52] *J. E. Zucker, K. L. Jones, T. H. Chiu, and K. Brown-Goebeler, "Strained quantum wells for polarization-independent electroopic wave- guide switches," J. Lightwave Technol., 10, 1926-1930, (1992)*

[53] *M. Bachmann, M. K. Smit, L. B. Soldano, P. A. Besse, E. Gini, and H. Melchior, "Polarization-insensitive low-voltage optical waveguide switch using InGaAsP/InP four-port Mach-Zehnder interferometer," in Proc. Conf. Opt. Fiber Commun. (OFC), 32-33, (1993)*

[54] *L. B. Soldano and Erik C. M. Pennings, "Optical Multi-Mode Interference Devices Based on Self-Imaging: Pinciples and Applications", J. Lightwave Technol., 13, (1995)*

[55] *P. R. Horche, M. Lopez-Amo, M. A. Muriel, J. A. Martin-Pereda, "Spectral behavior of a low-cost all-fiber component based on untapered multifiber unions" Photonics Technology Letters, 1, 184-187 (1989)*

[56] *Q. Wu, Y. Semenova, P. Wang, G. Farrell, "High sensitivity SMS fiber structure based refractometer – analysis and experimental" Optics Express, 19, 7937-7944 (2011)*

[57] *Q. Wu, A. Hatta, P. Wang, Y. Semenova, G. Farrell "Use of a Bent Single SMS Fiber Structure for Simultaneous Measurement of Displacement and Temperature Sensing", Electronics Letters, 46, (2010)*

[58] *R. X. Gao, Q. Wang, F. Zhao, B. Meng and S. L. Qu, "Optimal design and fabrication of SMS fiber temperature sensor for liquid" Optics Communications, 283, (2010)*

[59] *Z.-B. Liu, Y. Li, Y. Liu, Z.-W. Tan, S. Jian, "A Static Axial Strain Fiber Ring Cavity Laser Sensor Based on Multi-Modal Interference," Photonics Technology Letters, IEEE, 25, 2050-2053, (2013)*

[60] *M. A. Zawawi, S. O'Keffe and E. Lewis, "Intensity-modulated fiber optic sensor for health monitoring applications: a comparative review", Sensor Review, 33, 57-67 (2013)*

[61] *A. Cobo-Garcia and J. Echevarria-Cuenca, Handbook of Optical Fiber Sensing Technology, Chapter 11, Tranduction techniques based on intensity modulation of light, 209-224, Ed by J. M. Lopez-Higuera*

[62] *J. N. Fields et al., '' pressure sensor," J. Acoust. Soc. Am., 67, 816-818, (1980)*

[63] *J. N. Fields, "Attenuation of a parabolic-index fiber with periodic bends," Appl. Phys. Lett., 36, 799-801, (1980)*

[64] *D. F. Nelson et al., "Vibration-induced modulation of fiberguide transmission" in Proc. Topical Meet. on Optical Fiber Transmission TU-E7-I to TU-E7-4 (1977)*

[65] *J. W. Berthold, "Historical Review of Microbend Fiber-Optic Sensors" Journal of Lightwave Technology, 13, 1193-1199 (1995)*

[66] N. Lagakos et al., "Microbend sensor," Appl. Opt., 26, 2171-2180, (1987)

[67] D. Donlagic and B. Culshaw, "Microbend sensor structure for use in distributed and quasi-distributed sensor systems based on selective launching and filtering of the modes in graded index multimode fiber", Journal of Lightwave Technology, 17, 1856-1868 (1999)

[68] J. N. Fields and J. H. Cole, "Fiber microbend acoustic sensor", Applied Optics, 19, 3265-3267 (1980)

[69] M. Vaziri and C. Chen, "Optical-fiber strain sensors with asymmetric etched structures", Applied Optics, 32, 6399-6406 (1993)

[70] J. D. Waiss, "Fiber-optic Stain Gauge", Journal of Lightwave Technology, 7, 1308-1318 (1989)

[71] J. B. Freal, C. J. Zarobila and C. M. Davis, "A microbend horizontal accelerometer for borehole deployment", Journal of Lightwave Technology, 5, 993-996 (1987)

[72] P. Heinzmann and R. Hofstetter, "Temperature dependence of PCS fiber characteristics", Proc. SPIE, 584 (1985)

[73] C. Michie et al."A Fiber Optic/Hydrogel Probe for Distributed Chemical Measurements" Tenth OFS conference, Proc. SPIE, 2360, 130-133 (1994)

[74] J. C. Knight, T. A. Birks, P. St. J. Russell and D. M. Atkin, "All-silica single-mode fiber with photonic crystal cladding" Optics Letters, 21, 1547-1549, (1996)

[75] P. St. J. Russell, "Photonic-Crystal Fibers" Journal of Lightwave Technology, 24, 4729-4749, (2006)

[76] P. St. J. Russell, "Photonic Crystal Fibers" Science, 299, 358-362, (2003)

[77] A. M. R. Pinto and M. Lopez-Amo "Photonic Crystal Fibers for Sensing Applications" Journal of Sensors, 2012, 598178 (2012)

[78] P. R. Laurent Bigot and P. Roy, "Fibres à cristal photonique : 10 ans d'existence et un vaste champ d'applications," Images de la physique, pp. 71-80, (2007).

[79] S. A. Cerqueira, "Recent progress and novel applications of photonic crystal fibers,"Reports on Progress in Physics 73, pp. 024401, (2010).

[80] A. M. R. Pinto, "Photonic Crystal Fibers for Sensing Applications" PhD Thesis, Universidad Pública de Navarra, (2012)

[81] O. Frazao, J. L. Santos, F. M. Araujo, and L. A. Ferreira, "Optical sensing with photonic crystal fibers," Laser and Photonics Reviews, 2, 449–459, (2008).

[82] P. M. Blanchard, J. G. Burnett, G. R. G. Erry et al., "Two dimensional bend sensing with a single, multi-core optical fibre," Smart Materials and Structures, 9, 132– 140, (2000).

[83] M. Bravo, A. M. R. Pinto, M. Lopez-Amo, J. Kobelke, and K. Schuster, "High precisionmicro-displacement fiber sensor through a suspended-core Sagnac interferometer," Optics Letters, 37, 202–204, (2012).

[84] S. Rota-Rodrigo, A. M. R. Pinto, M. Bravo and M. Lopez-Amo, "An In-Reflection Strain Sensing Head Based on a Hi-Bi Photonic Crystal Fiber" Sensors, 13, (2013)

[85] *Y. Zhao, R. Q. Lv, Y. Ying, and Q. Wang, "Hollow-core photonic crystal fiber Fabry-Perot sensor for magnetic field measurement based on magnetic fluid," Optics and Laser Technology, 44, 899–902, (2012).*

[86] *T. Martynkien, G. Statkiewicz-Barabach, J. Olszewski et al., "Highly birefringent microstructured fibers with enhanced sensitivity to hydrostatic pressure," Optics Express, 18, 15113–15121, (2010).*

[87] *D. Monzon-Hernandez, V. P. Minkovich, and J. Villatoro, "High-temperature sensing with tapers made of microstructured optical fiber," IEEE Photonics Technology Letters, 18, 511–513, (2006).*

[88] *W. G. Chen, S. Q. Lou, L. W. Wang, H. Zou, W. L. Lu, and S. S. Jian, "Highly sensitive torsion sensor based on Sagnac interferometer using side-leakage photonic crystal fiber," IEEE Photonics Technology Letters, 23, 1639–1641, (2011).*

[89] *C. M. Jewart, T. Chen, E. Lindner et al., "Suspended-core fiber bragg grating sensor for directional-dependent transverse stress monitoring," Optics Letters, 36, 2360–2362, (2011).*

[90] *R. Jha, J. Villatoro, and G. Badenes, "Ultrastable in reflection photonic crystal fiber modal interferometer for accurate refractive index sensing," Applied Physics Letters, 93, Article ID 191106, (2008).*

[91] *G. Rajan, M. Ramakrishnan, Y. Semenova et al., "Analysis of Vibration Measurements in a Composite Material Using an Embedded PM-PCF Polarimetric Sensor and an FBG Sensor," IEEE Sensors Journal, 99, (2011).*

[92] *O. Frazao, S. H. Aref, J. M. Baptista et al., "Fabry-Perot cavity based on a suspended-core fiber for strain and temperature measurement," IEEE Photonics Technology Letters, 21, 1229–1231, (2009).*

[93] *A. M. Cubillas, M. Silva-Lopez, J.M. Lazaro,O. M. Conde, M. N. Petrovich, and J. M. Lopez-Higuera, "Methane detection at 1670-nm band using a hollow-core photonic bandgap fiber and amultiline algorithm," Optics Express, 15, 17570–17576, (2007).*

[94] *M. T. Myaing, J. Y. Ye, T. B. Norris et al., "Enhanced two photon biosensing with double-clad photonic crystal fibers," Optics Letters, 28, 1224–1226, (2003).*

[95] *J.Mathew, Y. Semenova, G. Rajan, and G. Farrell, "Humidity sensor based on photonic crystal fibre interferometer," Electronics Letters, 46, 1341–1343, (2010).*

[96] *X. H. Yang and L. L.Wang, "Fluorescence ph probe based on microstructured polymer optical fiber," Optics Express, 15, 16478–16483, (2007).*

[97] *J. C. K. A. Ortigosa-Blanch, W. J. Wadsworth, J. Arriaga, B. J. Mangan, T. A. Birks, P. St. J. Russell, "Highly birefringent photonic crystal fibers," Optics Letters 25, 1325-1327, (2000).*

[98] *A. M. R. Pinto, O. Frazão, J. L. Santos, and M. Lopez-Amo, "Multiwavelength Raman Fiber Lasers Using Hi-Bi Photonic Crystal Fiber Loop Mirrors Combined With Random Cavities", Journal of Lightwave Technology, 29, 1482-1488 (2011).*

[96] *A. M. R. Pinto, M. Lopez-Amo, "Double random mirror Hi–Bi photonic crystal fiber Sagnac based multiwavelength fiber laser", Appl. Phys. B, 103, 771–775 (2011).*

[100] A. M. R. Pinto, O. Frazão, J. Santos, M. Lopez-Amo, "Multiwavelength fiber laser based on a photonic crystal fiber loop mirror with cooperative Rayleigh scattering", Appl. Phys. B, 99, 391–395, (2010).

[101] Albert Einstein, "Zur Quantentheorie der Strahlung," Phys. Z. 18, 121–128 (1917).

[102] A. Tünnermann, T. Schreiber, and J. Limpert, "Fiber lasers and amplifiers: an ultrafast performance evolution" Applied Optics, 49, 25, (2010)

[103] E. Snitzer, "Optical maser action of Nd+3 in a barium crown glass", Physical Review Letters, 7, 444-446 (1961)

[104] R. J. Mears, L. Reekie, S. B. Poole and D. N. Payne, "Neodymium-doped silica single-mode fiber lasers", Electronic Letters, 21, 738-740 (1985)

[105] A. Bellemare, "Continuous-wave silica-based erbium-doped fiber lasers", Progress in Quantum Electronics, 27, 211-266 (2003)

[106] L. E. Nelson, D. J. Jones, K. Tamura, H. A. Haus, and E. P. Ippen, "Ultrashort-pulse fiber ring lasers", Applied Physics B: Lasers and Optics, 65, 2, 277-294 (1997)

[107] R. A. Perez-Herrera, "Design and Characterization of Wavelength Division Multiplexed Sensor Systems Using Optical Amplification" PhD Thesis (2010)

[108] International Telecommunication Union (ITU-T), "Optical interfaces for multichannel systems with optical amplifiers", Recommendation G.692, 1-40 (1998)

[109] R. A. Perez-Herrera, S. Chen, W. Zhao, T. Sun, K. T. V. Grattan and M. Lopez-Amo, "Experimental optimization in terms of power stability and output power of highly erbium-doped fiber lasers with single and hybrid cavities", Fiber and Integrated Optics, 29, 106-120 (2010)

[110] P. Urquhart, "Review of rare earth doped fiber lasers and amplifiers", IEE Proc., 135, 6 (1988)

[111] A. Bellemare, M. Karasek, M. Rochette, S. LaRochelle and M. Tetu, "Room temperature multifrequency erbium-doped fiber lasers anchored on the ITU frequency grid", Journal of Lightwave Technology, 18, 825-831 (2000)

[112] N. Park and P. F. Wysocki, "24-line multiwavelength operation of erbium-doped fiber-ring laser", Photonics Technology Letters, 8, 1459-1461 (1996)

[113] L. Talaverano, S. Abad, S. Jarabo and M. Lopez-Amo, "Multiwavelength fiber laser sources with Bragg-grating sensor multiplexing capability", Journal of Lightwave Technology, 19, 553-558 (2008)

[114] Y. Han, G. Kim, J. H. Lee, S. H. Kim and S. B. Lee, "Lasing wavelength and spacing switchable multiwavelength fiber laser from 1510 to 1620 nm", Photonics Technology Letters, 17, 989-991 (2005)

[115] Y. Han, T. V. A. Tran and S. B. Lee, "Wavelength-spacing tunable multiwavelength erbium-doped fiber laser based on four-wave mixing of dispersion-shofted fiber", Optics Letters, 31, 697-699 (2006)

[116] L. Rodríguez-Cobo, M. A. Quintela, S. Rota-Rodrigo, M. López-Amo, and J. M. López-Higuera, "Single-

longitudinal mode laser structure based on a very narrow filtering technique", Optics Express, 21, 8, 10289-10294 (2013)

[117] *S. Rota-Rodrigo, L. Rodríguez-Cobo, M. A. Quintela, J. M. López-Higuera, and M. López-Amo, "Dual-Wavelength Single-Longitudinal Mode Fiber Laser Using Phase-Shift Bragg Gratings" IEEE Journal of Selected Topics in Quantum Electronics, 20, 5 (2014)*

[118] *S. Rota-Rodrigo, R. A. Perez-Herrera, M. Fernandez-Vallejo and M. López-Amo, " Low noise dual-wavelength erbium fiber laser in single-longitudinal-mode operation" Applied Physics B, 106, 3, 563-567 (2012)*

[119] *S. Rota-Rodrigo, I. Ibañez and M. López-Amo, "Multi-wavelength fiber laser in single-longitudinal mode operation using a photonic crystal fiber Sagnac interferometer" Applied Physics B, 110, 3, 303-308 (2013)*

[120] *R. H. Stolen and E. P. Ippen, "Raman gain in glass optical waveguides," Appl. Phys. Lett., vol. 22, no. 6, 1973.*

[121] *R. H. Stolen and C. Lin, "Fiber Raman lasers," in CRC Handbook of Laser Science and Technology, Supplement 1: Lasers, Boca Raton, FL: CRC Press, 1991.*

[122] *M. N. Islam, "Raman Amplifiers for Telecommunications", Journal of Selected topics in Quantum Electronics, 8, 3, (2002)*

[123] *J. L. Archambault and S. G. Grubb, "Fiber Gratings in Lasers and Amplifiers", Journal of Lightwave Technology, 15, 8 (1997)*

[124] *L. Jintong, L. Dan, D. Yitang, "A Review on Fiber Lasers", Optical Fiber Technology, 8, 1-15 (2012)*

[125] *Y. Han, T. V. A. Tran, S. Kim and S. B. Lee, "Multiwavelength Raman-fiber-laser-based long-distance remote sensor for simultaneous measurement of strain and temperature", Optics Letters, 30, 1282-1284 (2005)*

[126] *P. Peng, H. Tseng and S. Chi, "Long "Long-Distance FBG Sensor System Using a Linear-Cavity Fiber Raman Laser Scheme", Photonics Technology Letters, 16, 575-577 (2004)*

[127] *J. H. Lee, J, Kim, Y. Han, S. Kim and S. B. Lee, "Investigation of Raman fiber laser temperature probe based on fiber Bragg gratings for long-distance remote sensing applications", Optics Express, 12, 1747-1752 (2004)*

[128] *V. Karalekas, J. D. Ania-Castañon, P. Harper, S. A. Babin, E. V. Podivilov, and S. K. Turitsyn, "Impact of nonlinear spectral broadening in ultra-long Raman fiber lasers", Optics Express, 15, 16690-16695 (2007)*

[129] *S. A. Babin, V. Karalekas, E. V. Podivilov, V. K. Mezentsev, P. Harper, J. D. Ania-Castañon and S. K. Turitsyn, "Characterization of ultra-long Raman fiber lasers" Proc. SPIE, 6873, art. No 68731P (2008)*

[130] *H. Martins, M. B. Marques and O. Frazao, "300 km-ultralong Raman fiber lasers using a distributed mirror for sensing applications", Optics Express, 19, 19, 18149-18154 (2011)*

[131] A. E. El-Taher, M. Alcon-Camas, S. A. Babin, P. Harper, J. D. Ania-Castañón, and S. K. Turitsyn, "Dual-wavelength ultralong Raman laser with Rayleigh-scattering feedback", Optics Lett 35, 1100-1102 (2010).

[132] S. K. Turitsyn, S. A. Babin, A. E. El-Taher, P. Harper, D. V. Churkin, S. I. Kablukov, J. D. Ania-Castanon, V. Karalekas and E. V. Podivilov, "Random distributed feedback fiber laser", Nature Photonics, 4, 231-235 (2010)

[133] D. H. Kim and J. U. Kang, "Sagnac loop interferometer based on polarization maintaining photonic crystal fiber with reduced temperature sensitivity", Opt. Express 12, 4490-4495 (2004)

[134] A. E. El-Taher, P. Harper, B. Babin, D. Churkin, E. Podivilov, J. Ania –Castañon, S.K. Turitsyn, "Effect of Rayleigh-scattering distributed feedback on multiwavelength Raman fiber laser generation", Optics Lett, 36, 130-132 (2011).

[135] M. Bravo, M. Fernandez-Vallejo, and M. Lopez-Amo, "Internal modulation of a random fiber laser", Optics Lett 38, 9, (2013)

[136] D. Vatnik, D. V. Churkin, and S. A. Babin, "Power optimization of random distributed feedback fiber lasers", Optics Express 20, (2012).

[137] R. A. Perez-Herrera, M. Lopez-Amo, "Fiber optic sensor networks", Optical Fiber Technology, 19, 689-699 (2013)

[138] G. A. Cranch, P. J. Nash, C. K. R. Kirkendall, "Large-scale remotely interrogated arrays of fiber-optic interferometric sensors for underwater acoustic applications", IEEE Sensors Journal, 19, 19-30 (2003)

[139] P. J. Nash and A. Strudley, "High efficiency TDM/WDM architectures for seismic reservior monitoring," 20th OFS, 7503, T1-T4, (2009).

[140] Y. Liao, E. Austin, P. J. Nash, S. A. Kingsley, D. J. Richardson," Highly Scalable Amplified Hybrid TDM/DWDM Array Architecture for Interferometric Fiber-Optic Sensor Systems" Journal of Lightwave Technology, 31, 882-888, (2012).

[141] N. A. Riza, M. Sheikh, "All-Silicon Carbide Hybrid Wireless-Wired Optics Temperature Sensor Network Basic Design Engineering for Power Plant Gas Turbines",International Journal of Optomechatronics. 4, 83–91, (2010).

[142] I. Roberts, A. Albert, L. El Hares, M. Rossi, Society of Petroleum Engineers – SPE Intelligent Energy International 2012, 1, 532–544, (2012).

[143] A. Rogers, "Distributed optical sensing", in: Handbook of Optical Fibre Sensing Technology, John Wiley & Sons, New York, 2002 (Chapter 14).

[144] J. Hu, Z. Chen, X. Yang, J. Ng, C. Yu, "100-km Long Distance Fiber Bragg Grating Sensor System Based on Erbium-Doped Fiber and Raman Amplification", IEEE Photon. Technol. Lett. 22, 1422–1424 (2010).

[145] Y. Nakajima, Y. Shindo, T. Yoshikawa, "Novel concept as long-distance transmission FBG sensor system using distributed Raman amplification,", 16th-OFS, pp. 1–4 (2003).

[146] M. Fernandez-Vallejo and M. Lopez-Amo, "Optical Fiber Networks for Remote Fiber Optic Sensors" Sensors, 12, 3929-3951 (2012)

[147] E. Mehrani, A. Ayoub, "Evaluation of Fiber Optic Sensors for Remote Health Monitoring of Bridge Structures". Mater. Struct./Mater. Construct., 42, 183–199 (2009)

[148] T. Saitoh, K. Nakamura, Y. Takahashi,H. Iida, Y. Iki, K. Miyagi, "Ultra-long-distance (230 km) FBG sensor system". Proc. SPIE, 7004, 70046C-4, (2008).

[149] Z. L. Ran, Y. J. Rao, N. Nie, and R. R. Chen, "Long-distance fiber Bragg grating sensor system based on hybrid Raman/erbium-doped fiber amplification", Proc. SPIE 5855, 17th International Conference on Optical Fibre Sensors, 583 (2005);

[150] J. Hu, Z. Chen, X. Yang, J. Ng, and C. Yu, "100 km long distance fiber Bragg grating sensor system based on erbium-doped fiber and Raman amplification," IEEE Photon. Technol. Lett. 22, 1422–1424 (2010).

[151] Y. Han, T. V. A. Tran, S. Kim, S. B. Lee, "Multiwavelength Raman-fiber-laser-based long-distance remote sensor for simultaneous measurement of strain and temperature." Opt. Lett., 30, 1282–1284, (2005)

[152] T. Saitoh, K. Nakamura, Y. Takahashi, H. Iida, Y. Iki, K. Miyagi, "Ultra-long-distance fiber Bragg grating sensor system." IEEE Photonics Technol. Lett., 19, 1616–1618, (2007)

[153] J. H. Chow, I. C. M. Littler, D. E. McClelland, M. B. Gray, "Long distance, high performance remote strain sensing with a fiber fabry-perot by radio-frequency laser modulation." Proc SPIE. 6201, (2006)

[154] T. Saitoh, K. Nakamura, Y. Takahashi, H. Iida, Y. Iki, K. Miyagi, "Ultra-long-distance (230 km) FBG sensor system." Proc. SPIE. 7004:70046C–4 (2008)

[155] J. Hu, Z. Chen, X. Yang, J. Ng, C. Yu "100-km Long distance fiber bragg grating sensor system based on erbium-doped fiber and Raman amplification." IEEE Photonics Technol. Lett., 22, 1422–1424, (2010)

[156] H. Junhao, Z. Chen, J. T. Teo and C. Yu "100-km long distance FBG vibration sensor based on matching filter demodulation", Proc. SPIE 7753, 21st International Conference on Optical Fiber Sensors, 77538N (2011);

[157] M. A. Soto, S. Faralli, M. Taki, G. Bolognini, F. Di Pasquale, "BOTDA sensor with 2-m spatial resolution over 120 km distance using bi-directional distributed Raman amplification." Proc. SPIE. 7753 (2011)

[158] M. Fernandez-Vallejo, D. Leandro, A. Loayssa, M. Lopez-Amo, "Fiber Bragg grating interrogation technique for remote sensing (100 km) using a hybrid brillouin-Raman fiber laser" Proc. SPIE. 7753 (2011)

[159] D. Leandro, A. Ullan, M. Lopez-Amo, J. M. Lopez-Higuera, A. Loayssa, "Remote (155 km) fiber Bragg grating interrogation technique combining Raman, brillouin and erbium gain in a fiber laser." IEEE Photonics Techno. Lett. 23, 621–623 (2011).

[160] M. Fernandez-Vallejo, S. Rota-Rodrigo, M. Lopez-Amo, "Remote (250 km) fiber Bragg grating multiplexing system." Sensors,11, 8711–8720, (2011)

[161] M. Bravo, J. M. Baptista, J. L. Santos, M. Lopez-Amo, O. Frazão, "Ultralong 250 km remote sensor system based on a fiber loop mirror interrogated by an optical time-domain reflectometer." Opt. Lett. 36, 4059–4061 (2011)

[162] L. Zou, O. Sezerman, Coherent probe-pump-based Brillouin sensor for 100- um crack detection and 100-km distributed strain and temperature sensing, in: Proceedings of SPIE, vol. 7753, article no. 77532B (2011)

[163] O. J. Kwon, H. J. Kim, M. S. Yoon, S. Park, Y. Shim, S. B. Lee, Y. G. Han, "Long distance simultaneous measurement of bending and temperature based on a dual-wavelength Raman fiber laser", Proceedings of SPIE, 7753, article no. 77531D (2011).

[164] J. Hu, Z. Chen, and C. Yu, "150-km Long Distance FBG Temperature and ibration Sensor System Based on Stimulated Raman Amplification" Journal of Lightwave Technology, 30, 1237-1243 (2012)

[165] M. Bravo, M. Fernández Vallejo, M. Lopez-Amo, "Hybrid OTDR-fiber laser system for remote sensor multiplexing" IEEE Sens. J. 12, 174–178 (2012)

[166] J. Cai, G. Xu, J. Hu, R. Wang, Zhongguo Jiguang/Chin. J. Lasers 39, article No. 1214002, (2012)

[167] M. Bravo, M. Fernández-Vallejo, M. Echapare, M. López-Amo, J. Kobelke, and K. Schuster, "Multiplexing of six micro-displacement suspended-core Sagnac interferometer sensors with a Raman-Erbium fiber laser" Optics Express, . 21, . 2971-2977 (2013)

[168] M. Fernandez-Vallejo, M. Bravo, M. Lopez-Amo, "Ultra-long laser systems for remote fiber Bragg gratings arrays interrogation", IEEE Photon. Technol. Lett., 25, 1362–1364, (2013)

[169] S. Rota-Rodrigo, L. Rodríguez-Cobo, M. A. Quintela, J. M. López-Higuera and M. López-Amo, "Switchable fiber optic laser system for high and low-strain fiber optic sensors remote multiplexing", Proc. SPIE, 5th EWOFS, 8794, 87943U (2013)

[170] M. Bravo, M. A. Erro, J. M. Algueta, S. Diaz and M. Lopez-Amo, "Remote fiber optic switch powered by light for robust interrogation of fiber Bragg grating sensor networks" Meas. Sci. Technol. 24, 4pp (2013)

[171] X. H. Jia, Y. Rao, Z. N. Wang, W. L. Zhang, C. X. Yuan, X. D. Yang, J. Li, H. Wu, Y. Y. Zhu and F. Peng, "142.2km BOTDA based on ultra-long fiber laser with a ring cavity" Proc SPIE, 4th Asia Pacific OSC, 8924, 89241A (2013)

[172] H. F. Martins, S. Martin-Lopez, M. L. Filograno, P. Corredera, O. Frazão and M. Gonzalez-Herraez, "Comparison of the use of first and second-order Raman amplification to assist a phase-sensitive optical time domain reflectometer in distributed vibration sensing over 125 km", Proc. SPIE, 23rd OFS, 9157, 91576K (2014)

[173] J. Yuan, Ch. Zhao, M. Ye, J. Kang, Z. Zhang and S. Jin, "A Fresnel Reflection-Based Optical Fiber Sensor System for Remote Refractive index Measurement Using an OTDR" Photonic Sensors, 4, 48-52 (2014)

[174] M. Bravo, V. DeMiguel-Soto, A. Ortigosa, and M. Lopez-Amo, "Fully switchable multi-wavelength fiber

laser based interrogator system for remote and versatile fiber optic sensors multiplexing structures" Proc. SPIE, 23rd OFS, 9157, 91576P (2014)

[175] *A. D. Kersey, A. Dandridge, "Distributed and multiplexed fiber-optic sensor systems", Journal of the Institution of Electronic and Radio Engineers, 58, S99-S111 (1988)*

[176] *L. Thévenaz, "Next generation of optical fiber sensors: new concepts and perspectives", Proc. SPIE, 23rd OFS, 9157, 9157AN (2014)*

[177] *N. Linze, "Development of optical fiber vibration sensors based on light polarization properties", Université de Mons, (2013)*

[178] *S. D. Personick, "Photon probe-An optical fiber time domain reflectometer," Bell Syst. Tech. J., 56, 355-366 (1977)*

[179] *D. E. N. Davies, "Signal processing for distributed optical fiber sensors," in Proc. Second OFS conference, 285-295 (1984)*

[180] *D. Uttam, B. Culshaw, "Precision Time Domain Reflectometry in Optical Fiber Systems Using a Frequency Modulated Continuous Wave Ranging Technique", Journal of Lightwave Technology, LT-3, 5, 971-977 (1985)*

[181] *Pinto, N. M. P., Frazao, O., Baptista, J. M., and Santos, J. L., "Quasi-distributed displacement sensor for structural monitoring using a comercial OTDR", Optics and Lasers in Engineering, 44, 771-778 (2006)*

[182] *Luo, F., Liu, J., Ma, N., and Morse, T. F., "A fiber optic sensor for distributed sensing application in the structural strain monitoring", Sensors and Actuators, 75, 41-44 (1999)*

[183] *Guangping, X., Keey, S. L., and Asundi, S., "Optical time-domain reflectometry for distributed sensing of the structural strain and deformation", Optics and Lasers in Engineering, 32, 437-447 (2000)*

[184] *Binu, S., Pillai, V. P. M., and Chandrasekaran, N., "OTDR based fiber optic microbend sensor for distributed sensing applications in structural pressure monitoring", Journal of Optics, 35, 36-44 (2006)*

[185] *W. Eickhoff and R. Ulrich, "Optical frequency domain reflectometry in singlemode fiber", Applied Physics Letters 39, 693-695 (1981)*

[186] *Luna Technologies white paper, "Optical vector network analyzer for single scan measurements of loss, group delay and polarization mode dispersion", www.lunatechnologies.com (2005)*

chapter II
DEVELOPMENT OF NEW FIBER OPTIC SENSING HEADS

INTRODUCTION

Fiber optic transducers are one of the main subsystems in a fiber optic sensor system. Fiber optic sensors are composed of 3 different subsystems: the optoelectronic unit, the transmission channel and the sensing transducers. In point sensors systems, these transducers are inside the sensing heads; being these the most characteristic subsystem.

This PhD work is focused on the measurement of different physical parameters for applications related with remote sensing and SHM. Typical parameters to be measured in those applications are temperature, strain and sometimes vibration and displacement. In this chapter, three specific point sensing heads that were developed for measuring displacement and strain are detailed, although in following chapters fiber optic transducers for measuring temperature, magnetic field and pressure will be also developed.

Fiber optic sensor systems are usually an expensive way to measure a single point, however, their capability to multiplex a large number of sensors makes this technology very attractive and cost efficient. The proposed sensors in this chapter try to reduce the cost of a single sensing head improving well known techniques.

2.1. PHOTONIC CRYSTAL FIBER SENSING HEADS

Photonic crystal fibers are a recently popularized kind of optical fibers [1], which present a geometry characterized by a periodic arrangement of air-holes running along the entire length of the fiber, centered on a solid or hollow-core. The major difference between PCFs and single mode fibers (SMFs) relies on the fact that waveguide properties of photonic crystal fibers are not due to spatially varying glass composition as in conventional fibers, but typically from an arrangement of very tiny and closely spaced air-holes going through the whole fiber length. In contrast with standard optical fibers, photonic crystal fibers can be made of a single material and have several geometric parameters that can be manipulated offering a great flexibility of design. Therefore, PCFs present a diversity of new and improved features when compared to common SMFs, introducing innovative solutions in the sensing field [2]. For example, conventional optical fibers contain two different materials with different thermal (thermal expansion coefficient) and mechanical properties (Young's modulus and Poisson's ratio), generating high thermal stress when the fiber is subjected to temperature variations, consequently changing the birefringence of the fundamental mode. Since a kind of PCFs called Hi-Bi PCFs are made of a single material, they do not present thermal stress, and thus, Hi-Bi PCF temperature associated variations were experimentally measured to be negligible [3]. The special guiding characteristics of the PCFs and the huge number of different fiber configurations offer a great potential for their use as sensors.

2.1.1. Micro-displacement sensing head based on a Suspended Core PCF in a Sagnac structure

Sensing solutions based on bending mechanisms in optical fibers have been widely studied over the years [4]. Using SM fiber bendings, different strain/displacement sensors have been proposed. [5-8]. These sensors presented good sensitivity and stability, but the output signal presented wavelength dependent losses due to core-cladding modal coupling. Other successful approaches for the utilization of fiber bends took advantage of birefringence based interferometric sensors. Thus, Sagnac loop based strain sensors using PCFs have been proposed: by employing one high birefringence PCF loop filter without polarization optimization [9], or by using a four-hole suspended-core fiber Sagnac [10], or even by applying two concatenated Sagnac interferometers [11]. The use of Hi-Bi PCF based Sagnac loops presents high extinction ratios and high insensitivity to temperature [12].

Figure 2.1 illustrates the first proposed transducer using PCFs of this PhD work. A broadband source provided the illumination to the sensing system through a 90:10 op-

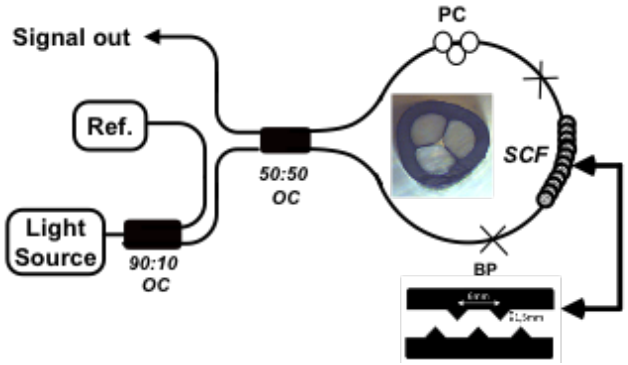

Figure 2.1 – Sensor system configuration. Inset: photograph of the suspended-core fiber used. ✂Splice point.

tical coupler (OC), which divided the light between the Sagnac interferometer and the reference output. The Sagnac loop filter was formed of a 50:50 OC, ~52 cm of a suspended-core fiber (SCF) and a polarization controller (PC). The SCF was spliced to the OC output fibers (single mode fiber-SMF), adding both splices a total loss of ~3 dB. The suspended-core fiber was fabricated at the IPHT (Institute of Photonic Technology, Jena, Germany) and consists of three big holes with a diameter of ~45 µm surrounding a ~6 µm diameter core (inset figure 2.1).

Stress was induced in the SCF using two bending plates (BP), shown in figure 2.1. Three different instruments were used for the output signal measurement: an OSA with a maximum resolution of 10 pm, a semiconductor photo-detector (New Focus 1811, 125 MHz, 900-1700 nm, high trasinpedance gain, 4x104 V/A, low noise equivalent power (NEP) and 3 ns rise time) and the optical backscattering reflectometer OBR4600 developed by Luna Technologies.

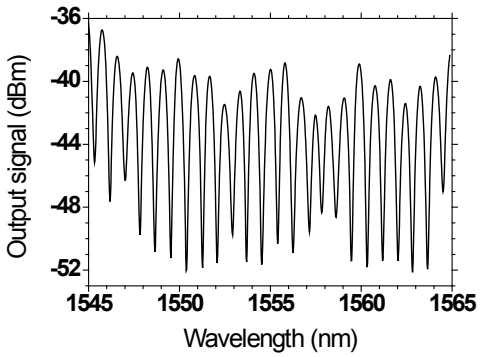

Figure 2.2 – Transmission output signal of the Sagnac loop filter.

The two main advantages of using this structure with the SCF for displacement measurements are: its insensitivity to temperature variations (0.009 dB/°C) in this configuration and its negligible core-cladding mode coupling problems. The geometry of the utilized fiber provides a high birefringence, and implies a high refractive Index difference for the different polarizations excited. The small core achieves a high confinement of the light into the core and low critical bend radius [13], leading to no core-cladding modal coupling setbacks with bendings (difficult to achieve using standard fibers) and a multimodal behavior.

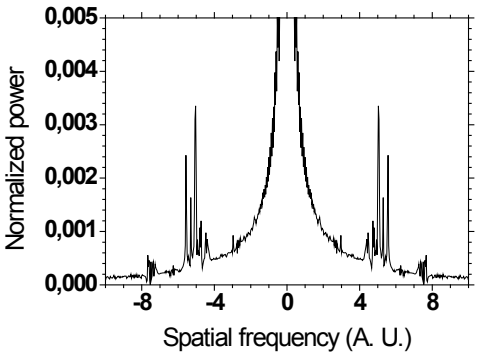

Figure 2.3 – FFT of the multimode oscillatory pattern.

The transmission output signal of the Sagnac interferometer is presented in Figure 2.2. As it can be seen in this figure, the output signal interference is not purely due to birefringence, but presents also another oscillatory pattern due to its multimodal behavior. In order to properly characterize the SCF, a detailed study was carried out via the OBR. This equipment provides high spatial resolution (~10 μm) for different measurable magnitudes, such as amplitude, polarization states and return loss in the frequency domain. By using it, while the SCF was stressed, the multimodal behavior and the polarization variation were studied. As so, a fast Fourier transform (FFT) of the SCF multimode oscillatory pattern was calculated, as it can be seen in figure 2.3. The effect of different propagation modes can be observed: 5 high energy interferences are visible and some other interferences appeared, although with less energy. The beating between these modes makes the output spectrum versus wavelength to exhibit an oscillatory pattern. In the interface zone between the SMF and the SCF the fundamental LP01 mode of the SMF couples to the modes supported by the multimode SCF. In the SCF-SMF interface, the propagation modes, propagated along the SCF length, interfere. During the stress induced measurements, it was observed that the propagating modes´ energy gets scram-

bled as the induced stress varies. Since the light is extremely confined in the SCF's core, the propagating modes transport a negligible amount of power through the cladding. As mentioned before, this feature insures the overcoming of core-cladding mode coupling problems, typical in bending based sensor systems. It also insures that the average output power of the propagating modes is maintained constant during stress variations on the fiber (while illuminated by a broadband source).

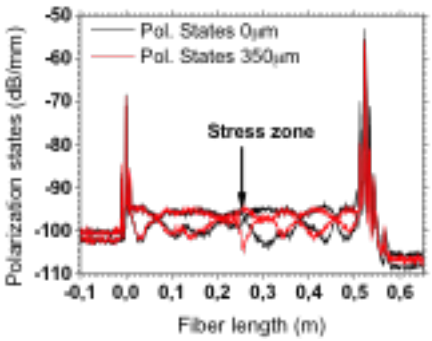

Figure 2.4 – OBR measured polarization states for two different stress situations as a function of the fiber length (0m<LSCF<0.528m)

A study of the SCF polarization states was preformed for several stress conditions. In figure 2.4 the polarization states for two different stress situations applied to the SCF are shown. The fiber length at which the stress variations were induced is indicated by an arrow in figure 2.4. The information obtained from figure 2.4 is the location and behavior of the splicing zones, the exact length of the SCF used and the relative variation of polarization states. The first observation that can be made is related to the higher peaks, corresponding to the splice zones between the SMF and the SCF. Through this observation the length of the SCF can be easily calculated, being accurately 0.528 m. But the most valuable information that can be extracted from figure 2.4 is the polarization variation with the length of the fiber. For lengths lower than 0 m and higher than 0.528 m (SMF zone) there are no visible polarization variations. While for the length corresponding to the SCF (0m<L<0.528m) a roughly periodic variation of the polarization components can be observed, confirming the existence of birefringence in the SCF. A change of the polarization states can be seen in the stress zone when stress is induced in the SCF. The change of the polarization states modifies the reflected and transmitted power in the Sagnac interferometer. As the light is highly confined, there is no loss inside the loop and the controlled polarization change induced by the bending plates modifies proportionally the transmitted and reflected signal as depicted in figure 2.5.

Another observable phenomenon is an increase in power between both splices, which we attribute to Rayleigh backscattered light: the SCF's core is expected to present more inhomogeneities distributed along the fiber than a SMF, thus presenting more Rayleigh backscattered light.

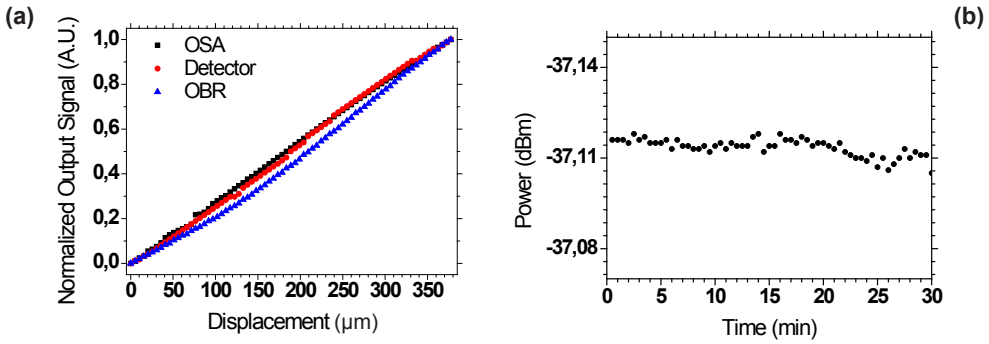

Figure 2.5 – a) Sensor response with displacement variation, when measured with an OSA, a detector and an OBR. b) Sensor signal power fluctuations.

After the study of the SCF properties, the SCF fiber was tested in the sensing setup, presented in figure 2.1, in order to measure micro-displacements. The measurements were performed with a high precision motorized stage, obtaining a range of displacement of 380 μm, with a step of 5 μm. The output signal monitoring variation with displacement was made through three different detection equipments: an OSA, a detector and the OBR. The sensor response to displacement variations is presented in figure 2.5 (a). It can be seen that the output signal response is highly linear regardless of the monitoring instrument. Stability measurements were made in order to determine the power fluctuations of the sensor output signal. As it can be observed in Figure 2.5 (b), these fluctuations did not exceed 0.03 dB in a 30 minutes lapse. As so, the measurement error due to the system stability was ~0.45 μm .

2.1.2. Strain sensing head based on a Hi-Bi PCF

An in-reflection interferometric Hi-Bi PCF sensing head for strain measurement is also proposed. A study of the sensing head characteristics is shown, being the theoretical study in accordance with the experimental data obtained through the OBR. Finally, a cost efficient sensing system based on this transducer is demonstrated.

2.1.2.1. Operation Principle

The operation principle of the sensor is based again on two main properties of the Hi-Bi PCF, high birefringence and low temperature sensitivity. The low temperature sensitivity characteristic, as it was explained before, is a direct consequence of the fabrication of the fiber using a single material. On the other hand, when light travels through a high birefringence fiber the speed difference between the two polarization axes causes the resulting polarization state to vary along the length of the fiber in a controlled manner. As it was presented in section 1.1.1, the beat length (LB) is defined as the distance to which the polarization rotates 360 degrees:

$$L_B = \frac{\lambda}{b} \qquad (2.1)$$

where λ is the wavelength at which the beat length is measured and b is the birefringence of the fiber. Since the sensing head works in reflection, the interference pattern is proportional to twice the fiber length and its wavelength dependence that can be expressed by eq. (2.2), where l is the fiber length, A is the amplitude of the transfer function and ϕ is the total phase:

$$R(\lambda)\big|_{dB} = 10Log\left[A \cdot Cos\left(2\pi \cdot \frac{2l \cdot b}{\lambda} - \phi\right)\right]^2 \qquad (2.2)$$

The total phase is defined as $\phi = \phi_0 + \Delta\phi$. Where ϕ_0 is the initial phase and $\Delta\phi$ is the phase change induced by external perturbations. When strain is applied to the fiber, the phase variation will be given by:

$$\Delta\phi(\lambda) = \frac{2\pi}{\lambda} \cdot (\Delta b \cdot 2l + 2\Delta l \cdot b) \qquad (2.3)$$

where Δl and Δb are the length and birefringence variations, respectively.

2.1.2.2. Sensing Head Characterization

The Hi-Bi PCF sensing head was obtained by splicing one end of ~20.8 cm Hi-Bi PCF to a SMF (maximum loss of 2 dB) and cleaving the other end. The Hi-Bi PCF is a polarization maintaining photonic crystal fiber, PM-1550-01 from NKT Photonics with a beat length of ~3.65 mm @1550 nm and a 1 dB/Km attenuation (a photograph of its cross section can be seen in figure 2.6(b)). Figure 2.6 (a)presents the setup used to characterize the sensing head. The OBR, a linear polarizer, a polarization controller (PC) and the Hi-Bi PCF sensing head were utilized.

The output light from the OBR was polarized by the linear polarizer while the polarization controller allowed adjusting the alignment angle between the source and the PCF. When the light was propagated along the PCF, a phase shift was generated between the two polarization axes.

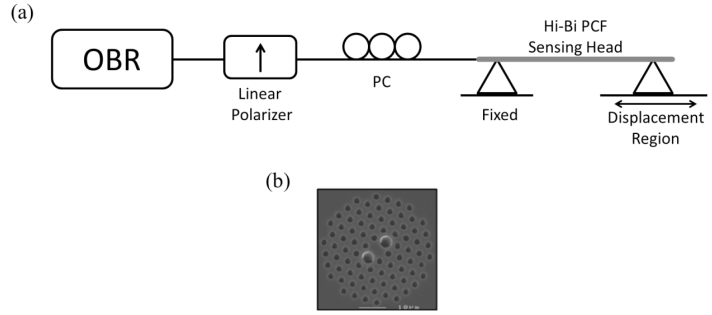

Figure 2.6 (a) Schematic of the experimental setup used to characterize the Hi-Bi PCF sensing head and (b) optical microscopic picture of the Hi-Bi PCF cross-section.

The light was reflected in the cleaved end and when the light reaches the linear polarizer, the phase shift between the polarization states occurred resulting in an interference pattern in the linear polarizer. The interferometric signal obtained for the sensing head is presented in figure 2.7.

Since the sensing head is based on a Hi-Bi PCF, it is sensitive to the angle between the input polarized light and the polarization axes of the fiber. According to theory, if this angle is 0° or 90° there is no interference signal, however, if the angle is 45° both components will have the same optical input and the interference will be maximum. Figure 2.8 presents the interferometric spectra obtained for different angles between the input light and the polarization axes.

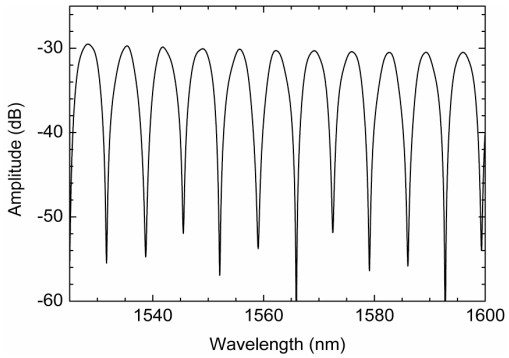

Figure 2.7. Reflected spectrum of the Hi-Bi PCF interferometer in a relaxed position, when no external force is induced on the sensing head.

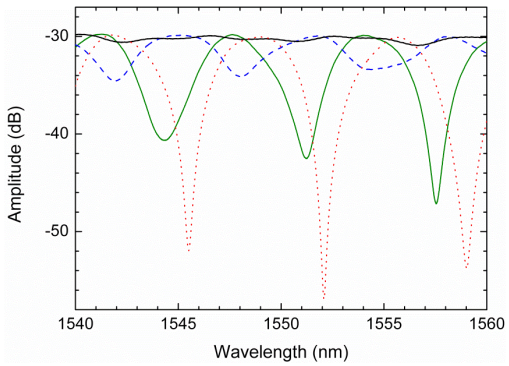

Figure 2.8. Interferometer spectra obtained for different polarization controller positions.

When strain variations were applied to the PCF, the interference output signal (presented in figure 2.7) shifted in wavelength. Figure 2.9 displays the experimental and theoretical results obtained for three different strain variations (0 με, 500 με and 1,000 με). As it can be seen in figure 2.9, the spectrum presents a wavelength shift when strain variations are forced into the sensing head, conforming to the simulations also presented in the same figure. Based on this characterization, strain measurement can be achieved by monitoring the interference wavelength shift, which presents a proportional behavior with strain variations.

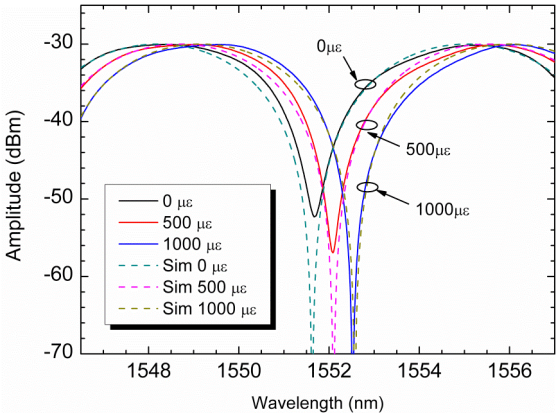

Figure 2.9. Experimental results (solid line) and theoretical simulations (dash line) of the reflected output signal for three different strain induced variations.

2.1.2.3. Sensor System and Results

After the Hi-Bi PCF sensing head characterization, the response to strain variations was measured through a cost efficient intensity based setup depicted in figure 2.10. The experimental configuration consisted of a semiconductor tunable laser source @1554 nm (Ando AQ8201-13), a circulator, a linear polarizer, a polarization controller, the Hi-Bi PCF sensing head, and an OSA. After the circulator, the laser light was linearly polarized and the polarization angle optimized before reaching the Hi-Bi PCF sensing head. The reflected signal that interfered in the linear polarizer passes again through the circulator before reaching the OSA.

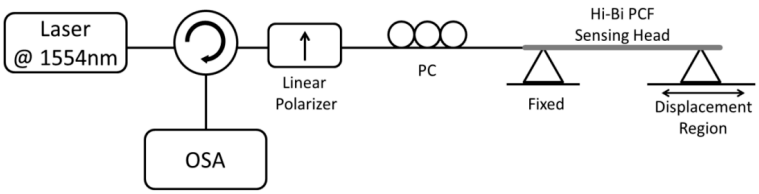

Figure 2.10 Experimental setup for strain measurement with an interferometric in-reflection Hi-Bi PCF sensing head.

When strain changes are applied to the Hi-Bi PCF, a phase shift in the interference pattern occurs proportionally to this strain (figure 2.9). Using the cost effective system illustrated in figure 2.10, the sensing head interrogation is undertaken by modulating the laser intensity. When the interference slope shifts with the strain, the laser power

varies proportionally. The observed power variation due to strain is depicted in figure 2.11. To achieve this plot, the fiber was fixed to a stepper motor with increments of 22.2 με. The Hi-Bi PCF sensing head response shows a quadratic behavior followed by a linear region. The linear region shows a sensitivity to strain variations of 7.96 dB/mε in 1200 με range. The breaking point of the sensing head was close to 5000 με.

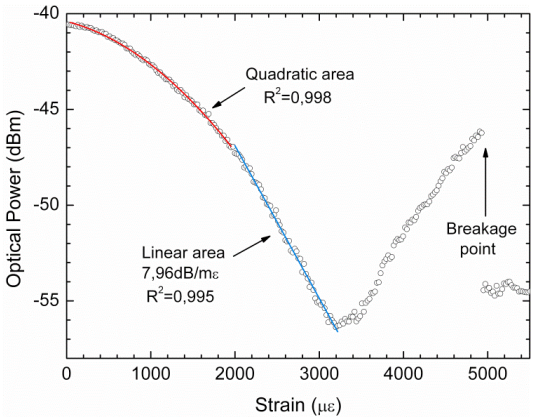

Figure 2.11. Measured optical power variation with strain.

This interferometric sensing head shows an appropriate response to strain variations, opening the possibility to obtain even better performance with a proper auto-referenced interrogation scheme such as a highly stable in-quadrature dual-wavelength fiber laser [14]. Also, the use of this system in-reflection is an attractive choice as a basic sensing element since it is simple, compact and presents the ability of remote sensing and multiplexing. Even more, reflective sensors enable the possibility for interrogation from a network header using a single fiber, as done in OTDR interrogation systems; that are explained briefly in the following chapter.

2.2. OTHER SENSING HEADS

Throughout this PhD. Work, diverse kinds of point fiber optic sensing heads will be used in different applications. Part of them are based on the modulation of the intensity of light that circulates through the transducers. The latest sensing head in this chapter may be considered as a new configuration in order to improve the dynamic range of those sensors. An intensity displacement sensor is inserted into a fiber ring resonator

structure, improving the dynamic range of the fiber optic transducer. This method can be applied to enhance the performance of other intensity sensors when needed.

2.2.1. Slow-light based micro-displacement sensor

Light-matter interactions are normally weak in most optical media in conventional conditions. Slow light structures allow a large reduction of the group velocity of the light signals travelling through them, and, as a consequence, a great enhancement of light-matter interactions [15]. These interactions include various linear and nonlinear effects.

From the point of view of fiber sensors, the possibility of enhancing light-matter interactions may favor the development of more compact and sensitive devices. Some research effort has been devoted to understanding the exact enhancement values given by slow light in different light-matter interactions. For instance, the role of slow light in enhancing nonlinear effects has been theoretically and experimentally investigated [16, 17]. The enhancement factor in Kerr effect has been shown to scale as n_g^2 (n_g being the group index of the structure). This enhancement effect has been explained as the combined effect of two contributions: the longer transit time of light pulses in the medium and the higher energy density due to spatial pulse compression. It has also been theoretically and experimentally proved that the extreme dispersion of slow light can lead to an enhancement in the spectral sensitivity of interferometers given by n_g [18]. The role of slow light in enhancing gyroscope performance [19] and Beer-Lambert-Bouguer (BLB) absorption [20, 21] has also been theoretically and/or experimentally investigated. Generally speaking, light-matter interactions have been found to be only enhanced in structural slow light systems (e.g. coupled resonators, Bragg gratings, etc.), i.e. systems relying on multiple interferences. Material slow light systems (e.g. stimulated Brillouin/Raman scattering, parametric amplification, etc.) do not follow the same rules, the origin of this difference being that the electromagnetic energy velocity in material slow light does not depend on the group index [22].

From the fiber sensing point of view, it is therefore interesting to find structural slow light media, i.e. passive structures in which the group index could be tuned widely. Such a system could be considered as a platform for the development of slow-light assisted sensors. Following it is theoretically and experimentally demonstrated a wide range tuning of the group delay in a lossy fiber-based ring resonator. This structure is shown to exhibit strong group delay changes close to the critical coupling regime. The strong group index variations observed are accompanied by strong absorption sensitivity en-

hancements, following similar scaling laws in both cases. For demonstrative purposes, a simple displacement sensor with sub-micrometric resolution is developed.

2.2.1.1. Theory

Basic Analysis of Lossy Ring Resonators and their attenuation sensitivity

In this section it is performed a theoretical study of slow and fast light in lossy fiber ring resonators. Depending on the coupling ratio and the loss in the resonator, the group delay of the ring resonator can be tuned from strong delay to strong advancement, in particular when the losses in the resonator are tuned close to the critical coupling regime.

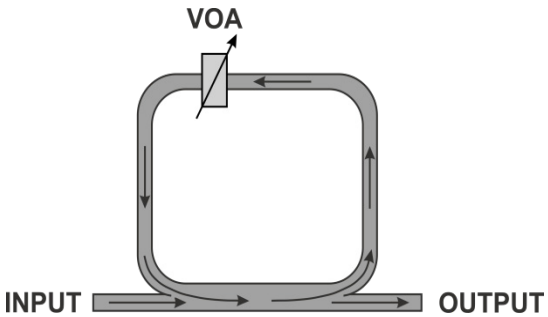

Figure 2.12. Fiber-based lossy ring resonator considered.

Figure 2.12, depicts a fiber ring resonator with a variable loss element inside. Despite not being shown, a polarization controller ensures that the polarization evolution over one round-trip remains constant. Our analysis of this structure is similar to the analysis found in [23] for resonator-coupled waveguides. A transfer function can be found:

$$\frac{E_0}{E_i} = \frac{\kappa \exp\left(\frac{i\omega nL}{c}\right) - a}{\exp\left(\frac{i\omega nL}{c}\right) - \kappa a} \qquad (2.4)$$

where κ and a are the coupling ratio (square root of the fraction of recirculated power) and the field transmission coefficient in the resonator (in unitless form) respectively. As expected, the transfer function leads to resonances in the spectrum with a periodicity given by c/nL. These resonances exhibit steep dispersion slopes close to the center,

leading to large group delays, especially when tuned close to the critical coupling case. It is possible to theoretically evaluate the group delay in the resonances by finding the phase of expression (2.4), obtaining the derivative with respect to ω, and evaluating the obtained expression at the resonant frequencies. The resulting expression for the group delay is:

$$\tau_g = \frac{nL}{c} \cdot \frac{a\left(1-\kappa^2\right)}{\kappa\left(a^2+1\right)-a\left(\kappa^2+1\right)} \qquad (2.5)$$

It can be seen that the delay in the resonator can be expressed as the regular single-pass delay of the resonator (nL/c) multiplied by a factor that may be varied continuously by changing only the attenuation and/or coupling ratio in the resonator. It can be easily shown that, when the losses exceed the coupling (undercoupling), negative group delays can be found at the resonances, while they remain positive in the opposite case (overcoupling). A discontinuity in function (2.4) is found for the critical coupling case (a = κ), where the group delay function displays a vertical asymptote, taking values of -∞ when a → κ- and +∞ when a → κ+. The evolution of the group delay close to the critical coupling can be described by $\tau_g \propto (\kappa\text{-}a)^{-1}$. The qualitatively different behavior of both regimes is depicted in figure 2.13.

Now is also possible to evaluate the transmission coefficient of the resonator in the center of the resonance as a function of the attenuation and coupling coefficients. The power transmission coefficient can be written as:

$$T = \left|\frac{a-\kappa}{\kappa a-1}\right|^2 \qquad (2.6)$$

As it can be seen, in the transmission coefficient, the case a = κ (critical coupling) corresponds to the case in which the transmission at the resonance center goes to zero. It is interesting to evaluate the sensitivity of the absorption/attenuation in the structure to small absorption/attenuation changes in the ring:

$$S = -\frac{d\ln T}{da} = \frac{2}{\kappa-a} + \frac{2}{\kappa a-1} \qquad (2.7)$$

In this equation, the sensitivity S has been defined as the attenuation sensitivity of a traveling-wave system (derivative of the log transmission).

The sensitivity of S to small variations in a can be extremely large under two conditions: when the losses and the coupling ratio are equal ($a = \kappa$) or when the $a\kappa \rightarrow 1$, which can only be achieved when the losses are low and the re-circulated intensity in the loop is maximized. This last case (high Q resonators) has been conventionally used in sensing, as strong field enhancements and long photon lifetimes can be obtained in the cavity. However, extremely high sensitivities can also be obtained in low-Q resonators by exploiting the region close to critical coupling ($a = \kappa$). This region has been far less exploited in the literature, and is the region in which the group delay can be made extremely large as shown before in this section.

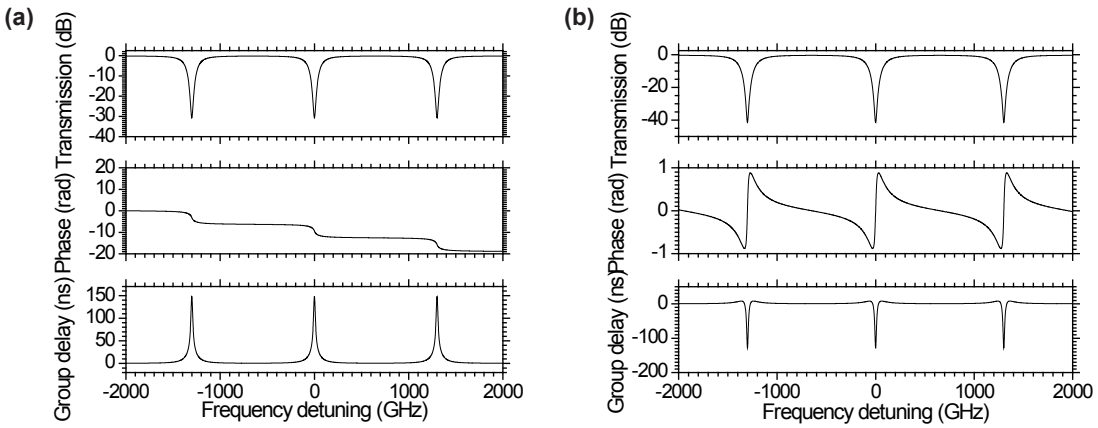

Figure 2.13. Phase, modulus and group delay response vs. frequency in a 1.59 meter and κ=0.7 (≈1.55 dB) fiber loop with (a) 1 dB attenuation and (b) 2 dB attenuation.

On the origin of sensitivity enhancement close to the critical coupling

It has been shown above that strong sensitivity enhancements occur close to critical coupling, and also strong group index changes. One may then wonder if this enhancement effect is related to the well-known field enhancement within a resonator or a photon lifetime increase in the cavity. However, as mentioned, these situations are only observed in high-Q resonators. The intensity recirculating into the cavity in resonance can be written as:

$$\left|\frac{E_{circ}}{E_i}\right|^2 = \left|\frac{1-\kappa^2}{1-a\kappa}\right|^2 \qquad (2.8)$$

As it is visible, the circulating intensity decays monotonically as the losses are larger, and only diverging in the high-Q case ($a\kappa \rightarrow 1$, i.e. when the losses are zero and the re-circulating power is maximized). In the critical coupling, the re-circulating power and the input power are equal. This is consistent with the fact that the transmission of the structure in this case is zero (all the energy is "kept" in the circulator). This storage picture is also consistent with the qualitative picture of slow light in a medium with infinite group delay.

In addition to the previous discussion, it is important to turn the attention to the photon lifetime in the cavity, which can be written as:

$$\tau = \frac{nL/c}{\delta} = \frac{nL/c}{\left(1-a^2\kappa^2\right)} \qquad (2.9)$$

Where δ represents the fractional power loss in one round-trip. As it is visible, the photon lifetime also decays monotonically with the loss inside the cavity, and does not present any special behavior in critical coupling case.

There is another interesting relationship with slow light by evaluating the expression of the sensitivity (2.7) and the group delay (2.5) close to the critical coupling. Both expressions hold similar evolutions close to critical coupling:

$$S\big|_{critical} \propto (\kappa - a)^{-1} \propto \tau_g\big|_{critical} \qquad (2.10)$$

To sum up, a theoretical study has been performed demonstrating the capability of lossy fiber ring resonator to tune between slow- and fast-light regimes by simply varying the coupling ratio or losses of the structure. Around the critical coupling, strong group delays can be observed which are expected to coincide with strong sensitivity enhancements to attenuation or absorption in the ring for a fixed coupling ratio.

The next sections explore these concepts experimentally, proving the aforementioned analysis and proposing a simple low-cost implementation of a displacement sensor ba-

sed upon these concepts. For this purpose, an Optical Vector Analyzer (OVA) has been used, obtaining both, the spectral response and the group delay variation as a function of the losses inside the ring. Furthering these, a functional setup is proposed which could measure sub-micrometric displacements in a simple setup with an assumable cost.

2.2.1.2. Experimental validation of the theory

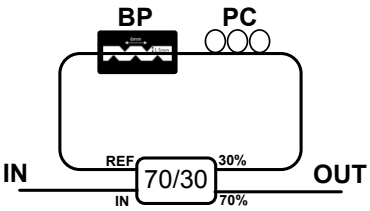

Figure 2.14. Experimental setup for the fiber ring under study. The structure is illuminated by "IN" port and the response is detected by "OUT". BP: Bending Plates; PC: Polarization Controller.

Figure 2.14 illustrates the experimental setup for the lossy ring resonator structure used in this work. A fiber coupler, a polarization controller and a high precision mechanic attenuator based on the stress-inducing plates also used in 2.1.1. (labeled BP in the figure 2.14), were used for creating the lossy fiber ring. The main component in the proposed structure was the 70:30 optical coupler. A polarization controller was placed inside the ring to adjust the polarization transfer function of the ring. The attenuation in the ring was varied by controlling the displacement of the bending plates through the high precision actuator. The attenuation response induced by the plates on the fiber is plotted in figure 2.15. The total length of fiber in the loop was ~1.59 meters. The OVA was then used to measure the transmission and group delay response of the structure.

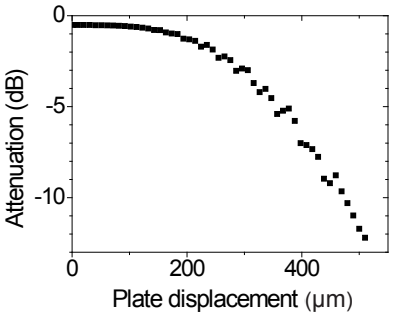

Figure 2.15. Attenuation profile of the bending plates versus the displacement.

Figure 2.16 depicts two sample transmission and group delay spectra obtained for two different attenuation values. The central wavelength for the analysis was set at ~1550 nm with 10 pm (1.25 GHz) measuring span. The separation between resonances (figure 2.16 (a) and (b)) corresponds to ~130 MHz as expected when ~1.59 m loop length was used. Figure 2.16 (a) illustrates the group delay (above) and transmission (below) spectra when the attenuation was set at ~1.43 dB, corresponding to the case a< κ. As expected from the previous analysis, this configuration gave positive group delays (slow-light regime), peaking in the resonances. In figure 2.16 (b) the attenuation was increased until ~-1.7 dB which corresponds to the case a>κ (fast light regime). In comparison of the response in figure 2.16 a), the peaks show negative values referenced to the ~150 ns mean delay, corresponding to the expected fast-light response.

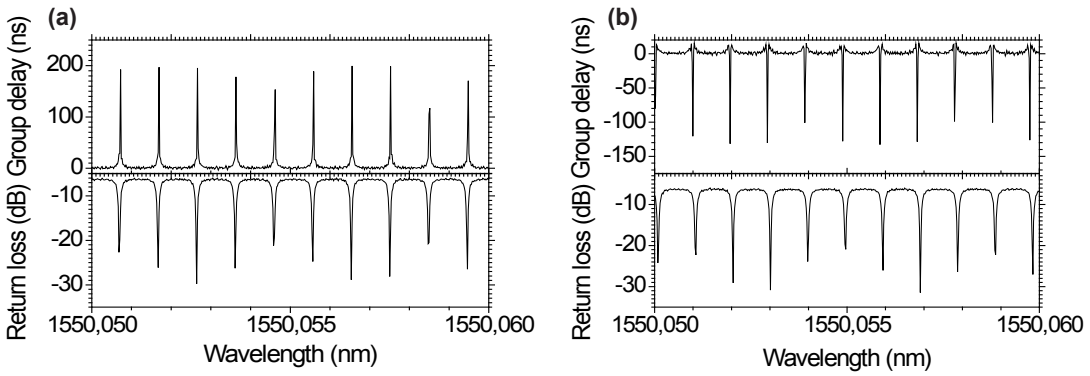

Figure 2.16. a) Group delay and power transmission in the ring vs. frequency when ~1.43 dB attenuation is inside the ring. b) Group delay and power transmission in the ring vs. when ~-1.7 dB attenuation is inside the ring.

In order to compare the theory with the experimental results, the group delay and transmission in the resonances were tracked as the ring loss was varied by shifting the plates. The results are depicted in figure 2.17 (a) and (b). The dots are the experimental data and the lines correspond to the theoretical expectation obtained from the model developed in the theory. A good agreement can be seen between the results obtained experimentally and the theoretical model. At critical coupling (~1.55 dB attenuation), the transition between positive group delay and negative group delay is visible (slow-fast-light switch). Close to this point, the sensitivity to small absorption/attenuation is clearly visible, small absorption changes providing large transmission changes. It is important to highlight the enhanced loss sensitivity. In the following sub-section, it was taken the advantage of this characteristic for its use in a fiber optic sensing application.

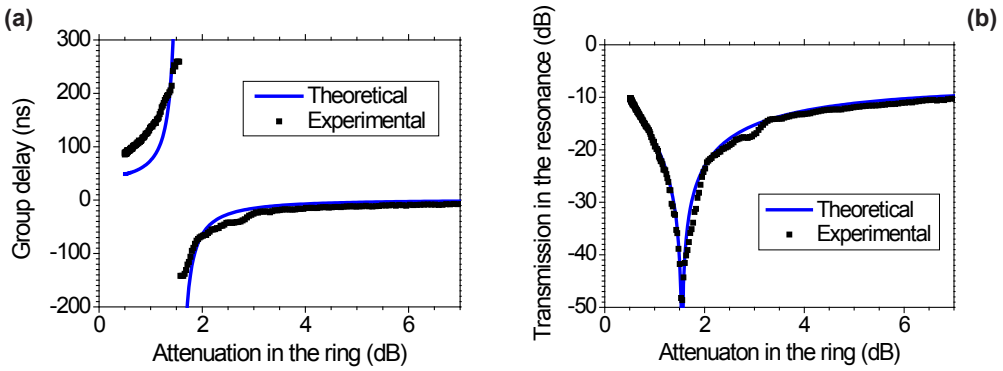

Figure 2.17. a) Measured peak group delay as a function of the attenuation induced in the ring. b) Measured peak loss as a function of the attenuation induced in the ring.

2.2.1.3. Enhanced sensitivity sub-micrometric fiber optic displacement sensor cost effective proposal

One of the main objectives of this section is to provide a functional and practical application of the previous structure. The measurements of the previous section already show that strong absorption sensitivity can be achieved in this structure. Translating the previous results in terms of displacement resolution, with this structure one can already measure sub-micron displacements of the plates using a simple transmission measurement in the resonances. However, the use of the OVA for the interrogation of the structure is a very expensive solution. Thus, a functional and cost-effective solution for the interrogation was crucial. The main idea was to track the transmission spectral dips as a function of the plates' displacement. Therefore, a high resolution tuning of a

laser was necessary to scan over several resonances. Linearity, stability, and narrow line-width of the laser were crucial to ensure that the transmission transfer function was correctly measured. In this case, a conventional external-cavity tunable laser with a line-with of 5 MHz was used as the sweeping source. The output power was detected by a simple narrowband photodetector. Figure 2.18 illustrates the results obtained with the proposed functional setup (black dots) in comparison with the OVA results previously obtained (blue line). Small oscillations due to cladding mode coupling effects are visible in the tunable laser measurement. Other non-idealities of the results can also be due to the much larger line-width of this source in comparison with the OVA source and the imperfect stability of the polarization. Still, the proposed setup shows reasonably high sensitivity around the critical coupling regime. In the particular case of the structure demonstrated in this work, the displacement sensitivity close to the critical coupling point exceeds 1 dB/μm. As a comparison, this sensitivity value is more than two times the sensitivity achieved with the developed sensor presented in section 2.1.1. Using low-cost acquisition methods, this sensitivity can easily allow sub-micron resolution in displacement values.

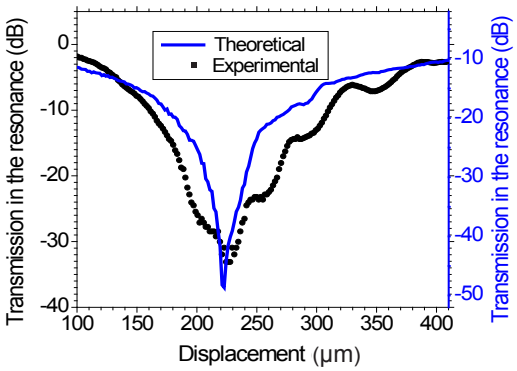

Figure 2.18. Power transmission as a function of the displacement for theoretical and experimental measurements.

2.3. CONCLUSIONS

The objective of this chapter was to describe three point sensors that have been developed during this PhD. work. Two of the three proposals are interferometric in nature and uses PCFs, and the last one is based on a fiber ring resonator structure in order to enhance the measurement sensitivity. All sensors were focused in high resolution and high dynamic range measurements of strain and displacement. They were developed in a simple way to be cost-effective sensors with a high performance behavior.

The first developed sensing head is an improvement of a well known bending technique for fiber optic sensing. Using a SC-PCF, light was highly confined, avoiding mode radiation and the unwanted effects of the cladding modes re-coupling that affect sensors that use standard SM fiber. The developed sensing head also offers self-referencing capability and a high resolution performance.

The second developed sensing head uses a HiBi-PCF as transducer. By straining the fiber, high resolution measurements have been obtained in a cost effective setup based on the modulation of the intensity of a laser source avoiding the use of expensive devices such as OSAs.

Finally, a sensing head based on a ring structure to improve an intensity sensor sensitivity is proposed and demonstrated. To this end, a study of the group velocity into the structure was carried out. It has been experimentally demonstrated that large group delays occur when the loss in the resonator is tuned close to the critical coupling regime. Using the proposed structure, it is demonstrated that the sensitivity of intensity sensors may be improved around twice.

The results presented in this chapter were published in [24-29]

2.4. REFERENCES

[1] J. C. Knight, T. A. Birks, P. S. Russell, D. M. Atkin, "All-silica single-mode optical fiber with photonic crystal cladding". Optics Letters, 21, 1547–1549 (1996)

[2] A. M. R. Pinto, M. Lopez-Amo, "Photonic crystal fibers for sensing applications" Journal of Sensors 2012, (2012)

[3] D. H. Kim, J. U. Kang, "Analysis of temperature-dependent birefringence of a polarization-maintaining photonic crystal fiber" Optics Engineering, 46, 075003 (2012)

[4] J. L. Santos, M. Lopez-Amo, J. Kobelke, K. Schuster, "Interrogation of a suspended-core Fabry-Perot temperature sensor through a dual wavelength Raman fiber laser" J. Lightwave Technology, 28, 3149–3155 (2010)

[5] V. Arya, K. A. Murphy, A. Wang, R. O. Claus, "Microbend losses in singlemode optical fibers: theoretical and experimental investigation," J Lightwave Technology, 13, 1998-2002 (1995).

[6] F. Luo, J. Liu, N. Ma, T. F. Morse, "A fiber optic microbend sensor for distributed sensing application in the structural strain monitoring," Sensors and Actuators, 75, 41-44 (1999).

[7] X. Guangping, S. L. Keey, A. Asundi, "Optical time-domain reflectometry for distributed sensing of the structural strain and deformation," Optics and Laser in Engineering, 32, 437-447 (2000).

[8] C. Li, Y. Zhang, H. Liu, S. Wu, C. Huang, "Distributed fiber-optic bi-directional strain-displacement sensor modulated by fiber bending loss," Sensors and Actuators A 111, 236-239 (2004).

[9] M. Bravo, M. Fernandez-Vallejo, M. Lopez-Amo, "Hybrid OTDR-fiber laser system for remote sensors multiplexing," IEEE Sensors Journal, 12, 174-178 (2011).

[10] X. Dong, H. Y. Tam, P. Shum, "Temperature-insensitive strain sensor with polarization maintaning photonic crystal fiber based Sagnac interferometer," Applied Physics Letters 90, 151113- (2007).

[11] O. Frazao, J. M. Baptista, J. L. Santos, J. Kobelke, K. Schuster, "Strain and temperature characterisation of sensing head based on suspended-core fibre in Sagnac interferometer," Electron Letters, 44, 1455-1456 (2008).

[12] O. Frazao, J. L. Santos, J. M. Baptista, "Strain and temperature discrimination using concatenated high-birefringence fiber loop mirrors," IEEE Photonics Technology Letters 19, 1260-1262 (2007).

[13] J. Villatoro, V. Finazzi, G. Badenes, V. Pruneri, "Highly sensitive sensors based on photonic crystal fiber modal interferometers," Journal of Sensors 2009, 11 (2009).

[14] P. S. J. Russell, "Photonic-crystal fibers," J. Lightwave Technology, 24, 4729-4749 (2006).

[15] J. B. Khurgin and R. S. Tucker, "Slow light: Science and applications," CRC Press, Boca Raton, (2009).

[16] M. Soljacic, S. G. Johnson, S. Fan, M. Ibanescu, E. Ippen, and J. D. Joannopoulos, "Photonic-crystal slow-light enhancement of nonlinear phase sensitivity," J. Opt. Soc. Am. B, 19, 2052, (2002).

[17] C. Monat, B. Corcoran, M. E. Heidari, C. Grillet, B. J. Eggleton, T. P. White, L. O'Faolain and T. F. Krauss, "Slow light enhancement of nonlinear effects in silicon engineered photonic crystal waveguides," Opt. Express, 17, 2944-2953 (2008).

[18] Z. Shi, R. W. Boyd, D. J. Gauthier and C. C. Dudley, "Enhancing the spectral sensitivity of interferometers using slow-light media," Optics Letters, 32, 915-917 (2007).

[19] M. Terrel, M. J. F. Digonnet and S. Fan, "Performance comparison of slow-light coupled-resonator optical gyroscopes," Laser & Photon. Rev., 3, 452-465, (2009).

[20] N. A. Mortensen and S. Xiao, "Slow-light enhancement of Beer-Lambert-Bouguer absorption," Appl. Phys. Lett., 90, 141108, (2007).

[21] S. Chin, I. Dicaire, J. Beugnot, S. Foaleng-Mafang, M. Gonzalez-Herraez, and L. Thévenaz, "Material Slow Light Does Not Enhance Beer-Lambert Absorption," in Slow and Fast Light, OSA Technical Digest (CD) (Optical Society of America), paper SMA3, (2009).

[22] M. Santagiustina, "Electromagnetic Energy Velocity in Slow Light," in Slow and Fast Light, OSA Technical Digest (CD) (Optical Society of America), paper SLTuB5, (2011).

[23] J. Heebner and R. W. Boyd, "Slow and fast light in resonator-coupled waveguides," J. Mod. Optics, 49, 2629-2636, (2002).

[24] Bravo M, Pinto A. M., Lopez-Amo M., Kobelke J. and Schuster K., "High precision micro-displacement fiber sensor through a suspended-core Sagnac interferometer", Optics Letters, 37,202-204 (2012)

[25] S. Rota-Rodrigo, A. M. R. Pinto, M. Bravo and M. Lopez-Amo, "An In-Reflection Strain Sensing Head Based on a Hi-Bi Photonic Crystal Fiber", Sensors, 13, 8095-8102 (2013).

[26] X. Angulo-Vinuesa, M. Bravo, S. Martin-Lopez, M. Lopez-Amo and Miguel Gonzalez-Herraez, "Wide range group delay tuning in lossy fiber ring resonator", Proc SPIE, 22nd OFS conference, 8421, 842197 (2012).

[27] M. Bravo, X. Angulo-Vinuesa, S. Martin-López, M. Lopez-Amo and M. González-Herráez, "Versatile all-fiber slow-light assisted sensor", Proc. SPIE, Advances in Slow and Fast Light VI, 8636, 86360K (2013).

[28] M. Bravo, X. Angulo-Vinuesa, S. Martin-Lopez, M. Lopez-Amo and Miguel Gonzalez-Herraez, "Turning a low Q fiber resonator into a high-sensitivity displacement sensor using slow light concepts" Proc. SPIE 5th EWOFS, 8794, 879420 (2013).

[29] M. Bravo, X. Angulo-Vinuesa, S. Martin-Lopez, M. López-Amo, and M. González-Herráez, "Slow-Light and Enhanced Sensitivity in a Displacement Sensor Using a Lossy Fiber-Based Ring Resonator", Journal of Lightwave Technology, 31, 3752-3757 (2013).

chapter III
FIBER OPTIC TIME DOMAIN REFLECTROMETRY FOR SENSORS INTERROGATION

INTRODUCTION

Optical time domain reflectometry (OTDR) is a suitable technique to interrogate intensity sensors and thus, to measure the induced change in the optical intensity at different locations on the fiber. Parameters such as strain and displacement can be measured by detecting the variations of the Rayleigh backscattered light. OTDR is one of the most suitable sensor measurement techniques and its importance in structural health monitoring (SHM) has increased due to its suitability for real time monitoring of the large civil engineering structures deformations [1-5].

In this chapter, different examples are presented showing how conventional OTDR instruments can be used as fiber optic sensor interrogation devices. Firstly, they have been used to characterize single sensors and, afterwards, they have been utilized for diverse multiplexing and remote monitoring applications. The study is focused on demonstrating the advantages that the OTDR, initially developed for fiber network characterization, offers in fiber optic sensor systems. The commercial OTDR used in this work is the EXFO FTB-7423B-B.

3.1. SINGLE FIBER OPTIC SENSING HEADS INTERROGATED BY OTDR

This section is devoted to the development of three single sensing heads to be interrogated by the utilized OTDR. The main characteristic of these sensors is that they work in reflection, so they are well suited for the selected interrogation method. Two micro-displacement and one magnetic field sensing heads are following presented.

3.1.1. Fiber loop mirror combined with a long period Grating micro-displacement sensing head.

The first proposed sensor was based on the utilization of the fiber loop mirror (FLM) structure and the bending sensitivity of the LPGs. Thus, when a LPG is inserted into the loop of the FLM structure (figure 3.1), it modulates the reflected intensity proportionally to the fiber bend.

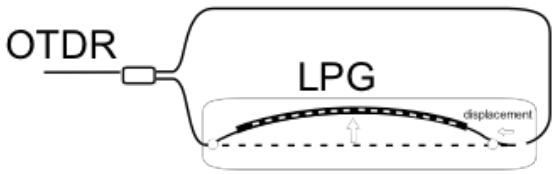

Figure 3.1. FLM/LPG displacement sensing head.

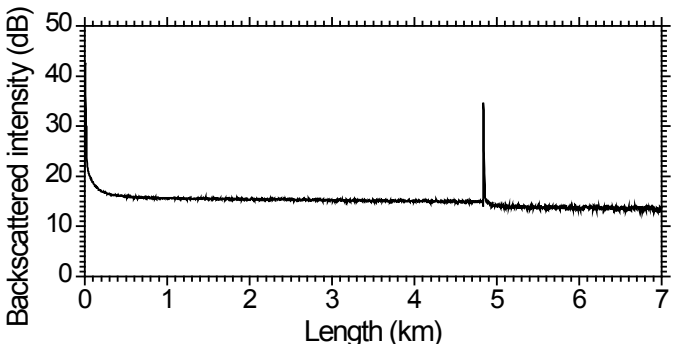

Figure 3.2. FLM/LPG sensor reflection peak measured by the OTDR.

Figure 3.2 illustrates an OTDR trace when the FLM/LPG sensor was arranged between two 5 km fibers spools by using a 90:10 optical coupler. Around the 5th kilometer, where the FLM/LPG sensor was placed, it is visible a high reflection peak from the FLM/LPG structure which allows performing high sensitivity displacement measurements. To characterize the sensor structure, both LPG extremes were fixed in two points on a translation stage, as shown in figure 3.1. The displacement of this translation stage was controlled by a computer to achieve more accurate results. The displacement steps programmed for each measurement had a value of 50 μm. Figure 3.3 (a) presents the displacement behavior of the sensor. It shows two different linear regions with different sensitivity each.

One important characteristic of the proposed sensing head is its theoretical temperature insensitivity, which was also experimentally studied. In figure 3.3 (b) is shown the measured power from the sensor against temperature variations, showing a very stable behavior.

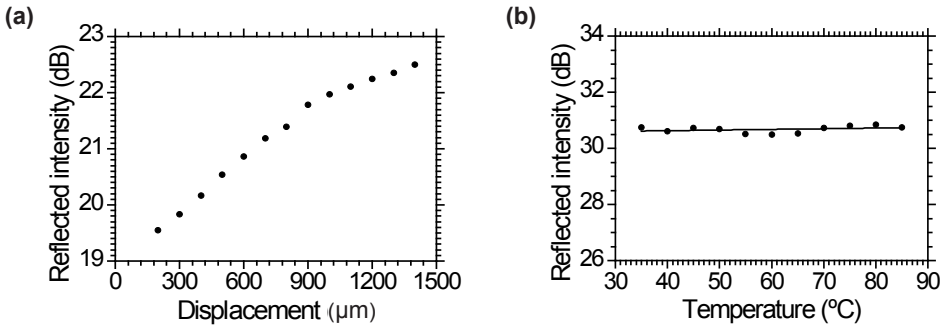

Figure 3.3. a) FLM/LPG displacement characterization result and b) experimental temperature insensitivity demonstration.

In what concerns the FLM and comparing to a good metalized end facet of the fiber, the FLM has a simpler implementation, since it only requires a coupler and a splice. Moreover, it is a more robust device, because it is not so prone to any undesirable mechanical or chemical damage and does not degrade with time, being its performance very stable.

3.1.2. Micro displacement sensor based on an air cavity inserted in a fiber ring structure

In this section other approach is presented in order to perform micro-displacement measurements with the OTDR. An air cavity, which is formed by two cleaved and aligned SMF28 fibers, is placed inside a fiber ring configuration as figure 3.4 illustrates. The ring is formed by a 90:10 low insertion loss optical coupler. This structure has been interrogated using the previously mentioned OTDR.

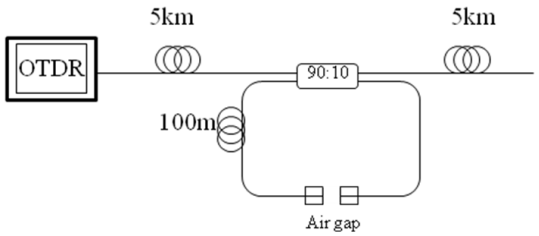

Figure 3.4. Experimental setup of the fiber ring resonator combined with the proposed sensing head for OTDR interrogation.

To properly understand the measuring procedure utilized in this structure it is important to take into account the OTDR basis explained in section 1.4.2.1. The OTDR measures the backscattered and reflected signal generated by an optical pulse launched by itself at the fiber input. Figure 3.5 shows two different traces: The thickest one belongs to the OTDR structure response presented in figure 3.4 without the air gap cavity; on the contrary, the second trace displays the OTDR response for the structure shown in figure 3.4, comprehending the fiber ring with the cavity. Both of them are thoroughly explained below.

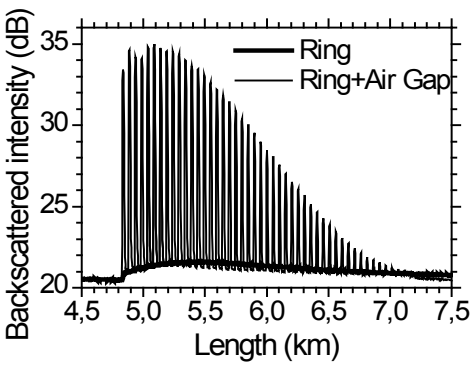

Figure 3.5. OTDR traces when the air cavity is placed into the ring and the OTDR response of the ring structure without the air gap.

In the first case, the thickest trace, a small power increment due to the contribution of the Rayleigh scattering. This scattering is generated into the ring and also in the 5 km spool connected after the sensor. Therefore, when the OTDR pulse reaches for first time the sensor, part of its power is divided in an unevenly way (90:10). 90% of this pulse goes to the 5 km spool, located after the coupler, generating some Rayleigh scattering which is added to the Rayleigh produced by the 10% pulse power which enters into the 100 m fiber section of the ring. When the pulse traveling through the ring reaches the coupler again, part of its power (10%) is coupled back to the first 5 km spool and the rest of its power (90%) is coupled again to the ring. The effect of this recirculated pulse can be appreciated for some time (equivalent to some kilometers in the OTDR).

The second trace is taken when the air-gap cavity is placed inside the ring, thus ~4% of light is reflected in each facet of the air cavity. This plot shows a behavior similar to the ring without the cavity, with the exception of the peaks corresponding to the 4% reflection at each pulse recirculation into the ring.

It must be highlighted that the peaks also offer information of the ring length. The OTDR measured distance between two peaks is about 50 m when ~100 m is the real length; this is due to the OTDR principle of operation. The OTDR calculates each point power position with the basic expression $D = (c\,t)/2n$. Taking into account that the distance to each event (D) depends directly with the light velocity (c), the pulse flight time (t), and the refractive index of the fiber (n). Thus, one event generated in a point of the fiber reaches the OTDR after the light arrives at this event and goes back to the OTDR. In this situation, when the pulse arrives to the ring, each peak is created every ~50 μs which is the time that it takes for the optical pulse to complete a recirculation. To calculate the distance that corresponds to the time interval between consecutive peaks, this data is replaced in the previous equation and the solution, as it is measured with the OTDR, is ~50 m.

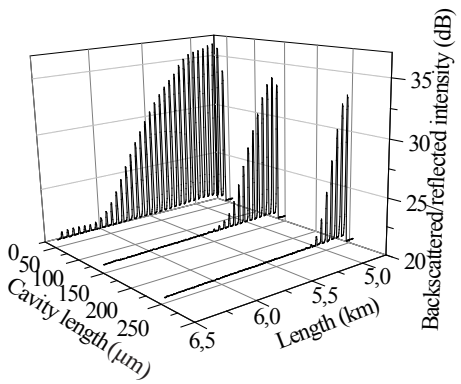

Figure 3.6. OTDR trace evolution as displacement increases.

Therefore, when the air-gap length changes, an increment of the losses in the ring is discernible. In fact, figure 3.6 depicts the peaks evolution while the cavity length changes. As is explained above, the higher the loss into the cavity, the lesser the time the pulse is spinning inside the ring. Hence, this information can be used for micro-displacement measurement purposes.

3.1.3. Magnetic field fiber optic sensor interrogated by an OTDR

Finally, a magnetic field sensor is proposed. Unlike previous schemes, this sensor is only based on the Fresnel reflection variation due to the refracting index changes generated by a nano-particles ferrofluid. It is a commercial hydrocarbon based ferrofluid EMG905 fabricated by Ferrotec. It has a saturation magnetization of 440 Gauss, 7.1% volume concentration of magnetite and 9 mPas viscosity. The diameter of the Fe_3O_4 dispersed particles is around 10 nm, while its carrier liquid is a synthetic isoparaffinic solvent.

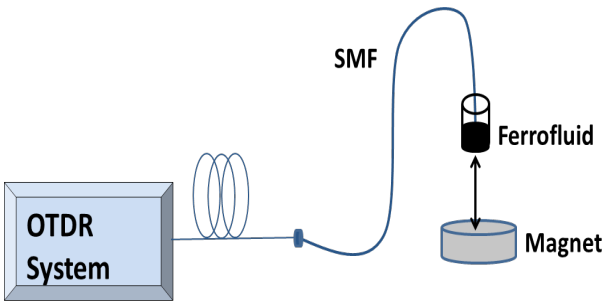

Figure 3.7. Schematic of the setup used for the magnetic field sensing.

The EMG905 ferrofluid is opaque, its absorption loss at 1550 nm is 6.84 μm^{-1} and the measured refracting index is 1.58 ± 0.01. The high refractive index of the ferrofluid can lead to high enough reflectivity if applied onto the end face of a cleaved SMF, allowing high signal-to-noise-ratio measurements when interrogated using OTDR sensor interrogation techniques.

A rectangular magnet (15 x 40 x 5 mm) with a magnetic strength of ~2 kGauss was fixed to a linear stage mounted on a stepper motor guided by ad-hoc software that allowed movement in the direction of the fiber axis. An amount of 0.5 ml of ferrofluid was placed in a plastic cuvette in order to avoid magnetic interferences during the measurements.

The magnet was initially positioned 4.5 cm far from the ferrofluid in which was placed the SMF end face, as shown in figure 3.7.

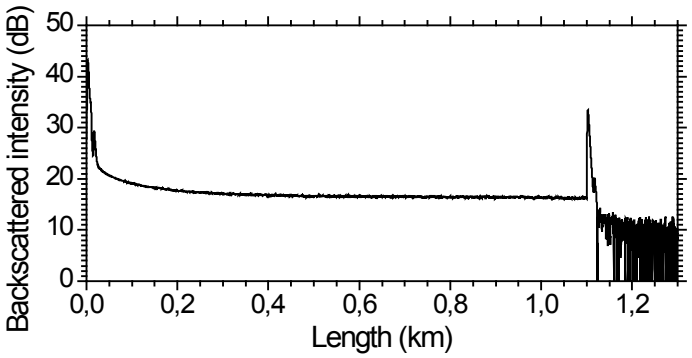

Figure 3.8. OTDR trace for the reflection peak when the cleaved fiber end is inserted into the ferrofluid cuvette.

Measurements were carried out in automatic mode, by moving the magnet with a step of 0.425 mm while a PC connected to the OTDR system was remotely recording the back-scattered and reflected intensity of the fiber. Before realizing the experimental measurements with ferrofluid, the probe of a Gauss-meter, having a resolution of 1 Gauss and appropriately calibrated, has been placed in the same position of the fiber tip, perpendicular to the magnetic field vector, to provide the reference value for the magnetic field for each position of the magnet. Figure 3.8 illustrates the OTDR trace with the reflected peak from the cleaved fiber placed approximately 1100 m away from the OTDR and figure 3.9 depicts the result when the previous process is performed.

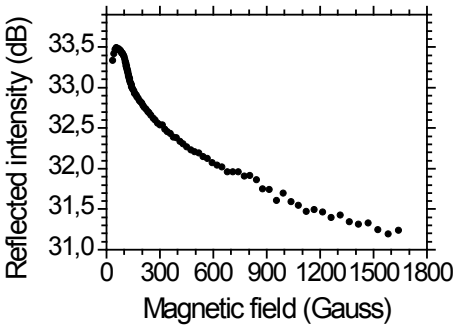

Figure 3.9. Reflected peak evolution when the magnetic characterization was performed.

In fact, the decrease of the backscattered intensity reported in figure 3.9 corresponds to the modulation of the refractive index and the attenuation of the ferrofluid with the magnetic field. Such a magneto viscous effect of the ferrofluid under magnetic stimulus changes the coupling conditions between the fiber and the magnetic liquid in which it is immersed, incrementing the amount of light leakage from the fiber core, thus reducing the amount of backscattered intensity reflected to the OTDR, as reported in figure 3.9.

3.2. REMOTE INTERROGATION OF FIBER OPTIC SENSORS USING AN OTDR

The fiber optic sensor systems, unlike electric sensors systems, provide the possibility to develop remote sensing without the requirement of local biasing for the remote components. This feature results quite interesting for applications where it is not possible or it is very expensive to place active equipment, such as, oil pipe monitoring, landslide detection, tsunami predicting systems etc. [6].

Due to the capability of the OTDR for monitoring ultra-long fiber networks, it is a suitable device for remote sensor interrogation [7]. It allows to measure fiber networks up to 260 km. In this section, two of the previous sensing heads were interrogated remotely, furthermore, a FLM/LPG sensor placed 253 km away has been interrogated. To the author´s knowledge, this is the longest distance achieved for fiber optic sensing without any amplification up to date.

3.2.1. Ultra long displacement sensor based on FLM/LPG and OTDR

The high reflectivity of the FLM/LPG sensor previously described is used as a pulse reflector and this pulse can be easily observed at 253 km away without any amplification or complex setup, only with the OTDR.

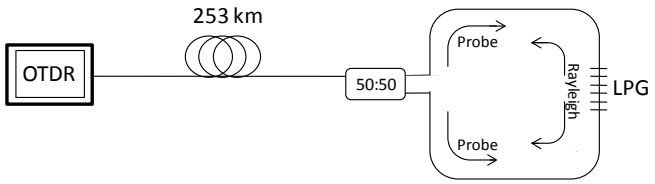

Figure 3.10. Ultra long FLM/LPG sensor system setup.

To achieve this sensing distance, an experimental setup as depicted in figure 3.10 was developed, formed by the FLM/LPG sensor, the SMF transmission channel (up to 253

km) and the OTDR. In this setup, the high reflectivity of the fiber loop mirror combined with the LPG allows the easy detection of displacement. The displacement sensitivity of the sensor is achieved by shifting the LPG profile at the OTDR operation wavelength. Thus, the FLM/LPG sensor reflected light is modulated.

To reach ultra-long distances, it is necessary to configure the OTDR parameters to interrogate ultra long networks. It allows to measure up to 260 km by using a 20 μs pulse time and configuring an acquisition time of 31 seconds. The device acquires more than 1 trace per second, which are averaged during the acquisition time to reduce the measured noise level.

The experimental procedure to characterize the FLM/LPG sensor was to fix both LPG extremes on two points, as it is shown in figure 3.1, in a translation stage. The displacement of this translation stage was controlled by a computer to achieve more accurate results. The displacement steps programmed for each measurement had a value of 50 μm.

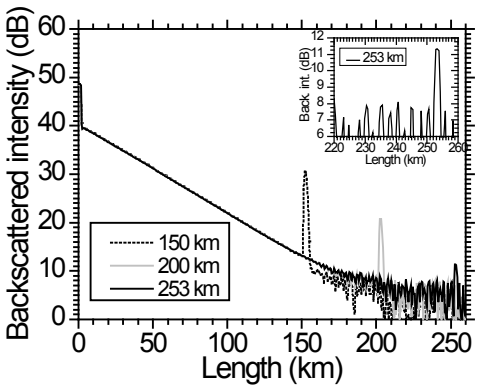

Figure 3.11. OTDR acquired traces for a maximum reflectivity of the sensor for 150, 200 and 253 km

Figure 3.11 shows the traces obtained by measuring the FLM/LPG displacement sensing head at a distance of 150, 200 and 253 km, respectively. The signal to noise ratio, which is achieved by illuminating the FLM allows reaching these ultra long distances without any amplification. In the 253 km trace, showed in the upright corner inset of figure 3.11, a zoom of the FLM/LPG sensor reflection peak between the trace noise pulses is observed. The low SNR achieved is enough to carry out correct displacement measurements, as illustrated in figure 3.12.

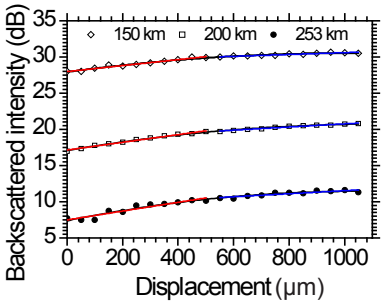

Figure 3.12. 150, 200 and 253 km sensor displacement behavior.

Figure 3.12 depicts the displacement sensor characterization; obtained for different fiber distances. Each measurement has different backscattered intensity levels, corresponding to the attenuations of the different fiber lengths. This attenuation increases ~9 dB for each 50 km of fiber (Figure 3.12). The achieved dynamic range is ~3 dB. The measured sensor behavior is similar for the different fiber lengths and corresponds to the FLM/LPG response reported in section 3.1.1. Two linear regions can be found, as noticed in the non remote results. For the range between [0, 500 μm] the sensitivity is ~5 dBm/μm and for [500, 1050 μm] is ~2 dBm/μm. The resolution of the sensing head using this configuration is 0.5 μm.

3.2.2. Remote magnetic fiel sensor using an OTDR and nano-particles' ferrofluid.

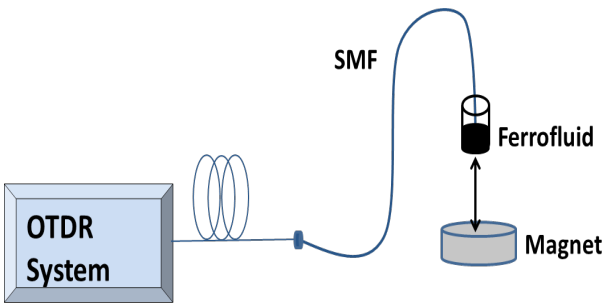

Figure 3.13. Remote magnetic field sensor setup.

Now, the setup characterized in section 3.1.3 is extended tens of kilometers, in order to be considered a remote sensing application. Thus, the ferrofluid based magnetic sensor

aforementioned, is remotely monitored up to 150 km. The utilized cleaved fiber tip is less reflective than a fiber loop mirror; therefore, the reached distance is lower than in the previous section.

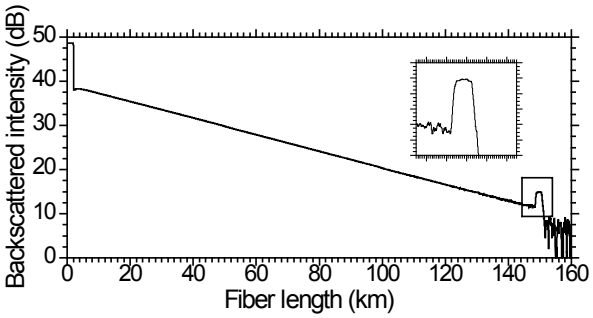

Figure 3.14. OTDR trace of the 150 remote magnetic field sensor.

The trace measured at 0 Gauss is reported in Figure 3.14, showing the backscattered intensity along the sensing fiber system. The measurements in remote configuration at 150 km were carried out using a pulse width of 2.5 μs following the same experimental process explained in 3.1.3. Focusing on the sensing area represented by the final highlighted area in figure 3.14, a clear decrease of the backscattered intensity with the applied magnetic field is observed as reported in figure 3.15

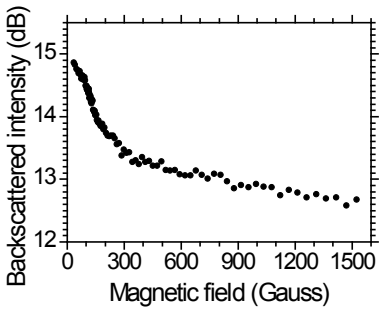

Figure 3.15. Backscattered intensity for the remote configuration vs. magnetic field strength.

The sensor, as demonstrated in the non remote 1 km characterization, presents a modulation range of around 2.2 dB. The magnetic response is distinguishable up to 1468 Gauss, which is 57 Gauss smaller than the field measured using the system at 1 Km

(figure 3.9). The launched signal travels 300 km before coming back to the detector. Now the received power is much lower in comparison with the configuration of 1 km. With the increment of the magnetic field, the reflected power decreases, reaching the level of the background signal.

3.3. FIBER OPTIC INTENSITY SENSORS MULTIPLEXING BUS STRUCTURE BASED ON COUPLERS AND INTERROGATED BY AN OTDR

OTDR systems, besides of its main aim, have been used before as interrogation systems for point, quasi-distributed and distributed sensor networks [8-10]. Figure 3.16 shows the basic structure used in the three multiplexing networks studied in this section. A bus configuration has been selected in order to avoid the crosstalk between sensors. The sensors (S^n) have been added to the main optical path by optical couplers (OC) separated by different fiber spools (L_n).

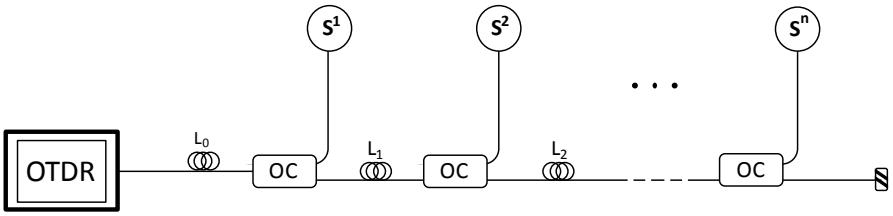

Figure 3.16. Basic scheme for intensity sensors multiplexing interrogated by OTDR.

The coupling ratio has to be studied in order to calculate the maximum number of sensors the network can bear. Thus, theoretically, the maximum number of sensors, in a network as described, is calculated as:

$$n = \frac{OTDR_{SNR}}{CR + Ln} \qquad (3.1)$$

If we consider that all fiber spools are the same, as well as the coupling ratios of the couplers, the number of sensors (n) we can measure are directly proportional to the OTDR dynamic range ($OTDR_{SNR}$), and inversely proportional to the loss introduced by the couplers in the main path (CR) plus the fiber spool loss (Ln).

The following three structures, which use the sensors presented in 3.1, demonstrate this multiplexing ability by measuring two sensors with different coupling configu-

rations. In this way the sensors sensitivity, stability and the system crosstalk will be characterized.

3.3.1. FLM/LPG sensors multiplexing

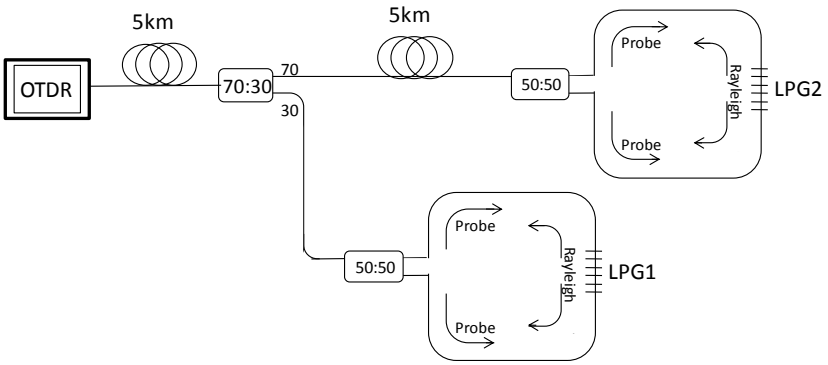

Figure 3.17. Multiplexing sensor system setup.

Two LPG/FLM-based displacement sensors previously presented in section 3.1.1 are multiplexed using the configuration shown in figure 3.17. This configuration is based on the basic multiplexing structure presented in figure 3.16. The experimental setup consists of the commercial OTDR, two 5 km long SMF28 fiber reels and two FLM/LPG sensors. A 70:30 coupler is used to balance the received optical power from each sensing head.

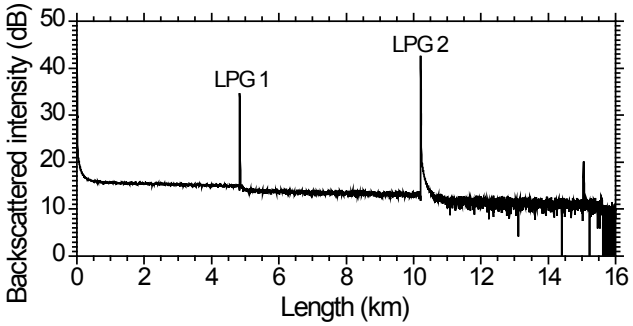

Figure 3.18. FLM/LPG sensors as seem on the OTDR trace.

Figure 3.18 illustrates the trace obtained by measuring the structure shown in figure 3.17. The trace shows the reflection peaks from each LPG inside the fiber loop mirrors and some ghost reflections generated by the structure.

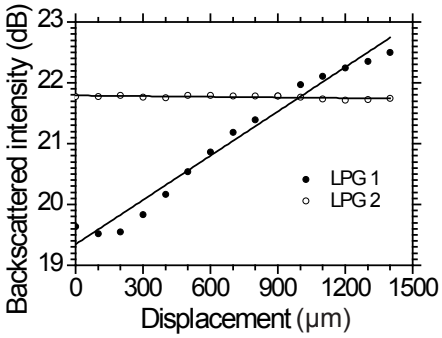

Figure 3.19. Displacement measurement of sensor LPG1 when no displacement is applied to sensor LPG2.

Figure 3.19 presents simultaneously the sensor system behavior against the applied displacement to LPG1 and the non stressed LPG2, in order to check the structure crosstalk. The experiment consisted on fixing the LPG on two points and afterwards, displace these points 100 μm steps. The sensors present a good linear behavior along 1 mm displacement range.

3.3.2. Multiplexing of fiber optic micro-displacement sensors based on fiber rings and air-cavities

The following multiplexing system shown in this section is also based on the basic structure presented in figure 3.16 and the micro displacement sensing heads explained in 3.1.2. Figure 3.20 illustrates the developed experimental setup.

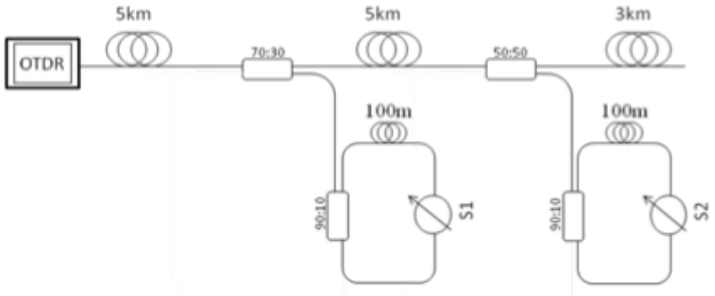

Figure 3.20. Experimental setup for Fiber ring air-gap sensors multiplexing.

Figure 3.21 presents a measured trace for both sensors. The plot depicts sensors' peaks responses, starting the second sensor´s response about 3 dB lower from the Rayleigh threshold due to the 50:50 coupler used for multiplexing it.

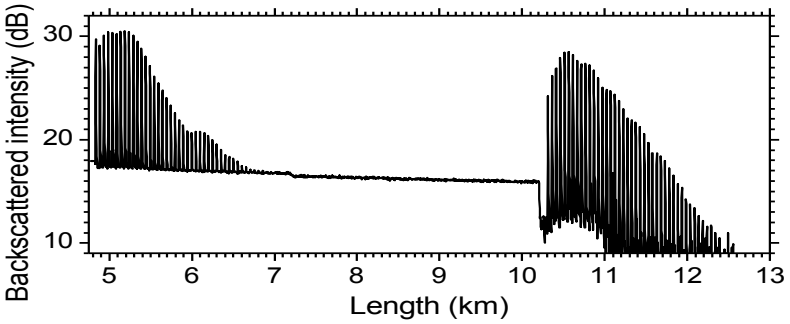

Figure 3.21. OTDR trace of the two sensors when no displacement is applied to both sensors.

The sensors characterization have been performed with two micrometer translation stages in which the two cleaved fibers are placed one in front of the other creating the air-gap cavity. Both translation stages have a precision of 1 μm per step.

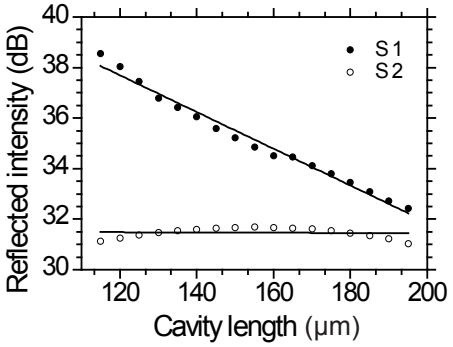

Figure 3.22. Sensor longitudinal displacement behavior in a multiplexed network of two sensors.

The developed system was designed to measure displacements only in a free axis. Thus, we can measure longitudinal axis displacements, or alternatively, free lateral displacements. Figure 3.22 shows the behavior of one sensor when longitudinal displacement is applied and the behavior of the second one when it is not stressed. The displacement measurement from the first cavity length (S1) was obtained by averaging the values

of the fifth, sixth and seventh peaks of the acquired pulse train. These peaks had been selected after a study which analyzed each peak behavior. After comparing the contribution of each peak, this study established which peaks showed the best characteristics to be used, mainly the best SNR. The experiment consisted on increasing the S1 cavity length by 5 μm steps. The results were taken for a 115 μm initial cavity length and showed a quasi linear behavior in the 80 μm measurement range. A sensitivity of 0.07 dB/μm was obtained with a dynamic range of ~6 dB. A variation of the intensity returned from sensor 2 (~ 1 dB) was observed.

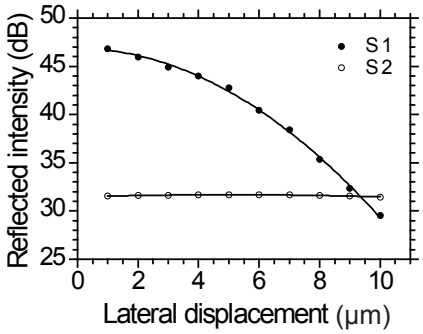

Figure 3.23. Received power from sensor (S1) behavior when a lateral displacement is induced.

A cavity lateral misalignment test was also carried out, obtaining the results presented in figure 3.23. For these last measurement series, a fixed 40 μm long cavity length was used, and steps of 1 μm for lateral displacement were applied (although any longitudinal cavity length could be chosen). A linear behavior for the first 5 μm was obtained, and after that, the received light intensity dropped abruptly as it was expected. For the first 5 μm measurement range, the misalignment sensor showed a sensitivity of 2.67 dB/μm. In this case the variations of sensor 2 output were observed to be negligible.

Intensity based sensors suffer from the problem of system optical power fluctuations not related with those induced by the measurand changes. OTDR offers information of all intensity events along the fiber and it can be used as reference information to compensate spurious changes of intensity. Furthermore, the first peak of each train of pulses, that does not recirculate into the ring, was used as a power reference for the rest of the pulses.

3.3.3. Multiplexing of fiber optic magnetic field sensors

The last sensor scheme interrogated in this chapter is devoted to the multiplexing of two magnetic field sensors. The first sensor was placed at 2 km of distance from the source and the second one at 6.2 km (Figure 3.24). Besides the two peaks related to the sensors S1 and S2, in figure 3.24 (b) we observe two other reflections caused by the second coupler and by the reflection of the fiber which continues along the system. These sensors have been arranged from the main path with two 90:10 low insertion loss optical couplers. In order to demonstrate the crosstalk free operation, the first sensor was not magnetically stimulated while the second sensor was tested as was previously shown.

On the other hand, due to the OTDR characteristics in accounting for the network losses, the Rayleigh information along the fiber can be used as reference for the sensors. Its response revealed a good modulation under magnetic stimulus, in agreement with the previous measurements and thus, demonstrating the feasibility of multiplexing.

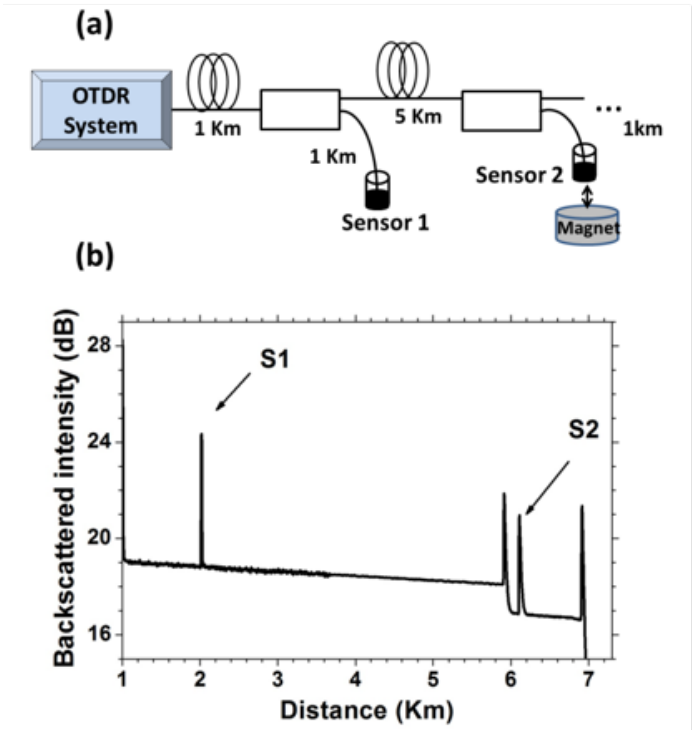

Figure 3.24. a) Schematic of the setup used to multiplex the magnetic sensors. b) Backscattered intensity along the multiplexed sensing system at 0 Gauss.

The detection threshold is 1166 Gauss, which is 25% less than the one achieved at a distance of 1 km. This value corresponds to the detected power which is no longer clearly distinguishable from the background noise. The sensors dynamic range was measured to be 1.8 dB. The minimum fiber length that can be located between two sensors is proportional to the spatial resolution of the interrogation system used. For the proposed configuration which uses a pulse width of 100 ns, a minimum fiber length of 30 m between the coupler and the fiber tip is necessary to clearly distinguish the sensors reflection peaks.

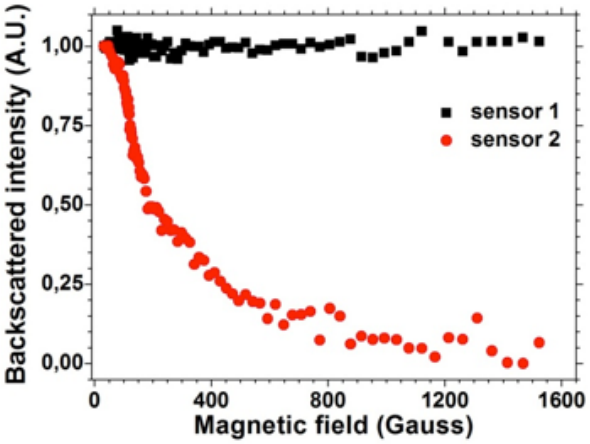

Figure 3.25. Normalized backscattered intensity for both sensors reveals a high sensitivity of the magnetic sensor even in multiplexing mode.

This work demonstrates the capability of multiplexing 2 magnetic sensors; however, if a higher OTDR pulse length were employed, the dynamic range could grow and the system could support more sensors as those calculated with equation 3.1.

3.4. REMOTE FBG-BENDING SENSORS MULTIPLEXING

To finalize this chapter, a remote hybrid sensor multiplexing scheme based on the combination of the interrogation of intensity sensors using the OTDR and the wavelength selective interrogation of FBG sensors in the same network is studied. The system comprises a basic structure in which the OTDR is only used in reflection, and another measurement alternative wherein the OTDR is used also in transmission.

The main objective is to multiplex four sensors based on two different technologies: Two

temperature FBG sensors based on wavelength coding and two bending sensors which are based on intensity modulation. The information of the bending sensors is interrogated by the OTDR at the same time as they are also measured by two fiber ring sensor lasers formed of two FBGs as wavelength selectors.

3.4.1. Basic remote hybrid sensor multiplexing setup

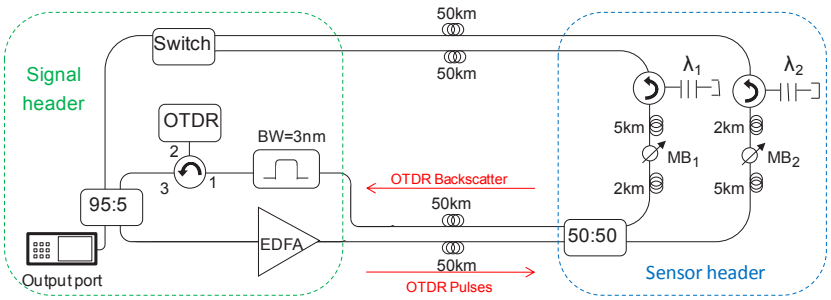

Figure 3.26. Schematic diagram of the remote sensing system for the simultaneous measurement of displacement, using an OTDR, and temperature, deploying FBGs. (MBi: microbender).

The basic scheme of the long-distance remote sensing system developed is illustrated in figure 3.26, which uses standard single-mode fiber (SMF) to connect the signal header and the sensor system. As previous presented remote setups, all the active components are placed at the signal header, whereas all the devices located at the sensor head are passive components.

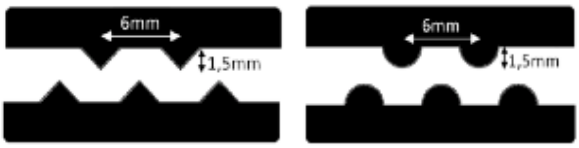

Figure 3.27. Microbender sensors teeth geometry.

The working principle is as follows. Two interrogation techniques are used simultaneously in the system. The OTDR separates the received and the emitted signal by using a circulator. The OTDR signal is amplified by the EDFA before the outward 50 km fiber.

After the 50 km fiber spool, the OTDR signal is divided in two almost identical branches. Each branch is formed by 7 km of fiber and, for the OTDR interrogation purposes, a circulator is used. As the circulator isolates the reflected signal after it, the rest of the network is not visible by the OTDR. The bending sensors, in order to identify them in the OTDR, are placed in different positions. The first microbender is placed after 2 km and the second one after 5 km. The two bending plates, for studying which bender geometry is better, have different teeth shapes: circular and triangular. The bending plates' diagrams are depicted in figure 3.27. Finally, the key device of this system is the 50:50 coupler. It splits the laser and OTDR signals into the two branches of the sensor system and also collects the backscattered light from the two 7 km sections towards the OTDR. It has other important task, it is placed after the 50 km of fiber because is important to prevent the extra Rayleigh backscattering noise produced by the EDFA from reaching the OTDR. Only the Rayleigh produced in the sensor system section is detected by the OTDR. Finally, the Rayleigh signal produced only in the sensor system reaches the OTDR, previously filtered by a 3 nm filter to avoid noise.

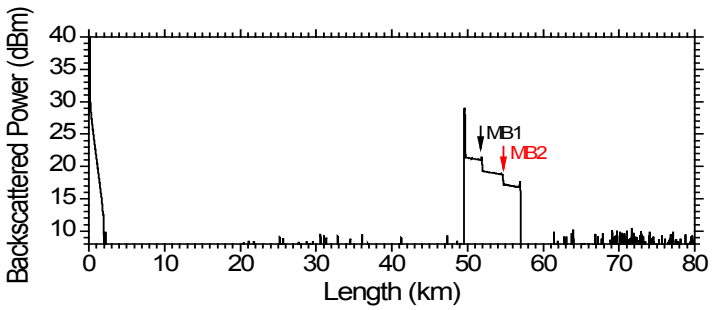

Figure 3.28. Measurement trace as seen in the OTDR.

Figure 3.28 illustrates an OTDR trace acquired in the setup presented in figure 3.26. The OTDR acquisition parameters were configured as following: acquisition range of 80 km, 275 ns pulse width and 15 s of measurement time. The two discontinuities, marked as MB1 and MB2 (inset of figure 3.28), conform to the position where the bending is applied. Here is shown why two different fiber delays were used in the sensor system. The Rayleigh zone following these discontinuities is the data used for the calculation of the displacement of each bending sensor. The processing method consists on calculating the sum in all the recorded points inside the measuring zone. For this reason, the higher number of recorded points stored, the better resolution is obtained. The relative power shown in figure 3.28 has two parts that correspond to each microbender losses.

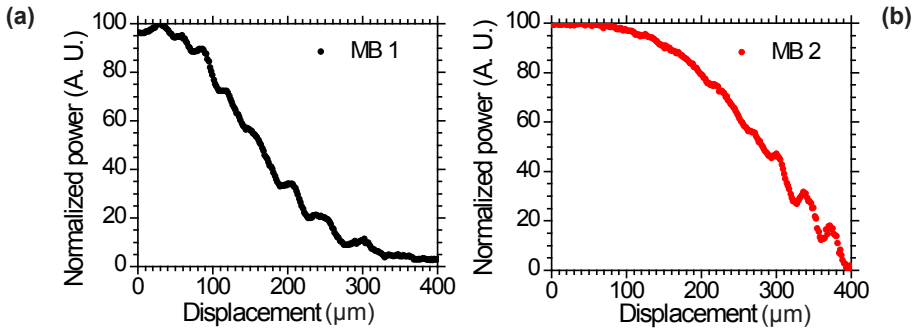

Figure 3.29. Displacement results by processing OTDR traces.

On the other hand, a fiber ring laser structure based on the EDF amplification as gain medium was formed in parallel to the aforementioned OTDR technique to interrogate the FBGs. The two FBGs are interrogated sequentially by controlling which one is selected by a FOSw. Thus, the 50:50 coupler separates the EDFA gain profile in the two sensing branches. The EDFA contributions are filtered by the circulator-FBG sensor combination. Thus, only the line selected by the FOSw recirculates inside the ring. When a switch channel change occurs, the other line start to lase. Once the channel to be interrogated is selected, a 5% of the light is monitored by an OSA by arranging it with a 95:5 coupler. The remaining 95% is recirculated and amplified again, if and when the gain overtakes the network loss. It is important to highlight that by using the switch, the undesired gain competition among emission lines, usually affecting to EDF based multi-wavelength fiber lasers, is overtaken. FBGs are centered at 1532.5 nm and 1531.05 nm in order to be located in the highest zone of the EDFA gain profile and separated wide enough from the OTDR signal.

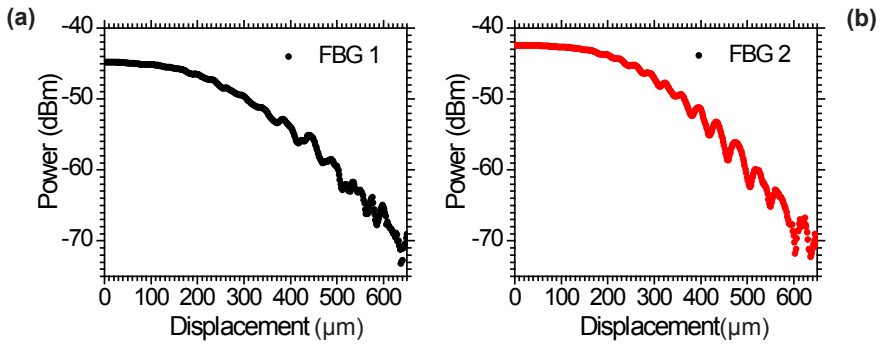

Figure 3.30. Laser channel attenuation vs. tooth blocks displacement.

Figure 3.29 depicts the results using different microbender geometries and interrogated by the OTDR technique. These results were obtained by placing the bending plates on two high precision motorized stages. For each of the 648 samples acquired for each characterization, the tooth blocks were displaced in 1.7 μm steps. At first sight, it is noted that there are some discontinuities due to the cladding-modes coupling. Microbender 1 corresponds to a circular geometry bending plate and microbender 2 to the triangular shape one.

In the same way, the lasing channels created with the FBGs are also intensity modulated and figure 3.30 illustrates the results obtained by tracking the output power of each emission line. The dynamic range obtained is around 25 dB, much higher than when a microbender modulates a source directly in transmission (about 12 dB). This is due to the lasing process. The sensor sensitivity is enhanced because of the lasing medium, and the loss dependence is not linear. Moreover, when the induced loss in the cavity by the bender overcomes the EDFA gain, the lasing condition is not fulfilled.

Analyzing thoroughly both OTDR and FBG displacement results, it is shown that OTDR measurements provide better accuracy because they have a higher resolution, although the FBG lasing system offers a higher sensitivity. Nevertheless, FBG lasing channels show more sensitivity to cladding-modes coupling.

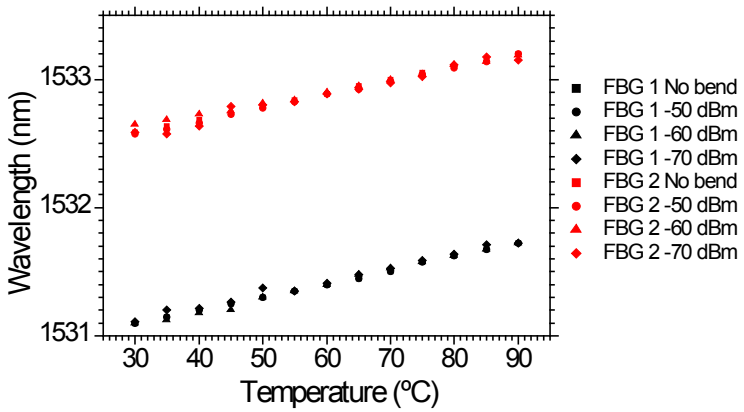

Figure 3.31. FBG temperature characterization for different microbender induced attenuations

When the FBGs are characterized in temperature, they presented the behavior shown in figure 3.31. A 10 pm/ºC FBG wavelength shift can be measured for all the different

attenuations. At -70 dBm some measured points are slightly shifted in comparison to higher power measurements because the FBG peak level is close to the noise threshold.

3.4.2. Improved remote hybrid sensor multiplexing setup

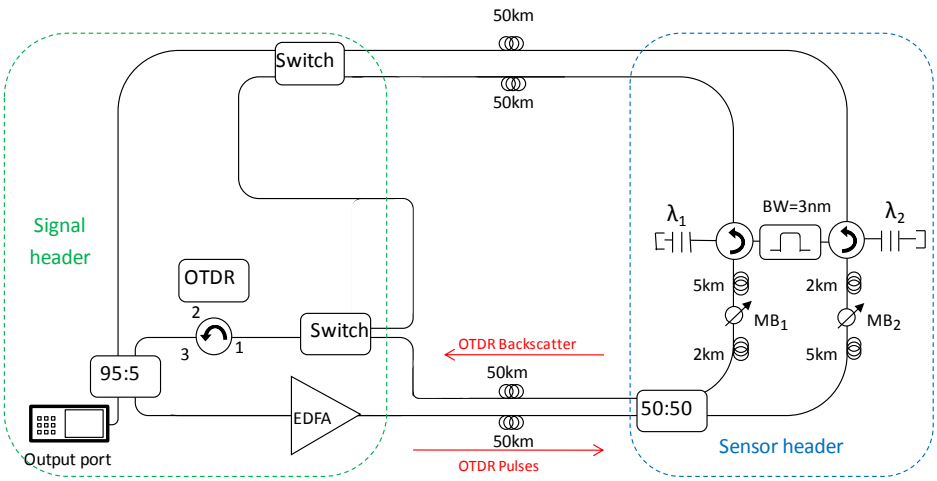

Figure 3.32. Improved remote sensing system.

The improved system, schematically depicted in figure 3.32, allows the OTDR to be used in transmission mode and detect the entire network power. To achieve this feature, the FGBs were connected with a 3 nm filter between them. The filter is centered at the wavelength of the OTDR pulse for enabling the OTDR signal to travel trough the ring. In the event that the λ_1 branch were switched on, the OTDR pulses and λ_2 travel through the other branch, and the 2x2 switch directs them towards a second 1x2 switch. This 1x2 switch is also included in the sensors header in order to select the signal reaching the OTDR detector: either the OTDR backscattering signal or the OTDR transmission pulses. Figure 3.33 shows the OTDR trace acquired with the parameters used for this improved system: 80 km distance, 1 μs pulse width and 15 s acquisition time. The peak shown is the OTDR 1560 nm received signal power.

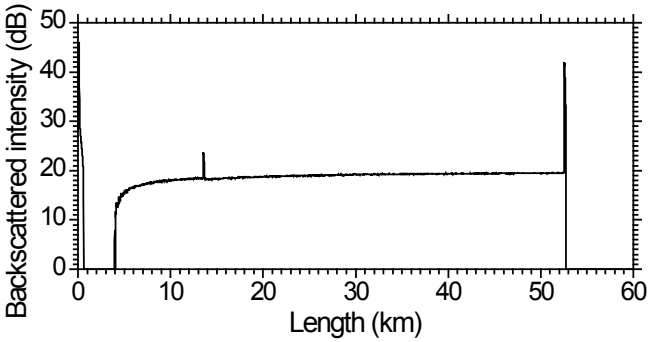

Figure 3.33. Transmission OTDR trace.

Other improvement performed in this setup is devoted to avoid the cladding-modes coupling. A fiber section before the bending plates is rolled up making 4 loops, each one of 35 mm of diameter. Figure 3.34 presents the displacement results. Comparing figures 3.29 and 3.34, we note at a glance that the discontinuities due to cladding-modes coupling have almost disappeared.

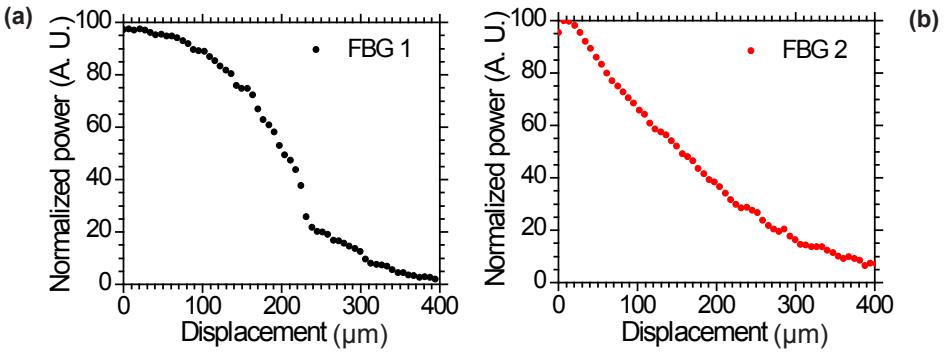

Figure 3.34. Displacement results by processing OTDR traces.

Figure 3.35 shows the relative power of the OTDR signal when the microbenders are displaced in case of the network being configured to perform OTDR measurements in transmission. Graphics in figure 3.35 shows the results when the network is configured to perform transmission measurements. The received amplitude peaks traveling around the network were attenuated by the benders. These results are similar to the FBG lasing channel results shown in figure 3.36.

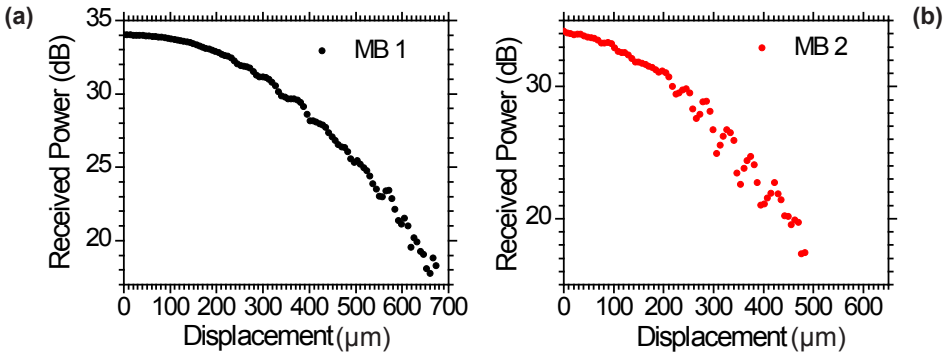

Figure 3.35. OTDR results when the network is configured to perform OTDR measurements in transmission.

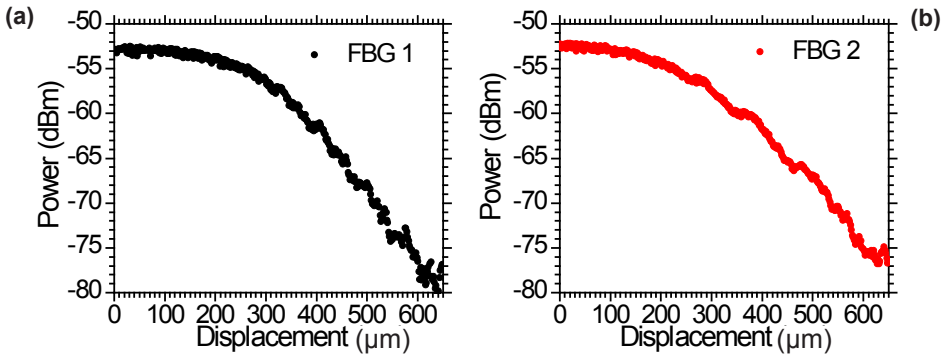

Figure 3.36. Laser channel attenuation vs. tooth blocks displacement.

The FBGs temperature behavior is the same than in the basic sensor system shown in figure 3.31.

3.5. CONCLUSIONS

In this chapter a commercial OTDR has been used for the interrogation of single, remote and multiple fiber optic sensors. Three intensity sensing head structures based on three different reflecting processes have been studied. Those sensors have been multiplexed successfully in a bus multiplexing topology. Furthermore, two of the sensors were interrogated remotely and, in particular, the FLM/LPG sensor was measured at a distance of

253 km, being, for the author´s knowledge, the farthest distance in which one fiber optic sensor has been interrogated without amplification.

These results have been published in [11-13]

Finally, two hybrid multiplexing setups were introduced, which are able to include different sensing techniques and sensors in a single network.

These results have originated the publications of references [14-15]

3.6. REFERENCES

[1] *N. M. P. Pinto, O. Frazao, J. M. Baptista, and J. L. Santos, "Quasi-distributed displacement sensor for structural monitoring using a comercial OTDR", Optics and Lasers in Engineering, 44, 771-778 (2006).*

[2] *F. Luo, J. Liu, N. Ma, and T. F. Morse, "A fiber optic sensor for distributed sensing application in the structural strain monitoring", Sensors and Actuators, 75, 41-44 (1999).*

[3] *X. Guangping, S. L. Keey, and S. Asundi, "Optical time-domain reflectometry for distributed sensing of the structural strain and deformation", Optics and Lasers in Engineering, 32, 437-447 (2000).*

[4] *S. Binu, V. P. M. Pillai, and N. Chandrasekaran, "OTDR based fiber optic microbend sensor for distributed sensing applications in structural pressure monitoring", Journal of Optics, 35, 36-44 (2006).*

[5] *J. W. Berthold, "Historical review of microbend fiber optic sensors", Journal of Lightwave Technology, 13, 1193-1199, (1995).*

[6] *M. Fernandez-Vallejo and M. Lopez-Amo, "Fiber-optic networks for remote sensing," Sensors 12, 3929-3951, (2012).*

[7] *J. Yuan, Ch. Zhao, M. Ye, J. Kang, Z. Zhang, and S. Jun, "A Fresnel Reflection-Based Optical Fiber Sensor System for Remote Refractive Index Measurement Using an OTDR" Photonic Sensors, 4, 48-52, (2014).*

[8] *O. Frazão, R. Falate, J. M. Baptista and J. L. Santos "Optical bend sensor based on a long-period fiber grating monitorid by an optical time-domain reflectometer" Optical Engineering Letters, 44, 110502-1-3, (2005).*

[9] *E. Cibula, and D. Donlagic, "In-line short cavity Fabry-Perot strain sensor for quasi distributed measurement utilizing standard OTDR" Optics Express, 15, 8719-8730, (2007).*

[10] *M. Bravo, J. M. Baptista, J. L. Santos, M. Lopez-Amo, and O. Frazao, "New Interrogation Technique for Multiplexing LPG-Fiber Loop Mirrors Based Displacement Sensors Using an OTDR" procedings Sensors, 2011 IEEE Sensors Conference, 341,342, (2011).*

[11] *M. Bravo, J. M. Baptista, J. L. Santos, M. Lopez-Amo, and O. Fraz ao, "Micro-Displacement Sensor combined with a Fiber Ring Interrogated by an Optical Time-Domain Reflectometer" IEEE Sensors Journal, 14, 793-796, (2014).*

[12] *M. Bravo, J. M. Baptista, J. L. Santos, M. Lopez-Amo, and O. Frazao, "Ultralong 250 km remote sensor system based on a fiber loop mirror interrogated by an optical time-domain reflectometer." Optics Letters, 36, 4059-4061 (2011).*

[13] *A. Candiani, M. Bravo, S. Pissadakis, A. Cucinotta, M. Lopez-Amo, and S. Selleri, "Magnetic Field Sensor Based on Backscattered Intensity Using Ferrofluid", IEEE Photonics Technology Letters, 25, 1481-1483, (2013).*

[14] *M. Bravo, M. Fernandez-Vallejo and M. Lopez-Amo, "Hybrid OTDR-fiber laser system for remote sensor multiplexing," Proc. SPIE, 7653, 765340-1-4, (2010).*

[15] M. Bravo, M. Fernandez-Vallejo and M. Lopez-Amo, "Hybrid OTDR-fiber laser system for remote sensor multiplexing," IEEE Sensors Jounal, 12, 174-178, (2012).

chapter IV
RANDOM DISTRIBUTED FEEDBACK FIBER OPTIC LASERS

INTRODUCTION

Random distributed feedback (RDFB) based on Rayleigh scattering through Raman amplification have been the subject of intense theoretical and experimental studies [1]. Random lasers are characterized by open-cavities or mirror-less-cavities which means that, unlike conventional fiber lasers, their principle of operation rely on distributed scattering events along the fiber cavity. Since the demonstration in 2010 of the RDFB laser based on Rayleigh scattering [2], some research groups are devoted to use its interesting characteristics to propose different lasing structures. For instance, there are applications as tunable random fiber lasers [3, 4], multi-wavelength laser generation [5-11], sensing applications [12-14] and other studies characterizing some parameters of the structure [15-16]. All this papers and others can be found in a complete review performed by S. A. Babin et al. in [17].

Laser sources are one of the basic elements in most part of fiber optic sensor systems. In this PhD. work, some new fiber optic laser sources have being studied and developed for their utilization in fiber optic sensing. In this chapter three new lasing structures based on RDFB are presented. Two of them are devoted to achieve multi-wavelength fiber lasers (MWFL) and the last one explores the modulation possibilities of this structure based on the distributed reflection of light in the random mirror based fiber lasers.

4.1. MULTI-WAVELENGTH FIBER LASERS BASED ON RANDOM DISTRIBUTED MIRRORS

One of the most promising applications of random distributed mirrors is their utilization in multi-wavelength fiber lasers (MWFL). These lasers have recently attracted much interest because of their potential in wavelength-division-multiplexing (WDM) communications, high-resolution spectroscopy, fiber optic sensing, etc [13]. Since 2010 several research groups have proposed some MWFL solutions based on RDFBs in combination with different filtering structures. RDFB fiber lasers based on Raman amplification offer a great potential for MWFL due to their high stability, broadband operation, and low gain competition between emission lines, among others [5-11]. Thus, in this section two new multi-wavelength fiber lasers assisted by distributed mirrors are studied. The first one consists of a dual-random mirror configuration combined with a FLM/SC fiber interferometer, and the second one is a versatile real time switchable MWFL.

4.1.1 Multi-wavelength Raman dual-random mirror fiber laser

Figure 4.1 illustrates the experimental setup studied in this section. It is formed by two DCF based distributed mirrors illuminated by a Raman pump laser which is divided in order to reach both mirrors by a 50:50 low insertion loss coupler. Two 1445/1550 WDMs are used to combine the power from the pump laser and the 1550 nm signal inside the same fiber. These WDMs are connected to a structure based on a FLM interferometer that includes a high birefringence suspended core fiber. This last structure has a comb-shape spectral transfer function and was presented as a sensor in section 2.1.1.

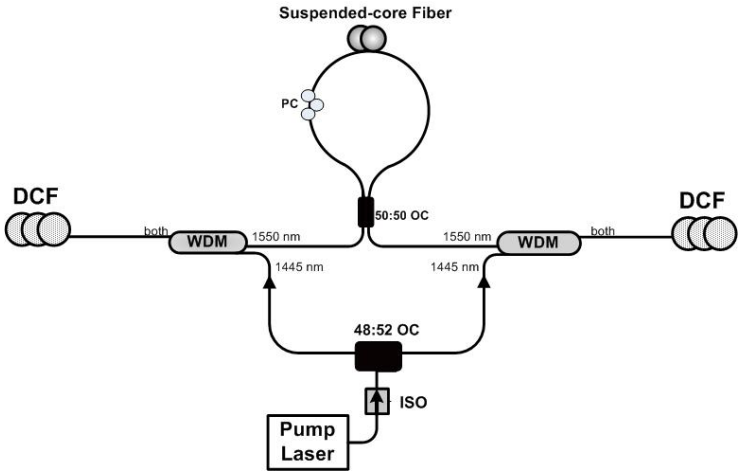

Figure 4.1. Experimental set up for the proposed Raman fiber laser.

The system's principle of operation is as follows. The double-random mirror acts as a broadband fiber laser, whereas the suspended-core FLM loop acts as a shaping element of the output spectrum. The asymmetry induced in the pump power reaching the DCFs leads to slightly different random mirrors. By using the configuration presented in figure 4.1 without the FLM interferometer, a broadband laser emission is obtained. Each of the DCFs acts as a random mirror, which leads to a stable laser in the lasing span defined by the fibers' Raman gain. Figure 4.2 presents the spectral response of the double-random Raman fiber laser for a pump power of 1.4 W.

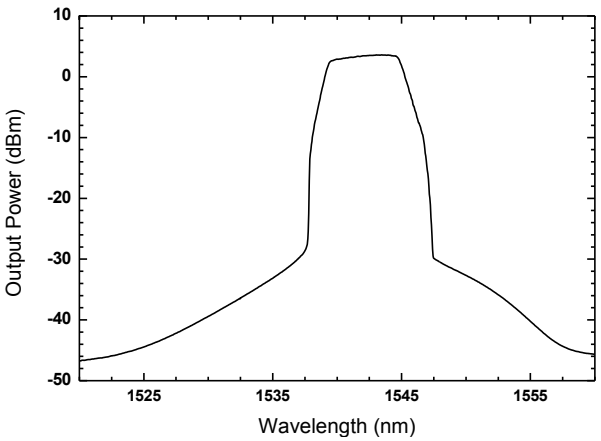

Figure 4.2. Double-random mirror induced laser output signal for a pump power of 1.4W.

A lasing range of ~10 nm was obtained with a broadband shape spectrum and a signal-to-noise ratio (SNR) of ~30 dB. Closely observing the output spectrum in figure 4.2, a little asymmetry in the shape of the spectrum can be noticed. This asymmetry is partially introduced by the 48:52 OC, which ensures 4% more of pump power to one of the DCFs, generating a small difference between the random mirrors forming the fiber laser. The random lasing is achieved simply throughout multiple Rayleigh scattering and Raman amplification induced in both DCF spools. This random fiber laser is based on the same structure as the one presented in reference [2].

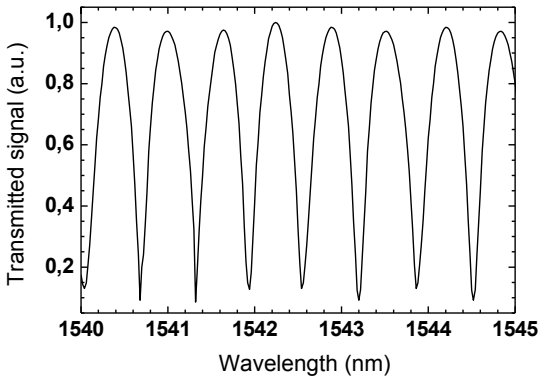

Figure 4.3. Transfer function of the FLM interferometer used within the fiber laser.

Figure 4.3 presents the experimental transmission spectra for the FLM interferometer used as the selective wavelength filter in the fiber laser, presenting 8 maxima in a span of 5 nm with ~0.625 nm spacing between two consecutive maxima. One of the advantages of using this interferometer as the wavelength selecting unit is the ability to easily tailor the output spectrum. By simply changing the length of the suspended-core fiber, one can modify the wavelength spacing between consecutive peaks and consequently the number of lasing channels in a given span. Another great advantage of this filter is its insensitivity to environmental changes. Since the two interfering waves counter propagate in the same fiber and are exposed to the same environment, the FLM interferometer (due to the SC fiber propagation characteristics) is almost insensitive to environmental perturbations.

By combining the double-random mirror induced laser with the FLM wavelength selector, a MWFL is obtained. Figure 4.4 presents the output spectrum of the fiber laser configuration introduced in figure 4.1. The utilized pump power was 1.4 W and the polarization control was adjusted to optimize the output spectrum. This spectrum presents 7 lasing channels in a 5 nm span, with ~0.71 nm spacing between two consecutive peaks and a minimum OSNR of about 25 dB.

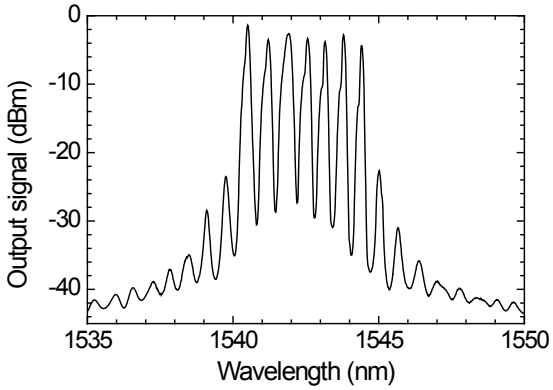

Figure 4.4. Output spectrum of the dual random-mirror fiber laser for a pump power of 1.4 W.

The Raman gain and multiple Rayleigh scattering events are the only new contribution from figure 4.3. The difference in the wavelength spacing due to the multiple Rayleigh scattering events running in both directions in the FLM interferometer, leads to a slightly broadening of the peaks [6].

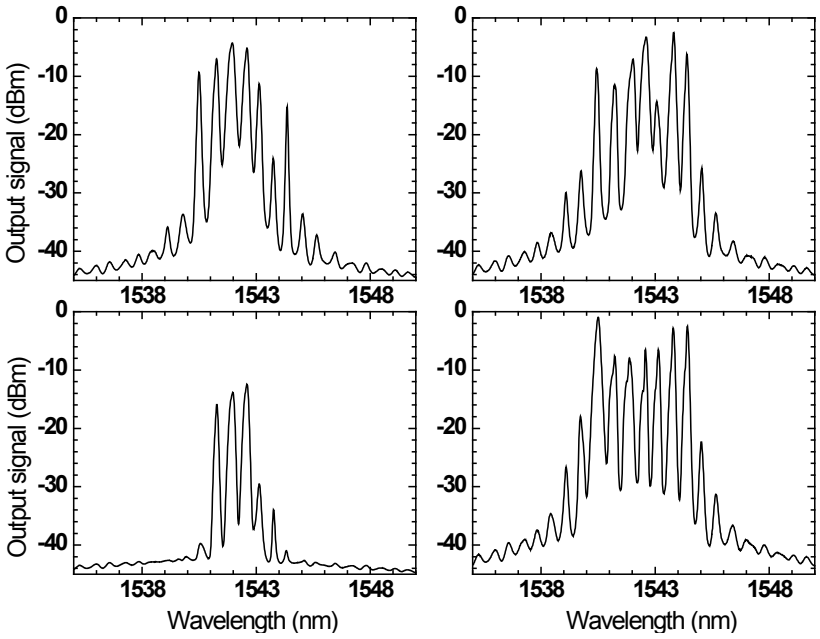

Figure 4.5. Polarization dependence of the output spectrum of the developed fiber laser, for a pump power of 1.4 W.

Since this laser includes a FLM interferometer, the multi-wavelength output spectrum will be highly sensitive to polarization induced alterations. By changing the polarization, distinct output spectra can be found. Figure 4.5 presents some of the output spectra that can be obtained by changing the polarization controller parameters.

The shape, SNR and number of lasing channels of the spectrum can be tailored by the polarization controller. Consequently, the laser output spectrum can be modified in order to obtain the desired spectrum for a given application.

The MWFL presents a characteristic output behavior when pumped-with higher powers, as it can be seen in figure 4.6. With increasing pump power, the output power maximum shifts to longer wavelengths, due to the effect of cascaded Raman scattering. The same was already observed by other authors [7], were the laser's distribution became flatter but less uniform.

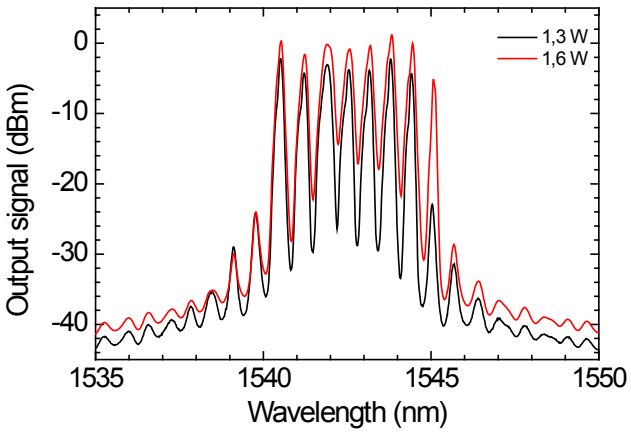

Figure 4.6. Output spectrum of the fiber laser for two different pump powers.

Figure 4.7 shows the measured laser's output power evolution for each pump power. For small pump powers, below the threshold pump power (~1 W), an exponential growth was found. From the threshold level and up to 1,8 W, a linear relationship was observed, corresponding this zone to the stimulated emission regime.

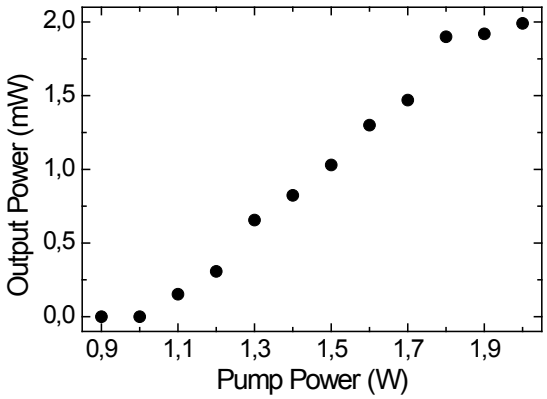

Figure 4.7. Fiber laser's output power vs pump power.

In order to determine the stability of the presented fiber laser, the power fluctuations of the laser were measured during one hour, at time intervals of 2 minutes. Figure 4.8 illustrates the optical power fluctuations of one lasing peak randomly chosen. As it can be observed, in a time window of one hour the fiber laser presents a maximum power variation of ~0.5 dB. This value is much lower than the presented in stability studies of non-random fiber lasers [11].

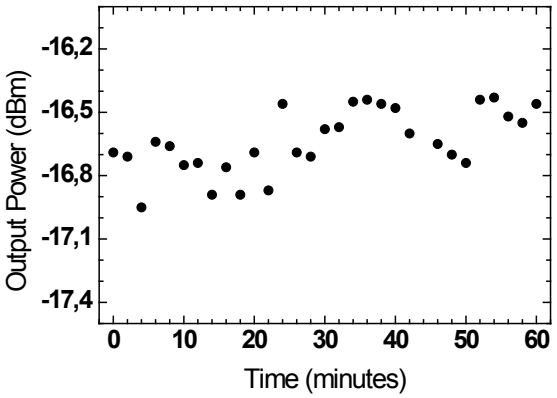

Figure 4.8. Fiber laser's peak power fluctuations.

4.1.2 Real-time switchable MWFL

In this section, a fiber laser which utilizes a random mirror has been dynamically filtered by a novel mirror-filtering structure to achieve a switchable and reconfigurable fiber optic laser. The dynamical filtering is possible by using the Finisar WaveShaper 1000S, which will be also used in chapter 5, and that was initially reported by other authors for dynamic equalization of optical pulses for communication purposes [19]. Here, two different active fibers as Raman amplification media are studied. The fibers used are a ~2.5 km long DCF and a 50 km SMF.

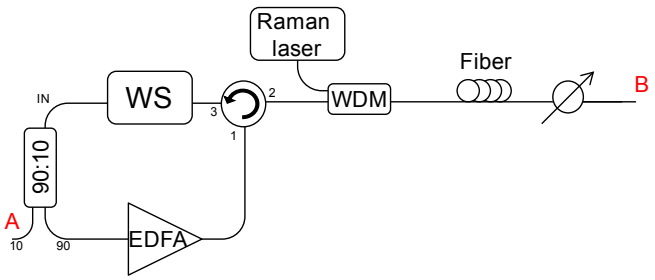

Figure 4.9. Schematic representation of the setup for the switchable and reconfigurable multi-wavelength random fiber laser. WS: WaveShaper programmable filter

Figure 4.9 illustrates the schematic setup of the switchable and reconfigurable laser. The laser is based on a linear cavity formed by two mirrors. The first one (right side), is a RDFB based mirror generated into, in one case, a ~2.5 km DCF reel and in the other, a 50 km reel of SMF. The second mirror (left side) is formed of a loop mirror created by connecting the input/output ports of a circulator as shown in figure 4.9. This mirror has the role of filtering the light into the cavity to select the spectrum profile of the switchable and reconfigurable multi-wavelength random laser. In order to perform this feature, the programmable tunable filter (Finisar WaveShaper 1000S) was used. On the other hand, an Erbium doped fiber amplifier (EDFA) was also used because the combination of the Erbium gain profile and the Raman´s one allows us to have a broad comb laser spectrum (15 nm) and up to 10 dBm output powers.

The operation mode of the system is as follows. The circulator based mirror receives the reflected light from the distributed mirror at port 2. Once the light is inside the mirror (between port 3 and 1), it is filtered by the programmable filter and amplified by

the EDFA. Then, the light is launched through port 2 towards the distributed mirror. This key part of the structure that depends on this reconfigurable mirror enlarges the available bandwidth of the laser because the EDFA gain spectrum is different from the achieved with the Raman amplified section. The programmable filter is able to create a custom filter profile up to 40 nm with a minimum width of 0.08 nm. It has a wavelength resolution of 8 pm in the communications C Band (1527.4-1567.4 nm) providing an attenuation precision of 0.01 dB in a 35 dB attenuation range. For filtering in this structure, a sequence of comb-shape filters is set for achieving a multi-wavelength random mirror assisted laser. The center of each filter is located at the maximum emission wavelength.

Following, the characterizations of two MWFL are presented. The lasing performance, the maximum number of emission lines, the lines' widths and the lines' separation were studied. Although this configuration is able to create any multi-wavelength laser configuration, the ITU grid specifications were taken as a reference for this study. 200, 100 and 50 GHz separation distances were tested in the proposed setup. Thus, a custom program was developed for controlling the programmable filter. This software fully meets the desired requirements by selecting the suitable comb filter configuration. An equalization feature and other facilities for the studies presented were also developed.

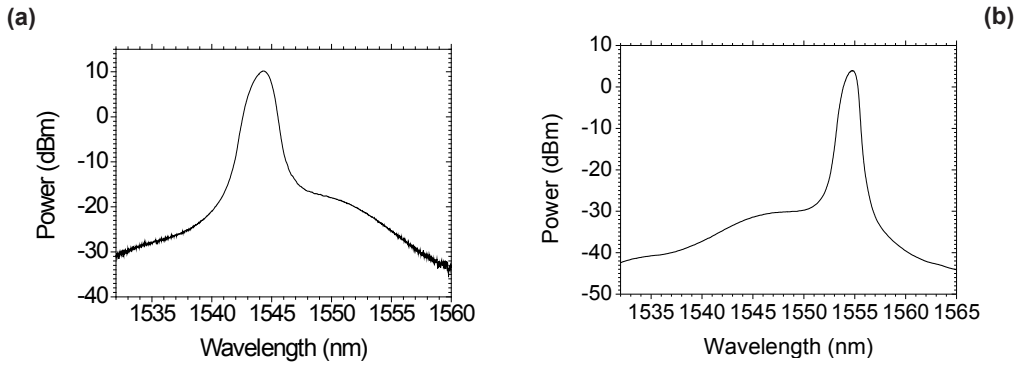

Figure 4.10. Both, DCF (a) and SMF (b) laser spectrum when the WaveShaper filter is off.

First of all, figure 4.10 shows the laser spectrum of two systems under study when the WhaveShaper filter is off. As it was aforementioned, two different lasers were developed using two different fiber spools. The first one is a DFC one with a length of 2,5 km, a -343 ps/(nm*km) first order dispersion coefficient at 1545 and an effective area of 21 μm^2. The other one is a standard single-mode fiber reel of 50 km. The main difference between both lasers is the broader spectrum shape of the SMF scheme although the

maximum power achieved is lower than the in the DCF one. Thus, it is expected to reach a broader comb laser performance with the DCF, but achieving less emitted power.

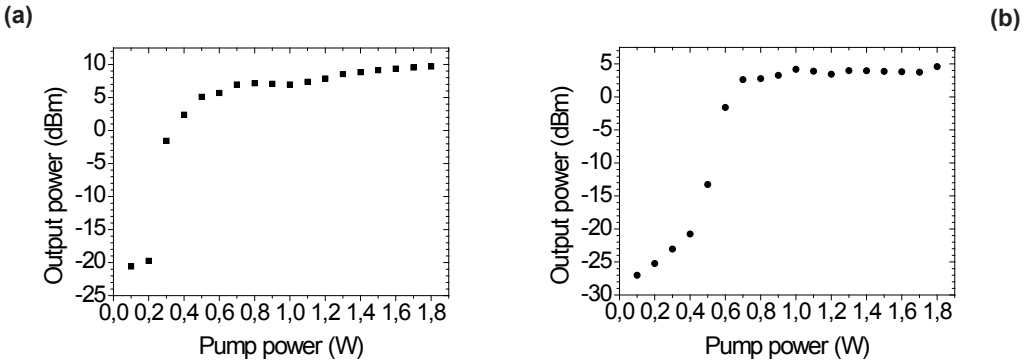

Figure 4.11. Laser power evolution versus pump power obtained for DCF (a) and SMF (b) lasers

The two first system characterizations depicted in figure 4.11 and figure 4.12 consisted of, on the one hand, the lasing power evolution versus the Raman pump power and, on the other hand, the power stability along time. Both figures include the results obtained for the DCF (left column) and the SMF (right column). These results were obtained for the highest peak power of 23 emission lines with a 100 GHz separation and without any equalization, (figure 4.15 (a) and (b)). As figure 4.11 shows, the lasing threshold in the DCF laser occurs when the Raman pump power is 200 mW lower than in the SMF laser. This behavior is caused by the DCF fiber nonlinearities, that is higher than in the SMF, being Raman amplification effect more efficient when DCF fiber is used. Anyway, as it will be explained next, the selected pump power for operation was 1.6 W in both cases.

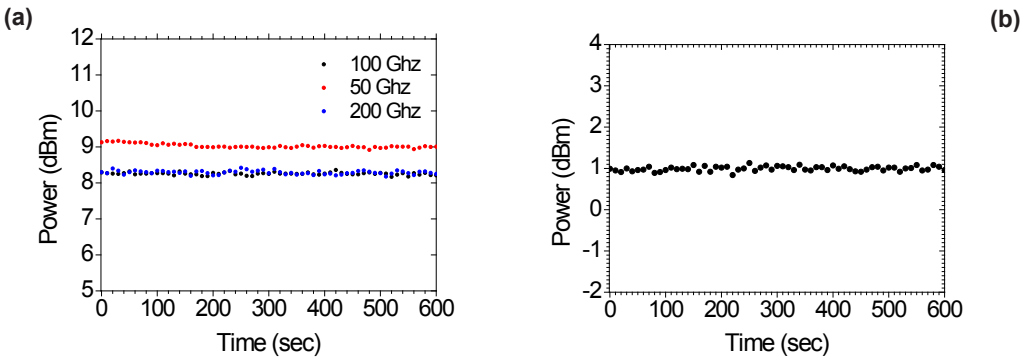

Figure 4.12. Power stability evolution obtained with both fibers (DCF (a) and SMF (b))

Figure 4.12 shows the measured output power instability for both fibers that are lower than 0.2 dB which fits with the typical high stability Raman fiber lasers performance. In figure 4.12 (a) instability for 50, 100 and 200 GHz is also included in order to demonstrate that the system instability fluctuations are similar.

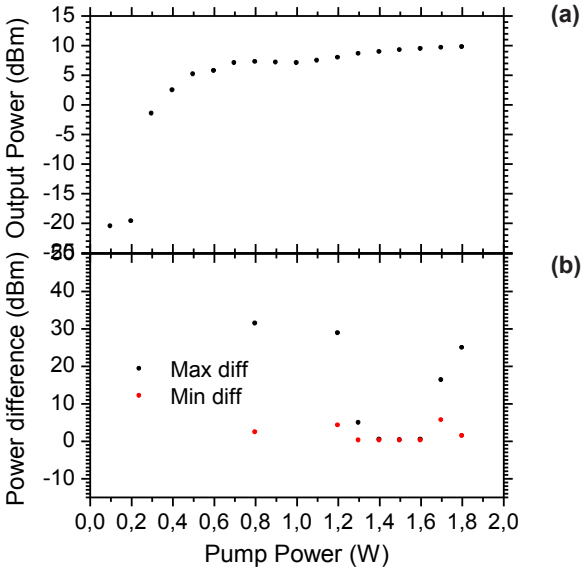

Figure 4.13. Graphical demonstration of the pump power choice. The lasing power evolution vs the pump power(a) is compared with the system stability (b), which depicts the emitted power difference for the best and worst case.

In order to justify the 1.6 W pump power used for the measurements, in figure 4.13 (b) the evolution of the stability of the output power against the Raman pump is depicted (measured for the higher and lower peaks of the achieved spectrum). The minimum power instability is located around 1.5 W. Although the system efficiency in that point is lower than when the Raman pump power is 0.6 W, the stability is higher, as depicted in figure 4.13 (b) in red.

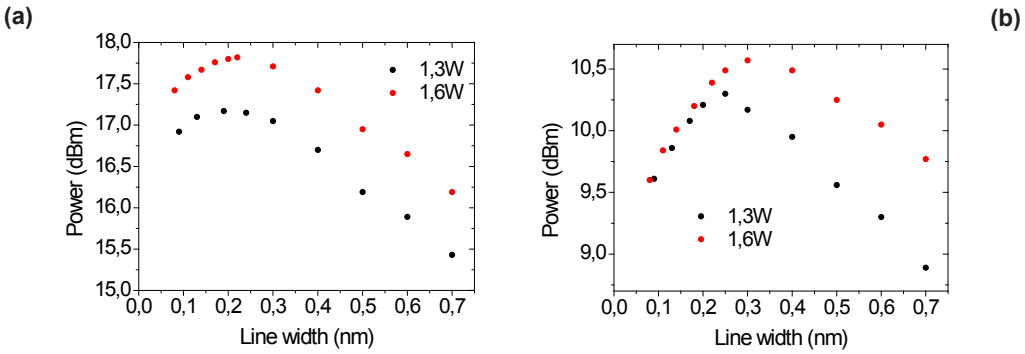

Figure 4.14. One emission line output power evolution when the line width is varied. (a) DCF and (b) SMF.

One important parameter to take into account in the design of a fiber laser with long fiber spools is its line width. As it was studied before in [20], the laser performance is proportional to its line width. This is because the generation of Brillouin scattering and other nonlinear effects, which cause that the narrower the line is, the higher line depletion occurs when it propagates along the fiber. On the other hand, the broader the line is, the less efficient the amplification is. Therefore, using the developed software, the maximum power value of one emission line was tracked while the line width was varied in a controlled way. Figure 4.14 shows the results obtained for the DCF and SMF spools. For a fixed pump power, an optimum line width can be empirically obtained for achieving a maximum emitted peak power. For the DCF an optimal value of ~0.2 nm width was obtained. For the SMF study, the optimal value is broader, about 0.25 nm. Notwithstanding, in a multiwavelenght laser we have to take care of more factors: stability, pump power needed and maximum number of emission lines. Finally, the optimum line widths selected were 0.24 nm for the DCF setup and 0.17 nm for the SMF one. These values offer the best performance to maximize the number of emission lines having good line output power stability.

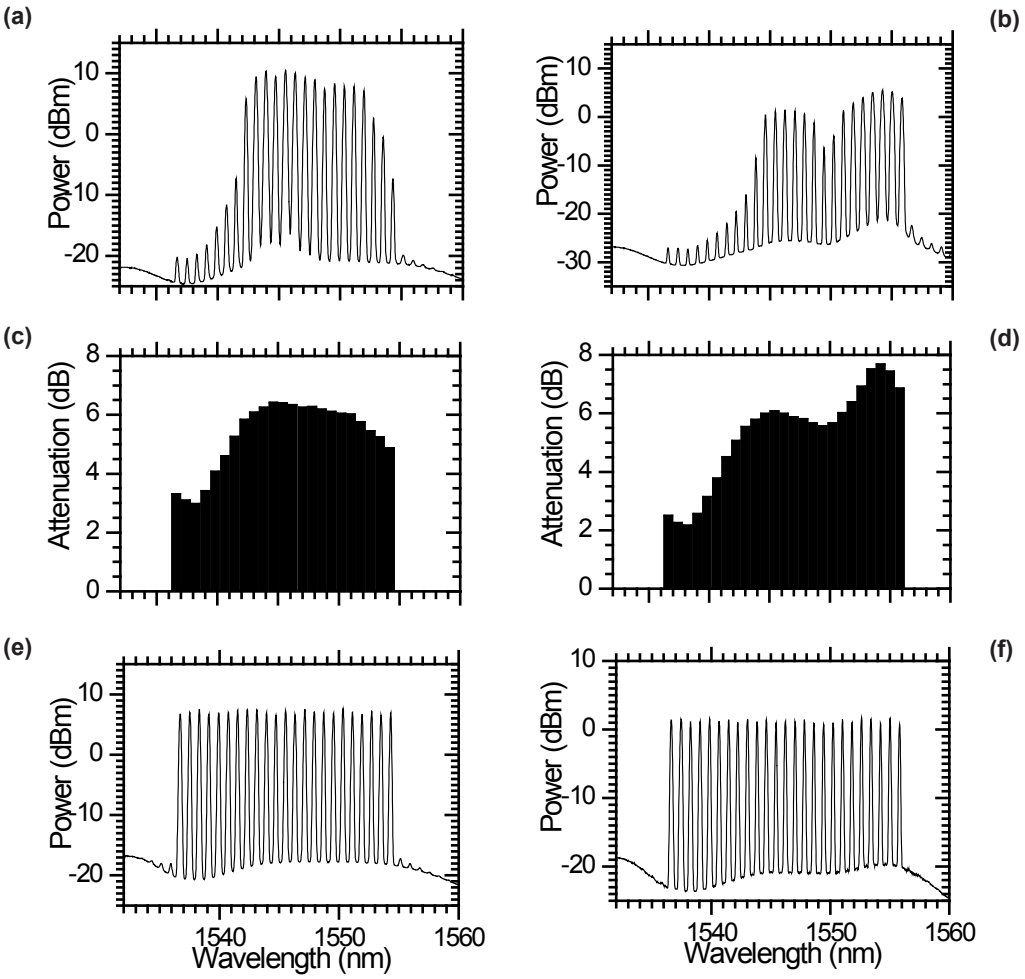

Figure 4.15. Maximum number of emission lines for the DCF (a) and SMF (b) lines separation without equalization. (c) and (d) are the attenuation profile to equalize the spectrum depicted in (a) and (b) with the result illustrated in (e) and (f) for the DCF and the SMF respectively.

The developed MWFL control software includes a feature to equalize the power of the emission lines. The equalization procedure of the emission lines is a key performance of the system because the equalization defines the whole spectral behavior, enhancing the number of emission lines and, of course, the flatter multi-wavelength shape. In this

way, the software equalizes the lines by comparing the power difference between all the lines with the lowest one. Then, a proportional attenuation is applied to each one until the power difference fulfils a value set by the user. This proportional factor is another value to take under consideration. It is important that the software does not induce unjustified loss into the cavity. This factor imposes the equalization accuracy. In figure 4.15 the equalization process is illustrated for the 100 GHz ITU grid specification. The first row depicts the maximum number of emission lines when they are not equalized. In the second row, the attenuation profile previously calculated is shown, giving way to the third row which is the maximum number of emission lines for the two fibers already equalized. When the attenuation profiles (figure 4.15 (a) and (b)) are analyzed, the first bar of the attenuation profile refers to the attenuation of the lowest line depicted in figures (a) and (b); which in both cases are close to 0. When the equalization starts, the amplification efficiency improves the power of this line and fulfills the lasing condition unlike the previous non equalized result. The equalization process continues until the power difference, as was aforementioned, is lower than the threshold set by the user, in this case 0.5 dB. We have to remark that the threshold should not be fixed at a lower value than the system worst instability.

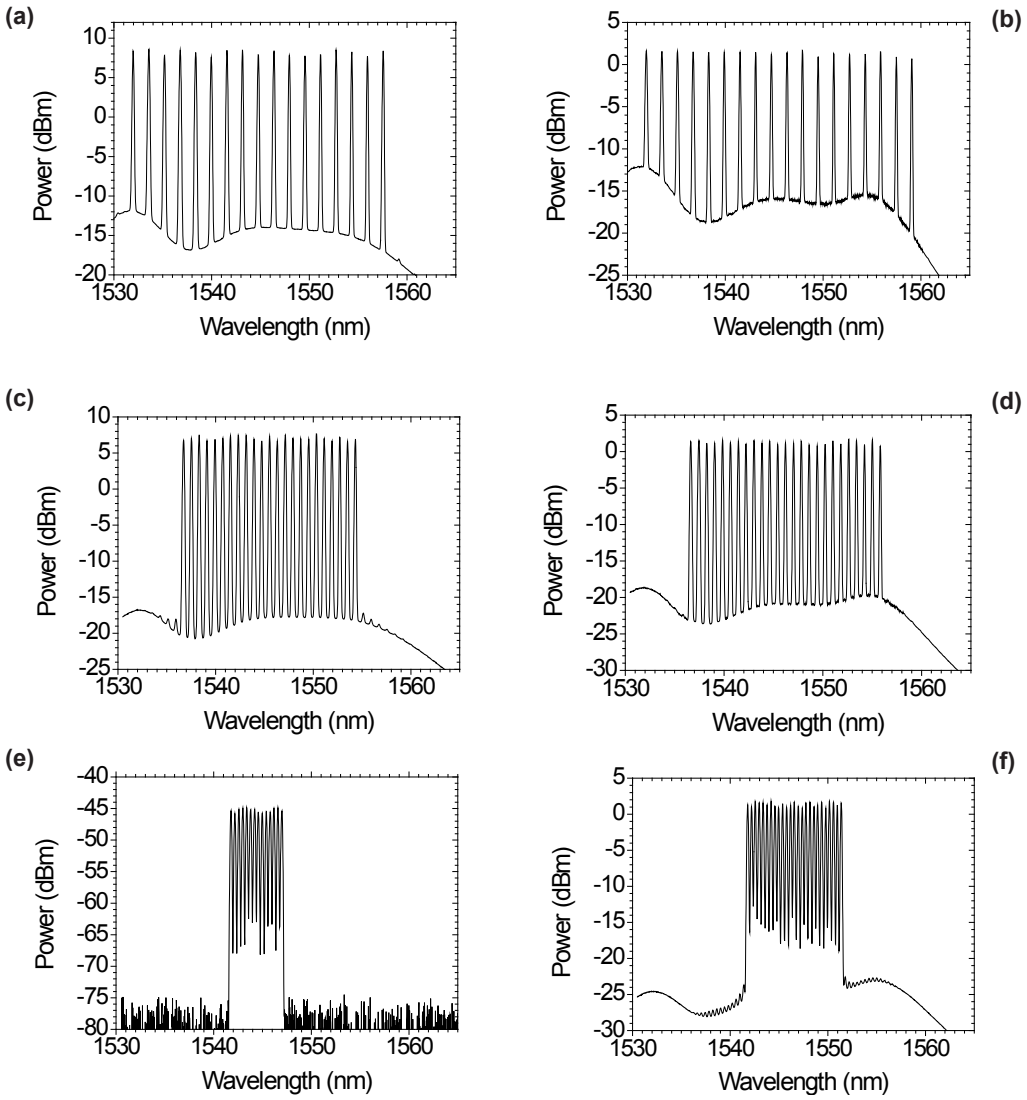

Figure 4.16 Equalized results for the 200, 100 and 50 GHz ITU grid measured for the DCF (a, c and e respectively) and the SMF (b, d and f respectively).

Figure 4.16 depicts the maximum number of emission lines for wavelength spacings of 200 GHz, 100 GHz and 50 GHz respectively; for the two different distributed mirrors. As in the previous figures, left column refers to the DCF based distributed mirror and the right one to the SMF spool. Emission lines spacings are shown by rows. First row refers

to 200 GHz, the second one to 100 GHz and the third one to 50 GHz spacing between emission lines. There is some difference in the number of emission lines achieved using both fibers. The greatest difference appears in the 50 GHz case where there is a difference of 11 peaks between the SMF and the DCF. This can be attributable to different gain spectra and non-linear behavior presented in both fibers. DCF fiber with a smaller effective area concentrates all the amplification and higher non linear effects [21] in 2.5 km of fiber unlike the SMF, which distributes these effects along 50 km of fiber to achieve a similar gain.

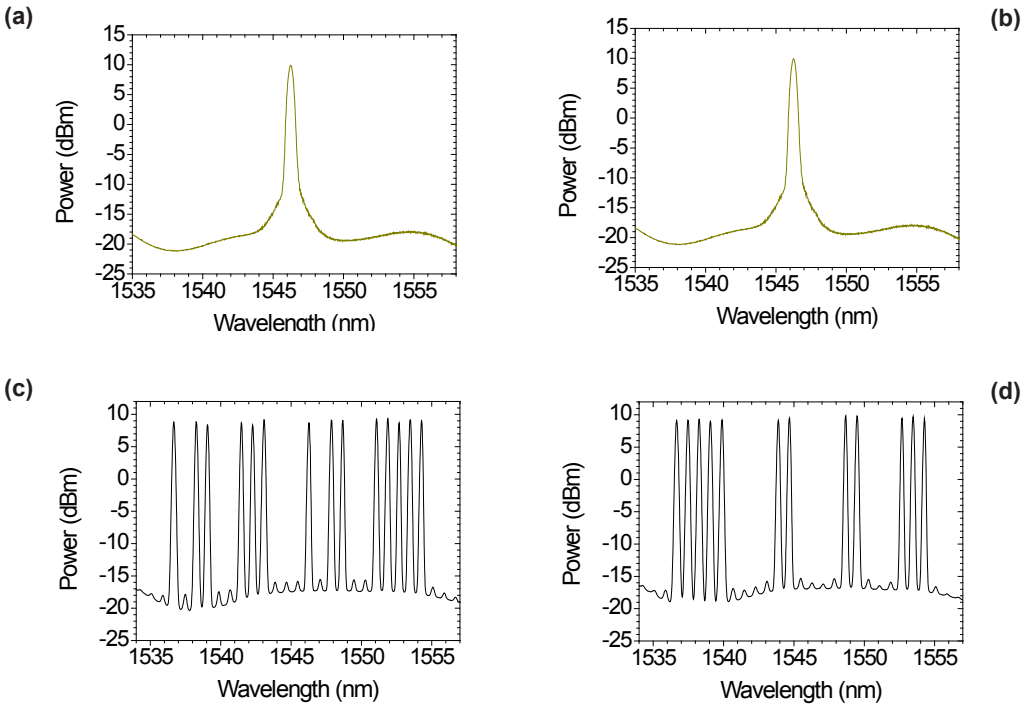

Figure 4.17. Different emission lines configurations measured in B. Single wavelength (a), 5 wavelengths (b), 14 wavelengths (c), 11 wavelengths (d), single wavelength sweep (e) and multi-wavelength sweep (f).

The last characteristic to be studied is the switching ability of the lasers´ spectra. Figure 4.17 shows different configurations of the filter already equalized when the distributed mirror was illuminated with 1.6 W Raman pump power. Figure 4.17 also illustrates the reconfigurability of the proposed system showing different emission patterns of lines already equalized.

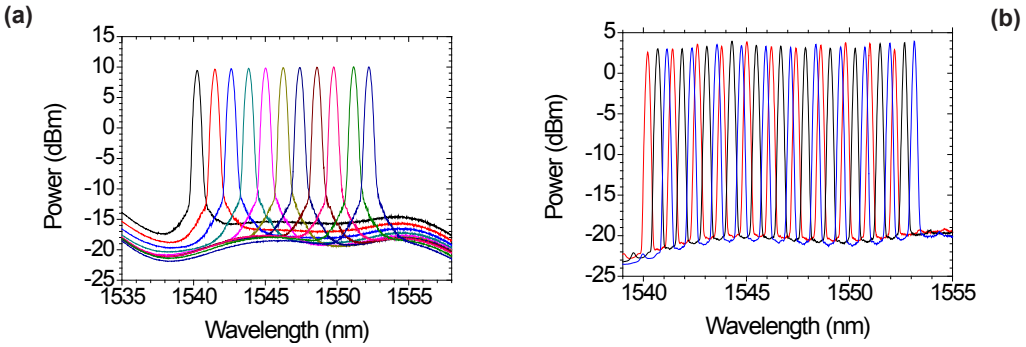

Figure 4.18. MWFL configuration for single wavelength sweep (a) and multi-wavelength sweep (b).

Figure 4.18 presents two different ways to make a wavelength sweep. In order to reduce the sweep steps and the sweeping time, the developed laser system allows us to perform a multi-wavelength sweep, depicted in 4.18 (b). Once fixed the wavelength range to be scanned, the MWFL sweeps the spectrum spending a lower number of sweep steps. Thus, the number of steps is inversely proportional to the number of emission lines chosen. For example, while a single wavelength sweep need twenty cycles to sweep a band, a five lines multi-wavelength laser sweep only needs four.

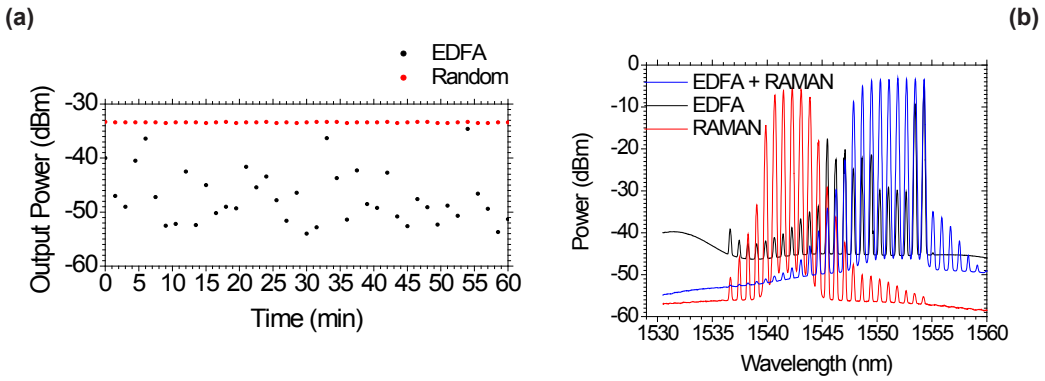

Figure 4.19. (a) Output power variations of the multi-wavelength random laser in comparison with a non-distributed (EDFA based) laser cavity and (b) a comparison of different spectra when different amplification media were used.

Figure 4.19 (a) shows a comparison of the stability for the distributed mirror based cavity and an EDFA based linear cavity. For this study, an emission lines configuration

of 30 lines for a 100 GHz grid was selected. It demonstrates the high stability of the laser when the distributed mirror is used unlike the high instabilities achieved with the non random configuration. Gain competition between emission lines is shown in this last case. Therefore, the use of the Raman based distributed mirror is crucial, making this structure stable. In addition, when the amplification process is complemented with EDFA gain, a broader result is obtained. Figure 4.19 (b) shows the comparison of the laser cavity spectra when different amplification media are used. This figure also demonstrates the importance of the combination of both amplification methods to achieve a more stable and broader result.

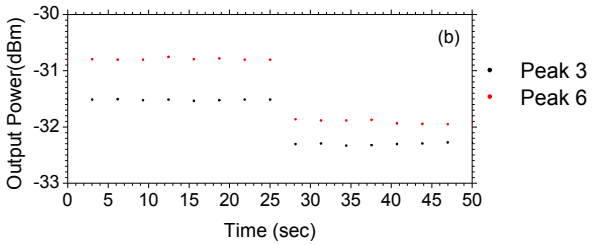

Figure 4.20. Evolution of the power of two emission lines when the filter configuration is switched

Finally, figure 4.20 shows the output power stability evolution when a specific configuration of emission lines is switched. The measurements were obtained when the laser switches from the configuration depicted in figure 4.17 (c) to the configuration depicted in figure 4.17 (d). Traces correspond to the emission lines which are present in both configurations. With this result it is delimited the switching time, being it less than the OSA sweep time, 3 seconds.

4.2. INTERNAL MODULATION OF A RAMAN RANDOM LASER

While conventional lasers have longitudinal modes associated to the cavity length; random lasers, which have infinite distributed cavities along the fiber, excite the whole of the available amplified spectrum, achieving an emission line as wide as the optical gain spectrum permits. This characteristic allows modulating random lasers without the locking frequency problems of the conventional fiber laser configurations as will be presented below.

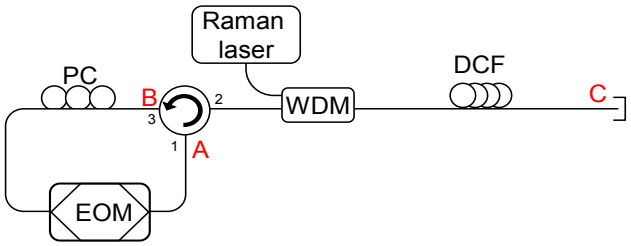

Figure 4.21. Schematic setup for the modulated random laser system. Point C fiber tip is adapted with index matching gel. PC: Polarization controller. EOM: Electro-optical modulator. WDM: Wavelength division multiplexer. DCF: Dispersion compensating fiber.

Here, a random fiber laser cavity which has been modulated through an intensity modulator is presented. In conventional mode-locked lasers the length of the laser resonator is also an essential parameter because it determines the repetition rate when modulated and filters the modulating signal at RF frequencies [22-23]. In our modulated RDFL, the modulation frequency can be adjusted without restrictions. To the best of the author's knowledge, this is the first demonstration of an internally modulated random fiber laser.

Figure 4.21 depicts the schematic setup of the internally modulated random fiber laser using a 1445 nm pump laser. This random laser is based on a linear cavity made up of two different mirrors: the first one (right side), is a distributed mirror created by using the ~2.5 km DCF reel and the second one (left side), is a loop mirror by connecting the inputs/outputs of a circulator as shown in figure 4.21. Basically it is the same lasing scheme shown in the previous section. Now the circulator based mirror is changed as explained next.

The loop mirror structure receives the reflected light from the distributed mirror in port 2. Once light is inside the mirror (between port 3 and 1), this light is modulated by a LiNb03 Mach-Zehnder EOM (Electo-Optical Modulator) with an extinction ratio of ~20 dB. The signal selected to modulate the structure has a pulsed shape which causes the on/off states in the emitted light. Once the light is modulated, it is launched through port 2 towards the distributed mirror. It is important to highlight the role of the loop mirror structure because the reflected signal is always modulated. It could be called "modulating mirror structure"; specifically the mirror modulates the backscattered contribution generated by the distributed mirror. Due to the particular features of the random cavity, its feed-back action does not correspond to a fixed length; and the cavity adapts without distortion to each selected frequency of modulation. It means that the laser cavity does not filter periodically in frequency the amplified signal, as happen when a ring cavity

is employed for fiber lasers [24]. Thus, the contribution of each point of the DCF fiber, which arrives to the modulator in phase, will be re-coupled into the mirror. When the gain compensates the loss, creates a positive feedback achieving the laser condition. The entire backscattered signal created in the cavity is accumulated at point B.

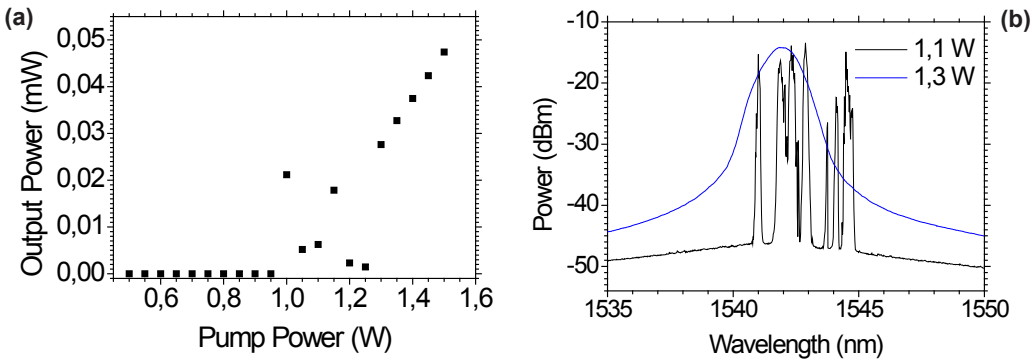

Figure 4.22. (a) Output power evolution vs. pump power variation. (b) Output spectrum measurements for two different pump powers.

The output power evolution versus the Raman pump power was measured in order to demonstrate the lasing behavior of the structure (Figure 4.22 (a)). In this figure, two different zones are noticed. The first one corresponds to an unstable behavior (from 1 to 1.3 W) before the stable lasing behavior is achieved. In Figure 4.22 (b) the output spectra corresponding to both zones are depicted with a resolution of 0.1 nm. The black trace refers to the aforementioned unstable state where different hopping lasing lines are noticeable; and the blue one belongs to the broadband stable operation regime of the proposed modulated random laser. The measurements corresponding to Figures 4.22 (a) and (b) have been taken at point A. The spectrum has been also checked in points B and C obtaining similar results in order to confirm the laser operation along the whole cavity. The output spectra of points A and B were measured using a 90:10 low insertion loss coupler and the measurement at C was taken directly from the fiber tip. It is important to remark that modulating internally the laser, the cavity loss is initially kept at a high level until the pumped gain medium has stored a certain amount of energy. The cavity loss is then quickly reduced to a small value, which allows the intense stimulated laser radiation to establish quickly in the cavity [13].

Thus the modulated signal obtained in A is different from the obtained by modulating directly the output signal of a CW random mirror laser. In addition, the measured extinction ratio of the modulated random laser is 4 dB higher than the extinction ratio of the EOM.

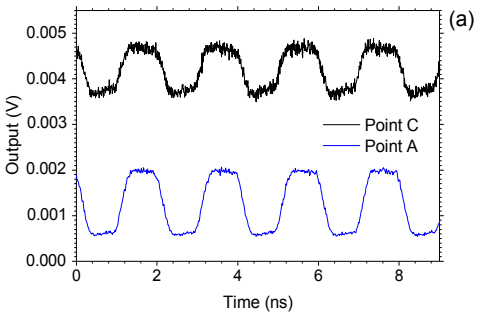

Figure 4.23. Time domain laser behavior in A and C when 500 MHz square signal modulates the system.

Figure 4.23 displays a pulsed output signal of the random laser, measured simultaneously at points A and C when a 500 MHz square signal is applied to the EOM. Although the signal in both points is rather similar, signal in point C offers a much lower contrast than signal in point A. The signal in point C is noisier because it travels through the DCF along with the Raman pump; the signal is not only amplified by the Raman Effect but also it is affected by additional undesired effects such as the double backscattering which modifies the signal in point C. Furthermore, point A offers a low-noise signal due to the fact that the electro-optical modulator removes much of the extra noise. So this figure demonstrates how the system is able to modulate the laser in a pulsed regime. Because of the frequency limitations of our modulating devices for square signals, no measurements over 1 GHz were carried out. In fact, in figure 4.23, frequency filtering effects of our signal generator make the signal shape smoother. A higher frequency operation, nevertheless, is expected with the suitable equipment.

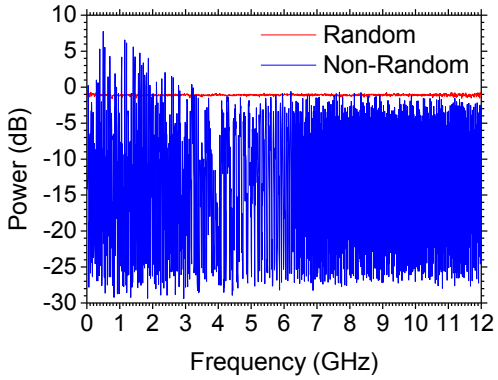

Figure 4.24. Frequency response of the proposed random cavity in comparison with a linear cavity.

The laser behavior for a high frequency analog modulation was also characterized. Figure 4.24 compares the frequency behavior of the random mirror laser and a conventional linear cavity laser. A network analyzer was used to characterize both systems from 300 kHz to 12 GHz using a frequency resolution of 200 kHz. Both cavities have the same length and topology to compare the lasers performance. The random mirror laser has been transformed into a two discrete mirrors linear cavity laser introducing a FBG (centre wavelength: 1549.6 nm, bandwidth: ~0.25 nm, reflectivity: ~97%) at C to reflect the output power. Thus, the reflected signal overrides the effect of the distributed mirror, being the new cavity length the ~2.5 km of the DCF. It is remarkable the flat behavior of the random laser independently of the frequency in comparison to the periodic spectral response of the non-distributed cavity. This frequency dependence is evident in the blue plot from Figure 4.24 which shows the high number of frequency minima present in the non-distributed cavity. Although a time-domain comparison of the conventional random vs. non-random cavity fiber laser is not presented here, one can argue that modulating the conventional laser would produce a regular pulse sequence similar to that in figure 4.23 only when the modulation frequency matches the longitudinal cavity mode spacing and would otherwise result in a distorted response (see Refs. [22, 25]).

4.3. CONCLUSIONS

Three different applications of the RDFB effect for multi-wavelength and modulated fiber lasers have been experimentally demonstrated. These new laser structures try to contribute to show the potential that RDFB offers to fiber optic technologies.

In the first section, the basic random-laser structure presented in [2] was filtered by a FLM interferometer which includes a Hi-Bi SC-PCF. The MWFL is composed by this FLM, which filters the emission spectrum and a double-random mirror laser. The double-random mirror acts by itself as a broadband laser with a 30dB SNR, being the result of multiple Rayleigh scattering produced in the dispersion compensating fibers by the Raman amplification. The MWFL's output has a multi-peak spectrum showing 7 lasing channels with a minimum OSNR of ~25dB. The wavelength spacing between lasing channels and the number of lasing channels can be easily tailored by changing the length of the suspended-core fiber. In addition, the fiber laser's output is highly sensitive to polarization induced changes in the Sagnac filter. As such, by adjusting a polarization controller, different shapes, SNR and number of lasing channels can be obtained. This multi-wavelength Raman fiber laser presents suitable characteristics for sensors interrogation. Even more, the proposed configuration can be used as laser sensor by simply exploiting the sensing skills of the Sagnac configuration.

The second demonstrated configuration tries to improve the previous developed laser by using a programmable filter in order to select the desired lasing wavelengths in real time. To achieve this feature, a specific software application was developed. This laser shows high stability, a broad-band response, reconfigurability, versatility and high power emission lines. A maximum band of ~20 nm can be reconfigured with a minimum distance of 50 GHz between lasing channels. However, the best performance of the laser is achieved when the emission lines distance is 100 GHz. This structure can be easily equalized and switched fulfilling the 100 GHz ITU grid specification for telecommunication or sensing purposes.

In the final section, a modulated random mirror laser using the same basic blocks utilized in the switchable MWFL, has been experimentally demonstrated. In order to modulate the emitted signal, an EOM was used instead of the programmable filter. This structure can be internally modulated with no restrictions attributable to the cavity length.

These results have originated the publications in references [8, 26-27]

4.4. REFERENCES

[1] *Y. J. Rao, and W. L. Zhang, "Recent progress in random fiber lasers" Proc. Opt Comm and Networks (ICOCN) Art no 6617202 (2013)*

[2] *S. K. Turitsyn, S. A. Babin, A. E. El-Taher, P. Harper, D. V. Churkin, S. I. Kablukov, J. D. Ania-Castañon, V. Karalekas and E. V. Podivilov, "Random distributed feedback fibre laser", Nature Photonics, 4, (2010).*

[3] *S. A. Babin, A. E. El-Taher, P. Harper, "Tunable Random Fiber Laser", Physical Reviews A, 84, 021805 (2011)*

[4] *A. R. Sarmani, R. Zamiri, M. H. A. Bakar, "Tunable Raman Fiber Laser Induced by Rayleigh Back-Scattering in an Ultra-Long Cavity", J. Europe Optical Society, 6, 11043 (2011).*

[5] *A. M. R. Pinto, O. Frazão, J. Santos, M. Lopez-Amo, "Multiwavelength fiber laser based on a photonic crystal fiber loop mirror with cooperative Rayleigh scattering", Appl. Phys. B, 99, 391–395, (2010).*

[6] *A. M. R. Pinto, M. Lopez-Amo, "Double random mirror Hi–Bi photonic crystal fiber Sagnac based multiwavelength fiber laser", Appl. Phys. B, 103, 771–775 (2011).*

[7] *A. M. R. Pinto, O. Frazão, J. L. Santos, and M. Lopez-Amo, "Multiwavelength Raman Fiber Lasers Using Hi-Bi Photonic Crystal Fiber Loop Mirrors Combined With Random Cavities", Journal of Lightwave Technology, 29, 1482-1488 (2011).*

[8] *A. M. R. Pinto, M. Bravo, M. Fernandez-Vallejo, M. Lopez-Amo, J. Kobelke and K. Schuster "Suspended-core fiber Sagnac combined dual-random mirror Raman fiber laser", Optics Express, 19, 11906-11915 (2011).*

[9] *A. E. El-Taher, P. Harper, B. Babin, D. Churkin, E. Podivilov, J. D. Ania–Castañon, S.K. Turitsyn, "Effect of Rayleigh-scattering distributed feedback on multiwavelength Raman fiber laser generation", Optics Lett, 36, 130-132 (2011).*

[10] *S. Sugavanam, Z. Yan, V. Kamynin, A. S. Kurkov, L. Zhang, D. V. Churkin, "Multiwavelength generation in a random distributed feedback fiber laser using an all fiber Lyot filter", Opt. Express, 22, 2839–2844 (2014).*

[11] *M. Fernández-Vallejo, S. Diaz, R.A. Perez-Herrera, R. Unzu, M. A. Quintela, J. M. López-Higuera and M. López-Amo," Comparison of the Stability of Ring Resonator Structures for Multiwavelength Fiber Lasers Using Raman or Er-Doped Fiber Amplification", IEEE J Quantum, 45, 1551-1557 (2009).*

[12] *Z. Wang, N. Y. J. Rao, H. Wu, "Long-Distance Fiber-Optic Point-Sensing Systems Based on Random Fiber Lasers", Optics Express, 20, 17695-17700 (2012)*

[13] *H. Martins, M. B. Marques, and O. Frazão, "300 km-ultralong Raman fiber lasers using a distributed mirror for sensing applications", Optics Express 19, 18149-18154 (2012).*

[14] *H. Martins, M. B. Marques, and O. Frazão, "Temperature-Insensitive Strain Sensor Based on Four-Wave Mixing Using Raman Fiber Bragg Grating Laser Sensor with Cooperative Rayleigh Scattering", Applied Physics B, 104, 957-960 (2011).*

[15] D. V. Churkin, I. D Vatnik, S. K. Turitsyn and S. A. Babin, "Random Distributed Feedback Raman Fiber Laser Operating at 12 μm Wavelength Range", Laser Physics, 21, 1525-1529 (2011)

[16] D. V. Churkin, A. E. El-Taher, I. D Vatnik and S. A. Babin, "Experimental and Theoretical Study of Longitudinal Power Distribution in a Random DFB Fiber Laser", Optics Express, 20, 11178-11188 (2012)

[17] S. A. Babin, and I. D Vatnik, "Random-Distributed Feedback Fiber Lasers Based on Rayleigh Scattering", Optoelectronics, Instrumentation and Data Procesing, 49, 3-29 (2013)

[18] R. A. Perez-Herrera and M. Lopez-Amo "Multi-wavelength fiber lasers" in "Current Developments in Optical Fiber Technology", S. W. Harun, ed. (Intech open 2013), 449-479 (2013)

[19] R. Schmogrow, S. Ben-Ezra, P. C. Schindler, B. Nebendahl, C. Koos, W. Freude, and J. Leuthold, "Pulse-Shaping With Digital, Electrical, and Optical Filters-A Comparison" Journal of Lightwave Technology, 31, 2570-2577 (2013)

[20] M. Fernandez-Vallejo, S. Rota-Rodriguez, and M. Lopez-Amo, "Remote (250 Km) fiber Bragg grating multiplexing system" Sensors, 11, 8711-8720 (2011)

[21] A. R. Chraplyvy, "Limitations on Lightwave Communications Imposed by Optical-Fiber Nonlinearities", Journal of Lightwave Technology, 8, 1548-1557 (1990).

[22] B. Vizoso, M. C. Vázquez, R. Civera, M. López-Amo, M. A. Muriel, "Amplified fiber-optic recirculating delay lines", Journal of Lightwave Technology, 12, 294-305 (1994).

[23] C.E.S. Castellani, E.J.R. Kelleher, Z. Luo, K. Wu, C. Ouyang, P.P. Shum, Z. Shen, S.V. Popov, and J.R. Taylor "Harmonic and single pulse operation of a Raman laser using grapheme", Laser Phys. Lett., 9, 223-228 (2012).

[24] B. Dong, J. Hao, J. Hu, C. Liaw, "Short linear-cavity Q-switched fiber laser with a compact short carbon nanotube based saturable absorber", Optical Fiber Technology, 17, 105-107 (2011).

[25] M. Fernandez-Vallejo, S. Rota-Rodrigo and M. Lopez-Amo, "Comparative study of ring and random cavities for fiber lasers", Applied Optics, 53, 3501-3507 (2014).

[26] V. DeMiguel-Soto, M. Bravo and M. Lopez-Amo, "Fully-switchable multi-wavelength fiberlaser assisted by a Random mirror", Optics Letters, 39, 2020-2023 (2014).

[27] M. Bravo, M. Fernandez-Vallejo, M. Lopez-Amo, "Internal modulation of a Random fiber laser", Optics Letters, 38, 1542-1544 (2013).

chapter V
NEW FIBER OPTIC SENSORS IN SHM

INTRODUCTION

This PhD work, as it was explained in previous chapters, is devoted to study and propose different fiber optic sensor configurations for structural health monitoring (SHM) purposes and, thus, someday, the developing of smart structures.
In this chapter it will be explored some of the most important characteristics of the fiber optic sensor technology to be applied to the SHM objectives: sensor multiplexing and remote interrogation. These topics were also explored in chapter 3 by using OTDR interrogation techniques. It is important to highlight that chapter 3 could be contained in this one, but all the work done with the OTDR, deserved to have its own chapter. On the other hand, in order to improve the applications in sensors multiplexing of remote networks, it will be also explored the remote feeding of optoelectronic devices by using power by light techniques.
Because of the length of this chapter, it is organized following the achieved results. Firstly, it will be presented the intensity sensor multiplexing and remote schemes used in the multiplexing of these networks. After them, the wavelength based remote and multiplexing schemes and power by light switching multiplexing schemes are presented. Finally, an overall overview of all the schemes are summarized in a versatile sensor system which contributes to justify the potential that fiber optic sensing technologies offers.

5.1. FIBER OPTIC INTENSITY SENSOR NETWORKS

Usually intensity fiber-optic sensors are interrogated by illuminating the sensing structure and detecting the intensity variation induced by the measurand. Because of this, the multiplexing of intensity sensors without suffering crosstalk is a challenge [1]. In this section three different solutions are presented. In the same way than the OTDR intensity sensors interrogation techniques presented in chapter 3, a TDM remote interrogation proposal in transmission is presented. On the other hand, two schemes which use WDM techniques for remote interrogation of multiple sensors are also presented.

5.1.1. Remote Time Division Multiplexing of Bending Sensors

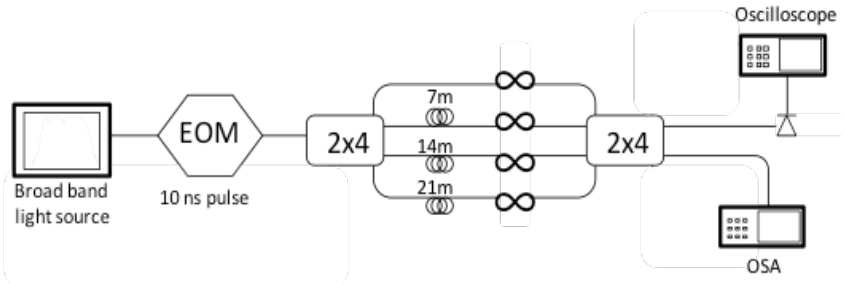

Figure 5.1. TDM sensor system schematic diagram used for non remote characterization of the sensors.

The leading idea of this first proposed network is the multiplexing of intensity bending sensors by launching an optical pulse and delaying it by using different fiber delays for each sensor. Figure 5.1 illustrates the basic scheme of the developed network.

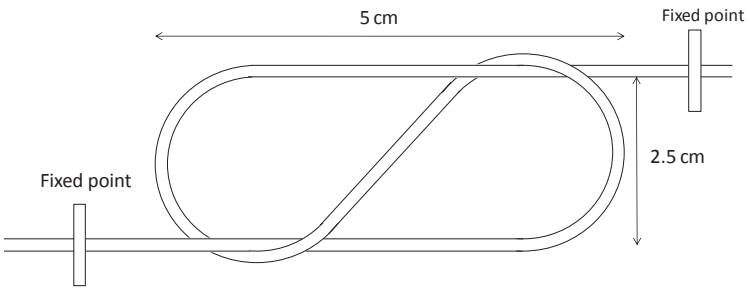

Figure 5.2. Bend tie sensors diagram, including initial dimensions for a non-stressed sensor.

The sensing unit consists of four intensity sensors arranged in a star configuration. The sensors are based on the bend tie sensor diagram firstly proposed by F. Sienkiewicz *et al.* (figure 5.2) [2]. This sensor is able to measure large displacements and, consequently, high deformations when the ends of the sensor are attached to two points of a structure. In order to characterize the sensors, their input and output fiber sections (described as "fixed point" in figure 5.2) are placed on two high precision motorized stages which makes that the tie shape shrinks or extends following a lineal displacement. Therefore, a curvature change is generated, which increases or decreases the loss. The minimum displacement step that the motorized stages provide is 17 nm and, and in order to control it, a custom software was developed. The software integrates all the instruments to make measurements of the displacement of the sensors each 3.4 mm. To improve the sensor performance and repeatability, the fiber of the tie sensor was smeared of lithium grease. The characterization setup allows making high resolution measurements.

The principle of operation is presented below. A broad band light pulse of 10 ns is modulated by using an EOM (electro optical modulator). Afterwards the pulse is divided by the first 2x4 coupler in four almost identical pulses travelling through different fiber delay lines before been modified by the sensors. The sensors modulate the intensity of each pulse following the selected displacement between the fixed points. Afterwards, the pulses are re-coupled by the second 2x4 coupler shown in Figure 5.1. Finally, four different pulses corresponding to the sensors are detected by a high sensitivity photodetector (New Focus 1811, 125 MHz, 900-1700 nm) and monitored by an oscilloscope. In order to monitor and control the optical signal, an OSA is connected at the extra coupler output. Although no OSA is necessary for the sensor ordinary measuring process, we use it for the system calibration and adjusting purposes.

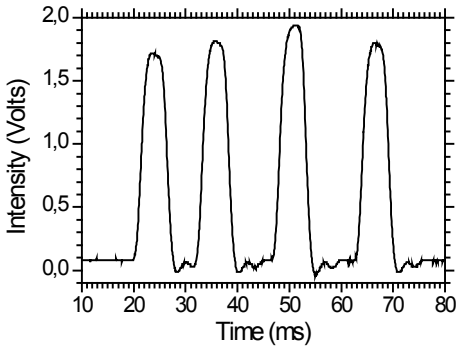

Figure 5.3. Oscilloscope view of the four sensors´ received pulses.

Figure 5.3 shows the received signal from the 4 sensors. For the experiment it was tested each sensor separately and the influence on its behavior of the other sensors (the crosstalk) was also checked. A delay of approximately 20 ns (corresponding to a 7 m fiber length) has been applied to the pulse corresponding to this sensor. The number of sensors that can be multiplexed using this scheme is limited by the received optical power from each sensor. Theoretically, in a non-remote setup is possible to multiplex up to 32 sensors using our topology and equipments. However, for remote applications, this number should be reduced for achieving a good SNR, if the same resolution is desired.

The broadband light source used (Nettest fiberwhite SPL), covers a wavelength spectrum from 1525.5 to 1611.7 nm, with a maximum output power of 18.8 dBm and power stability of 0.005 dB. This broadband source avoids the oscillations measured in the curvature loss function because of the cladding-mode coupling process when a narrow band laser is used. This effect was firstly observed in chapter 3 section 3.4. The cladding-mode excitation causes a wavelength displacement according to the bending radius. Therefore, the losses caused by curvatures are completely dependent on the wavelength. By using the broadband source a loss averaging of this dependence is achieved, reducing the unwanted effects of the cladding-mode re-coupling. Because of the non-uniform spectrum profile of the broadband source, it was referenced the measurements regarding the first spectrum obtained with a non-stressed sensor. On the other hand, the utilization of short bending radius loops as mode scramblers, as presented in chapter 3.4.2 contributes to attenuate the excited cladding-modes improving the accuracy of the measurements as well. These fiber loops were optimized for each sensor. The loops configuration was developed after several empirical tests, showing the optimum cladding-mode suppression behavior. In the experimental set-up, only one loop before two of the sensors was used (the second and the fourth sensor).

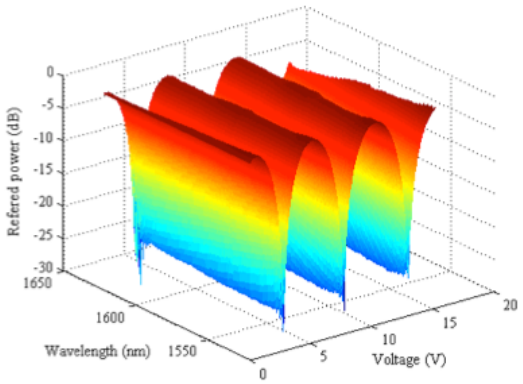

Figure 5.4 EOM response to the Biasing point variation.

An electro-optic amplitude modulator, LiNbO3 "UTP APETM 2x2 interferometric switch", was utilized. It generates short pulses when connected to the output of the continuous wave (CW) light source. The EOM transfer function and its biasing point are two crucial parameters to be controlled. Intuitively, the reader can think that modulating a broadband source by an interferometric switch is not the most efficient way of modulating an optical signal because the switch extinction ratio is wavelength dependent. For the main purpose of the system, the sensor response improvement due to the broadband source justifies it. Figure 5.4 shows the characterization of the modulator response to the changes of the biasing point. A computer controlled DC source increased with 0.01V steps the biasing point in each measurement and registered them using an OSA. This 3D graph shows the EOM output power versus the wavelength and the polarization voltage applied. The polarization point is a crucial parameter to be controlled and to stabilize. The transfer function of the EOM modifies the spectrum of the source while the biasing point controls the amplitude of the pulses.

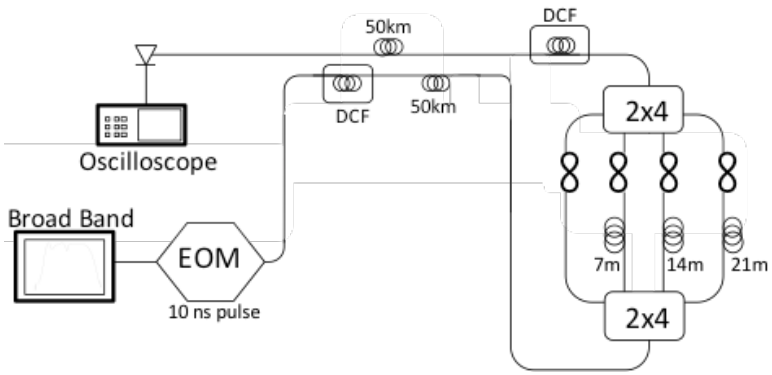

Figure 5.5. Remote (50 km) sensor system.

In order to check the application of this structure for remote sensing, the network was extended up to 50 km. Figure 5.5 depicts the schematic diagram of the remote application of the multiplexing network. Dispersion is a crucial aspect to be taken into account when pulses are transmitted through long distances. Pulses duration can be enlarged too much because of dispersion, and the overlap of the different pulses received from the different sensors can cause crosstalk in this TDM system. Because of it, two dispersion compensating fiber (DCF) sections are used to balance the dispersion caused by the 100 km of standard single mode fiber (SMF28) added to the network. However, the price to pay is an additional 7.8 dB loss.

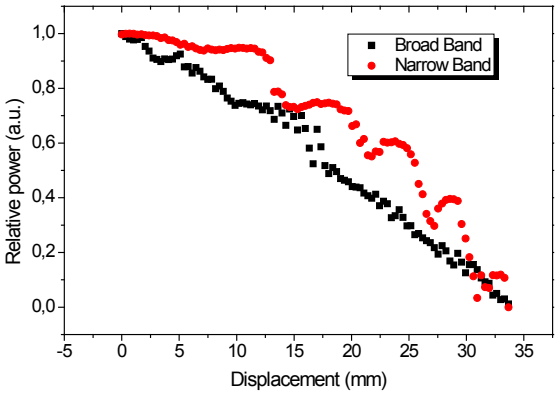

Figure 5.6. Measured transfer function of a displacement sensor when a laser diode (red) and a broadband light source (black) are used.

Figure 5.6 illustrates the displacement characterization of one of the intensity sensors when displacement is applied and the two different light sources are used. The red trace corresponds to the measurement of the sensor when the OTDR laser is used in an in-transmission configuration, as studied in chapter 3.4.2. The non linear behavior limits the resolution and applicability of the sensor. It corresponds to the excitation of new cladding modes when the bending radius is reduced with the applied displacement. However, this excitation also depends on wavelength [3]. Thus, when a broadband light source is used and all its spectral components are simultaneously introduced into the bending sensor, an average effect is obtained and the linearity of the transfer function is improved.

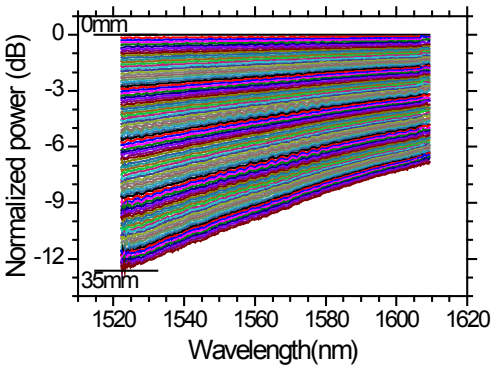

Figure 5.7. Spectrum evolution according the applied displacement after the sensor (the displacement applied is marked inside).

Figure 5.7 shows the evolution of the attenuation spectra as the bending radius changes. The first trace is taken as the reference one. Thus, to calculate the attenuation, the trace taken in each bending state is subtracted to the reference one. The results shown in Fig. 5.7 confirm the dependence of macro-bending with the wavelength.

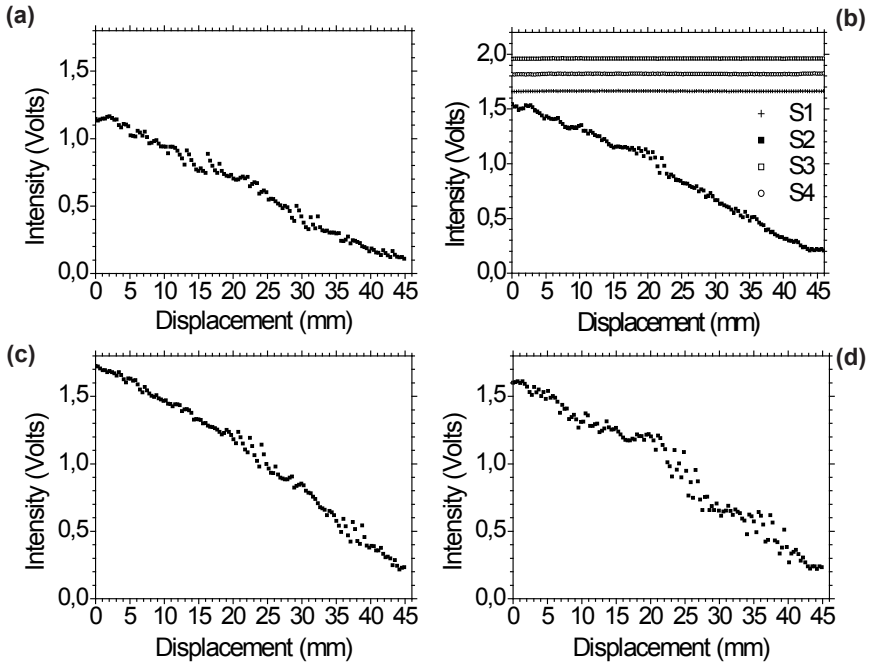

Figure 5.8. All sensor received signals evolution when displacement is applied. Graph (b) shows S2 displacement characterization and the rest of sensors when they are not stressed.

Figure 5.8 depicts the measured displacement behavior of the four sensors. The received signal levels are different because of the different calibration parameters of the mode scrambler loops explained before. An important parameter to study is the crosstalk between sensors. In this study the crosstalk was checked for each sensor. Figure 5.8 (b) shows the second sensor behavior and the simultaneous signal variations obtained from the others. The size of the launched pulse and the delay of each branch must be well controlled to prevent pulse overlapping, avoiding crosstalk.

This figure (5.8) demonstrates the crosstalk free behavior of this system because the received pulses, corresponding to each sensor have them own time slot without suffering overlapping.

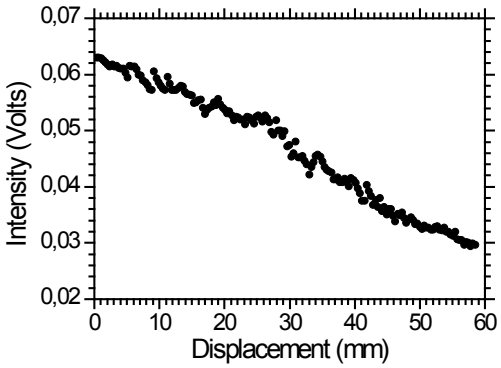

Figure 5.9. Remote sensor detected signal evolution vs. displacement.

We have also made an identical characterization of the sensors using the remote sensor system configuration, placing the sensors 50 km away from the monitoring header. On this occasion (figure 5.9), the sensor's voltage evolution is as linear as the previous one but the dynamic range in this case is much lower. However it is still enough for the system requirements.

Finally, the system resolution, accuracy and repeatability have been studied for both systems: local and remote systems. Because the light source and the photo-detector will introduce the corresponding intensity noise and quantum and thermal noise, the received signal was averaged. Using these data it was calculated the system resolution and accuracy. The non remote sensor system resolution turned out to be ±0.5 mm and the remote sensor configuration resolution was ±1 mm in the measurement range of 35 mm. These results were obtained making an averaging of 64 oscilloscope traces in order to reduce the noise. The repeatability, defined as the maximum difference between the consecutive readings of the sensors [4], was ±1.14%. The measurement frequency can be as fast as 1 Hz, being the real limitation the oscilloscope acquisition speed and data processing time. Finally, we would like to point out that other possible measurement errors, coming from instabilities from the EOM and sensor network instabilities, may be reduced using an intensity referenced scheme, for example, as the referenced schemes for intensity sensors presented in chapter 2.

5.1.2. Multiplexing of six micro-displacement suspended-core Sagnac interferometer sensors with a Raman-Erbium fiber laser

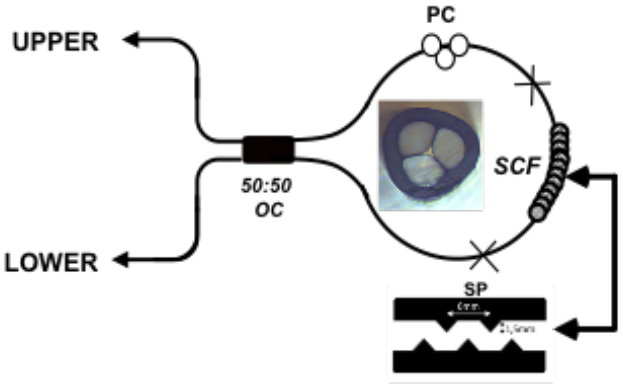

Figure 5.10. Micro-displacement PCF sensing head structure.

Multiplexing networks for fiber optic sensors are totally dependent on the kind of sensor to be multiplexed [5]. In this case, It was designed a new WDM multiplexing structure for transmisive PCF/FLM based sensors. The selected sensors were the high sensitivity micro-displacement fiber sensors using a suspended-core Sagnac interferometer depicted in figure 5.10 and previously detailed in chapter 2.1.1. Although these sensors have an interferometric nature, finally the measured parameter is coded into the intensity of the transmitted signal and not in the wavelength. Thus, this is the reason to include their multiplexing networks in this section.

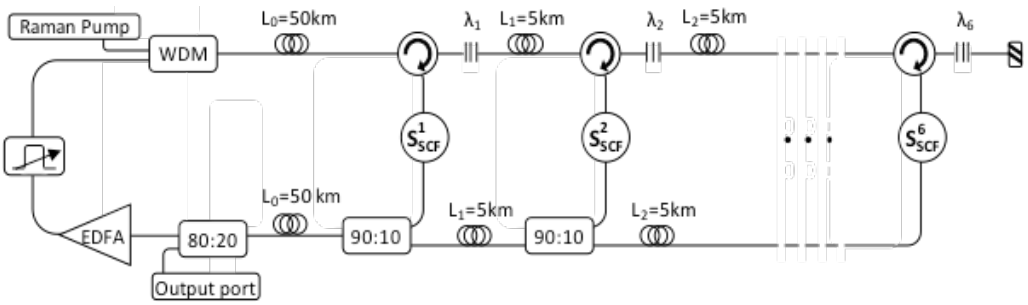

Figure 5.11. Experimental set up for the proposed remote multiplexing PCF sensor system.

The proposed multiplexing system set-up, suitable for remote monitoring of such a kind of sensors, is shown in figure 5.11. It is composed by the three basic parts already presented in chapter 1: the sensor network itself, the monitoring station and the transmission channel.

The sensor network itself is based on a ladder structure. The upper path is composed of circulators whose isolation is ~56 dB, FBGs centered between 1544.79 nm – 1550.79 nm and having reflectivities around 96-97%, and fiber spools. The circulators redirect the reflected light from each FBG towards the PCF sensors, where it will be intensity modulated, and finally towards the lower path. It seems important to point out that the circulators isolate the reflection signal of each sensing head and force each peak to travel through the correct sensing head. For this reason, crosstalk is avoided. This means that one of the most challenging issues for multiplexing intensity sensors is addressed. The main function of the lower path is to collect each modulated sensor signal. After an empirical coupling ratio study carried out using a variable coupler, 90:10 couplers have been selected for this purpose. For performing a more realistic scheme, 5 km fiber spools have been placed between each sensing head, which simulates that each PCF sensor is placed in a different location. Thus, the distance from the first sensor to the last one is 25 km, therefore, the first PCF sensor is placed 50 km away from the monitoring station and the last one is located after 75 km.

This dual-bus PCF sensing head sensor network is connected with the monitoring station by two 50 km SMF fiber spools. One is connected to the upper path and the other to the lower one achieving an up to 75 km remote PCF sensor multiplexing network.

Finally, the network is completed by the monitoring station. It is composed of a Raman 1445 nm pump laser whose power is launched into the ring by a WDM in order to obtain Raman amplification; the programmable tunable filter (Finisar WaveShaper 1000S) which sequentially selects each FBG wavelength; a commercial EDFA and finally, an optical spectrum analyzer (OSA) that detects the output signal.

The operation mode of the system is based on a multiple cavity fiber ring laser. Each FBG creates a lasing channel whose intensity is modulated by the PCF sensing head located into the upper-lower bus interconnections. Once the signals are coupled in the lower bus, an 80:20 coupler takes out 20% of light to be detected by an OSA. The remaining optical power is amplified by the EDFA (13 dB gain) and afterwards it is filtered using the tunable programmable filter. This filter plays two important roles: on the one hand, it selects each lasing channel and, on the other hand, it eliminates the amplified spontaneous emission (ASE) noise generated previously by the EDFA. As the selected

amplified bandwidth is limited by the narrow filter width, the Raman amplification is much more efficient.

The six PCF multiplexing sensor system is achieved by using a circulator based dual-bus sensor network. The system uses Raman-EDFA hybrid amplification to compensate the high cavity losses and thus, it is possible to achieve the lasing condition. By using the programmable tunable filter, a wavelength sweep was done to tune each FBG based laser channel wavelength.

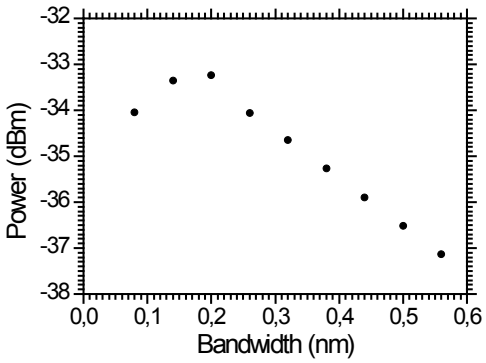

Figure 5.12. Evolution of the output power vs. the filter bandwidth.

Raman distributed amplification, needed to achieve the lasing condition, has to be optimized along with other design parameters. As M. Fernandez-Vallejo *et al*. demonstrated in [6], when the pump power increases, the lasing channel bandwidth broadens and unwanted effects appear when the output power is depleted. And this fact is directly related to the channel width. For this reason, a complete study of the influence of the filter width on the output power was carried out in order to reach the most efficient Raman amplification. For this purpose, the utilized filter offers two interesting characteristics: it is possible to select the bandwidth from 40 to 0.08 nm and it is also possible to choose the filter center wavelength with a precision of 8 pm in the communications C Band (1527.4-1567.4 nm). In this work, the evolution of the output power of one of the laser emission lines against the filter bandwidth has been assessed. Figure 5.12 shows the result. As it was expected, the narrower the bandwidth is, the more stimulated Brillouin scattering (SBS) spreading is observed. On the other hand, once established an optimum bandwidth; for broader bandwidths, lower Raman amplification efficiencies were obtained. Finally, for these amplification conditions, that will be detailed below, the optimum filter-bandwidth empirically obtained was ~0.2 nm, as illustrates figure 5.12.

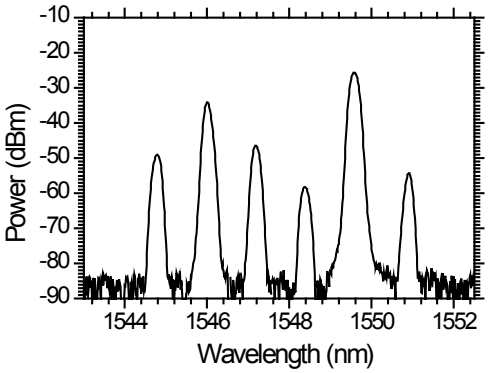

Figure 5.13. Different lasing channels spectrum overview.

Taking into account that the proposed fiber ring laser does not work in multi-wavelength operation, the results depicted in figure 5.13 are the combination of each lasing channel spectrum, corresponding to the six sensors. The power difference between each peak is due to the difference of length and losses between each sensor cavity.

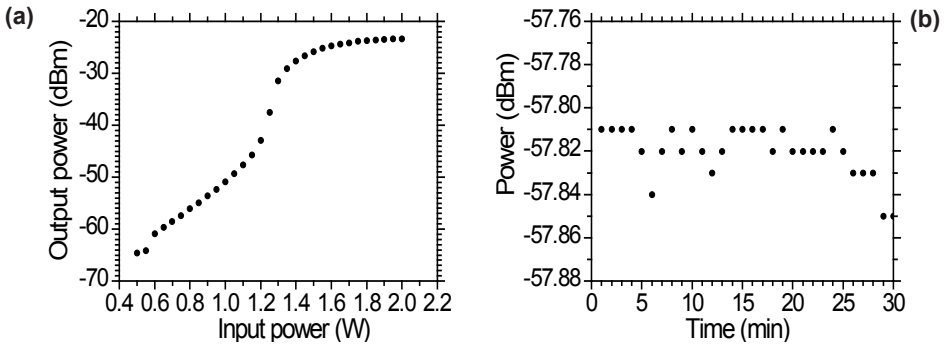

Figure 5.14. Laser condition characterization and stability overview for 30 minutes.

Figure 5.14 (a) shows the results of the study of the output power versus the Raman pump power which demonstrates that the Raman amplification compensates the total losses of the cavity, achieving the laser condition. Specifically, this plot depicts the evolution of the output power regarding the input Raman pump power for the laser channel centered at 1549.6 nm. There are two clear turning points: the first one, ~1.2 W, indicates that the cavity reaches the lasing threshold pump power and the second one, ~1.5 W,

clearly suggests that the cavity reaches the saturated region. Thus, the selected Raman pump power was ~1.5 W.

Taking into consideration the high influence of the output power instabilities in the precision of the measurements; the stability of the fiber laser was analyzed. Figure 5.14 (b) provides the stability against 30 minutes time of the channel centered at 1548.44 nm whose maximum deviation is 0.04 dB. The power of this channel is the lowest, which means that the worst case is being considered.

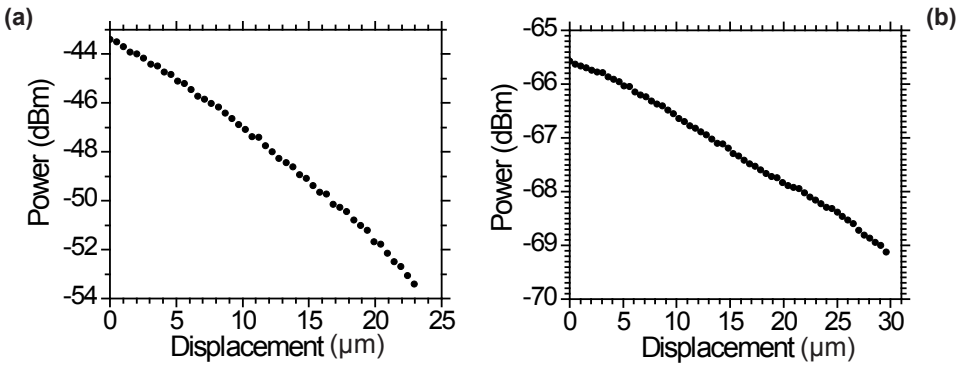

Figure 5.15. PCF sensor behavior for the best (a) and the worst case (b).

To validate the behavior of the PCF sensors when they are inside the sensors network, the performance of the sensors when strain is applied has been studied. Sensitivities of 0.043 and 0.012 dBm/μm have been obtained for the best and worst case respectively, as it is shown in figure. 5.15. Both results have a very high linear fitting with a standard deviation less than 0.01. On the other hand, the repeatability of the system has been studied with a result of ±0.8% accuracy between consecutive sensor readings. Taking into account the 0.04 dB instability and the ±0.8% repeatability results, the final precision of the sensor system for the best case is ±0.9 μm and in the worst case is ±3 μm. These results are in very good agreement with the measured data obtained when they act in single- sensor systems as shown in section 2.1.1.

5.1.3. Remote sensors multiplexing by using optical add-drop multiplexers

In this section, two remote sensing network schemes for WDM addressing of intensity sensors by using optical add-drop multiplexers (OADM) are presented. The OADM was

originally developed for communication purposes. This device has the capability of extracting and adding one single wavelength from a, usually, WDM (wavelength-division multiplexing) network for telecommunications. For fiber optic sensor applications, R. Perez-Herrera *et al*. have been previously proposed a robust fiber optic sensor multiplexing network based on this kind of devices [7].

5.1.3.1. Remote interrogation of intensity sensors arrays by using OADMs.

Figure 5.16 depicts the first proposed setup, which is composed by three main blocks: the monitoring station, the transmission channel and the sensing unit. The monitoring station utilizes a semiconductor tunable laser (TLS) which sequentially selects each sensor wavelength and also, launches in each scanning cycle an additional reference wavelength. Its light is coupled to the transmission channel by a circulator which also collects the sensors signal to be detected by a handheld power meter. This power meter might be replaced by a semiconductor detector and the corresponding electronics in a real application.

The sensing unit includes four OADMs arranged in bus structure. The new design proposed here for remote sensing connects the monitoring station and the remote sensing unit using a unique 50 km long SMF section. The available SNR is limited by the non-ideal isolation between ports of the circulator; in this case, the signal SNR is ~13 dB. Analytically the SNR can be calculated as follows:

$$SNR = I_{C13} - L_{NET} \qquad (5.1)$$

where I_{C13} refers to the isolation between circulator's port 1 and 3 and L_{NET} is the total loss of the network between the source and the output port. In this system, I_{C13}~47dB and L_{NET}~34dB. Thus, the 13 dB SNR were analytically demonstrated. Therefore, the maximum length achievable is limited by the isolation between circulator's port 1 and 3.

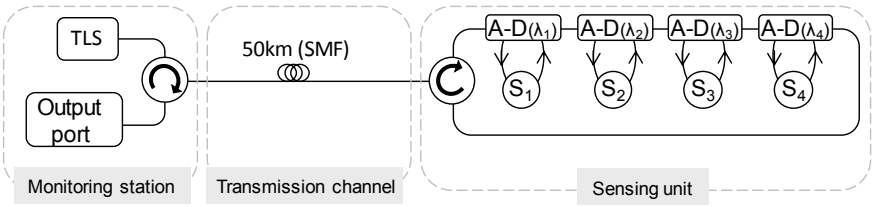

Figure 5.16. Experimental setup for the proposed sensor array

The principle of operation of the proposed sensor system is based on the wavelength selective behavior of the OADMs. There are two different alternatives. Firstly, when the TLS wavelength does not match with any OADM operation wavelength, the TLS signal is not affected by the OADMs and it is transmitted back to the monitoring station. However, when the TLS wavelength does fit with one of the OADMs wavelengths, the signal is launched through the "drop" port where an intensity sensor will be placed. This sensor modulates the extracted signal that will be re-coupled to the bus that connects the OADMs using the "add" port. By using different wavelength coding for the selected OADMs, the system distinguishes each intensity sensor. The OADMs central wavelengths chosen were 1540, 1543, 1544.5 and 1548 nm. Unlike others wavelength coded sensor multiplexing systems which use high sophisticated detection devices, because of the sequential emission of the different wavelengths, this system can use a low-cost power-meter if the fixed wavelengths emitted are synchronized with the detection system.

Other important issue to take into account in intensity modulated sensor systems is the sensor intensity referencing. This structure is able to solve this matter by using an additional wavelength, centered in 1550.25 nm, which is launched to the network before each sensor reading to characterize the fiber network loss unassociated to the sensors and other laser fluctuations, for avoiding measurement errors. This sensor multiplexing structure has been designed for any "in-transmission" intensity sensors multiplexing showing the versatility of the proposed sensor system. Moreover, the low insertion loss presented in the OADMs allows the multiplexing of a large amount of sensors limited by the OADMs bandwidth and the TLS wavelength range.

Four different intensity sensors for displacement measurements were selected in order to experimentally demonstrate the system versatility: a sensor based on an LPG, another on a fiber-optic taper; a third one based on micro-bending using a single mode fiber and finally a high sensitivity structure based on the a photonic crystal fiber (PCF) which is inserted into a fiber loop mirror previously presented in chapter 2.1.1. It is important to highlight the ability of the proposed system of multiplexing any "in-transmission" intensity sensor, such as strain, displacement or any parameter whose dynamic range fits within the available SNR.

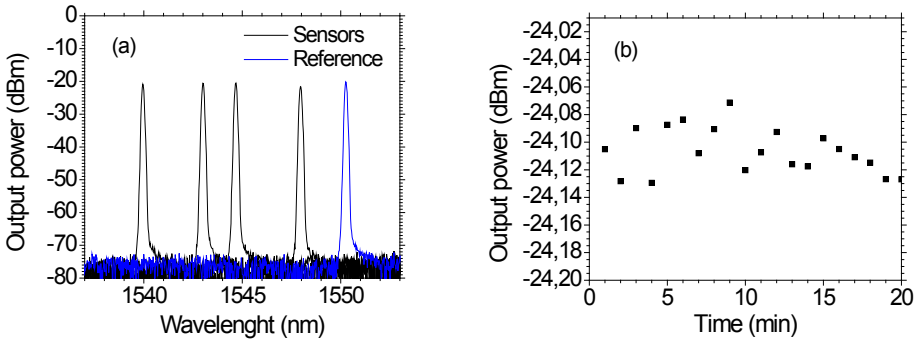

Figure 5.17. (a) Spectra of the different sensors and (b) power stability of the 1544,4 nm emission line.

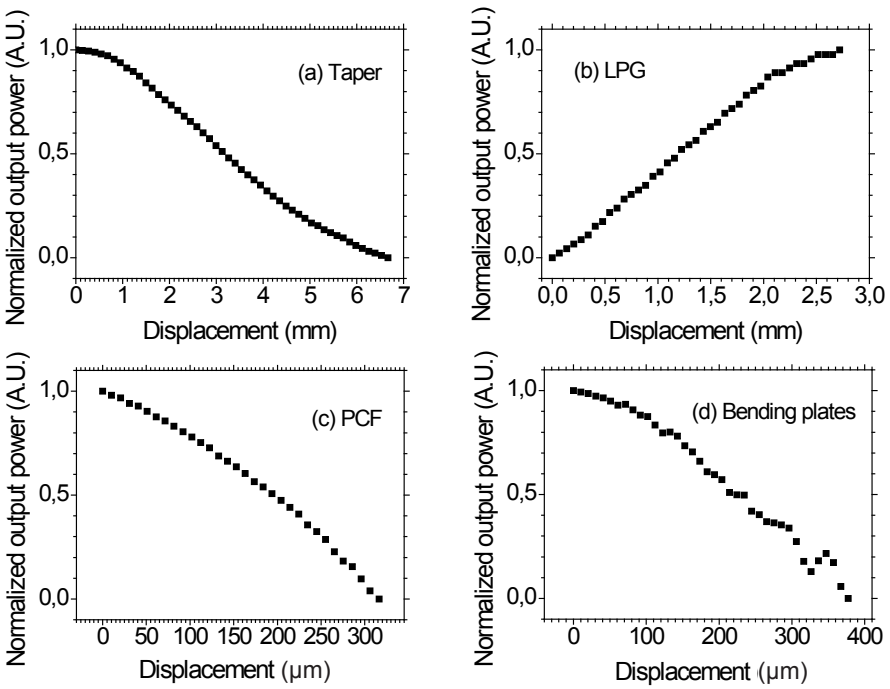

Figure 5.18. Experimental results for the different sensors tested. (a) Taper, (b) Long Period Grating, (c) Photonic Crystal Fiber sensor and (d) Single Mode Fiber microbending sensor.

The optical spectrum of each sensor and the aforementioned additional reference wavelength was measured. Figure 5.17 (a) depicts the spectra lines of the sensors (black) and reference (blue). As the tunable laser does not work in multi-wavelength operation, the trace shown in Figure 2 (a) is the combination of each sensor wavelength and the reference wavelength. Although, the reference signal allows differentiating between power variations induced by the sensor and other power oscillations, there is always certain inherent instability which belongs to the TLS which will affect directly to the final sensor resolution. For this reason, the TLS stability has been studied and its result is depicted in figure 5.17 (b). It presents a 0.08 dB of maximum deviation measuring one trace per minute during 30 minutes.

Figure 5.18 presents the characterization of the sensors. Figure 5.18 (a) depicts the taper strain behavior when it is placed in a high precision motorized stage fixed in both extremes of the sensor achieving a fiber bending. The taper is placed in the point of maximum bending to achieve a sensitivity of 0.73 dB/mm. In the same way, the LPG is characterized. It is also placed in the motorized stages for achieving the maximum bending in the point where the LPG is placed. Thus, the LPG filter, which is approximately centered in the selected wavelength, makes a frequency shift proportionally to the strain as it is shown in figure 5.18 (b). The frequency shift varies the intensity of the laser source taking into account the LPG filter shape. It presents a sensitivity of 1.83 dB/mm.

Figure 5.18 (c) shows the PCF micro displacement sensor behavior when it is stressed with two bending plates. The bending plates are controlled by the same high precision motorized stages. The fiber is placed inside a Sagnac interferometer and this interference varies proportionally to the stress applied as in 2.1.1. The sensor offers a sensitivity of 4.82 dB/mm. Finally, presented in figure 5.18 (d), a basic micro-displacement sensor based on a SMF bended by the same bending plates was characterized. This last sensor is as simple as a SMF placed between the “add” and “drop” port is bent. This sensor presents a 15.5 dB/mm sensitivity with the sole drawback of the cladding mode coupling effects observable in the results.

5.1.3.2. 100 km remote PCF intensity sensors multiplexing by using OADMs

As was mentioned in the previous section, the utilization of an optical circulator to launch and receive signals using a single fiber cable limits the achievable SNR. In the previous case, for a 50 km long remote application, using a TLS with an output power of 10 dBm the crosstalk introduced by the circulator limited the SNR to 13 dB. If longer remote multiplexing networks are desired, the network should include optical amplification, or alternatively, to use different fibers for launching and receiving the signals,

eliminating the circulator in the header of the network. This last option was employed for an ultra-long (100 km) multiplexing system, that also used OADMs, designed for PCF based sensors. Again, because PCF sensors multiplexing is, up to date, a challenge, the PCF/FLM micro-displacement structure presented in section 2.1.1 and depicted in figure 5.10 was used into the multiplexing network, being the sensors mentioned as S1...S4 into figure 5.19 schematic setup.

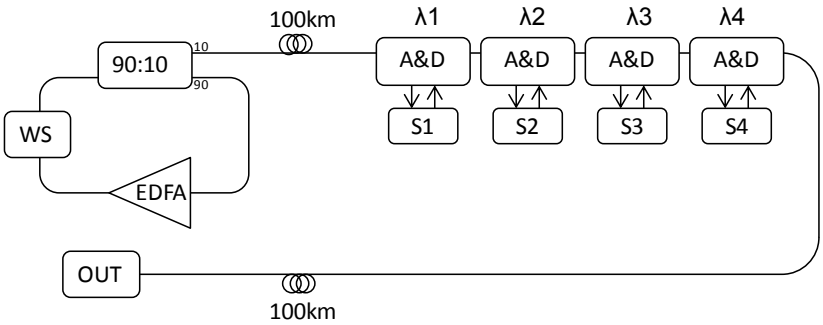

Figure 5.19. Schematic setup of the proposed remote PCF sensor multiplexing system. WS: WaveShaper tunable filter, EDFA: Erbium Doped Fiber Amplifier, A&D: Add-Drop Multiplexer.

The sensor network based on OADMs is the same as the previous system. The OADMs were arranged in a bus configuration, where the sensors were placed between the "drop" and "add". The only difference is how the signals travel from the monitoring station to the sensor network. As aforementioned, one fiber reaches the input branch of the sensor network and a different fiber leaves the network towards the detection stage.

Now, the monitoring station is formed by a home-made fiber optic laser based on a ring structure. This laser structure presents better stability (0.04 dB) than the semiconductor TLS used in the previous system (0.08 dB) which, finally, affects to the maximum measurement resolution. The laser consists of an EDFA as gain medium; the programmable tunable filter also employed in section 5.2.2 (Finisar WaveShaper 1000S) which sequentially selects each OADM wavelength; and a 90:10 low insertion loss coupler. On the other hand, the output port is composed by two different monitoring devices: an optical spectrum analyzer (OSA) and the low cost solution, a handheld power-meter.

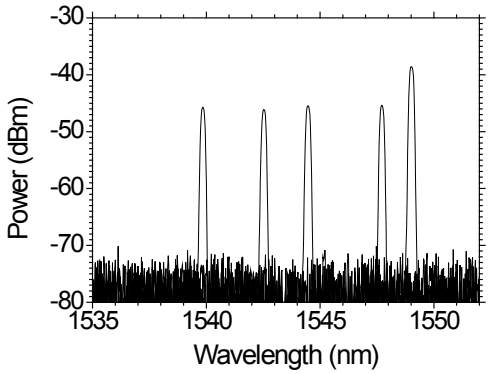

Figure 5.20. Spectrum overview of the four sensors and the additional reference line

Figure 5.20 depicts each sensor laser wavelength and again, an additional wavelength for referencing the system losses. Taking into account that the fiber laser does not work in multi-wavelength operation, the results depicted in Figure 5.20 are the combination of each OADM channel laser spectrum and the reference wavelength. The reference wavelength is different than the others OADM operation wavelengths because it travels directly to the detection stage carrying the network loss or fiber failure information.

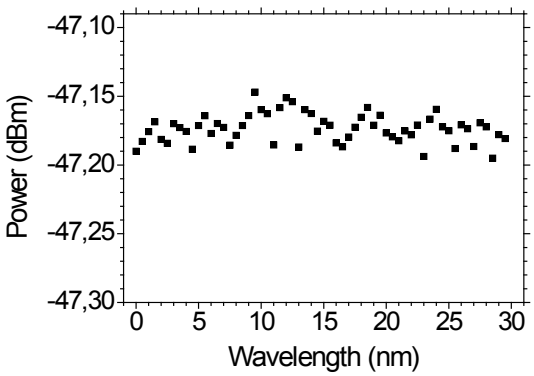

Figure 5.21. Stability measurements along 30 minutes each 30 seconds

The instabilities have high influence in the precision of the intensity sensor system. Consequently, the stability of the fiber laser is a key parameter to be assessed. Figure 5.21 provides the system stability along 30 minutes. The maximum deviation measured was

~0.04 dB which corresponds to the 1548 nm sensor. This high intensity stability guarantees the high resolution operation of the selected PCF sensing head.

Figure 5.22 depicts one sensor behavior. The graph shows the 1539 nm PCF sensor when it is detected using an OSA (black squares) and with a power meter (red circles). Both experimental results were in good agreement. The little deviation between each detection method is attributed to the extra power displayed by the power meter. It gives the integration of the entire operation spectrum, and the OSA shows the maximum power of each detected peak.

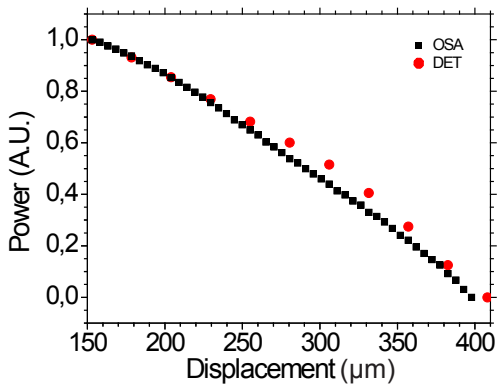

Figure 5.22. Micro displacement result measured with an OSA (black squares) and with a power-meter (DET, red circles).

The sensor showed a sensitivity of 0.026 dB/μm. In addition, a repeatability study has been done with a result of ±0.8% accuracy between consecutive sensor readings. Taking into account the 0.04 dB stability and the ±0.8% repeatability results, the final precision of each sensor is ±1.5 μm. These results were also in very good agreement with the measured data obtained in section 2.1.1. Finally, it can be considered other post processing techniques for enhancing the linearity of the sensors may be used as reported in [8].

5.2. ULTRA-LONG LASER SYSTEMS FOR REMOTE FIBER BRAGG GRATINGS ARRAYS INTERROGATION

In section 5.1.2 a 75 km long multiplexing lasing structure was demonstrated to monitoring PCF transmissive sensors. This section is devoted to explore the length limits of

these lasing networks. Now it was selected FBGs as sensors in order to codify the sensing information into wavelength and not into intensity. In this way, the intensity dynamic range of each sensor is not going to be altered when measuring. Thus, an array of 11 FBG sensors is going to be remotely interrogated using two different lasing structures: a linear laser cavity and a ring cavity.

5.2.1. 100 km sensor laser structure based on a ring cavity

Figure 5.23 schematically depicts the demonstrated 100 km long distance fiber ring laser for FBG sensors multiplexing. The sensing unit includes a linear array of 11 FBGs (centered from 1540 nm to 1552 nm with a free bandwidth of 1.2 nm between two consecutive FBGs. The bandwidths of the FBG are in the range of 0.23-0.25 nm and the reflectivity's are around 96-97%). They play simultaneously a dual-role: as wavelength selective reflectors for the lasing structure and as the sensing transducers elements of the sensor system. As the picture shows, the FBGs are connected to the transmission channel through a circulator which inserts the FBGs' reflected signals into the ring, ensuring unidirectional operation and therefore avoiding undesired effects such as spatial hole-burning (SHB).

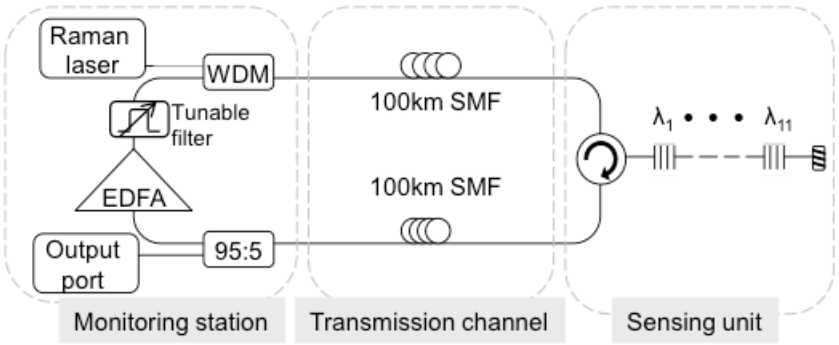

Figure 5.23. Experimental set up for the 100 km-long distance fiber ring laser which interrogates eleven FBGs.

The transmission channel is composed of two paths of 100 km-long of SMF. The need to double the fiber length may seem detrimental to the cost of the system, however, it has an ancillary impact if the total expense of a real installation is considered. From a technical point of view, this double path configuration addresses one of the principal problems of remote sensor system, the double-Rayleigh scattering, because the reflec-

ted signal travels though a different path than the launched signal and the distributed Raman amplification.

Finally, regarding the monitoring station, it consists of: a Raman laser from IPG Fibertech emitting at 1445 nm; a commercial EDFA from MPB technologies; and the programmable tunable filter from Finisar (WaveShaper 1000S). As mentioned before, this last device offers two interesting characteristics: it is possible to select the bandwidth from 40 to 0.08 nm and it is also possible to choose the filter center wavelength with a precision of 8 pm in the communications C Band (1527.4-1567.4 nm). The monitoring station also includes a wavelength division multiplexer (WDM) which combines the signal and the Raman pump, and a 95:5 coupler to extract a 5% of the laser output power from the ring.

The operation mode of the ultra-long fiber laser scheme as mention before, obeys the basic requirement of any fiber laser: lasing will take place when the total gain in the cavity overcomes the total cavity losses. The laser is set above the lasing threshold thanks to the distributed Raman amplification and the extra EDFA amplification. Then, the tunable filter sweeps in wavelength and select which FBG is going to overcome the laser condition at each time. Therefore, this device has a key function: on the one hand, it avoids the multi-wavelength operation and thus, the serial configuration of the FBG is not an obstacle; and on the other hand, it removes the amplified spontaneous emission from the EDFA outside the lasing wavelength, increasing the efficiency of the Raman amplification in the wavelength of interest. Furthermore, the tunable laser bandwidth is wide enough so that non-linear effects do not arise. More specifically it avoids stimulated Brillouin scattering (SBS), which was the most concerning process because of its low threshold.

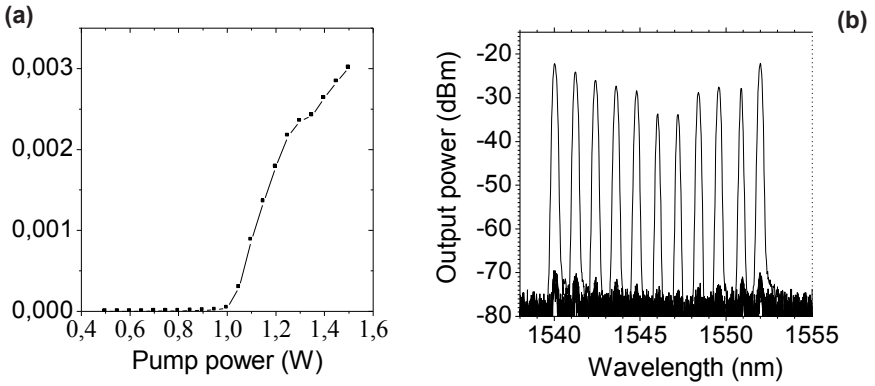

Figure 5.24. Results of the 100 km remote sensor system: (a) Output power of the laser depending on the Raman pump power; (b) Spectrum of the reflected signals from the eleven remotely multiplexed FBGs.

Figure 5.24 (a) presents the output power behavior of the 100 km system when the Raman pump power varies. Unsurprisingly, there is an evident threshold power around 1 W and from this value the output power increases linearly. Thus, this fact confirms that the 100 km system is based on a fiber ring laser having a 200 km-long cavity. Figure 5.24 (b) shows the spectra of the 100 km remote sensor system when P_{pump} Raman=1.2 W and P_{EDFA}=15 dBm are launched into the system and the OSA sensitivity used was -75 dBm and 0.1 nm resolution. Eleven channels are observed because eleven FBGs are inserted in the array. From this figure, the optical signal to noise ratio (OSNR) varies from 48 dB, in the best case, to 38 dB in the worst case. The OSNRs are determined by the non-uniform shape of the hybrid amplification EDF-Raman gain profile and the position of the FBGs in the array. Nevertheless, this difference in the OSNR does not have any influence in the sensor system itself; due to the fact that, as it is well known, FBGs encode the information into the wavelength which is an absolute parameter. It is important to mention that the figure superposes the individual measurements carried out when the tunable filter is tuned into each FBG and the spectra when the laser has completed a full scan of the bandwidth of interest.

The high signal to noise ratio shown in Figure 5.24 (b) implied reaching further distances and the sensors could be located further away from the monitoring station.

5.2.2. 200 km sensor laser structure based on a distributed cavity.

The set-up of the second interrogation fiber Bragg grating system in order to reach further distances is displayed in figure 5.25. Drawing a first comparison between figure 5.23 and figure 5.25, it is obvious that the sensing unit and the transmission channel of both schemes are identical; while the monitoring station of both systems are completely different, and thus, their operation modes are also different.

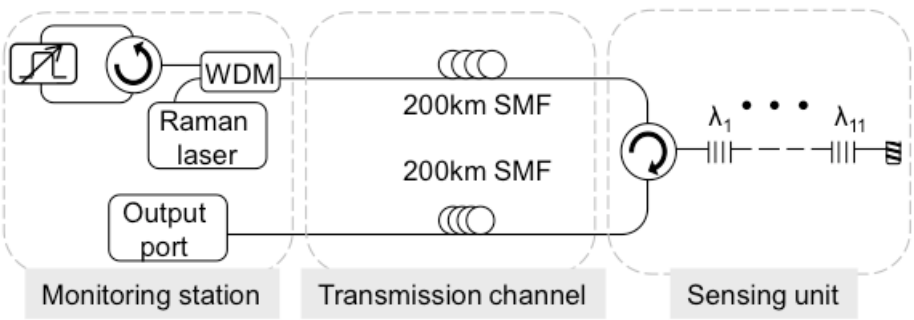

Figure 5.25. Experimental set-up for the 200 km long distance system based on a random fiber laser which interrogates eleven FBGs.

The operation mode of the 200 km remote sensor system is based on a random fiber laser. As previously mentioned, any fiber laser needs an optical cavity with the purpose of trapping the light. The first mirror of the cavity is composed by a loop which is able to reflect all the light. This mirror is constituted by a circulator and a tunable filter (bandwidth of 0.25 nm). The second mirror is based on a random distributed feedback using Rayleigh backscattering, it can be seen as an open cavity but it contributes to the positive feedback in order to reach the threshold lasing operation. The process of Rayleigh scattering in a standard single mode fiber involves a small percentage of the total power. However, the situation changes significantly when the Rayleigh scattering is amplified. Thus, the Rayleigh scattering is built up along the fiber and is amplified in such a way that the total gain in the cavity overcomes the total losses, and as a direct result, the laser signal is created. This laser signal can be tuned in wavelength by the tunable filter and is then used to interrogate the fiber Bragg gratings located 200 km away from the monitoring station. Finally, the reflected signal is sent through the second path to the output port where an optical spectrum analyzer (OSA) collects the information.

An identical study than the previous ring laser was made for this 200 km remote sensor system. First of all, the output power of the laser depending of the Raman pump power was assessed as can be seen in figure 5.26 (a). The random fiber laser has a power threshold of 1.2 W. Taking into account this power threshold, the study of the 200 km remote sensor system has been carried out with P_{pump} Raman=1.5 W and a OSA-resolution of 0.1 nm and a sensitivity of -75 dBm was used. Figure 5.26 (b) displays that the OSNR vary from 17 dB, in the best case, to 10 dB in the worst case.

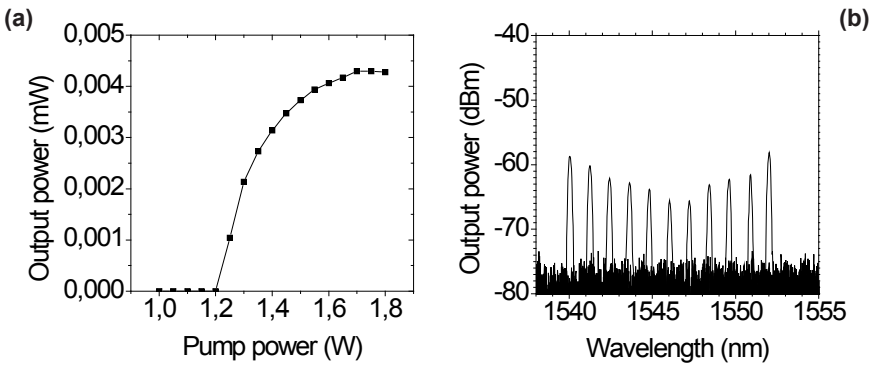

Figure 5.26. Results of the 200 km remote sensor system: (a) Output power of the laser depending on the Raman pump power; (b) Spectrum of the reflected signals from the eleven remotely multiplexed FBGs.

Finally, to evaluate the sensing performance of the 200 km long system the wavelength shift has been analyzed varying the temperature from 25 ºC to 70 ºC. Thus, the last FBG of the array has been placed into a climatic chamber in order to observe its behavior. The shift of the Bragg wavelength of the FBG sensors can be precisely interrogated when they are remotely placed: the center wavelength shift presents a linear behavior and the temperature sensitivity is 11.3 pm/ºC.

5.3. REMOTE POWERED BY LIGHT FIBER OPTIC SWITCH FOR SENSOR NETWORKS APPLICATIONS.

Optical powering is a key enabler for a new generation of autonomous multifunctional intelligent subscriber and sensor networks [9]. Power by light optical switching was already demonstrated by Ogawa, who developed a multi-point optical sensing system presented in [10]. This author proposed a new multi-point optical system (MPOSS), based on both technologies of optical pass switching and remote power supply to the node using a high-power light source. This section is devoted to the development of a fiber optic switch supplied remotely using power by light techniques, for its use in fiber optic sensor networks applications. Although the proposed solution is focused on the design of a remotely controlled fiber optic switch, this technique can be adapted to control other electro-optical or electro-mechanical devices.

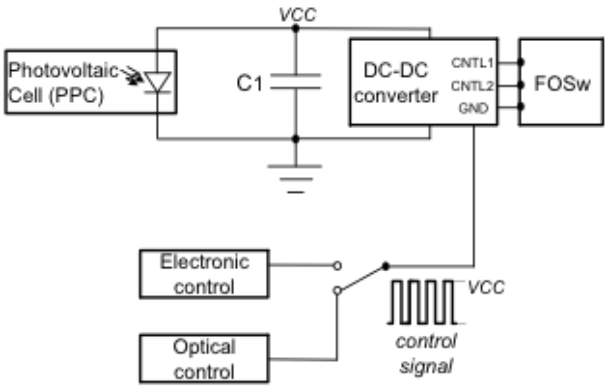

Figure 5.27. Electronics setup for the powered by light remote control of the fiber optic switch.

One of the main components of the setup is the photovoltaic power converter (PPC) PPC9LW made by JDSU. This cell converts 125 mW of a pump laser source that emits at a wavelength of 1445 nm, to a maximum of 44.79 mW (4.05 V-11.06 mA) of electrical power. It is remarkable that the 1445 nm operation wavelength was chosen because of the achievable Raman pump laser for amplification of the FBGs sensors signals. Therefore, the 1445 nm laser can be used for illuminating the PPC and, on the other hand, for Raman amplification purposes. Another important component is the fiber optic switch (FOSw) itself. For the proposed application, the most important feature of the FOSw is the power consumption. A MEMS FOSw made by DiCon Fiberoptics, Inc (MEMS 1 x 2 Switch) was chosen. Its power consumption is lower than 120 μW, satisfying the low-power requirements. The main drawback of this device is the optical channel selection method. It has 3 electrical inputs. One of the inputs is the reference arm and the other two have different voltages configurations to select each fiber optic channel. In this case the voltage configuration is: for channel 1 CNTL 1=15.715 V and CNTL 2=10.127 V; for channel 2 CNTL 1=22.078 V and CNTL 2=10.098 V. Because of this, the electronics involved is more complex slightly increasing the power consumption of the system. On one hand, the supply voltage required by the switch is higher than the voltage provided by the PPC. On the other hand, it is essential to achieve low power operation. Thus, the adopted solution, depicted in figure 5.27, consists of three electronic blocks: the integration stage, the channel selection control and the voltage converters.

The main purpose of the integration stage is to accumulate the electrical charge generated by the PPC, improving simultaneously the stability of the circuit. A 1 mF grounded capacitor was chosen for this aim. Finally, a 5 V DC converter has been used at the output of the block to set the supply voltage of the following stages.

Next, the channel selection stage is formed by three different ways to control the FOSw. The simplest technique consists of using a digital function generator with amplitude of 5 V to control the channel selection as aforementioned. In the automatic mode of operation, an electronic channel controller of the FOSw (figure 5.27) was designed by using a classical astable circuit based on NOT logic gates. Inverter gates from the CMOS 4000 series have been employed due to their good performance in terms of power consumption. The limited speed of this family of logic gates is not critical in this case, as a very low frequency control signal is required. The frequency is tuned by a variable resistor and the system is stable from ~1 Hz to ~0.05 Hz (20 s.). It has been also developed an alternative optical control system for the switch if remote control is preferred. Channel 1 is selected when an optical intensity, higher than ~-28 dBm at 1560 nm, illuminates a PIN detector. When this wavelength is not present or, when the power level reached by the photo-detector at the selected wavelength is below ~-28 dBm, channel 2 is active.

The final step is the DC-DC conversion stage. Two independent DC-DC converters have been used, because two different voltage combinations for each FOSw cantilever are needed. A high-efficiency integrated circuit MAX1771 DS fabricated by MAXIM was employed. The selection of the output voltage of the chip is externally controlled by an adjustable resistive network, whose equivalent resistance is adjusted by employing electronic switches controlled by the channel selection stage. Because each converter has to generate two different voltages for the FOSw channel selection, four different configurations of the resistive network are required in total.

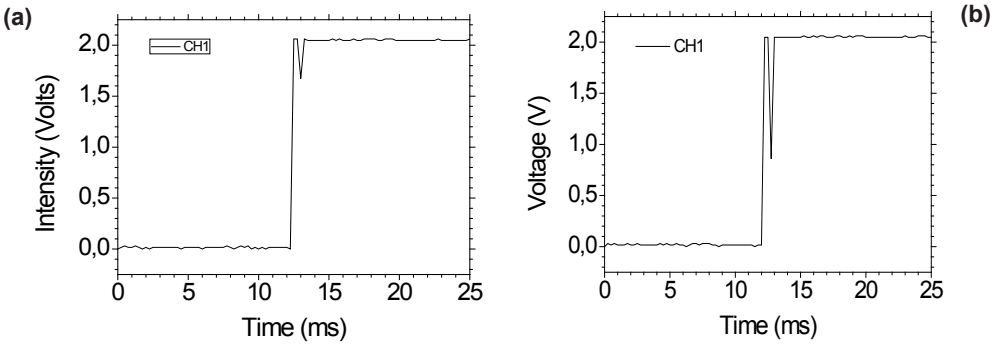

Figure 5.28. Zoom of the FOSw rise flank response of one channel 50 (a) and 100 km (b) fiber away.

Once the electronics were designed, assembled and tested, the powered by light remote FOSw was checked. The system performs correctly using, in a first approach, a 50 km fiber length with a pump power of 400 mW @1445 nm and a maximum of 100 km was achieved using ~3 W power from the same laser source. Figure 5.28 shows a zoom of the rise flank of one FOSw channel operating at 50 km (a) and 100 km (b) from the header of the system. In order to measure the FOSw response, the light at the output ports of the FOSw was detected and monitored by an oscilloscope. The measured switching time was ~2 ms. Both results are in good agreement demonstrating the system performance independence when the feeding power is enough. The design of the electronics fixes an input voltage threshold. When it is overcome, the switching behavior is independent to the incoming optical power and fiber length.

5.3.1 Remote powered by light fiber optic switch for robust interrogation of FBG sensor networks

Structural health monitoring FBG sensor systems usually presents network breakages. During the strain sensing, if the payload applied on the FBG is over its limitation, FBG breakage will occur. Furthermore, the fiber-fault of FBG-based sensing network also could affect it survivability and reliability. Some authors have proposed some solutions to these problems by using resilient sensor networks based on switching at the network header [11, 12] or inside the network, that implies local electrical biasing [13].

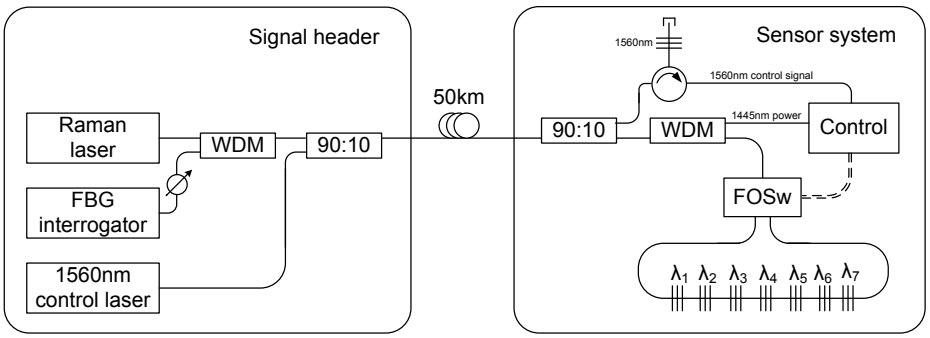

Figure 5.29. FBGs resilient remote network experimental set-up.

Figure 5.29 shows a proof of concept sensor system that is meant to solve the failures usually presented in the FBG strain sensor arrays. The main idea is to interrogate the network remotely by both ends of the FBGs sensor array. In order to achieve this goal, the powered by light FOSw aforementioned is utilized. If one network breakage occurs, all the sensors are interrogated successfully. For example, if a breakage were to happen between the FGS that reflect λ_3 and λ_4 (see figure 5.29); λ_1 λ_2 and λ_3 will be interrogated during the first switching cycle. On the other cycle, λ_4, λ_5, λ_6, and λ_7 will be detected. The FOSw selects each branch of the sensor network to be interrogated alternately. Therefore, the control signal has to be synchronized with the commercial FBG interrogation unit (SM125 by Smartec), thus, the FOSw will be in phase with the interrogator.

In the proposed setup it was arranged a 7 FBG sensors array and each end of the array was connected to the 2 outputs of the FOSw. The FBG interrogator was used to interrogate the sensor array placed 50 km away from the signal header. Although the FOSw is able to work up to 100 km, for the proposed setup, this distance was limited to ~50

km. This was because of the Rayleigh scattering and non linearities generated by the Raman amplification process which finally masked the FBGs´ signals. As it is previously explained, in order to interrogate the sensors, each branch of the FBG sensor network was connected to each output port of the 1x2 FOSw. The 0.5 W of Raman pump power was multiplexed and de-multiplexed in both extremes of the 50 km network. In this case, because of the Raman gain, the reflected interrogating signal level was high enough to saturate the receiver of the interrogator. Thus, a variable attenuator was used to attenuate the received signal at the interrogator input as depicted in figure 5.29. Finally, the FOSw control wavelength was introduced by using two extra 90:10 couplers at the extremes of the network.

In summary, seven FBG sensors were multiplexed successfully 50 km from the signal header, even, when a network failure occurs. The powered by light fiber optic switch was used for achieving a passive remote sensor system using a single fiber as transmission channel.

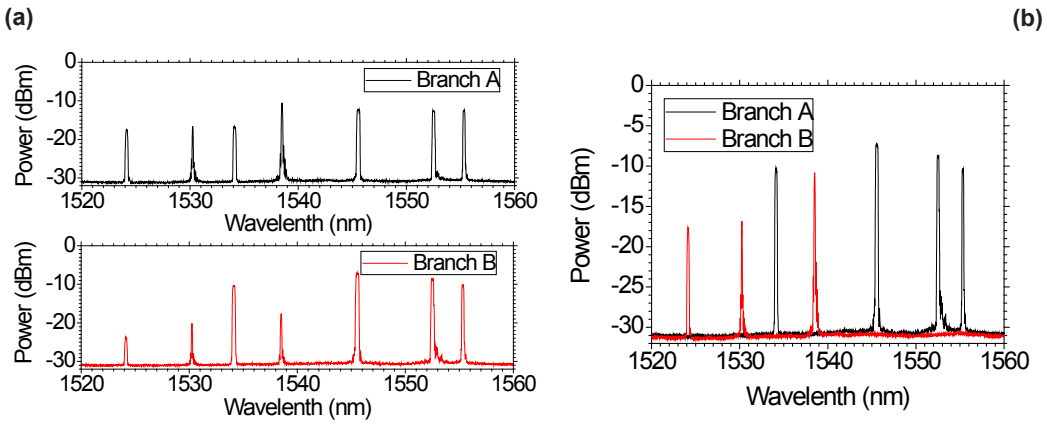

Figure 5.30. FBGs interrogated from both array´s ends.

Figure 5.30 shows the results obtained measuring each branch of the FBG network. The reflections of each branch, depending of the FOSw cycle, are shown in figure 5.30 (a). The reflected signal from each sensor had different amplitude depending on the selected output of the switch. Thus, with this structure, as it is depicted in figure 5.30 (a), the sensors array was interrogated from both branches, having double measurements corresponding to both directions. Figure 5.30 (b) shows the result obtained when a breakage occurs between $\lambda 3$ and $\lambda 4$. In this situation, the first switching cycle measures the first three sensors and in the other cycle the other four ones were measured. Thus, the full sensor network scanning time is doubled, being this its main drawback.

5.3.2. Application of the Remote Power-by-Light Switching in a Simplified BOTDA Sensor Network

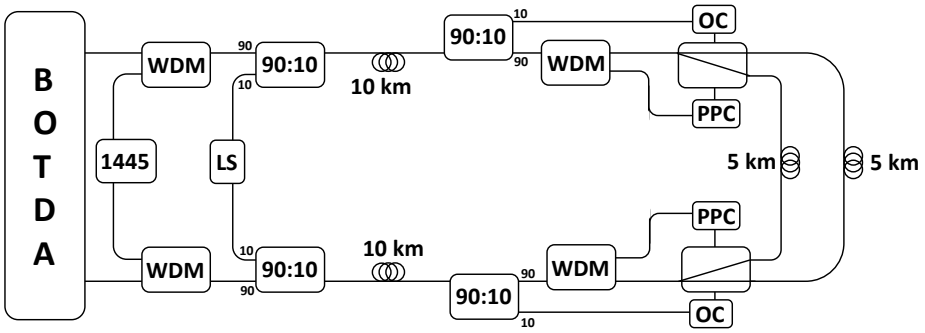

Figure 5.31. Structure of the BOTDA sensor network. WDM: wavelength division multiplexer; PPC: photoelectric cell; OC: optical control; LS: Laser Source; 1445: 1445 nm Raman pump.

The proposed sensor network is depicted in figure 5.31. It consists of a BOTDA system, previously proposed in [14], used to interrogate a 25 km long fiber channel, where the central 5 km are connected through two RFOSw, where the structures to be sensed and multiplexed are intended to be located. For controlling these switches different elements have to be added to the typical BOTDA network. The powered by light remote switches need, on one hand, a high power pump source at 1445 nm to feed both photoelectric cell that supplies the power to the switches. On the other hand, a control signal is necessary to select the output port of the switch. The 1445 nm Raman pump laser was used to feed the cell attached to the switches, and it was inserted into the network using two 1445/1550 nm WDMs. Another optical signal was introduced in the fiber lines to remotely control both switches´ positions by two 90:10 couplers. These couplers are optimized to operate in the O (1300 nm) and C (1550 nm) bands, however, they do not introduce higher loss at the 1445 nm pump wavelength. Just before the switches, both signals are subtracted. The control signals were extracted by other two 90:10. The 10% signal for controlling the switch also included a 10% portion of the Raman pump and of the Brillouin signal. Thus, this light was filtered by a circulator and FBG centered at the control signal wavelength. Before arranging the control signal, the Raman pump necessary to feed the switch is removed by other two WDMs with the same characteristics as the previous ones.

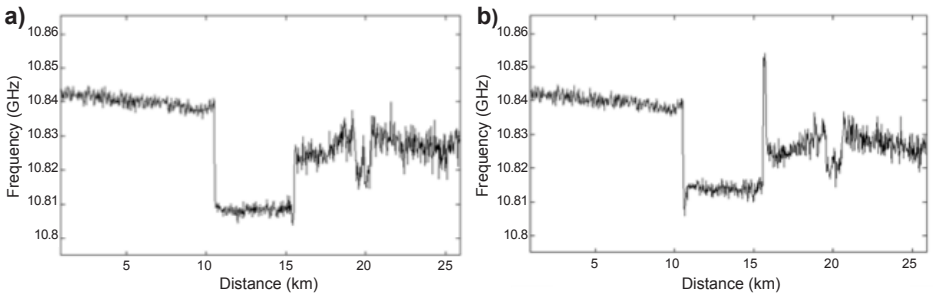

Figure 5.32. Brillouin frequency shift along the sensing channel 1 (a) and the sensing channel 2 (b).

In order to check the performance of the full sensor network, proof-of-concept experiments were carried out. 400 mW of Raman pump were launched into the fiber (200 mW on each branch) to feed up the photoelectric cells that act as a power supply for the optical switches. The Raman signal would also contribute to compensate the optical losses of the two 10 km common sections due to the induced distributed Raman gain along the fiber; however, given the deployed power, the Raman gain was negligible in the current setup. Another optical signal was needed to remotely control the switch position. A tunable laser source tuned at 1546 nm was used but, any stable light source is appropriate as long as the receiver gets at least –28 dBm at any wavelength between 1310 and 1550 nm. The power of the continuous probe wave was –8 dBm, and the power of the pump pulses was 24.4 dBm at the entrance of the network. The pulses were 20 ns long, so the measurements have 2 m as spatial resolution.

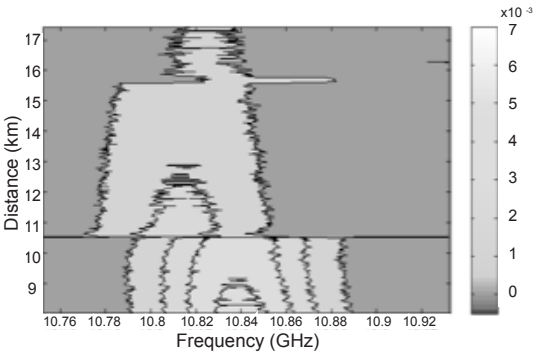

Figure 5.33. Brillouin gain spectra along the sensing channel focused on the 5 km section with 180 m heated to 60 °C.

In the section to be monitored, between the switches, 2 fiber spools of 5 km SMF were placed. At the end of one of them, 180 m of the same fiber was added. The temperature of this extra section was kept constant at 60 °C. Figure 5.32 shows the value of υ_B for each sensed branches. It is clearly distinguished the two 10 km long sections before and after the 5 km spools. Note that the second section of 10 km is the ensemble of two spools of 6 and 4 km, respectively, spliced together. Figure 5.32 (b) illustrates the results obtained for the spool to which 180 m of heated SMF was added. It is clearly visible that υ_B in this region has moved up to 10.852 GHz, 39 MHz higher than υ_B for the previous 5 km, kept at room temperature. This agrees with the well known υ_B shift ratio in SMF of 1.15 MHz/°C [15]. The difference observed between the two measurements in the 5 km section (υ_B varies from 10.808 to 10.813 MHz) is due to slight differences in the two spools, i.e., different winding tension. The measured temperature precision in the 5 km was estimated to be 2.8 °C. In Figure 5.33 the Brillouin spectra along the 5 km + 180 m section is observed. It can be seen that the Brillouin gain curve shifts to lower frequencies when entering the 5 km section from the 10 km SMF channel, and moves up in frequency for the heated 180 m long section.

5.4. FULLY-SWITCHABLE MULTI-WAVELENGTH FIBER LASER BASED INTERROGATOR SYSTEM FOR REMOTE AND VERSATILE FIBER OPTIC SENSORS MULTIPLEXING STRUCTURES

The final section of this chapter shows a sensor system structure which collects, in general terms, the philosophy and many concepts used in this PhD work. The switchable MWFL presented in the previous chapter is used for interrogating different sensor technologies in a remote network using the power by light switch proposed before. A well known FBG sensors array is interrogated sequentially and in the same monitoring cycle, a group of seven PCF intensity sensors deployed in a star structure are also monitored.

Wavelength reconfigurable laser sources for sensing purposes are a research field wherein other researches had focused their attention [16]. For example, S. Rota-Rodrigo *et al.* proposed a switchable MWFL based on Erbium-doped fiber amplifier for FBG remote sensing [17].

Figure 5.34 shows the experimental setup for a new interrogation system for fiber sensors based on a switchable laser. It is formed by two main blocks highlighted in red dotted boxes labeled as “Switchable laser source” and “Sensor network”. The switchable laser source is explained thoroughly in the previous chapter; therefore, this section is focused on explaining the whole sensor network system.

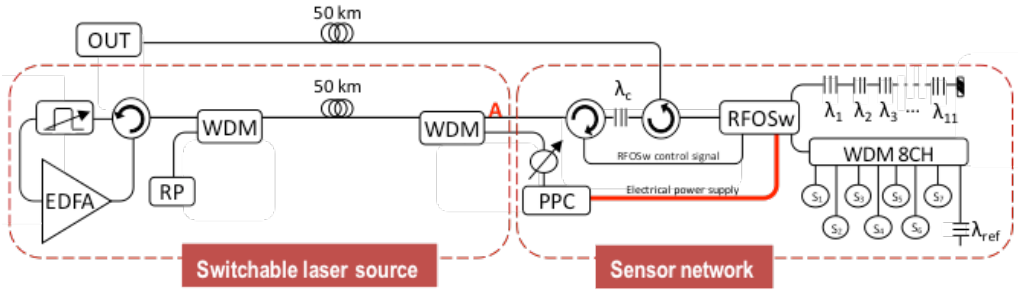

Figure 5.34. Experimental setup for the MWFL and the proof of concept sensor network.

The sensor network, shown inside the right box of figure 5.34 includes two switched sets of sensors which are based on completely different operation modes. The first group of sensors is placed into a star network and consists of 7 PCF interferometric strain sensors. The other group of sensors is the previously utilized array of 11 FBG wavelength based temperature/strain sensors.

PCF sensors are formed by connecting ~1.5 m of HiBi PCF (PM-1550-01 from NKT Photonics) into a Sagnac loop mirror structure. When the fiber is strained the achieved inter-polarization-modes interference shifts in wavelength. Thus, when a fixed wavelength illuminates the structure, it is reflected and its intensity is modulated proportionally to the interference position corresponding to the applied strain. Therefore, the 7 sensors were connected to an 8 channel WDM (from 1536.61 to 1547.72 in 200GHz ITU grid spec) and the free channel was connected to a FBG which acts as sensors' reference. The other sensor sub-network was the previously mentioned FBG array configuration connecting 11 FBG sensors in series. The FBGs are centered from 1540 to 1552 nm each 1.2 nm.

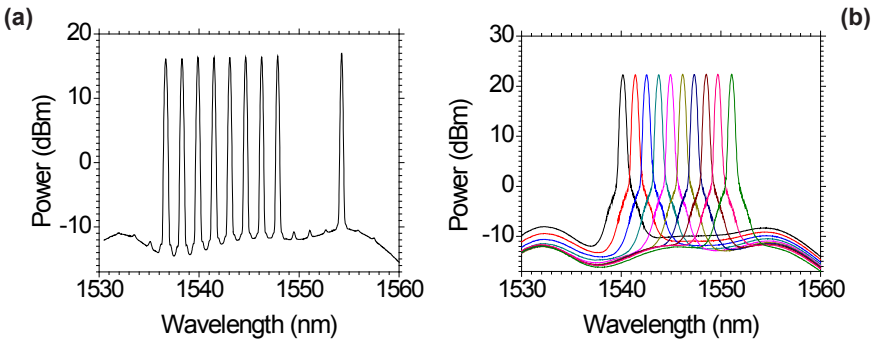

Figure 5.35. (a) MWFL configuration for interrogate the PCF intensity sensors network. (b) A composition of a wavelength sweep of a single emission line.

Both sub-networks are connected to a remote powered by light fiber optic switch (RFOSw), previously reported in section 5.3, which selects alternatively both networks depending on a channel selection signal, also labeled as "RFOSw control signal" in figure 5.34. When the signal is ON, the PCF sensor network is selected. Therefore, the versatile MWFL creates the two laser configuration needed to interrogate both sensor networks and to control the RFOSw. The laser spectrum used to interrogate the PCF sensors sub-network is depicted in figure 5.35 (a). The Raman pump excess of the random mirror structure is also used to feed this RFOSw. The RFOSw converts 125 mW of the residual Raman pump of the distributed mirror onto 35 mW of electrical power with the photovoltaic power converter (PCC) already presented. The residual Raman pump is collected from the distributed mirror by a 1445/1550 WDM and attenuated because it is too high and can damage the PPC.

The 8 emission lines which correspond with the 8 WDM channels and the control signal on the right (@1554.13 nm) are shown in figure 5.35 (a). When the control signal is OFF, FBG sensors channel is selected. In this mode, the laser structure works as a wavelength sweep laser with 0.1 nm resolution. Figure 5.35 (b) illustrates 11 emission lines which correspond with the 11 FBG sensors. Through the 1550 port (A) the MWFL laser result is launched. The control signal, only for the PCF sensors case, is filtered and redirected to the RFOSw by the first circulator of the sensors network and it is selected using a FBG centered at its wavelength. The following second circulator has the objective of illuminating the RFOSw and collecting the sensor information towards the system output port placed after 50 km fiber at the signal header.

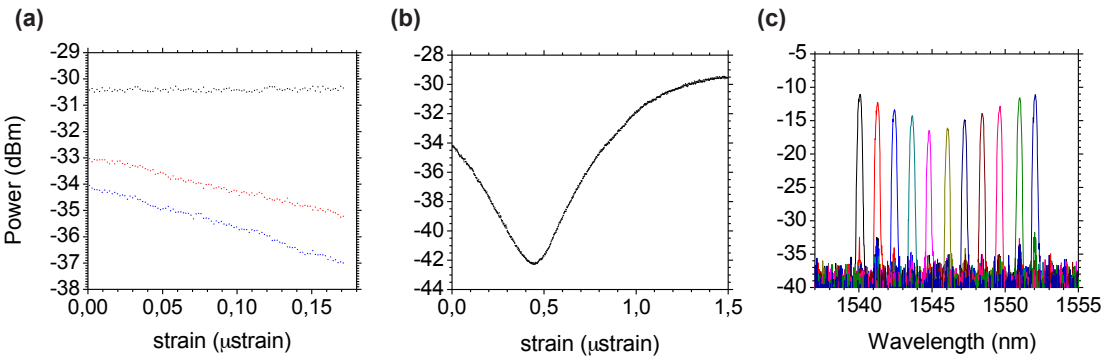

Figure 5.36. (a) Second and fifth PCF strain sensors characterization while the first sensor is non stressed. (b) Full range strain characterization of the seventh sensor until breackage and (c) spectral composition of the FBG sensors network result.

Figure 5.36 shows both sensors networks characterization. Figure 5.36 (a) depicts an example of 2 intensity sensors behavior when the first sensor is not strained. These results confirm the good multiplexing network performance and crosstalk free operation. It was also tested the fiber breakage point. Figure 5.36 (b) shows the sensor response until the fiber was broken. It is visible the interference pattern of the Sagnac structure in this full measurement range. The measurements were focused on the 2000 μstrain linear zone before the interference valley. Finally, figure 5.36 (c) illustrates the FBGs network response reconstruction after the laser sweep. It is a multi-plot composition of the reflected wavelengths obtained from each FBG sensor.

5.5. CONCLUSIONS

This chapter was devoted to the development of new sensors multiplexing networks using sensors and laser sources previously shown in chapters 2, 3 and 4. With these sensors (point and distributed) and light sources, several demanding topics in sensors multiplexing have been explored. Particularly, PCF sensors multiplexing, remote multiplexing networks and robust multiplexing of point and distributed sensors, among another topics.

Some technologies limitations were also overcome. Summarizing the multiplexing networks in order of appearance, they were:

- A TDM architecture for remote multiplexing of intensity sensors based on bendings, developed by delaying 4 different optical paths 4 sensors were placed inside the network and an in deep study of the wavelength macro-bending influence was performed. This study confirmed the feasibility of remote TDM multiplexing of intensity sensors, taking into account problems such as dispersion and crosstalk.

- One of the main issues that this PhD work has addressed is the problem of PCF sensors multiplexing. Here it was proposed, first of all, a fiber optic laser system based in a ladder structure which multiplexed six PCF sensors by referencing them in wavelength. Thus, a 75 km long remote sensor network was developed, keeping the previously reported sensor´s performance. It was also studied the impact of the filter width on the output power, that was carried out in order to reach the most efficient system operation.

- OADMs have been demonstrated as suitable devices for WDM addressing of

different kind of sensors. The already used PCF interferometer sensors were remotely multiplexed without optical amplification using two different strategies. The last one, based on a two-fiber network allowed us to perform measurements up to 100 km. The system incorporated also a reference wavelength used to increase the resolution of the system.

• When optical amplification is used in multiplexing networks, longer remote multiplexing systems can be carried out. Two new ultra long multiplexing systems based on multi-wavelength lasing structures were presented. The novelty of the proposed systems lies in the topologies which entail attractive advantages such as reducing the effect of Rayleigh scattering and other limiting factors. It was demonstrated that they were able to multiplex up to 11 fiber Bragg gratings, but this number could be increased. Finally, due to the operation mode of the systems, they act as low noise configurations, where the OSNR of all the sensors was high enough to interrogate them up to 200 km away from the monitoring station.

• In order to add robustness and versatility to fiber optic sensor networks, a remote fiber optic switch which it is able to operate at distances up to 100 km was also developed. To the best of the author's knowledge, this is the maximum distance ever achieved when controlling any instrumentation powered by light. This FOSw can be controlled by a digital signal generator or by an automatic signal generator, which frequency could be tuned between 1 Hz to 0.05 Hz. Additionally, a fiber optic channel has been introduced into the system for controlling the FOSw using a binary optical signal. This is our control circuit proposal, but this remote FOSw allows the use of other control techniques As proof of concept applications, this PhD work experimentally demonstrated the suitability of this FOSw for controlling a resilient FBG sensors network located 50 km away from the interrogation unit and for Brillouin distributed sensing networks multiplexing.

• Finally, a versatile network structure based on the MWFL presented in section 4.5.1 was demonstrated for simultaneous multiplexing of different nature sensors. Two multiplexing sensors networks were simultaneously interrogated using the remote powered by light fiber optic switch. A sensor sub-network was interrogated using a multiwavelength emission of the laser, and the other one, by sweeping the emitted wavelength of the same laser. The Raman pump power excess of the random mirror of the laser was also used to feed the RFOSw. This technique can multiplex as many sensors networks as output

ports the switch have. Furthermore, as the control signal was generated by the fully switchable MWFL, the laser spectrum change also entails the RFOSw port selection.

All this chapter results have originated the publications in references [18-28]

5.6. REFERENCES

[1] K. T. V. Grattan and T. Sun, "Fiber optic sensor technology: an overview," Sensors and Actuators A-Physical, 82, 40-61, (2000)

[2] F. Sienkiewicz, A. Shukla "A simple fiber-optic sensor for use over a large displacement range" Optics and Lasers in Engineering, 28, 293–304, (1997)

[3] H. Renner "Bending Losses of Coated Single-Mode Fibers: A Simple approach" Journal of Lightwave Technology, 10, 544-551, (1992)

[4] D. S. Nyce, "Linear position sensor. Theory and Application" Ed. Wiley & Sons, 2004

[5] R. A. Perez-Herrera, M. Lopez-Amo, "Fiber optic sensor networks", Optical Fiber Technology, 19, 689-699 (2013)

[6] M. Fernandez-Vallejo, S. Rota-Rodriguez, and M. Lopez-Amo, "Remote (250 Km) fiber Bragg grating multiplexing system" Sensors, 11, 8711-8720 (2011)

[7] R. A. Perez-Herrera, D. Leandro, P. Urquhart, M. Schlüter and M. López-Amo, Resilient optical fiber ladder network with OADMs to multiplex sensors: experimental validation of binary state connectivity analysis, Proc. SPIE 22nd OFS, 8421, 84218C-1-4, (2012)

[8] H. M. Cao, Q. L. Xie, An optical fiber displacement sensor based on RBF neural network, Proceedings - 3rd International Conference on Measuring Technology and Mechatronics Automation, ICMTMA 2011 1 , art. no. 5720815, 443-446, (2011)

[9] R. Peña, C. Algora, I. R. Matias and M. López-Amo "Fiber-based 205-mW (27% efficiency) power-delivery system for an all-fiber network with optoelectronic sensor units" Applied Optics, 38, 2463-2466 (1999)

[10] O. Ogawa "A new multi-point sensing system based on optical pass switching and remote optical power supply" 21st International Conference on Optical Fiber Sensors, Proc. of SPIE., 7753, 775332, (2011)

[11] M. Fernández-Vallejo, R. A. Perez-Herrera, C. Elosua, S. Diaz, P. Urquhart, C. Bariáin and M. Lopez-Amo "Resilient Amplified Double-Ring Optical Networks to Multiplex Optical Fiber Sensors", Journal of Lightwave Technology, 27, 1301-1306, (2009)

[12] C. H. Yeh, C. W. Chow, P. C. Wu and F. G. Tseng, "A Simple Fiber Bragg Grating based Sensor Network Architecture with Self-Protecting and Monitoring Functions" Sensors, 11, 1375-1382, (2011)

[13] P. C. Peng, J. B. Wang and K. Y. Huang, "Reliable Fiber Sensor System with Star-Ring-Bus Architecture", Sensors, 10, 4194-4205, (2010)

[14] A. Zornoza, A. Loayssa, "Low cost Brillouin optical time domain analysis (BOTDA) distributed sensor setup", Proc. SPIE, 7653, 765334, (2010)

[15] J. M. Lopez-Higuera, "Handbook of Optical Fibre Sensing Technology", Ed. Wiley & Sons: Chichester, UK, (2002)

[16] R. A. Perez-Herrera, M. Fernandez-Vallejo, S. Diaz, M. A. Quintela, M. Lopez-Amo and J. M. Lopez-Higuera, "Stability comparison of two quadruple-wavelength switchable erbium-doped fiber lasers", Optical Fiber Tech., 16, (2010)

[17] S. Rota-Rodrigo, L Rodriguez-Cobo, M. A. Quintela, J. M. Lopez-Higuera, and Lopez-Amo, "Switchable fiber optic laser system for high and low-strain fiber optic sensors remote multiplexing", Proc. SPIE 5th EWOFS, 8794-47 (2013)

[18] M. Bravo and M. Lopez-Amo, "Remote-Time Division Multiplexing of Bending Sensors Using a Broadband Light Source", Journal of Sensors, 2012, 154586, 6pp (2012)

[19] M. Bravo, M. Fernández-Vallejo, M. Echapare, M. López-Amo, J. Kobelke, and K. Schuster, "Multiplexing of six micro-displacement suspended-core Sagnac interferometer sensors with a Raman-Erbium fiber laser", Optics Express, 21, 2971-2977 (2013)

[20] M. Bravo, A. Candiani, A. Cucinotta, S. Selleri, M. Lopez-Amo, J. Kobelke and K. Schuster, "Remote PCF-based sensors multiplexing by using optical add-drop multiplexers" Optics & Laser Technology, 57, 9-11 (2014)

[21] M. Bravo; M. Fernandez-Vallejo; M. Lopez-Amo; J. Kobelke; K. Schuster, "Fiber optic sensor networks based on OADM devices with a bus configuration", Proc. SPIE, 5th EWOFS, 8794, 87943V (2013)

[22] M. Fernandez-Vallejo, M. Bravo, and M. Lopez-Amo, "200-km long fiber ring laser for multiplexing fiber Bragg gratings array," Proc. SPIE, 22nd OFS conference, 8421, 84218J, 1–4, (2012)

[23] M. Fernandez-Vallejo, M. Bravo, and M. Lopez-Amo, "Ultra-Long Laser Systems for Remote Fiber Bragg-Gratings Arrays Interrogation", IEEE Photonics Technology Letters, 25, 14, 1362-1364 (2013)

[24] M. Bravo, M. A. Erro, J. M. Algueta, S. Diaz and M. Lopez-Amo, "Remote resilient FBG multiplexing network controlled by a powered by light fiber optic switch" Proc. SPIE, 22nd OFS, 8421, 84218F (2012)

[25] M. Bravo, M. A. Erro, J. M. Algueta, S. Diaz and M .Lopez-Amo, "Remote fiber optic switch powered by light for robust interrogation of fiber Bragg grating sensor networks", Meas. Science and Technology, 24, 94021 (2013)

[26] A Ullán, M. Bravo, A. Zornoza, A.Loayssa, M. Lopez-Amo, J.M. Lopez-Higuera, " BOTDA sensor network with power by light remote switching", Proc. SPIE, 22nd OFS conference, 8421, 84218E, 1–4, (2012)

[27] M. Bravo, A Ullán, A. Zornoza, A.Loayssa, M. Lopez-Amo, J.M. Lopez-Higuera, "Application of Remote Power-by-Light Switching in a Simplified BOTDA Sensor Network" Sensors, 13, 17434-17444 (2013)

[28] M. Bravo, V. DeMiguel-Soto, A. Ortigosa and M. Lopez-Amo, "Fully switchable multi-wavelength fiber laser based interrogator system for remote and versatile fiber optic sensors multiplexing structures" Proc. SPIE, 23rd OFS conference, 9157, 91576P (2014)

chapter VI
THREE APPLICATIONS OF FIBER OPTIC SENSORS IN SHM

INTRODUCTION

The development of the "smart cities" desired for the future requires creating "smart infrastructures" that, hopefully, we will enjoy, having enhanced safety systems, lower operations costs and minimized deleterious environmental effects. What makes unique the society's infrastructures such as buildings, roads and rail tracks, tunnels and bridges from current forms of civil constructions, is that when they fail unexpectedly they do not cause a huge economic disruption, or worse still, personal damages. That means to prevent and to solve degradation in buildings and civil constructions, or to avoid problems with the distribution of goods such as raw materials and fuel, the delivery of goods for commerce, the transportation of people to their place of work, or the transportation of emergency services to places in need of assistance.

University, research centers and spin-off companies offer different commercial products for fiber optic sensing using different kind of sensors. FBG technology is one of the most extended technologies that are commercially available. Distributed sensing field is also an attractive solution for large civil structures monitoring where some companies present different commercial products. [1-5]

During the lasts years, a number of improvements has been carried out in the fiber optic sensor field, showing in laboratories the great potential of this technology as an interface between the environment and the human modern applications as structural health monitoring (SHM), smart structures, biotechnology and others [6]. But it is also important to perform in-field tests to demonstrate the potential of the laboratory prototypes in real applications. Thus, this chapter is devoted to the testing of three different fiber optic sensor systems in real structures.

6.1. CONCRETE BEAM BENDING TEST MONITORING USING A HIGH STRAIN FIBER OPTIC SENSOR

This chapter is opened by a concrete beam bending test monitored by the high strain fiber optic bending sensor previously presented in chapter 5.1.1. This test has been monitored simultaneously using FBG sensors and the "eight-shape" intensity sensor. The sensors were interrogated during all the experiment process by a fiber Bragg grating interrogator and the OTDR.

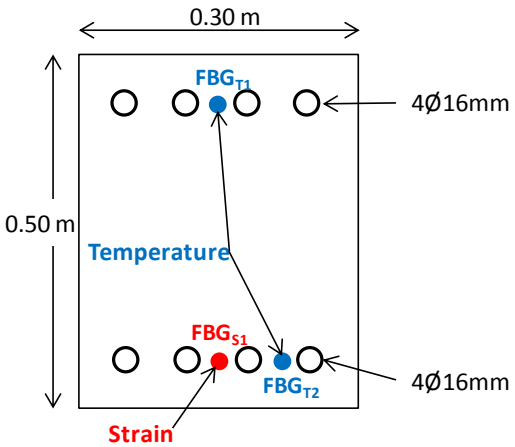

Figure 6.1. Beam transversal section showing the embedded FBG sensors distribution. Sensors are labeled as FBG for temperature sensors and FBG$_{S1}$ for the FBG strain sensor. 4Ø16mm: 4 steel beams of 16mm of diameter).

The concrete beam designed for the bending test was made for a HA25/P/20/2B concrete (Spanish normative). This is a reinforced concrete with 25Nw/mm^2 of plastic consistency, 20 mm of maximum gravel size and designed for normal external weather conditions. The beam reinforcement was made by 8 steel bars (rebar) of 16 mm diameter placed as shown in figure 6.1. The beam dimensions were 6 m length, 0.5 m height and 0.3 m width. The bending test consisted of a four point test. This means that the beam was placed on a testing bench fixed on two points and the load was applied at another two points to achieve a uniform bending moment in the center of the beam. Therefore, the tensile stress was suffered at the bottom and the compressive stress at the top of the beam. These areas of the beam are considered ideal for testing and, therefore, for the overall test purposes [7].

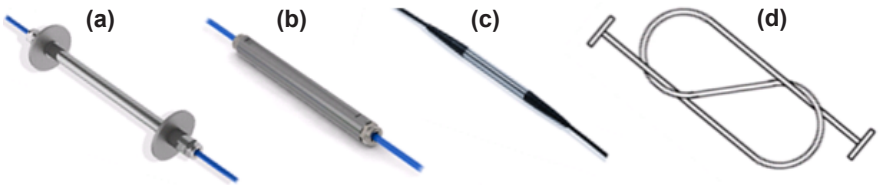

Figure 6.2. Strain and temperature FBG sensors from Fiber Sensing and the "eight-shape" sensor.

In order to demonstrate the suitability and strain limitations of different sensors, this experiment was designed to collect the data from the selected sensors in order to verify the behavior and measurement ranges of these sensors in concrete structures. Figure 6.2 illustrates the sensors which were used in the concrete beam bending test (FBG sensors pictures courtesy of FiberSensing™ - Sistemas Avançados de Monitorização, S.A [1]). They consist of one embedded FBG strain sensor (figure 6.2 (a)), one embedded temperature sensor (figure 6.2 (b)), two surface temperature sensors (figure 6.2 (c)) and the "eight-shape" strain sensor (figure 6.2 (d)). FBG based sensors were interrogated by the SM125 interrogation unit from Micron Optics, Inc. and the "eight-shape" strain sensor was interrogated by the EXFO OTDR unit.

Figure 6.3 High strain sensor setup used along the bending test.

Figure 6.3 presents the setup used to interrogate the "eight-shape" sensor. In this case the OTDR is only used for the measurements of the 1200 m section of single mode fiber SMF28 with the "eight-shape" sensor located at 200 m from the OTDR.

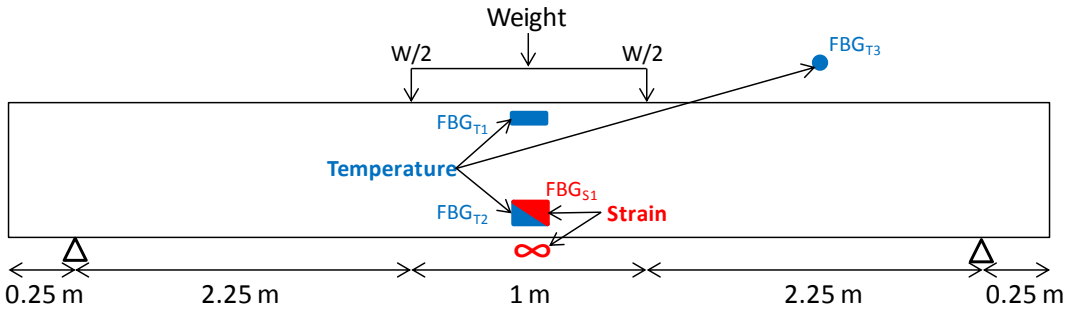

Figure 6.4 Beam longitudinal view with the sensors distribution and the bending test configuration setup. FBG sensors are labeled as FBG$_{T1, T2, T3}$ for temperature sensors and FBG$_{S1}$ for the FBG strain sensor.

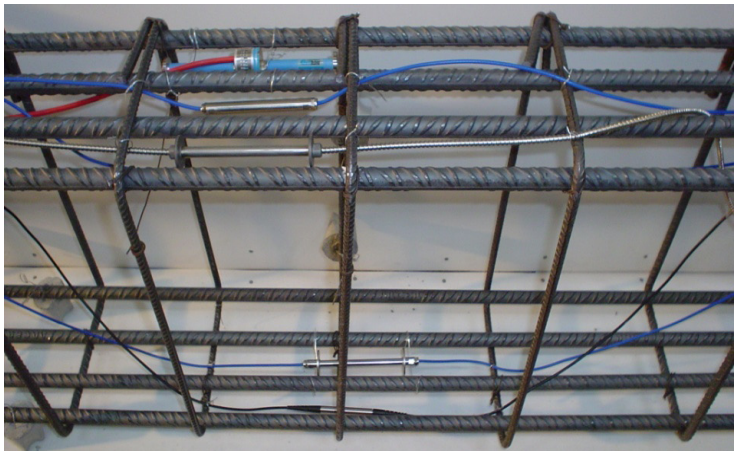

Figure 6.5 Picture of the sensors already installed just before the concrete pouring.

The embedded FBG sensors were installed in the concrete beam before the pouring, as it is illustrated in figure 6.5. It is visible that the sensors were installed with the help of the rebar armor using steel wire. On the other hand, the "eight-shape" sensor was installed just before the bending test. Figure 6.1 shows the beam transversal section also illustrating the sensor distribution. An external temperature FBG sensor was operative during all the experiment. Figure 6.4 shows the sensors distribution and the different beam dimensions. Figure 6.4 also illustrates the four point bending test set-up. The triangles at the bottom of the beam depict the beam support points and the arrows in the top of the picture indicate the points where the load is applied (shown as W/2).

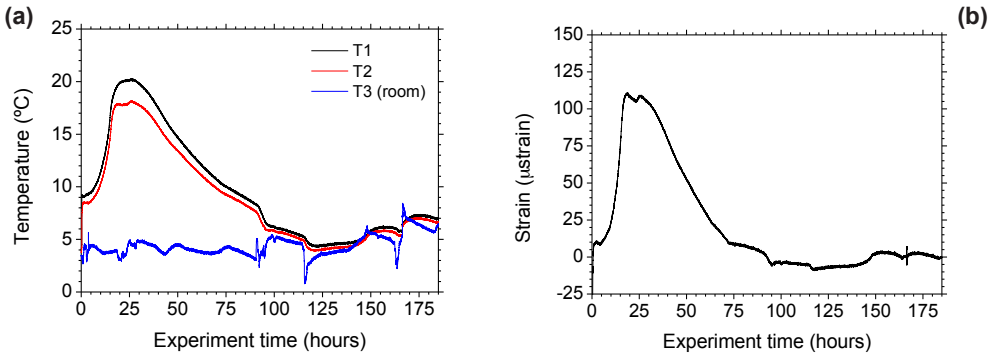

Figure 6.6. Temperature (a) and strain (b) FBG embebed sensors ($FBG_{T1,T2,T3}$ and FBG_{S1}) response during the concrete curing procces.

Figure 6.6 depicts the sensors` response during the first week of experiment. Figure 6.6 (a) shows the temperature response of the two internal sensors and the room temperature. During the first four days, the temperature difference between the room temperature and the embedded sensors was high due to the pouring process of the concrete. It is observable the well known inner temperature increment when the chemical process during the curing occurs [8]. Because the experiment was performed in winter and the ambient temperature was quite low, the maximum temperature reached by the beam was lower than the expected. The curing process can reach temperatures above 50 ºC, depending on the concrete volume and the room temperature. After this period, the beam internal temperature showed a good correlation with the room temperature. Nevertheless, when an abrupt room temperature change occurred, because the door was opened, for example; the internal temperature change was softer due to the material inertia.

Concerning the FBG strain sensor, in figure 6.6 (b) sensor`s response is presented. In order to have the more accurate result, the measurement was compensated using the data from the closest FBG temperature sensor installed. It is discernible an internal structural modification of the concrete during the curing process.

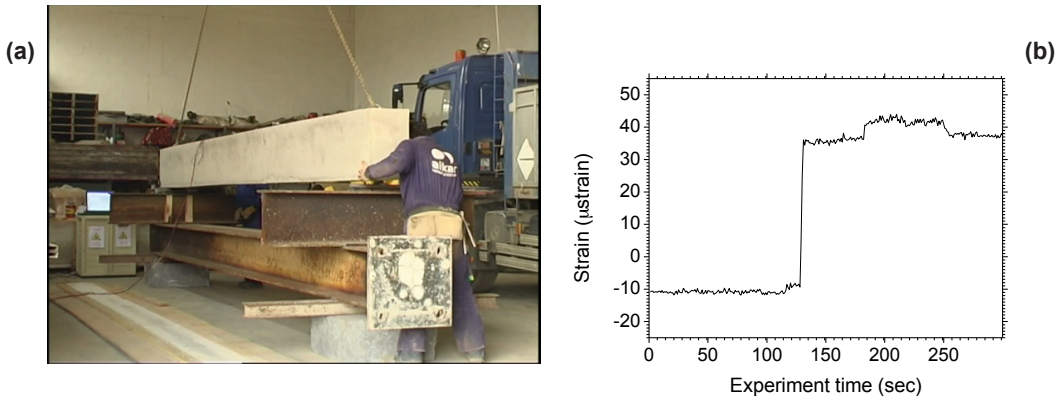

Figure 6.7. Picture (a) and strain sensor measurements (b) obtained during the beam lifting process.

Another step in the procedure was the beam lifting to the test bench. During this process sensors were measuring, obtaining the results depicted in figure 6.7. Figure 6.7 (a) is a picture when the beam was almost placed in its final position before the bending test. When the beam was lifted an abrupt tensile stress at the beam bottom was measured by the strain sensor, as figure 6.7 (b) illustrates. Once the beam was placed, a subsequent correction of the position was performed and it was also detected by the sensor.

Table 6.1: Applied load, deformation and events during the test

Load (kg)	FBG strain (micro-strain)	Event	Load (kg)	FBG strain (micro-strain)	Event
500	46,79		8000	1723,89	
1000	59,81		9000	1907,98	
1500	77,77		10000	2050,90	
2000	103,01		11000	2196,63	
2500	153,21		12000	2334,25	
2750	229,14		13000	2430,90	
3000	281,03		14000	2550,53	
3500	341,20		15000	2675,40	
4000	772,94		16000	2922,86	
4500	979,34	Crack	17000	3153,41	Beam breakage
5000	1105,22		17000	3320,06	Steel plastic deformation
6000	1315,94		17000	3890,07	FBG breakage
7000	1533,97				

After all sensors were installed, the beam was placed in the test bench and was prepared for the bending test, different weights were applied in the middle of the concrete beam. As Table 6.1 indicates, initially, 500 kilograms steps were applied from the beginning to the detection of the first crack on the surface of the beam. The crack was detected when applying a weight of ~4500 kilograms. After this first crack, weight increments of 1000 kilograms were applied until the breakage of the beam. At this point the steel came at a state of plastic deformation which indicates that the beam did not withstand more load. We introduced more deformation until the final breakage of the FBG itself. Figure 6.8 shows pictures taken of the pole structure before and after the bending test, respectively.

Figure 6.8. Pre and Post bending test beam pictures.

Both, concrete embedded FBG and "eight-shape" sensors were collecting data of the concrete beam behavior during the entire bending test. The plots in figure 6.9 show the strain measurements as a function of time and the weight applied to the beam, respectively. The FBG strain vs. time trace is visible during all the events in the bending test: the cracking point, all the weight steps and when the FBG broke. The FBG measurement range was overcome by about 1000 micro-strain above the company specifications. FBG pre-break measurements that exceeded this range cannot be considered as reliable. In both plots, OTDR-"eight-shape" strain sensor results are also shown.

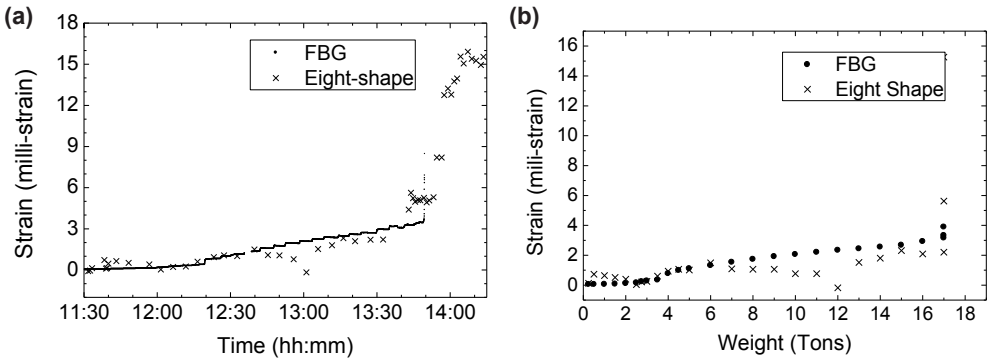

Figure 6.9. Measured strain by the inner FBG and the "eight-shape" sensor during the bending test (a) and measured strain by the inner FBG and the "eight-shape" sensor versus the applied weight (b).

These "eight-shape" sensor results adjust correctly to the more accurate FBG results. We would like to remark that the low cost "eight-shape" sensor has a higher measurement range than the utilized FBG. The figure 6.9 (a) plot shows two different events, the cracking point at 12:15h-4000 kg, and the failure point at 13:50h-17000 kg. The strain measurement at failure is significantly high. This strain increment, due to the overstrained steel, was measured only by the "eight-shape" sensor. Its measuring range was three times higher than FBGs one. After 1 hour and 30 minutes and when a weight of 12000 Kg was applied (see figure 6.9 (a) and (b)), some deviating points are shown in the graphic, due to cladding-modes coupling previously studied in chapter 5.1.1.

6.2. FIBER OPTIC SENSORS FOR CORROSION MONITORING IN CONCRETE REINFORCED STEEL BARS.

In this section a corrosion sensing approach for reinforced concrete structures based on highly birefringent (Hi-Bi) fibers combined with a fiber loop mirror is studied. This sensor instrumented on the re-bar of a concrete beam was fully calibrated on a laboratory pressure bench before being set inside concrete for an accelerated corrosion test.

The experimental setup, as shown in Figure 6.10, comprises of a fiber loop structure with a length of Hi-Bi fiber acting as a pressure sensor. When a transverse force, for example, induced by the rust forming process, is applied on the sensor, it causes a shift in the interference pattern generated using this technique [9]. In order to align the sensor appropriately onto the re-bar, and to calibrate the sensor, a specialized fiber alignment bench was set up. In this work, two different types of fibers were tested and their

performance was cross-compared. To ensure the sensor to be robust enough to survive the harsh working conditions during the whole test process, the sensors were protected by a suitable heat-shrink sleeve.

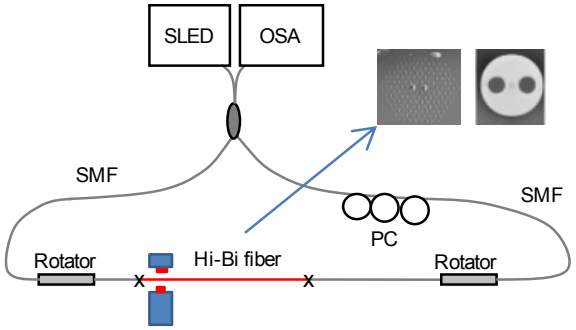

Figure 6.10. Schematic diagram of the fiber loop structure sensor. Both, PANDA and HiBi PCF are depicted inset.

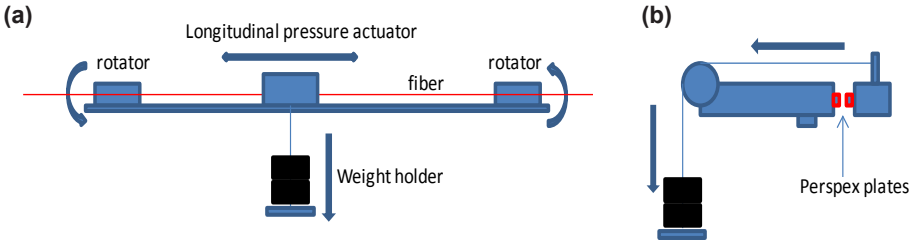

Figure 6.11. Schematic setup of the utilized fibre pressure test bench a) Front and b) lateral view of the mobile platform of the bench test.

It has already been demonstrated in [10] that the transversal force sensitivity of Hi-Bi fibers is directly dependent on the angle of the applied force. Therefore, the correct alignment of the fiber before it is installed onto the rebar is critical. In this work, a pressure bench was set up specifically to ensure the correct alignment of the fibers. As shown in Figure 6.11 (a), the bench includes two rotators which act as fiber holders and a longitudinal pressure actuator. The longitudinal pressure actuator is formed by a longitudinal mobile platform, incorporating two 1 cm^2 Perspex plates as contact surfaces (red squares in Figure 6.11 (b)), with one being fixed and the other connected to a pulley onto which different weights are added to control the applied force/pressure.

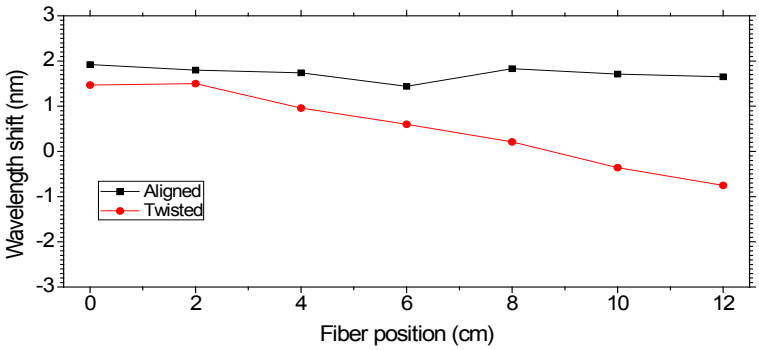

Figure 6.12. Obtained data during the sensor alignment process. The lower graph indicates the results obtained from a twisted fibre, showing the force sensitivity decreasing along the length of the fibre whilst the upper graph shows a significantly improved and uniform sensitivity as a function of fibre length due to the improvement in fibre alignment.

Figure 6.12 shows the wavelength shift caused in the interference output pattern of the PANDA fiber when a force of 5 N was exerted at discrete locations. If the fiber was twisted, for the same applied force, the wavelength shift varied from positive to negative values (red trace) depending on the position of the applied force. This unwanted behavior can be corrected by using the rotators. Thus, a much improved and uniform sensitivity (black trace) was achieved due to the enhanced alignment process. After the completion of the fiber alignment, the fiber was carefully glued onto the rebar.

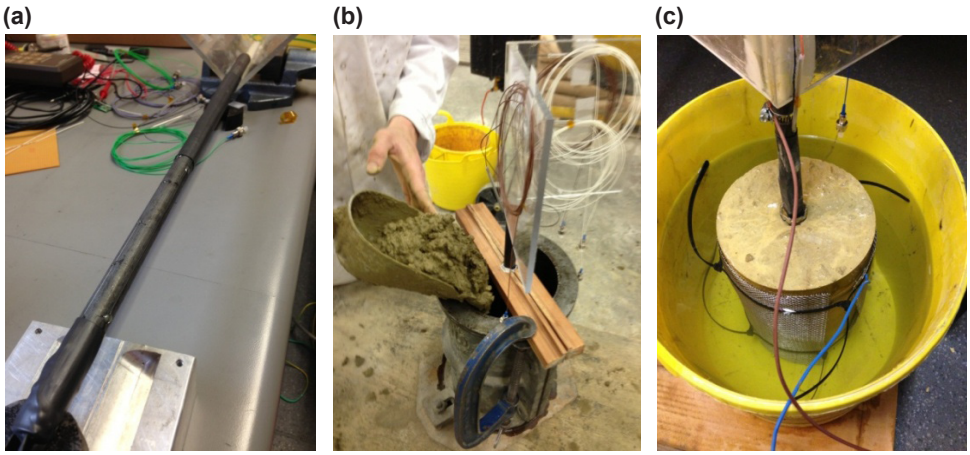

Figure 6.13. (a) Instrumented rebar prepared for the concrete sample; (b) the instrumented re-bar cast inside concrete. (c) Instrumented concrete cylinder prepared for the accelerated corrosion test.

For the accelerated corrosion tests, two concrete cylinders were prepared, each of them having an instrumented rebar. Figure 6.13 shows the sample preparation process, with the rebars being instrumented with sensors as shown in Figure 6.13 (a) before being casted inside concrete with a standard concrete mix proportion of 1:2:2.25 (cement:sand:gravel) as shown in Figure 6.13 (b). Two different cylinders, one of them shown in Figure 6.13 (c), were prepared. One of them was instrumented using a standard PANDA fiber sensor. The other cylinder used two highly birefringent photonic crystal fibers (HiBi-PCF 070107 developed by UMCS), called PCF1 and PCF2, that were positioned and protected on opposite extremes. The sensor characterization was divided into two phases: temperature logging for studying the temperature sensitivity of the fibers and pressure monitoring during the accelerated corrosion test.

Corrosion of steel in concrete may take months to start, even if it is accelerated in the laboratory by exposing the steel to either CO_2 or chloride. As corrosion is an electrochemical reaction, electrical methods can be used to accelerate the corrosion process [11]. This can be achieved in the laboratory by immersing a concrete-steel specimen in a solution of NaCl and connecting it to a current source. The positive terminal of the current source is connected to the rebar (anode) and the negative terminal is connected to a stainless steel mesh (cathode) as Figure 6.13 (c) illustrates.

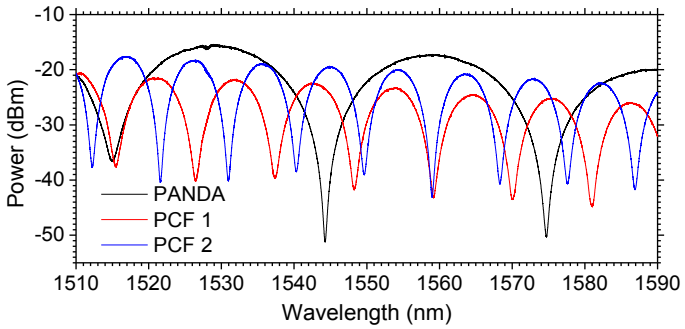

Figure 6.14. a) Interference patterns from different sensors.

Figure 6.14 depicts three interference patterns observed when the sensors are interrogated using a commercial FBG interrogator unit (Micron Optics SM125). Figure 6.15 demonstrates the temperature insensitivity of the PCF fiber whilst the PANDA fiber shows a considerable variation in response to a small room temperature variation. Room temperature was measured by a thermocouple electrical temperature sensor and a PC controlled data-logger.

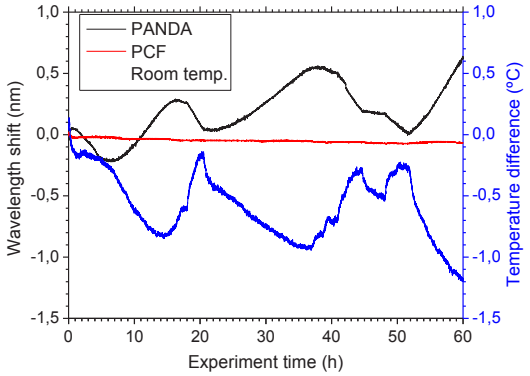

Figure 6.15. Sensor response to room temperature variation.

The accelerated corrosion test involves three stages. The first stage consisted of connecting the current after the concrete sample was immersed in fresh water. The second was a stationary state with no current being added to the rebar. At the final stage, the sample was immersed in salted water (a salt proportion of 5% with respect to the used cement) with the current being switched on.

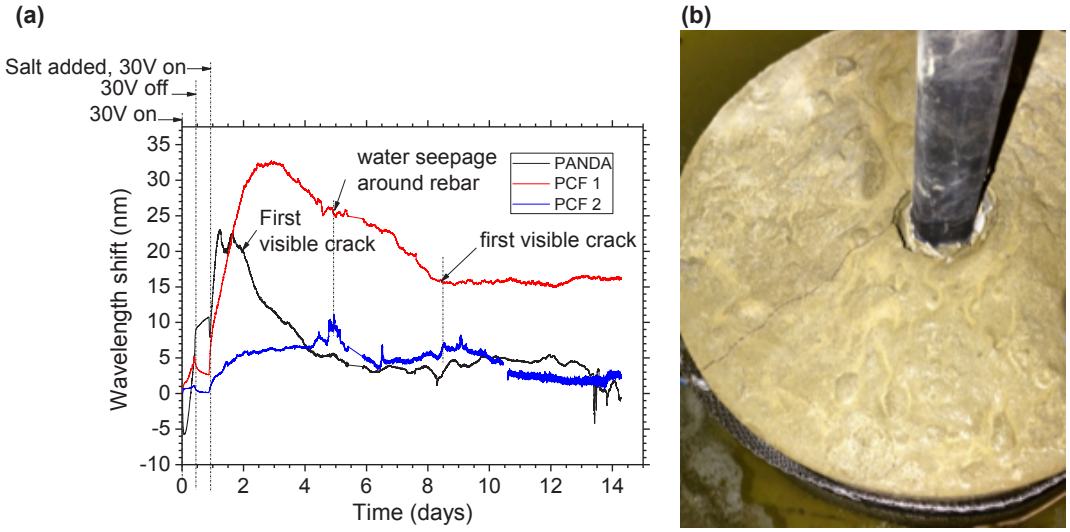

Figure 6.16. (a) The sensor data captured during the accelerated corrosion test and (b) picture of a cracked sample.

These three consecutive stages are clearly indicated in Figure 6.16 with three different curves representing the three sensors tested. At the start of the experiment all the sensors have shown an upward trend, showing the PANDA fiber sensor a more abrupt change, possibly due to its additional response to temperature variation when electrical current is added to the rebar. During the experiments, visual monitoring of the sample conditions was frequently carried out. In figure 6.16 (a), these features are labeled on the data plots, being cracking considered as the most significant event.

For the PANDA fiber, the first visible crack is marked by an arrow in the black plot. As expected, a decrease in pressure was observed when the first crack appeared (corresponding to a release in pressure between the concrete and the rebar). Although not many visible cracks appeared during the experiment, it was found that a sudden decrease in peak shifts (corresponding to the pressure release from internal failure of the concrete. Figure 6.16 (b) shows a big crack related to the one marked in the PANDA data curve. During the whole process, considerable differences in peak shifts were evident between PCF1 and PCF2 sensors. The installation, the concrete curing/compaction and other factors can affect the response of the sensors, but red trace results demonstrate the high sensitivity of the Hi-Bi PCF based sensors when protected with heat shrink tube in comparison with the PANDA fiber.

6.3. PRELIMINARY RESULTS ON TRAFFIC MONITORING ON ASPHALT PAVEMENT STRUCTURES USING FIBER OPTIC SENSORS.

Understanding the behavior of asphalt can result in optimized structures designs, thus reducing the rehabilitation costs associated with premature failures or with the long term conservation of roads. Although typical maintenance works of asphalt are focused in the superficial layer, fatigue in the deeper layers produces a continuous deterioration of the whole asphalt platform which entails permanent damages [12].

The principal responsible for the roads deterioration are certainly the overloaded vehicles. Therefore, an overload control system is extremely attractive for the organizations in charge of the roads' maintenance. The concept of Weigh-In-Motion (WIM) was introduced more than fifty years ago. WIM is the process by which the static weights of vehicles are determined by measuring wheel loads while the vehicles are in motion. There are several advantages of weighing vehicles while they are in motion rather than at rest [13]. These include savings in time and cost, and that they are safer to operate on busy roads. These systems have been used generally by public agencies for collecting vehicle weights as well as several other statistical traffic data, to aid in the pavement cons-

truction, maintenance, highway safety assessment and improvement, and other several transportation and highway related planning and design [14].

The last experiment of this chapter presents preliminary results obtained in the installation process and sensitivity test of the fiber optic when it is embedded in asphalt for monitoring traffic, structure degradation and detection of overloaded vehicles.

The experiment consisted of installing standard fiber for sensing using different protections. We also checked different installation methods to optimize fibers´ sensitivity when they are monitored by the distributed sensing system OBR 4600 by Luna, Inc.

Figure 6.17. Pictures of the fibers installation in asphalt. (a) and (b) are pictures of the groove opening and (c) is how the fiber is placed in the trench before protecting it.

Two different fiber cables were used. On the one hand, bare SMF28 fiber with the classical acrylate coating and, on the other hand, a cable of SMF28 fiber with a special glass fiber reinforced coating for direct installation in asphalt. The bare fiber was installed by two protecting methods in between the asphalt layers. The first method consisted of creating a groove in the asphalt layer surface to place the fiber into it and protected with an epoxy resin especially designed for asphalt applications. The other protection method was based on covering the fiber with tar instead resin when was placed also into the groove in order to achieve a more homogenous medium for the fiber. Tar is one of the raw materials of asphalt and it is considerably cheaper than the utilized special resin. Therefore, it is an interesting protection method to be tested.

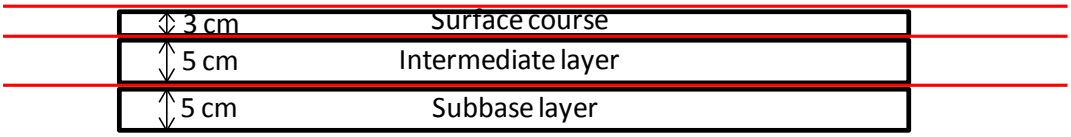

Figure 6.18. Schematical layer distribution of the asphalt platform built for the test. Lines in red correspond to the fiber distribution

An asphalt pavement platform of ~5 m^2 based on a basic three layer structure was built for the sensitivity test. The layer height configuration was composed of a sub-base and intermediate layer of 5 cm and 3 cm of surface course (figure 6.18). Therefore, in each layer three distributed fiber optic sensing lines were placed, corresponding with each protection and installation method. One sensing line contained the fiber reinforced with the glass fiber buffer, other line with the bare fiber inserted in a groove and protected with epoxy resin and, finally, the bare fiber inserted in other groove and protected with the tar. Figure 6.17 shows three pictures of the fiber sensors installation in the asphalt.

Figure 6.19. Pictures of the asphalt platform including optical fibers just before the sensitivity test.

Figure 6.19 illustrates three different pictures showing the pavement when the sensors were already installed. Picture (a) shows the final structure where the sensor fibers position are marked in luminous red. In (b) the glass fiber reinforced cable installed in the sub-base layer is visible and it was taken as reference to measure the layer height. Finally, the last figure shows a fiber appearing from the trench protected with epoxy resin.

Figure 6.20. Pictures of the sensitivity test when different loads are placed over the sensors.

Sensitivity of the fibers was tested by setting different loads over the different fiber sensors (Figure 6.20). In a first stage, it was checked which fibers bore in the installation process. The bare fibers covered by tar did not support the combination of the high temperatures needed to melt the tar (180° approximately) and the stress applied to them. When a little stress was applied to them, the fibers broke, thus this low-cost installation procedure did not work. In the same way, the glass fiber protection was not enough to be installed directly between layers, without groove in the inter-layers. The only successful technique was the epoxy resin protection for fibers inside grooves.

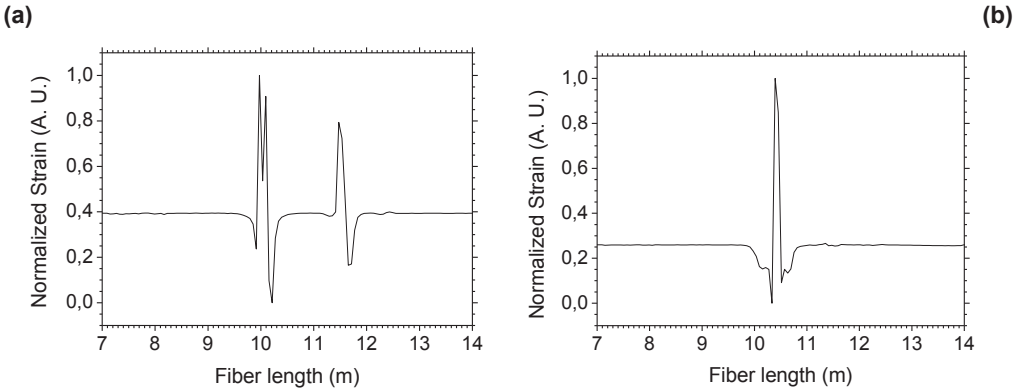

Figure 6.21. (a) Sensor response when a car is placed slightly misaligned respect to the fiber and (b) when one people is placed over the sensing fiber.

After the installation procedure, only three fibers were ready for the sensitivity test. Firstly, the surface fibers installed were not enough protected and when a car was pla-

ced over them, the fibers broke. So finally, in this test, only the internal fibers protected with epoxy resin were able for load measurements in asphalt. Figure 6.21 depicts two strain results obtained with the OBR4600 when it was configured as a distributed sensor interrogator. In chapter 1 it was explained the sensing procedure of the OBR4600 for distributed strain and temperature measurements. Plot (a) illustrates the distributed sensor response when a car was placed over the fiber. The two peaks refer to the load which each tire transferred to the asphalt. The amplitude peaks difference is due to the small misalignment of the car tire axle respect to the fiber. Figure 6.21 (b) is the sensor response when a person is placed on the asphalt. This result demonstrates the high sensitivity of the measuring system to loads. Moreover, when finally a truck was placed on the working fibers position (figure 6.20 (a)), its weight overstrained them and stop measuring.

6.4. CONCLUSIONS

The regular assessment of the structural integrity of the major civil infrastructures such as bridges, dams, tunnels and flyovers is essential as a result of deterioration and damage during their lifetime and to maintain services. This chapter presents three different applications of the fiber optic sensing technologies for SHM purposes. The learned concepts throughout the PhD work have been applied in 3 experiments offering in-field demonstrations of previously proven systems and sensors in laboratory experiments.

- The application of a low cost bending sensor for high strain measurements has been developed and demonstrated. A concrete beam bending test has been simultaneously monitored by FBGs and the low-cost intensity strain bending sensor. The ability for high strain measurement of the proposed sensor was demonstrated during the bending test, showing a wider range of operation than the FBG.

- A Hi-Bi fiber placed inside a fiber loop mirror for corrosion sensing was developed for monitoring reinforced concrete structures. This work presents the complete study of the sensing approach. Firstly, we developed an improved alignment process to achieve uniform pressure sensitivity along the fiber. Secondly, an accelerated corrosion test has been undertaken, confirming the effectiveness of using PCF fibers as sensors for corrosion onset monitoring. The Hi-Bi PCF fiber showed no temperature sensitivity in comparison with PANDA based sensors, being these last ones more sensitive. Moreover, the results gave important information about the state of the concrete structure

under test, such as detection of the onset of corrosion, corrosion rate, crack detection and crack propagation.

• Finally, some preliminary results on traffic monitoring over asphalt pavement structures using fiber optic sensors were presented. It was demonstrated the high sensitivity of the fiber when it was installed protected by epoxy resin in the intermediate asphalt layers. Thus it was demonstrated that it is sensitive to the load of just one person over the pavement. However, alternative installation proposals failed, although the fiber reinforced with glass fiber seems to have high potential when it is correctly installed. Therefore, it has been demonstrated the possibility of monitoring loads on roads with fiber optic distributed sensors systems, thus, in the future, improved installation methods will be checked as well as a more suitable asphalt deploying method will be developed for the usual lying machines.

Part of the previous experiments have been reported following publications [15-17].

6.5. REFERENCES

[1] *"FiberSensing, Sistemas Avançados de Monitorização, S.A." http://w3.fibersensing.com/.*

[2] *"Micron Optics, Inc." http://www.micronoptics.com/*

[3] *"OZ Optics Ltd" http://www.ozoptics.com*

[4] *"Omnisens" http://www.omnisens.com*

[5] *"Luna, Inc." http://lunainc.com/*

[6] *J. M. López-Higuera, "Introduction to fibre optic sensing technology," Handbook of Optical Fibre Sensing Technology, 1-23, (2002).*

[7] *W. K. Szaroletta, N. L. Denton, "Four Point Bending: A New Look" Proc. 2002 American Society for Engineering Education Annual Conference & Exposition, Session 2168, (2002).*

[8] *X. Zou, A. Chao, Y. Tian, N. Wu, H. Zhang, T. Y. Yu, X. Wang, "An experimental study on the concrete hydration process using Fabry–Perot fiber optic temperature sensors," Measurement, 45, 1077-1082 (2012).*

[9] *C. McCague, M. Fabian, M. Karimi, T. Sun, K. Grattan, L. Jaroszewicz, P. Mergo, M. Bravo, "Novel sensor design using photonic crystal fibres for monitoring the onset of corrosion in reinforced concrete structures," Journal of Lightwave Technology, 32, 891-896, (2014).*

[10] *M. Karimi, M. Fabian, T. Sun, K. T. V. Grattan, K. Schuster, L. Jaroszewicz, and P. Mergo, "Transverse force sensitivity of joint photonic crystal fibres", IEEE Sensors conference 2012, 1-4, (2012).*

[11] *T. El Maaddawy, and K. Soudki, "Effectiveness of impressed current technique to simulate corrosion of steel reinforcement in concrete", Journal of Materials in Civil Engineering, 15, 41-47, (2003).*

[12] *S. R. Sharp, K. A. Galal, and M. K. Elfino, "Using Fiber-Optic Sensor Technology to Measure Strains Under the Asphalt Layer of a Flexible Pavement Structure" Research report for the Virginia Transportation Research Council (2006). gttp:/www.virginiadot.org/vtrc/main/online_reports/pdf/07-r5.pdf*

[13] *C. E. Lee, "Standards for Highway Weigh-In-Motion (WIM) Systems." ASTM Standardization News, pp. 32-37 (1991).*

[14] *R. B. Malla, A. Sen, and N. W. Garrick " A Special Fiber Optic Sensor for Measuring Wheel Loads of Vehicles on Highways" MDPI Sensors, 8, 2551-2568 (2008).*

[15] *M. Bravo, J. Sáenz, M. Bravo-Navas, and M. Lopez-Amo, "Fiber optic sensors for monitoring a concrete beam high strain bending test", Proc, SPIE, 21st OFS conference, 7753, 775363, (2011).*

[16] *M. Bravo, J. Sáenz, M. Bravo-Navas, and M. Lopez-Amo, "Concrete Beam Bending Test Monitorization Using a High Strain Fiber Optic Sensor", Journal of Lightwave Technology, 30, 1085-1089 (2012).*

[17] *M. Bravo, C. McCague, M. Fabian, L. Jaroszewicz, P. Mergo, M. Lopez-Amo, K. T. V. Grattan and T. Sun, "Reinforced concrete structural corrosion monitoring using Hi-Bi photonic crystal fibers in a fiber loop structure", Proc. SPIE, 23rd OFS conference , 9157, 91579V, (2014).*

chapter VII
CONCLUSIONS AND OPEN RESEARCH LINES

7.1. CONCLUSIONS

7.1.1. ENGLISH

The potential use of optical fibers as transducers have attracted the scientific community attention, developing transducers for measurements of a variety of physical and chemical magnitudes. Fiber-optic sensing technology offers the ability of measuring in a distributed, quasi distributed or punctual way. In this technological framework, a study about new configurations of sensors, multiplexed and remote networks as well as laser sources for sensing has been presented in this PhD. work.

Chapter 2 is dedicated to describe three new point sensors. Two of the three proposals are interferometric in nature and uses PCFs, and the last one is based on a fiber ring resonator structure in order to enhance the measurement sensitivity. They were developed to be cost efficient while maintaining a high resolution and high dynamic range measurements of strain and displacement.

Chapter 3 is devoted to the development of sensors networks by using a commercial OTDR. Three intensity sensing head structures based on three different reflecting processes have been studied. These sensors have been multiplexed successfully using a bus topology. Furthermore, two of the sensors were interrogated remotely and, in particular, the FLM/LPG sensor was measured at a distance of 253 km. This distance is, for the author´s knowledge, the farthest distance in which one fiber optic sensor has been interrogated without amplification. It was also studied two hybrid multiplexing setups being able to include different sensing techniques in a single network.

In chapter 4, three different applications of the random distributed feed-back (RDFB) effect for multi-wavelength and modulated fiber lasers have been experimentally demonstrated.

In the first section, the basic random-laser structure was filtered by a fiber loop mirror (FLM) interferometer which includes a high birefringence suspended-core photonic crystal fiber (Hi-Bi SC-PCF) to generate a RDFB multi-wavelength fiber laser (MWFL). This multi-wavelength Raman fiber laser presents suitable characteristics for sensors

interrogation. Even more, the configuration can be used as a sensor by simply exploiting the sensing skills of its internal Sagnac filter.

The second configuration attempts to improve the previous laser by using a programmable filter in order to select the desired lasing wavelengths in real time. A maximum wavelength band of ~20 nm can be reconfigured with a minimum distance of 50 GHz between lasing channels. This structure can be easily equalized and switched fulfilling the 100 GHz ITU grid specification for sensing or telecommunication purposes.

In the final point of this chapter, a modulated random mirror laser has been experimentally demonstrated. For the author's knowledge, it is the first demonstration of the internal modulation of a RDFB laser. This structure can be internally modulated by an EOM with no frequency restrictions attributable to the cavity length. It can be modulated without the RF filtering problems or mode-locking characteristics of the conventional fiber laser configurations.

One of the main issues that this PhD. work has addressed is the problem of PCF sensors multiplexing. Chapter 5 presents new sensors multiplexing networks using sensors and laser sources previously developed in chapters 2, 3 and 4. With these and other sensors (point and distributed) and light sources, several demanding topics in sensors multiplexing have been explored. Particularly, PCF sensors multiplexing, remote multiplexing networks and robust multiplexing of point and distributed sensors.

A remote intensity bending sensors multiplexing based on a TDM architecture was performed. It was also developed an in deep study of the wavelength macro-bending influence in SMFs. This study confirmed the feasibility of remote TDM multiplexing of those intensity sensors, taking into account problems such as dispersion and crosstalk. An up to 75 km fiber optic laser system based on a ladder structure which multiplexed six PCF sensors is also presented in this chapter. The system includes a filter, whose bandwidth was optimized in order to reach the most efficient system operation.

Next, OADMs have been demonstrated as suitable devices for WDM addressing of different kind of sensors. The already used PCF interferometer sensors were remotely multiplexed without optical amplification using two different strategies. The last one network used a double-fiber transmission channel allowing us to perform measurements up to 100 km. The system incorporated also a reference wavelength used to increase the resolution of the system.

Two new ultra long multiplexing systems were presented in this chapter. The novelty of

the proposed systems lies on the topologies which entail attractive advantages such as reducing the effect of Rayleigh scattering. It was demonstrated that they were able to remotely multiplex up to 11 fiber Bragg gratings, but this number could be increased. Due to the operation mode of the systems, they act as low noise configurations, where the OSNR of all the sensors was high enough to interrogate them up to 200 km away from the monitoring station.

In order to add robustness and versatility to fiber optic sensor networks, a remote powered by light fiber optic switch which is able to operate at distances up to 100 km was also developed. To the best of the author's knowledge, this is the maximum distance ever achieved when controlling any instrumentation powered by light. By slightly changing the control electronics, it can be also used to control other low consumption devices. As proof of concept applications, this PhD. work experimentally demonstrated the suitability of this FOSw for controlling a resilient FBG sensors network located 50 km away from the interrogation unit and for the multiplexing of Brillouin distributed sensors.

Finally, a versatile network structure based on the switchable RDFB-MWFL was demonstrated for simultaneous multiplexing of sensors of different nature. Two multiplexing sensors sub-networks were simultaneously interrogated using the remote powered by light fiber optic switch. The Raman pump power excess of the random mirror of the laser was used to feed the RFOSw. This technique can multiplex as many sensors sub-networks as output ports the switch have. Furthermore, as the control signal was generated by the fully switchable MWFL, the laser spectrum change also entails the RFOSw port selection.

Chapter 6 presents three different in field applications of the fiber optic sensing technologies for SHM purposes applying sensors and systems shown in previous chapters. The first application proved a low cost bending sensor for high strain measurements in a concrete beam bending test. It showed a wider range of operation than the FBGs based sensors. Next, a Hi-Bi fiber sensor placed inside a fiber loop mirror for corrosion sensing was developed for reinforced concrete structures monitoring. The results gave important information about the state of the concrete structure under test, such as detection of the onset of corrosion, corrosion rate, crack detection and crack propagation. Finally, some preliminary results about traffic monitoring over asphalt pavement structures using fiber optic sensors were presented. The high sensitivity of the fiber was demonstrated when it was installed protected by epoxy resin in the intermediate asphalt layers.

7.1.2 CASTELLANO

La comunidad científica ha desarrollado a día de hoy, utilizando fibra óptica, transductores para la medida de una gran variedad de magnitudes físicas y químicas. Además, la tecnología de fibra óptica ofrece la posibilidad de medir de manera distribuida, cuasi distribuida o puntual. En este marco tecnológico, este trabajo de doctorado presenta un estudio sobre nuevas configuraciones de sensores, de multiplexación y de redes remotas, al igual que de fuentes de luz láser para interrogación de sensores.

Así, el capítulo 2 está dedicado a describir el desarrollo de tres sensores puntuales. Dos de las tres propuestas son de naturaleza interferométrica y utilizan fibras de cristal fotónico. La última está basada en una estructura resonante en anillo cuyo objeto es mejorar la sensibilidad de las medidas de los transductores. En concreto, estos anillos de coste reducido se desarrollaron para conseguir una alta resolución y gran rango dinámico en medidas de deformación y desplazamiento.

El capítulo 3 se centra en el desarrollo de redes de sensores utilizando un OTDR comercial. Para estas redes se han estudiado tres transductores de intensidad basados en tres procesos reflexivos diferentes. Estos sensores se multiplexaron satisfactoriamente utilizando una topología de bus. Además, se interrogaron remotamente dos de esos sensores y, en particular, se monitorizó un sensor FLM/LPG a una distancia de 253 km. Ésta es, en conocimiento del autor, la mayor distancia de interrogación remota obtenida para sensores de fibra óptica sin necesidad de utilizar amplificadores ópticos. También se estudiaron dos esquemas de multiplexación híbridos que permiten incluir diferentes técnicas de medida en una misma red.

En el capítulo 4 se demuestran experimentalmente tres aplicaciones del efecto de realimentación distribuida random para láseres multi-longitud de onda y también su modulación.

En la primera sección del capítulo, la estructura básica de un láser Raman de realimentación distribuida se filtra usando un interferómetro basado en un espejo en fibra (FLM). Este espejo, que incluye una fibra de cristal fotónico de núcleo suspendido altamente birrefringente (Hi-Bi SC-PCF), sirve para generar láseres multi-longitud de onda (MWFLs). Estos láseres pueden utilizarse para interrogar sensores o como sensores en sí mismos explotando las características internas del filtro Sagnac.

La segunda configuración trata de mejorar el láser anterior utilizando un filtro programable para seleccionar las líneas de emisión del láser en tiempo real. Permite confi-

gurar un ancho de banda máximo de ~20 nm con una distancia mínima entre líneas de emisión de 50 GHz. Esta estructura puede ecualizarse y conmutarse de manera sencilla, cumpliendo la rejilla de 100 GHz de la especificación ITU, para aplicaciones de sensores o de comunicaciones.

En el punto final de este capítulo, se demuestra experimentalmente un láser "random" modulado internamente. Esta es la primera vez, en conocimiento del autor, que se demuestra la capacidad de modulación de manera interna de un láser basado en el efecto RDFB. Esta estructura puede modularse internamente por un EOM (modulador electro-óptico) sin ninguna restricción frecuencial causada por reflexiones discretas dentro de la cavidad. Así, el láser puede modularse sin problemas de filtrado RF o sin exhibir los pulsos habituales generados por el enganche de modos en las configuraciones de láseres de fibra convencionales.

Uno de los principales objetivos en el que se ha centrado este trabajo de doctorado ha sido la multiplexación de sensores realizados con fibra de cristal fotónico. El capítulo 5 presenta nuevas redes de multiplexación de sensores utilizando los sensores y las fuentes láser anteriormente desarrolladas en los capítulos 2, 3 y 4. Así se han abordado algunos temas muy exigentes en el ámbito de la multiplexación de sensores. Particularmente, la multiplexación de sensores PCF, las redes de multiplexación de sensores remotos y la multiplexación robusta de sensores puntuales y distribuidos.

En este capítulo se presenta un sistema láser de hasta 75 km basado en una estructura en escalera en la que se multiplexan seis sensores PCF. Este sistema incluye un filtro cuyo ancho de banda fue optimizado para conseguir la mayor eficiencia en la operación del sistema.

A continuación se demostró la capacidad de los OADMs como dispositivos para la multiplexación en longitud de onda de diferentes sensores. Los sensores interferometricos PCF, ya utilizados anteriormente, se multiplexaron de manera remota sin necesidad de amplificación usando dos estrategias diferentes. En concreto, la segunda red presentada usa un canal de transmisión de doble fibra, permitiendo realizar medidas hasta a 100 km de distancia. El sistema también incorpora una longitud de onda de referencia utilizada para aumentar la resolución del sistema.

En el ámbito de los sensores desarrollados con fibras convencionales, se demostró un sistema de multiplexación de sensores de curvatura basado en la multiplexación en el dominio temporal. También se realizó un estudio en profundidad de la influencia en longitud de onda de las macro-curvaturas en fibras monomodo estándar. Este estudio

validó la medida remota y la multiplexación de estos sensores de intensidad, teniendo en cuenta los problemas de dispersión y diafonía.

Este capítulo también incluye dos sistemas ultra largos de multiplexación. La novedad de estos sistemas radica en las topologías desarrolladas. Éstas presentan ventajas atractivas como, por ejemplo, la reducción del efecto de la dispersión Rayleigh. Se demostró que eran válidas para multiplexar 11 sensores FBG, aunque este número podría incrementarse. Debido al modo de operación de los sistemas diseñados, éstos actúan como configuraciones de bajo ruido, y así la relación señal-ruido de todos los sensores es adecuada para interrogarlos a distancias de hasta 200 km, desde una estación de monitorización.

También se desarrolló, para añadir robustez y versatilidad a las redes de sensores de fibra óptica, un conmutador óptico tele-alimentado que puede operar a distancias de hasta 100 km. Esta distancia no había sido alcanzada previamente según nuestros datos. Mediante un diseño adecuado de la electrónica de control, puede usarse para controlar cualquier equipo de bajo consumo. Así en este trabajo de doctorado se demuestra experimentalmente la capacidad de este conmutador óptico para controlar una red de sensores FBG redundante localizada a 50 km de la unidad de interrogación. También se utilizó para la multiplexación de sensores distribuidos basados en el efecto Brillouin.

Finalmente, se demostró una red versátil basada en el láser RDFB-MWFL conmutable para la multiplexación simultánea de sensores de diferente naturaleza. Se interrogaron dos sub-redes de multiplexación de sensores utilizando también el conmutador óptico tele-alimentado. El exceso de bombeo Raman utilizado para la generación del espejo distribuido del láser se utilizó para alimentar el conmutador. Esta técnica permite multiplexar tantas sub-redes de sensores como salidas tenga un conmutador óptico. Además, como la señal de control se genera por el propio láser MWFL conmutable, el cambio de espectro del láser también conlleva la selección de puerto del conmutador tele-alimentado.

Por último, el capítulo 6 presenta tres demostraciones de campo de los sensores y de las tecnologías de medida presentadas en los capítulos anteriores para monitorización de salud estructural. La primera aplicación está dedicada a validar un sensor de curvatura económico para medidas de altas deformaciones durante la prueba de carga de una viga de hormigón. Se demostró un rango de operación mayor que los sensores FBG. A continuación, se desarrolló un sensor basado en una fibra altamente birrefringente incluida dentro de un espejo de fibra (FLM) para la medida de corrosión en estructuras de hormigón armado. Los resultados ofrecieron información importante sobre el estado

de la corrosión interna, sobre la cantidad de corrosión, y también sobre la detección y propagación de fisuras. Finalmente, se presentaron algunos resultados preliminares sobre monitorización de tráfico en estructuras de asfalto utilizando sensores de fibra óptica. Se demostró la alta sensibilidad de la fibra óptica para esta aplicación, instalándose nuestra fibra con protección de resina epoxi en las capas intermedias del asfalto.

7.2. OPEN RESEARCH LINES

Once the conclusions have been exposed, some open research lines should be considered in further detail for future. The most challenging research lines related to this PhD. work are going to be considered. These open lines entail the following topics: random lasers, PCF sensors development and multiplexing, remote sensing and power by light optoelectronic devices.

Regarding random lasers, the interesting lasing characteristics that this structure offers could be used for many new applications in the optical communications and sensing fields. For instance, once the internal modulation of these lasing structures was demonstrated, time domain sensor multiplexing or distributed sensing can be proposed based on them. The performance of the switchable multi-wavelength laser structure can also be improved. More emission lines, narrower emission lines and faster switching time are three topics to be improved.
Associated with the PCF sensors, there are promising open research lines to explore. The PCF's structures and propagation characteristics make them extremely interesting for sensing purposes. However, one of the main disadvantages of these fibers is their splicing complexity. Hence, new splicing methods of PCF should be studied. Ideally, smart splicing programs that auto configure its splicing parameters would be a solution. Other idea regarding the use of these fibers as sensors, is the fiber customization by using a femtosecond laser. Thus, different sensing structures such as FBGs on PCFs could be performed. Finally, the development of fiber networks which multiplex PCF sensors is a challenge to overcome in order to achieve cost efficient sensing solutions.

Finally, concerning remote sensing, the future lines might the following: to increase the distance, the signal to noise ratio and the number of sensors in the same network. In this regard, power by light optoelectronics feeding could be interesting to reach the challenges described. Therefore, different optoelectronic units should be adapted to power by light operation. MEMS technology seems to be the most suitable technology due to its low consumption characteristic.

7.3. PUBLICATIONS

In the frame of this PhD work, 18 journal contributions (12 as first author and 6 as co-author) and 15 conference papers (10 as first author and 5 as co-author) have been published, as listed in Appendix A.

appendix

Appendix A

List of publications related to the PhD work.

1. CONTRIBUTIONS TO INTERNATIONAL JOURNALS

[1] *A. M. R. Pinto, **M. Bravo**, M. Fernandez-Vallejo, M. Lopez-Amo, J. Kobelke and K. Schuster "Suspended-core fiber Sagnac combined dual-random mirror Raman fiber laser", Optics Express, Vol. 19, No. 12, pp. 11906-11915, (2011).*

[2] ***M. Bravo**, J. M. Baptista, J. L. Santos, M. Lopez-Amo, and O. Frazao, "Ultralong 250 km remote sensor system based on a fiber loop mirror interrogated by an optical time-domain reflectometer." Optics Letters, 36, 4059-4061 (2011).*

[3] ***M. Bravo**, M. Fernandez-Vallejo and M. Lopez-Amo, "Hybrid OTDR-fiber laser system for remote sensor multiplexing," IEEE Sensors Jounal, 12, 174-178, (2012).*

[4] ***M. Bravo**, A. M. R. Pinto, M. Lopez-Amo, J. Kobelke and K. Schuster, "High precision micro-displacement fiber sensor through a suspended-core Sagnac interferometer", Optics Letters, 37,202-204 (2012).*

[5] ***M. Bravo** and M. Lopez-Amo, "Remote-Time Division Multiplexing of Bending Sensors Using a Broadband Light Source", Journal of Sensors, 2012, 154586, 6pp (2012).*

[6] ***M. Bravo**, J. Sáenz, M. Bravo-Navas, and M. Lopez-Amo, "Concrete Beam Bending Test Monitorization Using a High Strain Fiber Optic Sensor", Journal of Lightwave Technology, 30, 1085-1089 (2012).*

[7] *S. Rota-Rodrigo, A. M. R. Pinto, **M. Bravo** and M. Lopez-Amo, "An In-Reflection Strain Sensing Head Based on a Hi-Bi Photonic Crystal Fiber", Sensors, 13, 8095-8102 (2013).*

[8] ***M. Bravo**, X. Angulo-Vinuesa, S. Martin-Lopez, M. López-Amo, and M. González-Herráez, "Slow-Light and Enhanced Sensitivity in a Displacement Sensor Using a Lossy Fiber-Based Ring Resonator", Journal of Lightwave Technology, 31, 3752-3757 (2013).*

[9] *A. Candiani, **M. Bravo**, S. Pissadakis, A. Cucinotta, M. Lopez-Amo, and S. Selleri, "Magnetic Field Sensor Based on Backscattered Intensity Using Ferrofluid", IEEE Photonics Technology Letters, 25, 1481-1483, (2013).*

[10] ***M. Bravo**, M. Fernandez-Vallejo, M. Lopez-Amo, "Internal modulation of a Random fiber laser", Optics Letters, Vol. 38, No. 9, pp. 1542-1544, (2013).*

[11] ***M. Bravo**, M. Fernández-Vallejo, M. Echapare, M. López-Amo, J. Kobelke, and K. Schuster, "Multiplexing of six micro-displacement suspended-core Sagnac interferometer sensors with a Raman-Erbium fiber laser", Optics Express, 21, 2971-2977 (2013).*

[12] M. Fernandez-Vallejo, **M. Bravo**, and M. Lopez-Amo, "Ultra-Long Laser Systems for Remote Fiber Bragg-Gratings Arrays Interrogation", IEEE Photonics Technology Letters, 25, 14, 1362-1364 (2013).

[13] **M. Bravo**, M. A. Erro, J. M. Algueta, S. Diaz and M .Lopez-Amo, "Remote fiber optic switch powered by light for robust interrogation of fiber Bragg grating sensor networks", Meas. Science and Technology, 24, 94021 (2013).

[14] **M. Bravo**, A Ullán, A. Zornoza, A.Loayssa, M. Lopez-Amo, J.M. Lopez-Higuera, "Application of Remote Power-by-Light Switching in a Simplified BOTDA Sensor Network" Sensors, 13, 17434-17444 (2013).

[15] **M. Bravo**, A. Candiani, A. Cucinotta, S. Selleri, M. Lopez-Amo, J. Kobelke and K. Schuster, "Remote PCF-based sensors multiplexing by using optical add-drop multiplexers" Optics & Laser Technology, 57, 9-11 (2014).

[16] **M. Bravo**, J. M. Baptista, J. L. Santos, M. Lopez-Amo, and O. Frazao, "Micro-Displacement Sensor combined with a Fiber Ring Interrogated by an Optical Time-Domain Reflectometer" IEEE Sensors Journal, 14, 793-796, (2014).

[17] C. McCague, M. Fabian, M. Karimi, **M. Bravo**, L. R. Jaroszewicz, P. Mergo, T. Sun and K. T. V. Grattan, "Novel Sensor Design Using Photonic Crystal Fibres for Monitoring the Onset of Corrosion in Reinforced Concrete Structures", Journal of Lightwave Technology, 32, 891 – 896, (2014).

[18] V. DeMiguel-Soto, **M. Bravo** and M. Lopez-Amo, "Fully-switchable multi-wavelength fiberlaser assisted by a Random mirror", Optics Letters, Vol. 39, No. 7, pp. 2020-2023, (2014).

2. CONTRIBUTIONS TO INTERNATIONAL JOURNALS UNDER REVIEW

[1] D. Leandro, **M. Bravo**, A. Ortigosa and M. Lopez-Amo, "Real-time FFT analysis for interferometric sensors multiplexing", acepted for publication in Journal of Lightwave Technology

[2] **M. Bravo**, V. DeMiguel-Soto, A. Ortigosa and M. Lopez-Amo, "Fully-Switchable Multi-Wavelength Fiber Lasers Based on Random Distributed Feed-Back for Sensors Interrogation", under consideration in Journal of Lightwave Technology

3. CONTRIBUTIONS TO INTERNATIONAL CONFERENCES

[1] **M. Bravo**, M. Fernandez-Vallejo and M. Lopez-Amo, "Hybrid OTDR-fiber laser system for remote sensor multiplexing," Proc. SPIE, 7653, 765340-1-4, (2010).

[2] **M. Bravo**, J. M. Baptista, J. L. Santos, M. Lopez-Amo, and O. Frazao, "New Interrogation Technique for Multiplexing LPG-Fiber Loop Mirrors Based Displacement Sensors Using an OTDR" procedings Sensors, 2011 IEEE Sensors Conference, 341,342, (2011).

[3] **M. Bravo**, J. Sáenz, M. Bravo-Navas, and M. Lopez-Amo, "Fiber optic sensors for monitoring a concrete beam high strain bending test", Proc, SPIE, 21st OFS conference, 7753, 775363, (2011).

[4] M. Fernandez-Vallejo, **M. Bravo**, and M. Lopez-Amo, "200-km long fiber ring laser for multiplexing fiber Bragg gratings array," Proc. SPIE, 22nd OFS conference, 8421, 84218J, 1–4, (2012).

[5] **M. Bravo**, M. A. Erro, J. M. Algueta, S. Diaz and M. Lopez-Amo, "Remote resilient FBG multiplexing network controlled by a powered by light fiber optic switch" Proc. SPIE, 22nd OFS, 8421, 84218F (2012).

[6] S. Rota-Rodrigo, **M. Bravo**, A. M. R. Pinto, and M. Lopez-Amo, "High-sensitivity PCF sensing head for strain measurement" Proc. SPIE, 22nd OFS, 8421, 842136, (2012).

[7] A Ullán, **M. Bravo**, A. Zornoza, A.Loayssa, M. Lopez-Amo, J.M. Lopez-Higuera, " BOTDA sensor network with power by light remote switching", Proc. SPIE, 22nd OFS conference, 8421, 84218E, 1–4, (2012).

[8] X. Angulo-Vinuesa, **M. Bravo**, S. Martin-Lopez, M. Lopez-Amo and Miguel Gonzalez-Herraez, "Wide range group delay tuning in lossy fiber ring resonator", Proc SPIE, 22nd OFS conference, 8421, 842197 (2012).

[9] **M. Bravo,** X. Angulo-Vinuesa, S. Martin-López, M. Lopez-Amo and M. González-Herráez, "Versatile all-fiber slow-light assisted sensor", Proc. SPIE, Advances in Slow and Fast Light VI, 8636, 86360K (2013).

[10] **M. Bravo**, X. Angulo-Vinuesa, S. Martin-Lopez, M. Lopez-Amo and Miguel Gonzalez-Herraez, "Turning a low Q fiber resonator into a high-sensitivity displacement sensor using slow light concepts" Proc. SPIE 5th EWOFS, 8794, 879420 (2013).

[11] **M. Bravo**; M. Fernandez-Vallejo; M. Lopez-Amo; J. Kobelke; K. Schuster, "Fiber optic sensor networks based on OADM devices with a bus configuration", Proc. SPIE, 5th EWOFS, 8794, 87943V (2013).

[12] **M. Bravo**, V. DeMiguel-Soto, A. Ortigosa and M. Lopez-Amo, "Fully switchable multi-wavelength fiber laser based interrogator system for remote and versatile fiber optic sensors multiplexing structures" Proc. SPIE, 23rd OFS conference, 9157, 91576P (2014).

[13] **M. Bravo**, C. McCague, M. Fabian, L. Jaroszewicz, P. Mergo, M. Lopez-Amo, K. T. V. Grattan and T. Sun, "Reinforced concrete structural corrosion monitoring using Hi-Bi photonic crystal fibers in a fiber loop structure", Proc. SPIE, 23rd OFS conference , 9157, 91579V, (2014).

4. CONTRIBUTIONS TO NATIONAL CONFERENCES

[1] **M. Bravo**, M. Fernández-Vallejo, M. Echapare, M. López-Amo, J. Kobelke, and K. Schuster, "Multiplexación de 6 sensores de micro-desplazamiento basados en un interferómetro Sagnac con fibra de núcleo suspendido mediante un láser de fibra Raman-erbio", VIII Reunion Española de Optoelectrónica (OPTOEL), Alcalá de Henares, (2014).

[2] M. Sozzi, S. Selleri, A. M. R. Pinto, **M. Bravo**, and M. López-Amo, "Polarimetric Hi-Bi PCF refractive index sensor for volatile liquids", Convegno Nazionale Sensori, Roma, (2012).